THE DISTANCE TO THE NORMA CLUSTER AND ITS RELATION TO THE GREAT ATTRACTOR

Thesis by
TOM MUTABAZI
BSc. Ed. (MUST), BSc. Hons. (UCT)

Submitted in total fulfilment of the academic requirements
for the degree of Doctor of Philosophy
Department of Astronomy

UNIVERSITY OF CAPE TOWN
SOUTH AFRICA

Supervisors:

Dr. Sarah L. Blyth, A/Prof. Patrick A. Woudt
Department of Astronomy, University of Cape Town

MAY 25, 2015

Abstract

The Local Group's peculiar motion with respect to the cosmic microwave background has been measured with high precision and found to be $\sim 627 \pm 22$ km s^{-1}, but the source of this motion is not clear. Studies to constrain the fractional contribution of the local mass overdensity, particularly in the Great Attractor region and the more distant Shapley Supercluster, remain contradictory. This work is an attempt to disentangle these contributions by measuring a redshift-independent distance to the Norma cluster, which lies at, or close to, the core of the Great Attractor, in order to determine its peculiar velocity. A reliable measurement of the distance and peculiar velocity of Norma will help clarify the velocity flows in the Great Attractor region. The challenge is with observing in the Zone of Avoidance since star crowding and Galactic extinction effects are severe at such low Galactic latitudes. High quality near-infrared images have been used in the photometric analysis for the Norma cluster sample so as to minimise the effect of Galactic extinction. In addition, the imaging cameras used have a small pixel scale resulting in well resolved images for reliable foreground star-subtraction hence accurate photometry.

In order to determine the redshift-independent distance, I applied two independent, complementary methods: the Fundamental Plane and the Tully-Fisher relations. The redshift-independent distance and the peculiar velocity of the Norma cluster were measured using 1) the K_s-band Fundamental Plane analysis for 31 galaxies using the 3.6 m New Technology Telescope (NTT) at the European Southern Observatory (ESO) 2) the J- and K_s-band Fundamental Plane analysis for 31 galaxies using the Japanese 1.4 m InfraRed Survey Facility (IRSF) at the South African Astronomical Observatory (SAAO) 3) the combined NTT and IRSF K_s-band Fundamental Plane analysis for 41 galaxies 4) the K_s-band Tully-Fisher analysis for 12 galaxies using near-infrared images from the IRSF and HI profiles obtained from the 64-m Parkes radio telescope.

The Fundamental Plane is a relationship between $\log(r_e)$, $\log(\sigma)$, and $\langle\mu_e\rangle$ for early-type galaxies, where r_e is the effective radius, $\langle\mu_e\rangle$ is the galaxy mean effective surface brightness (mean surface brightness within r_e), and σ is the galaxy central velocity dispersion. The relation is written as $\log(r_e) = a \times \log(\sigma) + b \times \langle\mu_e\rangle + c$, where a, b, are the slopes and c is the intercept or zero point. Since the Fundamental Plane relation is a secondary distance indicator, the well studied Coma cluster was used as the reference (calibrator). The calibration sample consists of 121 early-type galaxies. The distance to the Norma cluster was measured by constructing the Norma and Coma cluster Fundamental Planes and thereafter determining the zero point offset between these two clusters. Particular care was given to investigate possible sources of systematic uncertainties for this study at low Galactic latitudes. The simulations conducted in this work show no significant systematic contribution from sky background variations and star-subtraction effects, that is, -0.008 mag (~ 29 km s^{-1}) and -0.014 mag (~ 50 km s^{-1}), respectively. The worst effect of Galactic extinction corrections for the Norma sample is in the range 0.009 mag to 0.014 mag (-33 km s^{-1} to -51 km s^{-1}).

A simultaneous inverse least-squares fit to the Norma and Coma samples resulted in the Fundamental Plane fit parameters given by $a = 1.551 \pm 0.053$ and $b = 0.324 \pm 0.017$. The scatter in $\log\sigma$ is ~ 0.082 dex which corresponds to a distance uncertainty of $\sim 29\%$ per galaxy. The scatter of 0.082 dex along $\log\sigma$ is equivalent to 4.6% uncertainty in the distance to the Norma cluster given the sample of 41 galaxies. The zero point offset between the Fundamental Plane of the Norma cluster and the Coma cluster is 0.150 ± 0.013 dex. Assuming that the Coma cluster is at rest with respect to the cosmic microwave background frame and $z_{CMB}(\mathrm{Coma}) = 0.0240$, the derived peculiar velocity and distance to the Norma cluster are $v_{\mathrm{pec}} = -109 \pm 157$ km s^{-1} and $H_0 d = 5063 \pm 147$ km s^{-1}, respectively. Previous dynamical analysis of the Norma cluster by Woudt et al. (2008), using radial velocities of 296 Norma cluster member galaxies showed that the early-type (ellipticals + lenticulars) and the late-type (spirals + irregulars) galaxy populations are offset from the mean cluster velocity by $\Delta v \sim 108 \pm 101$ km s^{-1} and $\Delta v \sim 59 \pm 88$ km s^{-1}, respectively. Assuming the mean velocity of the early-type galaxy population gives a better estimate of the Norma cluster's mean radial velocity results in $v_{\mathrm{pec}} = -2 \pm 160$ km s^{-1}.

The Tully-Fisher relation relates the total luminosity (or absolute magnitude) and rotation velocity for spiral galaxies, that is, $L \propto W^{\beta}$. For this analysis, I obtained isophotal K_s-band magnitudes based on the 20 mag arcsec^{-2} isophote. These were combined with the HI line widths and an existing K_s-band isophotal Tully-Fisher template by Said (2013) was used to measure individual galaxy distances. The final sample, after HI line width and inclination angle cuts, consisted of 12 spiral galaxies. The measured individual galaxy distances showed a bimodal distribution although with small statistics. Of the 12 galaxies, six were found to be foreground galaxies with a mean distance of 28 ± 7 Mpc. The measured peculiar velocity using the remaining six Norma cluster member galaxies is 74 ± 332 km s^{-1}.

The Norma cluster's distance measured using the Tully-Fisher relation is in good agreement with that measured using the Fundamental Plane analysis, that is, the distances obtained using the Tully-Fisher and the combined K_s-band Fundamental Plane analyses are 65.1 ± 4.4 Mpc and 67.5 ± 2.0 Mpc, respectively (assuming $H_0 = 75$ km s^{-1} Mpc^{-1}). Norma cluster's measured peculiar velocities using the Fundamental Plane and Tully-Fisher analyses are small and within errors, consistent with zero. These measured peculiar velocities of the Norma cluster are lower than previously reported positive peculiar velocities for galaxies/groups/clusters in the Great Attractor region and hence the Norma cluster may indeed represent the core of the Great Attractor.

DEDICATION

To my parents; Mr. & Mrs. Hakiza Benon.
I gratefully thank you for your endless love and support.

SPECIAL THANKS:

To Dr. John Lucey, David Nzita, Jackson Byigero, Charles Manigera,
Dr. Maniraguha, David Rwarinda, Richard Mfitundinda, Bernard Nyirimanzi.
To friends & family, thank you for your support in very many different ways.

Plagiarism Declaration

I, Tom Mutabazi do hereby declare that I understand what plagiarism is, that this work is mine, and that it has never been and will never be submitted to another university for any purpose, for academic reasons or recognition, and where the work in this dissertation is not my original, the reference is indicated therein.

ACKNOWLEDGEMENTS

I am grateful to my supervisors, Dr. Sarah L. Blyth and A/Prof. Patrick A. Woudt for their constant encouragement and assistance, most times being patient with me, while being very supportive during the time the data were being reduced, analysed, interpreted, and put together in the form of a thesis. I would also like to extend my sincere gratitude and appreciation to Prof. Tom Jarrett for many useful discussions regarding quality near-infrared photometric analysis. Your expertise greatly improved the quality of this work.

To Dr. John Lucey for invaluable input regarding photometric analysis, Fundamental Plane fitting and bias corrections, and most especially how to measure relative distances using the modified Faber-Jackson relation. Many times you stayed up late, responding to my numerous queries via emails and I am very grateful. I would also like to thank you for kindly providing me with the K_s-band photometric data (PSF-corrected effective radii) for the Coma cluster early-type galaxies as well as the spectroscopic data (central velocity dispersions) for the Norma cluster galaxies used in the Fundamental Plane analysis. Your invaluable input to this work can not be described in words!

I am grateful to Dr. Chieng Peng for publicly making available the GALFIT software and especially for his invaluable help and time in replying various emails, explaining and giving me tips on how best to use the GALFIT software for quality and reliable results. To Dr. La Barbera for providing me with the MIST algorithm which I used in fitting the Fundamental Plane, to complement and compare with the results obtained from my inverse least-squares fit. Special thanks to Dr. Ihab Riad and Wendy Williams for their excellent contributions leading up to this work, through discussions about near-infrared observations and data reduction especially photometric calibration and star-subtraction. I would also wish to thank Khaled Said for his near-infrared Tully-Fisher calibration and making his template available for use in my K_s-band isophotal Tully-Fisher analysis.

To all staff at the SAAO (Sutherland, South Africa) and CSIRO (Parkes, Australia) observatories for their warm and kind assistance during the time of observations. Special thanks to Stacy Mader (at CSIRO – Parkes) and Takahiro Nagayama (Nagoya University – Japan) for their help with telescope operations and observations and providing excellent tips on data reduction. To Carol and Roz at UCT's department of Astronomy for helping out with administration-related work, and to Bianca for software installations and IT-related queries. The NTT K_s-band images used in this study were obtained by Dr. Anja Schröder. In addition, her expertise in Galactic extinction corrections and the 64 m Parkes HI data reduction and analysis greatly improved the quality of this work, and I am very grateful. To Dr. Maciej Billick for useful discussions regarding velocity flows and the Local Group's peculiar velocity.

I am very grateful, and sincerely acknowledge financial support from the South African SKA project for Human Capacity development for the entire period during which this thesis

was being prepared to its complete form. The trip to Australia for HI observations was jointly funded by the SA SKA and the department of Astronomy, University of Cape Town through the multi-wavelength financial support.

This work makes use of data products from the Two Micron All Sky Survey, which is a joint project of the University of Massachusetts and the Infrared Processing and Analysis Center/California Institute of Technology, funded by the National Aeronautics and Space Administration and the National Science Foundation.

The spectroscopic data (central velocity dispersions) for the Coma cluster sample were taken from the Sloan Digital Sky Survey Data Release 8 (SDSS DR8). Funding for the SDSS and SDSS-II has been provided by the Alfred P. Sloan Foundation, the Participating Institutions, the National Science Foundation, the U.S. Department of Energy, the National Aeronautics and Space Administration, the Japanese Monbukagakusho, the Max Planck Society, and the Higher Education Funding Council for England. The SDSS Web Site is `http://www.sdss.org/`.

This research has made use of NASA's Astrophysics Data System Bibliographic Services. I have also made use of the NASA/IPAC Extragalactic Database (NED). NED is operated by the Jet Propulsion Laboratory, California Institute of Technology, under contract with the National Aeronautics and Space Administration.

PREFACE

The results from the K_s-band Fundamental Plane analysis based on the imaging carried out using the New Technology Telescope (NTT) at the European Southern Observatory were published in the Monthly Notices of the Royal Astronomical Society (MNRAS, 2014, volume 439, pages 3666 — 3682) entitled **"The Norma cluster (ACO 3627) – III. The distance and peculiar velocity via the near-infrared K_s-band Fundamental Plane"** with the authors: T. Mutabazi, S. L. Blyth, P. A. Woudt, J. R. Lucey, T. H. Jarrett, M. Bilicki, A. C. Schröder, and S. A. W. Moore.

Short contents

Contents

List of Figures

List of Tables

CHAPTER 1

INTRODUCTION

The serendipitous discovery of the cosmic microwave background radiation (CMB) by Arno Penzias and Robert Wilson in the mid-1960s (Penzias & Wilson, 1965) provided crucial evidence for the Big Bang model. The discovery of this thermal radiation left over after the Big Bang led to more research being conducted in a bid to better understand the origin and structure of the universe and provide constraints to standard cosmological models. CMB observations and interpretation have since evolved over time; from the Cosmic Background Explorer (COBE) satellite (Efstathiou et al., 1992; Smoot et al., 1992; Wright et al., 1992; Mather et al., 1994; Bennett et al., 1996), to the Wilkinson Microwave Anisotropy Probe (WMAP) satellite (Hinshaw et al., 2009; Jarosik et al., 2011), and more recently by the Planck satellite (Planck Collaboration et al., 2014b,c). The observations show the CMB to be almost isotropic and homogeneous, with tiny temperature fluctuations of 1 part in 10^5. The stars, galaxies, clusters of galaxies, and the superclusters observed today are thought to have been seeded by the primordial fluctuations seen in the CMB when the universe was ~ 380,000 years old.

1.1 Large Scale Structures

The modern understanding of the size and structure of the universe began after the "Great Debate" between Harlow Shapley and Heber Curtis in the early 1920s, about the nature of the "spiral nebulae" and the size of the universe (Shapley & Curtis, 1921). The debate focussed on whether the observed nebulae were extragalactic or nearby objects within the Milky Way. It was soon after confirmed, that the "nebulae" were galaxies outside the Milky Way (Hubble, 1926). This marked the beginning of extragalactic distance measurements (redshifts) to map the distribution of galaxies in the universe (Hubble, 1929c). The redshift, z, is measured from the shift in spectral features from the wavelength at which they were emitted (λ_e) to the wavelength at which the light is actually observed (at wavelength λ_o). The redshift is calculated using

$$z = \frac{v}{c} = \frac{\lambda_o - \lambda_e}{\lambda_e}, \tag{1.1}$$

where c is the speed of light and v is the galaxy's apparent recession velocity ($v = cz$). For receding galaxies, the wavelength of the observed radiation, $\lambda_o = \lambda_e(1+z)$, is longer than the wavelength of

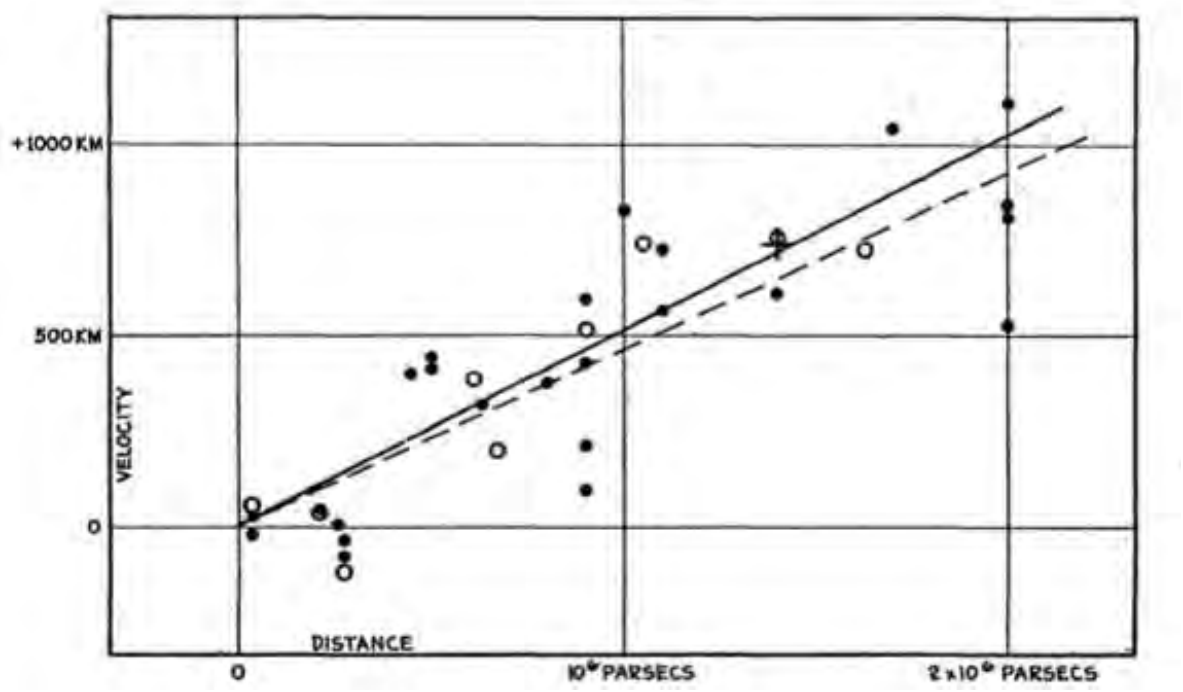

Fig. 1.1: The linear relationship between distance and redshift as observed by Hubble. Figure taken from Hubble (1929a).

the emitted radiation, λ_e, and they are said to be "redshifted". All galaxies we observe, apart from those in the Local Group, are redshifted. The Local Group is a gravitationally bound system which includes the Milky Way, Andromeda (also known as M31) and their satellites within ~ 1 Mpc (the most prominent of these satellite galaxies being M33, the Small and Large Magellanic Clouds). Hubble and others observed and measured galaxy redshifts and found the recession velocities to increase with the distance to the galaxy (see Figure 1.1). This has since been referred to as the Hubble law (Hubble, 1929b), that is,

$$v = cz = H_0\, d, \tag{1.2}$$

where d is the distance to the galaxy in Mpc. The interpretation of the Hubble law is that the universe is expanding and the value of H_0 is a measure of the present/current rate of expansion. The precise value of the global constant H_0 remains uncertain thus prompting the introduction of the parameter h so that $H_0 = 100\,h$ km s^{-1} Mpc^{-1} where $\frac{1}{2} \lesssim h \lesssim 1$. Hubble's initial value of the constant, H_0, was far too high, that is, $H_0 \sim 500$ km s^{-1} Mpc^{-1} (Hubble, 1929b, 1936). The over-estimated value was partly due to incorrect calibration (Baade, 1954) resulting from the fact that there are two different types of Cepheids (Baade & Minkowski, 1954; Baade, 1956). In addition, Sandage (1954) pointed out that some of the brightest stars used by Hubble were clouds of hot gas (ionised HII regions) and this led to the over-estimation of H_0. Significant improvements have since been made following the launch of the Hubble Space Telescope (Freedman et al., 2001). Current values of H_0 approach 70 km s^{-1} Mpc^{-1} with an uncertainty of $\leq 10\%$, for example, through optical and infrared observations of Cepheid variables (Riess et al., 2011), the Carnegie Hubble Program (Freedman et al., 2012), the Wilkinson Microwave Anisotropy Probe (WMAP) satellite (Spergel et al., 2007; Hinshaw et al., 2009; Jarosik et al., 2011; Bennett et al., 2013), Cosmic Flows Program (Tully et al., 2013; also see Sorce et al., 2014) and more recently the Planck satellite (Planck Collaboration et al., 2014a,b) — also see more recent results by Efstathiou (2014) and the excellent review by Freedman & Madore (2010) which discusses the significant improvements in the determination of the Hubble constant.

Despite the controversy about the value of the Hubble constant, the Hubble law has played a major role in studies of the large scale structure of the Universe through galaxy redshift surveys, such as the Two-degree Field Galaxy Redshift Survey (Colless et al., 2001a), the Sloan Digital Sky Survey (York et al., 2000; Abazajian et al., 2003; Aihara et al., 2011), the Six-degree Field Galaxy Survey (Jones et al., 2009; Beutler et al., 2011), the VIMOS[1] Public Extragalactic Survey (VIPERS, de la Torre et al., 2013; Garilli et al., 2014), and the Two Micron All-Sky Redshift Survey (2MRS, Huchra et al., 2000, 2012), allowing us a 3-D view of the structure of the Universe.

1.1.1 Structure Formation

The discovery of the cosmic microwave background radiation, the thermal radiation left behind after the Big Bang (Penzias & Wilson, 1965), has greatly shaped our understanding of the formation of the universe. The CMB radiation was found to be almost isotropic and homogeneous, covering the entire sky. Further CMB observations by the Cosmic Background Explorer (COBE) satellite (Figure 1.2), the Wilkinson Microwave Anisotropy Probe (WMAP) satellite, and more recently by the Planck satellite (Figure 1.3) have improved our knowledge of the structure and formation of the universe by revealing tiny temperature fluctuations in the CMB. These tiny temperature fluctuations are of the order of one part in 10^5, with the CMB spectrum resembling that of a blackbody with an average temperature, $T = 2.725$ K (Mather et al., 1999; Fixsen, 2009). Figure 1.2 shows the CMB as observed by COBE; the emission from the Milky Way is clearly visible in the middle panel. The map shows the CMB dipole (top panel), and the small temperature fluctuations (bottom panel); red is hot while blue represents cold regions on the sky. The temperature variations or the temperature differences between the red and blue regions are on the order of 10^{-5} K. The CMB dipole is a result of the Local Group's motion with respect to the CMB rest frame (see §1.2 for a detailed discussion).

In the framework of our current best theory of structure formation, Lambda cold dark matter model (ΛCDM; e.g, Springel & Hernquist, 2003), the dark matter is clumped in the regions of higher density and these higher density regions grew in both size and gravity as they attracted more matter. At first, radiation was "tied" to normal matter. After decoupling, normal matter was also gravitationally attracted to these higher density regions. The dense regions became more dense, contracted and collapsed resulting in the large scale clustering while the less dense regions formed what we currently observe as voids; see for example, Blumenthal et al. (1984) and Springel et al. (2005). The majority of the observed galaxies reside in sheets, walls and filaments. Voids are the empty spaces between filaments, that is, the walls and filaments surround the voids (see for example, Figures 1.4 and 1.5).

1.1.2 Mapping the Universe: Galaxy Redshift Surveys

Various redshift surveys have been undertaken in a bid to answer a number of outstanding questions regarding the nature, structure and formation of the universe. By applying the Hubble law, distances to extragalactic objects can be approximated from the redshift, measured either from spectroscopy or photometry, where the former is more accurate. The first spectroscopic galaxy redshift survey was conducted in late 1970s by researchers at the Center for Astrophysics (CfA), targeting $\sim$5,800 galaxies. The CfA survey mapped the large-scale structure of the universe, providing for the first time, 3-D maps showing the distribution of matter and the large scale clustering of galaxies in the Universe (Huchra et al., 1983). They identified voids,

[1]VIMOS: VIsible imaging Multi-Object Spectrograph.

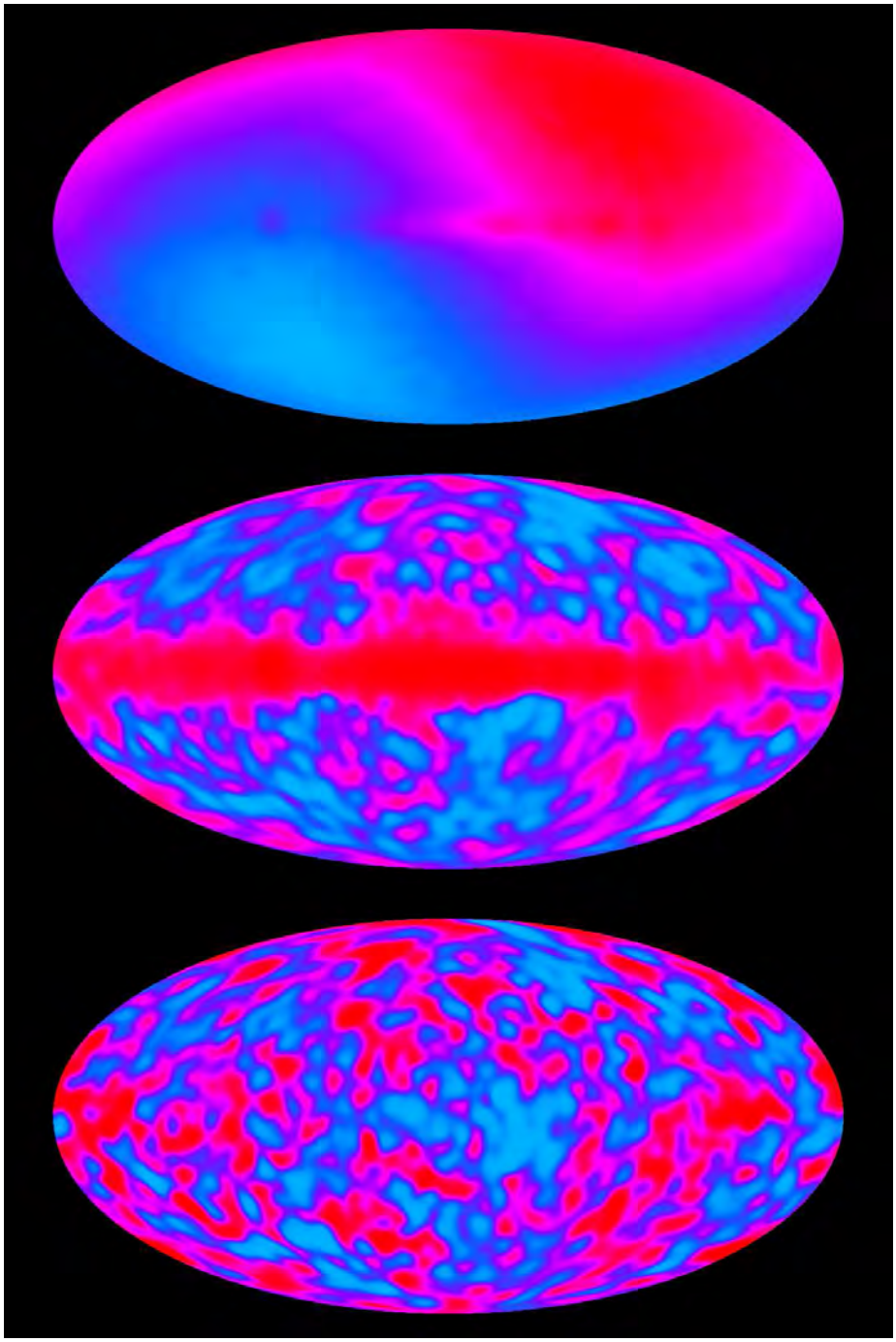

Fig. 1.2: The CMB from COBE. The top panel shows the dipole in the CMB, the middle panel shows the CMB, after subtracting the dipole while the bottom panel shows the CMB temperature fluctuations after both the dipole and radiation from the Milky Way have been subtracted. The image was taken from the Legacy Archive for Microwave Background Data Analysis (LAMBDA) data products. Credit: NASA and COBE Science Team.

walls, and filaments as well as galaxy clusters and superclusters where the filaments meet (see Figure 1.4). The survey also identified one of the greatest early discoveries – the Great Wall (Geller & Huchra, 1983, 1989) as seen in Figure 1.4 (see the top right and bottom left-hand panels), at a recession velocity, $cz \approx 10,000\,\mathrm{km\,s^{-1}}$. Around the same time, Fairall et al. (1983) published his southern redshift catalogue identifying a number of large voids and filaments.

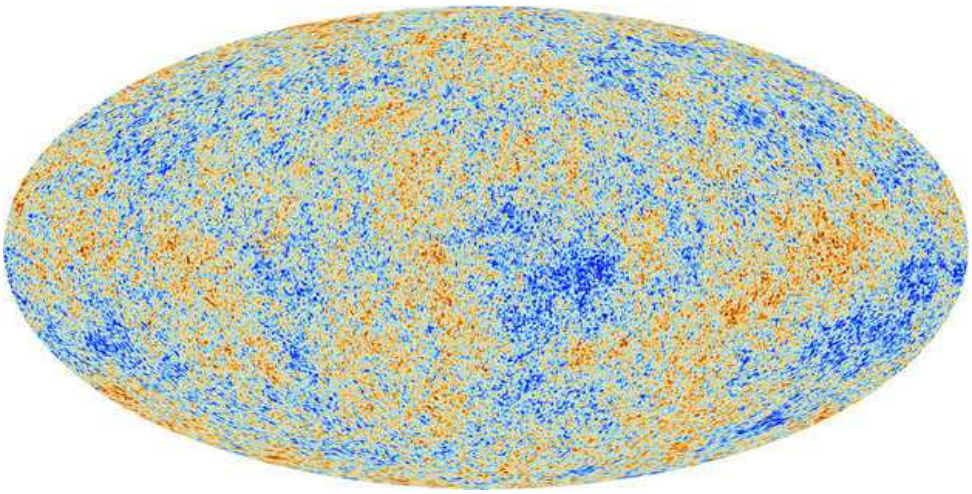

Fig. 1.3: The CMB as seen by Planck. The orange and blue represent warmer and cooler regions, respectively. Not only have the results from Planck provided a finer, small scale, well resolved temperature map (partly due to the Planck's greater sensitivity and better resolution than both COBE and WMAP satellites), but also found that the density of dark matter is slightly higher than originally found from the WMAP observations, that is, $\sim 27\%$ of the universe is in the form of dark matter. The values extracted indicate a lower Hubble constant, i.e, $H_0 = 67.8 \pm 0.77\,\mathrm{km\,s^{-1}\,Mpc^{-1}}$ (Planck Collaboration et al., 2014a) than that from WMAP data (Hinshaw et al., 2009). Credit: ESA/NASA and the Planck Collaboration.

With improved telescope ability and detector power, for example multi-object spectrographs, the survey size (area and volume being surveyed and hence the number of galaxies targeted) for more recent redshift surveys has increased tremendously. These surveys have been utilised in studying the formation and evolution of galaxies. This has, in turn, improved our understanding of the large scale structure of the universe. Such large-volume surveys include the Two-degree Field Galaxy Redshift Survey (2dFGRS; Colless et al., 2001a), which was conducted using the Two-degree field spectrograph on the Anglo-Australian Telescope. The 2dFGRS measured reliable redshifts of $\sim 221{,}414$ galaxies (with an extinction corrected magnitude limit of $b_J = 19^{\mathrm{m}}.45$); over ~ 2000 square degrees and a median redshift of $z = 0.11$ (Colless et al., 2001a; Cole et al., 2005).

More recently, the Sloan Digital Sky Survey (SDSS) has conducted a galaxy redshift survey up to $z \sim 0.7$ (York et al., 2000; Aihara et al., 2011) – this includes SDSS-I and SDSS-II (Abazajian et al., 2009) as well as SDSS-III/BOSS[2] (Eisenstein et al., 2011; Anderson et al., 2014). The SDSS is one of the largest redshift surveys conducted to date. The survey uses a 2.5 m wide-angle optical telescope, and performs both imaging (in five filters; u, g, r, i, z) and spectroscopy and contains spectra for $\sim 930{,}000$ galaxies (Abazajian et al., 2009), thereby revealing the large scale structure of the universe in a way it has never been seen before. It resulted in the detection of baryonic acoustic oscillations (Percival et al., 2010) and confirmed the Sloan Great Wall, which is thought to be the largest observed large scale structure to date. Currently, the Tenth SDSS Data Release (SDSS DR10) contains $\sim 1{,}880{,}584$ galaxy spectra, covering $\sim 14{,}555$ square degrees on the sky — this includes SDSS-I, SDSS-II and the ongoing SDSS-III[3] survey (Ahn et al., 2014). Some of the most recent results from the SDSS-III/BOSS

[2]Baryon Oscillation Spectroscopic Survey (BOSS) is part of the ongoing SDSS survey, targeting ~ 1.5 million luminous red galaxies to $z \approx 0.7$ and 160,000 quasars with $2.3 < z < 3$.

[3]Funding for SDSS-III has been provided by the Alfred P. Sloan Foundation, the Participating Institutions, the National Science Foundation, and the U.S. Department of Energy Office of Science. The SDSS-III web site is `http://www.sdss3.org/`.

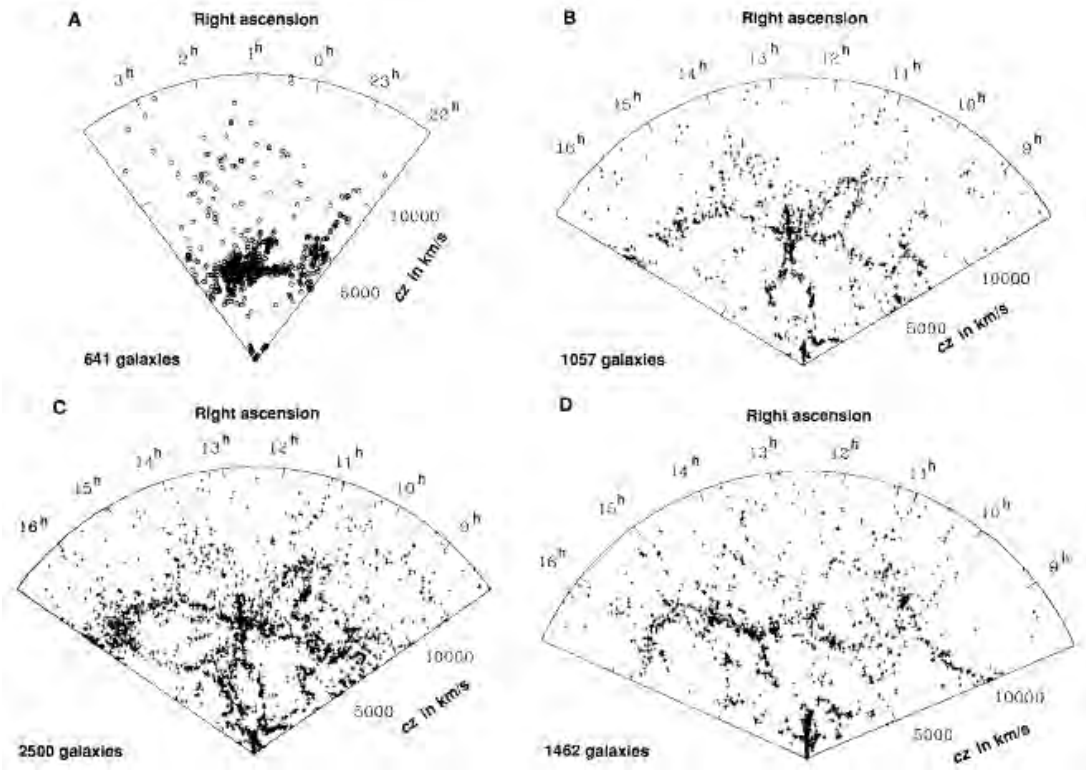

Fig. 1.4: Galaxy redshift distribution from the CfA survey: the top left-hand panel shows the galaxy distribution in Perseus-Pisces chain. The top right-hand panel represents declination angles in the range $26.^\circ5 \leq \delta < 32.^\circ5$, bottom left-hand panel shows the declination range $26.^\circ5 \leq \delta < 44.^\circ5$, covering the Coma cluster at 13^h and 28°. The bottom right-hand panel represents the declination range $8.^\circ5 \leq \delta < 14.^\circ5$ (the nearby Virgo cluster is clearly visible at 12.5^h and $12.^\circ5$) — Figure taken from Geller & Huchra (1989), their figure 3.

(Dawson et al., 2013) include the detection of the baryon acoustic oscillations (BAO) signal (Anderson et al., 2014). These baryon acoustic oscillations are the regular, periodic fluctuations in the density of the ordinary (or baryonic) matter left over from the pre-decoupling universe (see for example, Eisenstein et al., 2005). The main SDSS survey covers a median redshift of $z \approx 0.1$ with imaging data up to a depth of $r = 22.6$ mag (Abazajian et al., 2003).

Another recent galaxy redshift survey is the 2MASS Redshift Survey (2MRS, Huchra et al., 2000). By using the bright subsample of the 2MASS Extended Source Catalogue, Huchra et al. (2000) initiated the 2MRS so as to improve the depth ($z \sim 0.1$) and sky coverage. The 2MRS consists of a total of 44,599 2MASS galaxies with K_s-band total extrapolated magnitudes $\leq 11^{\mathrm{m}}.75$ (Huchra et al., 2012). The sample selection was based on the 2MASS Extended Source Catalogue (2MASS XSC; Jarrett et al., 2000; Skrutskie et al., 2006). Figure 1.5 shows the large scale structures in the 2MASS data (the 2MASS Extended Source Catalogue), colour coded according to redshift. Galaxy clusters and superclusters are marked and labelled, with the name and their corresponding measured distance (redshift). It should be noted that the Six-degree Field Galaxy Survey (6dFGS; Jones et al., 2004, 2005, 2009) used the 2MASS XSC (Jarrett et al., 2000; Skrutskie et al., 2006) as its input catalogue. A large number of redshifts for the galaxies in 2MRS were therefore taken from 6dFGS. A detailed description of 6dFGS is presented in § 1.3.1.3. The 2MRS is less sensitive to Galactic extinction than optical surveys, hence is more complete especially at low Galactic latitudes where optical surveys suffer from severe extinction

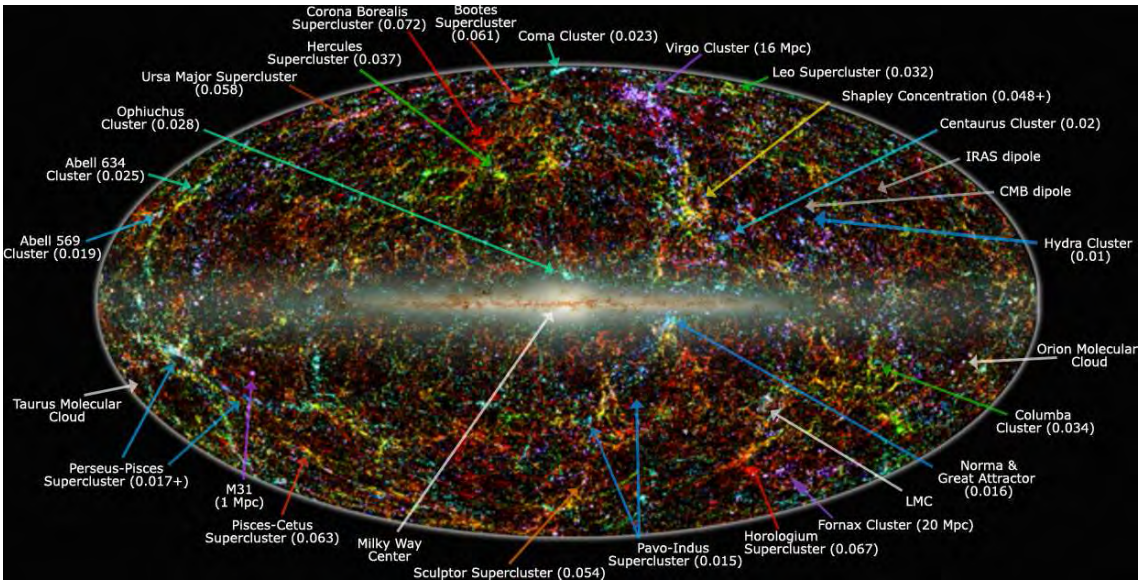

Fig. 1.5: 2MASS Large Scale Structures, galaxies are colour coded according to redshift; blue represents nearby sources ($z < 0.01$), yellow are moderate distances, i.e., $0.01 < z < 0.04$, and red are the most distant sources that can be resolved with 2MASS, that is, $0.04 < z < 0.1$ (see figure 1 in Jarrett 2004).

effects. The 2MRS however, remains incomplete close to the Galactic bulge, where the effects of both Galactic extinction and stellar confusion persist.

Due to the effect of Galactic extinction (and star crowding) close to the Galactic Plane and the Galactic bulge, the 2MRS sample is limited to Galactic latitudes: $|b| \geq 5^\circ$ away from the Galactic bulge and $|b| \geq 8^\circ$ towards the Galactic bulge (Huchra et al., 2012). Figure 1.6 shows the distribution of the 2MRS galaxy sample, colour coded according to redshift. The sample is 97.6% complete and covers 91% of the sky (Huchra et al., 2012). The full-sky coverage by 2MASS makes the survey suitable for studies of bulk motions, and hence the distribution of matter. The 2MRS provided the most complete infrared 3-D All Sky map showing the distribution of galaxies at a redshift $z < 0.1$ (see Figure 1.6), cf. PSCz catalogue (Saunders et al., 2000). Some of the recent results based on the 2MRS are discussed under §1.4 — see § 1.4.3.

1.2 Local Group – Peculiar Velocity

As discussed earlier, a galaxy's apparent recession velocity, cz, is proportional to its distance, d, implying that more distant galaxies have larger recession velocities. In the presence of massive structures (both dark and visible), the gravitational effect on the nearby galaxies leads to a distortion in the Hubble flow. The gravitational instability caused by the massive structures and overdensities results in a galaxy's motion in addition to the uniform Hubble flow, that is, deviations from the Hubble flow are due to inhomogeneities in the large scale distribution of matter. This additional motion is referred to as the peculiar velocity, and is, for non-relativistic motions, given by the approximation:

$$v_{\rm pec} \equiv c z_{\rm pec}, \tag{1.3}$$

where $z_{\rm pec}$ is the galaxy's peculiar redshift. The observed redshift ($z_{\rm obs}$) is related to the galaxy's peculiar redshift ($z_{\rm pec}$) and its cosmological redshift ($z_{\rm H}$) corresponding to the galaxy's co-moving distance as:

$$(1 + z_{\rm obs}) = (1 + z_{\rm H})\left(1 + z_{\rm pec}\right) \tag{1.4}$$

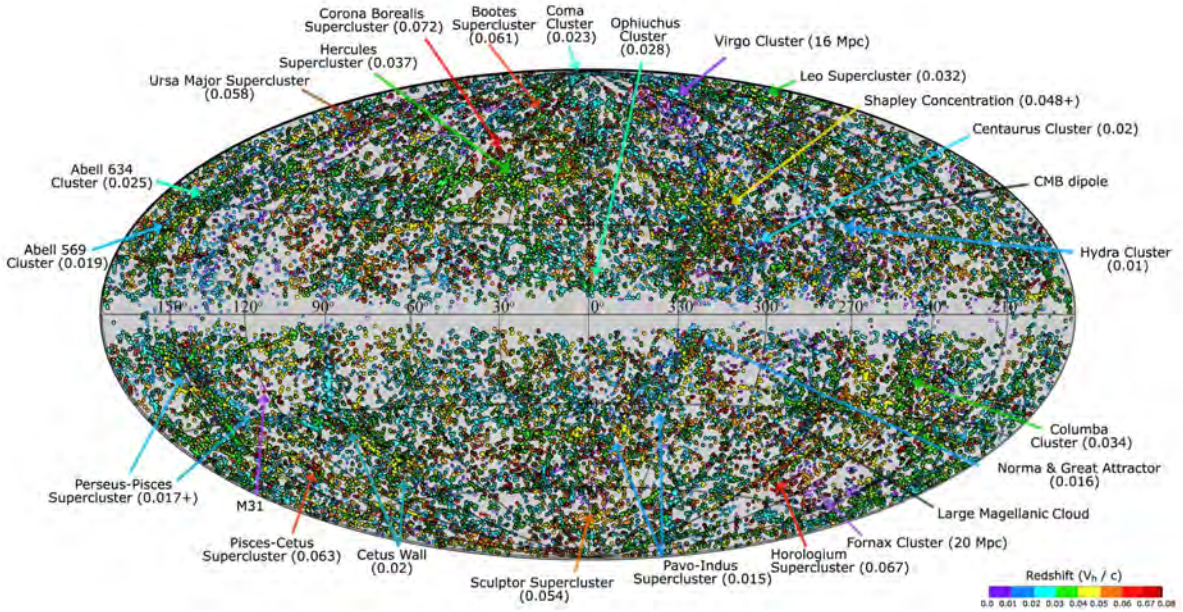

Fig. 1.6: 2MRS sample, galaxies are colour coded according to redshift; from the nearby (purple) to the most distant (red) galaxies in the survey. Figure taken from Huchra et al. (2012) — their figure 12.

At low redshifts, the peculiar velocity is given by the linear approximation:

$$v_{\rm pec} \approx cz_{\rm obs} - H_0\, d, \tag{1.5}$$

where $v_{\rm pec}$ is the line-of-sight component of the peculiar velocity, H_0 is the Hubble constant and d is the galaxy's co-moving distance. The peculiar velocity is therefore always included in the measured galaxy redshift unless a proper correction is applied. Since peculiar velocities are due to the gravitational influence on a galaxy/group/cluster resulting from inhomogeneities in the distribution of matter, accurate peculiar velocity measurements can be used to study the distribution of matter (both dark and visible) in the nearby Universe.

From Equation 1.5, we see that if the redshift-independent distance d is known, the peculiar velocity can be computed once a galaxy's apparent recession velocity is known. However, due to the errors or uncertainties associated with the currently used distance indicators , reliable peculiar velocity measurements are limited to the nearby Universe (distances less than 200 Mpc). However, Equation 1.5 leads to over-estimated peculiar velocities and therefore Equation 1.4 should be used. Davis & Scrimgeour (2014) show that the approximation $v_{\rm pec} = cz - H_0 d$ over-estimates the peculiar velocity by $\Delta v_{\rm pec} \sim 100$ km s^{-1} at $z \sim 0.04$ and as much as $\Delta v_{\rm pec} \sim 700$ km s^{-1} at $z \sim 0.1$ (see Figure 1.7). Although the effect is not significant at the redshift of Norma, Equations 1.3 and 1.4 were used in the peculiar velocity measurements of the Norma cluster presented in Chapter 3.

The techniques used to measure redshift-independent distances are presented and discussed later in §1.3. For distance measurements to more than ~100 Mpc, the error on the measured peculiar velocity will be greater than or equal to the measured peculiar velocity itself. The most accurately measured peculiar velocity to date is that of the Sun (from CMB observations – see discussion in §1.2.1). The source of the observed Local Group's peculiar velocity has however remained a topic of debate. This is partly due to the challenge posed by our own Galaxy which acts as a veil to extragalactic objects, leading to an incomplete view of the distribution of matter

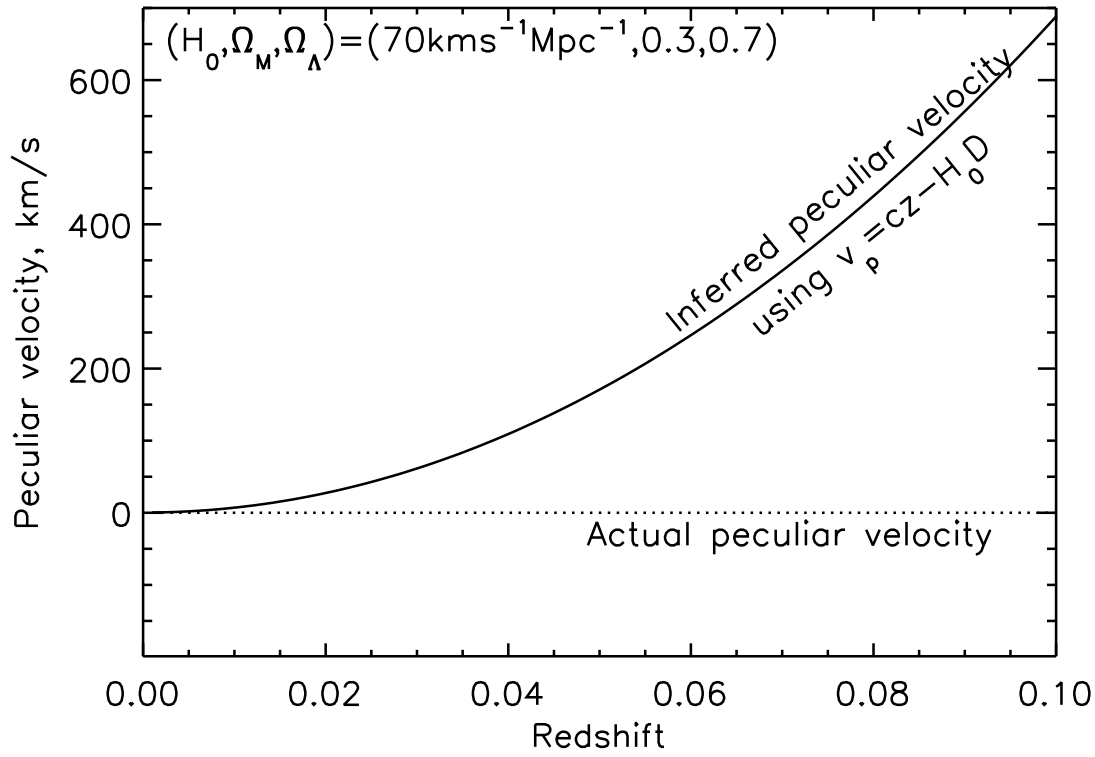

Fig. 1.7: The solid line shows the peculiar velocity inferred from the approximation: $v_{\rm pec} = cz - H_0 d$, when the actual peculiar velocity is 0 km s^{-1}. The x-axis shows the cosmological redshift due to recession only. Figure taken from Davis & Scrimgeour (2014), that is, their figure 2.

in the Universe. The Milky Way obscures approximately 20% and 10% of the extragalactic sky in the optical and near-infrared wavelengths, respectively (Kraan-Korteweg & Lahav, 2000).

1.2.1 CMB Dipole

The CMB is relatively warmer in one direction and colder in the other (i.e. the cold and warm poles or dipole, see Figure 1.2) due to the motion of the solar system with respect to the CMB rest frame. The velocity of the solar system with respect to the CMB rest frame is related to the CMB temperature via:

$$\frac{\triangle T}{T} = \frac{v}{c}, \tag{1.6}$$

where $\triangle T$, T, v are, respectively, the dipole amplitude, average CMB temperature, velocity with respect to the CMB, and c is the speed of light. The CMB has a dipole amplitude of $\triangle$T = 3.365 ± 0.027 mK (Kogut et al., 1993), in the direction $(\ell, b) = (264.^\circ4 \pm 0.^\circ3, 48.^\circ4 \pm 0.^\circ5)$. Substituting these values into Equation 1.6, results in the solar system speed, $v_\odot = 369.5 \pm 3.0$ km s^{-1} with respect to the CMB rest frame (see Kogut et al. 1993). This is in agreement with the recent results from Planck (Planck Collaboration et al., 2014d). The implied velocity (or the peculiar velocity) of the Local Group with respect to the CMB rest frame is $v_{\rm LG} = 627 \pm 22$ km s^{-1} in the direction $\ell = 276^\circ \pm 3^\circ$, $b = 30^\circ \pm 3^\circ$ (Kogut et al., 1993). The source of this motion is not clearly known and has, for the last two decades, remained a debate. However, two nearby overdensities, the Great Attractor (Lynden-Bell et al., 1988) and the Shapley Supercluster (Raychaudhury, 1989; Scaramella et al., 1989) have dominated the debate regarding the source of the Local Group's observed motion. The major challenge in disentangling between the two attractors is mainly due

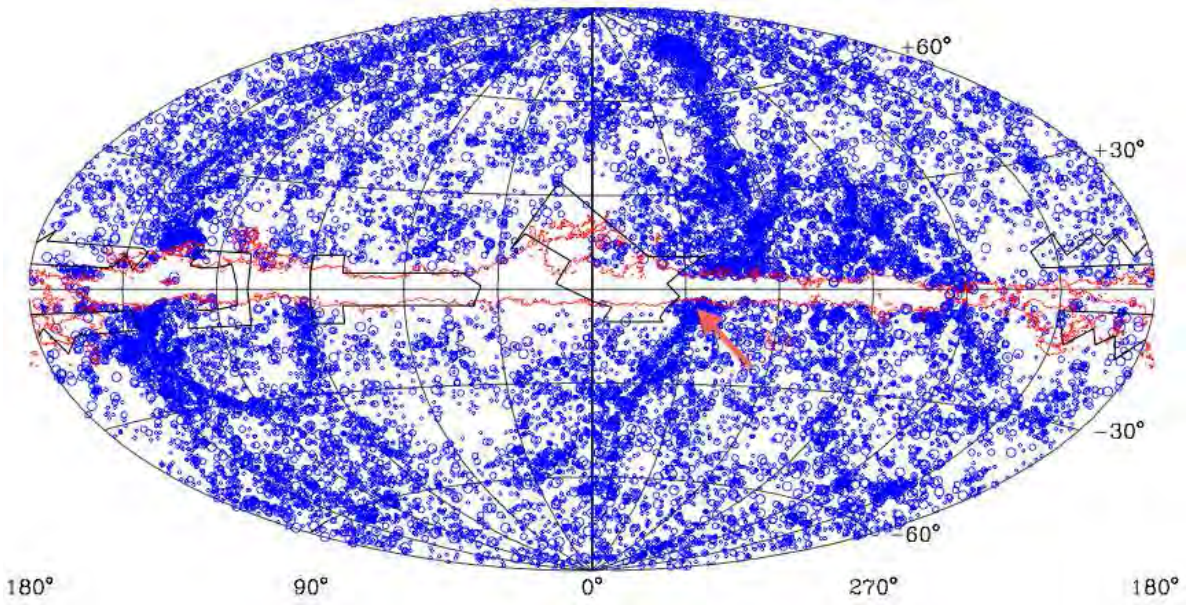

Fig. 1.8: Distribution of galaxies with angular diameter $D \geq 1\farcm3$ in Galactic coordinates. The galaxies are diameter-coded; small circles show galaxies with $1\farcm3 \leq D < 2'$, medium circles show $2' \leq D < 3'$, while the large circles represent $D \geq 3'$. The solid red contour represents a line of equal Galactic foreground extinction: $A_B \leq 1\overset{\mathrm{m}}{.}0$, from Schlegel et al. (1998). The red arrow marks the position of the Norma cluster. Figure taken from (Kraan-Korteweg & Juraszek, 2000).

to galaxy incompleteness within the Great Attractor region and more generally, in the Zone of Avoidance, where the effects of Galactic extinction and star-crowding do not allow us a complete view of the distribution of matter and the large scale structure of the Universe.

1.2.2 Zone of Avoidance

Due to the absorption and extinction effects by gas and dust in the plane of the Milky Way, with extinction more severe at low Galactic latitudes, the distribution of the observed galaxies results in a strip or region with few or no detected galaxies, running through the centre of the Milky Way, centred at the Galactic equator. Using the distribution of "Nebulae" in Sir John Herschel's General catalogue of Nebulae, this region was referred to as the "Zone of Few Nebulae" by Richard Proctor in 1878. This region, now referred to as the Zone of Avoidance has since been reduced in size (width) through optical, near-infrared and HI surveys — compare, e.g, the optical ZoA as seen in Figure 1.8 with the 2MASS near-infrared equivalent (Figure 1.5).

The observed galaxies, especially close to the Galactic Plane where Galactic extinction is severe, look fainter and smaller than they really are. The high stellar density also results in galaxies getting confused with the foreground point sources. The Galactic extinction effects are tremendously reduced at longer wavelengths, e.g. in the near-infrared and radio, leaving the high stellar density the most significant challenge to photometric analysis at these wavelengths. The ratio of Galactic extinction in the optical R-band ($\sim 0.70\,\mu$m) and the near-infrared K_s-band ($\sim 2.2\,\mu$m), using the extinction law by Cardelli, Clayton & Mathis (1989) for $R_V = 3.1$, is

$$A_{K_s} = 0.14 A_R. \tag{1.7}$$

R_V is the ratio of total to selective extinction, that is,

$$R_V = \frac{A_V}{E(B-V)}. \tag{1.8}$$

$E(B-V)$ is also referred to as the colour excess and is given by:

$$E(B-V) = A_B - A_V, \tag{1.9}$$

where A_B and A_V are the Galactic extinction in the B- and V-band, respectively.

Some of the deep surveys conducted in the Zone of Avoidance include the Arecibo L-Band Feed Array Zone of Avoidance survey (Henning et al., 2010; McIntyre et al., 2011), the HI Parkes Zone of Avoidance survey (Donley et al., 2005, 2006), the Galactic Plane Survey (Baum et al., 1997; Lawrence et al., 2007), deep optical surveys (Woudt & Kraan-Korteweg, 2001; Radburn-Smith et al., 2006), the Two Micron All Sky Survey (Jarrett et al., 2000), and the Deep Near-Infrared Southern Sky survey (Epchtein et al., 1997; Schröder et al., 2005). These multiwavelength observations and surveys have reduced the width of the Zone of Avoidance, and have revealed many more galaxies in the region, consequently improving the completeness in the galaxy distribution. The near-infrared observations and surveys, e.g. 2MASS, have detected a large number of previously unknown galaxies, especially faint galaxies close to the Galactic Plane where optical observations suffer from severe extinction. Short wavelength surveys such as X-ray surveys, e.g. by Boehringer et al. (1996) as well as the ROentgen SATellite (ROSAT) All Sky Survey (Ebeling et al., 1993) have also helped explore the Zone of Avoidance by unveiling more galaxies and galaxy clusters. For example, the recent discovery of galaxy clusters through the Clusters in the Zone of Avoidance survey (CIZA), an X-ray selected sample of clusters at low Galactic latitudes (Ebeling et al., 2002; Kocevski et al., 2007).

However, all-sky galaxy surveys, whether at optical or near-infrared wavelengths, still remain incomplete, especially close to the Galactic bulge. While the Milky Way is effectively transparent to radio wavelengths, HI surveys are incomplete in early-type galaxies as these are HI-deficient. Nonetheless, by finding gas-rich galaxies, HI surveys complement other surveys capable of detecting all galaxy morphologies (optical and near-infrared surveys). This galaxy incompleteness may partly be responsible for the long-standing controversy about the source of the observed Local Group's peculiar velocity and the convergence depth of the CMB dipole.

While some studies support convergence on small distance scales ($< 70h^{-1}$ Mpc), for example, da Costa et al. (2000a); Erdoğdu et al. (2006a,b), other studies support velocity flows at large distances ($d > 130h^{-1}$ Mpc). A significant contribution to the motion of the Local Group from structures up to $185h^{-1}$ Mpc has been claimed by Kocevski & Ebeling (2006) and Basilakos & Plionis (2006) for example, while Rowan-Robinson et al. (2000) found a convergence depth at 200 Mpc. The convergence depth thus remains controversial and debatable as some studies have measured bulk flow motions at scales $\sim 200-500h^{-1}$ Mpc (Hudson et al., 2004; Kashlinsky et al., 2008). While the direction of most recently measured bulk motions generally agree, their amplitude is a topic of debate. While some studies find bulk flow amplitudes comparable to the predictions of the ΛCDM (e.g., Turnbull et al., 2012; Ma & Scott, 2013; Ma & Pan, 2014), the amplitude of the bulk flow measured by Watkins et al. (2009) and Feldman et al. (2010) are in disagreement with the predictions from the ΛCDM and WMAP-5 cosmological parameters at 98% confidence level. Most importantly, however is that the direction of motion of these bulk flow measurements point close to or in the Zone of Avoidance. Surveying the Zone of Avoidance and studying the velocity flows in the region may thus help solve the controversies by mitigating the effects that would otherwise result from the lack of galaxy surveys behind the Galactic Plane (Loeb & Narayan, 2008). The most controversial result is probably the recent result by Kashlinsky et al. (2010) who measured a large bulk flow out to 800 Mpc (using luminous X-ray galaxy clusters) — see also Atrio-Barandela et al. (2011) and Kashlinsky et al.

(2012) for a summary of the measurements and implications of inhomogeneities ("dark flow") detected at 800 Mpc.

1.2.3 Great Attractor

The Great Attractor is a large concentration of mass located close to the Galactic Plane (in the Zone of Avoidance). The Great Attractor lies at an estimated distance of $\sim 40-80$ Mpc from the Milky Way in the direction of the Hydra and Centaurus concentrations. From the sky distribution of the Sc galaxy sample of Rubin et al. (1976) and the southern group catalogue of Sandage (1975), Chincarini & Rood (1979) found evidence for a supercluster in the Hydra-Centaurus region. This supercluster encompasses the rich clusters now catalogued as Abell S0636 (Antlia, $v_{\rm hel} \simeq 2800$ km s^{-1}), Abell 1060 (Hydra, $v_{\rm hel} \simeq 3800$ km s^{-1}), Abell 3526 (Centaurus, $v_{\rm hel} \simeq 3400$ km s^{-1}) and Abell 3574 (IC4329, $v_{\rm hel} \simeq 4800$ km s^{-1}) where $v_{\rm hel}$ is the heliocentric velocity. The Local Supercluster has a sizable motion (~ 300 km s^{-1}) towards this supercluster (Shaya, 1984; Tammann & Sandage, 1985) and the galaxy motions in the Local Supercluster have a shear that is directed towards Hydra-Centaurus (Lilje et al., 1986).

From a redshift survey of the Hydra-Centaurus region, da Costa et al. (1986) concluded that this supercluster extends to $v_{\rm hel} \simeq 5500$ km s^{-1}. They found a surprisingly large positive peculiar velocity for the dominant Cen30 sub-component of the Centaurus cluster, that is, $v_{\rm pec} = +1100 \pm 208$ km s^{-1}. While several studies confirmed the presence of these large positive peculiar velocities, for example, Aaronson et al. (1989) and Dressler & Faber (1990), a non-significant peculiar velocity for Cen30 of $+200 \pm 300$ km s^{-1} was measured by Lucey & Carter (1988).

Subsequently, the Supergalactic Plane redshift survey (Dressler, 1988) and the redshifts of IRAS galaxies in this region (Strauss & Davis, 1988) confirmed that there was a substantial concentration of galaxies in this region extending from 2000 to 5500 km s^{-1}. While in the literature the Great Attractor term has been used differently by various studies (see Lynden-Bell et al. 1989; Burstein et al. 1990; Rowan-Robinson et al. 1990; Mould et al. 2000; Courtois et al. 2012, 2013), an inclusive definition for the Great Attractor is the mass contained in the volume spanning $\ell = 260$ to 350°, $b = -35$ to 45°, $v_{\rm hel} = 2000$ to 6000 km s^{-1}. This broad definition encompasses the Hydra-Centaurus supercluster but extends across the Galactic Plane to include Pavo-I, Pavo-II and the Norma cluster (see Figure 1.17). The Norma cluster centred at $(\ell, b, v_{\rm hel}) = (325.^{\circ}3, -7.^{\circ}2, 4871$ km s$^{-1})$ forms the heart of the Great Attractor (Woudt, 1998; Woudt et al., 2008) – see Figure 1.12 (bottom panel) and Figure 1.17.

After more than two decades of study the nature and full extent of the Great Attractor is still not well established. The original work by Lynden-Bell et al. (1988) estimated the Great Attractor to have a mass of $\sim 5.4 \times 10^{16}$ M$_{\odot}$, centred at $(\ell, b) = (307^{\circ}, 9^{\circ})$ and $v_{\rm hel} = 4350 \pm 350$ km s^{-1}. From surface brightness fluctuation (SBF) distances for ~ 300 early-type galaxies, Tonry et al. (2000) placed the Great Attractor at $(\ell, b, v_{\rm hel}) = (289^{\circ}, 19^{\circ}, 3200 \pm 260$ km s$^{-1})$ with a mass $\sim 8 \times 10^{15}$ M$_{\odot}$, i.e., approximately six times less than the original derived mass. As the Great Attractor spans low Galactic latitudes, where the extinction is severe, our understanding of this important local large structure is still incomplete. The CIZA survey revealed galaxy clusters including the discovery of CIZA J1324.7-5736 (Ebeling et al., 2002; Kocevski et al., 2007). CIZA J1324.7-5736 is the second richest cluster in the Great Attractor region (Nagayama et al., 2006). Recently, many more galaxies in the Great Attractor region have been unveiled through a near-infrared galaxy search (Kraan-Korteweg et al., 2010; Riad, 2010).

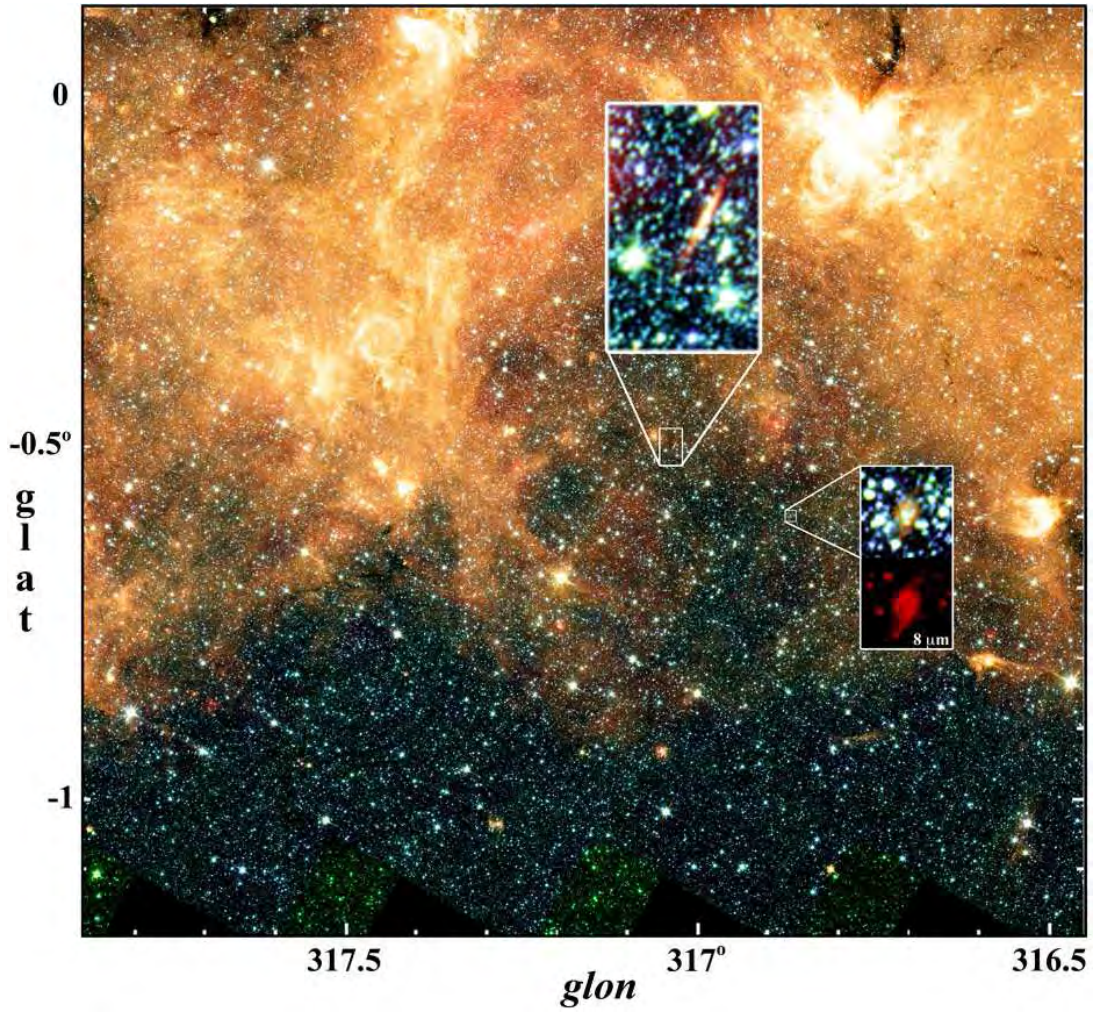

Fig. 1.9: Location of the two newly discovered spiral galaxies at very low Galactic latitudes. The colours are; blue: 3.6 μm, green: 4.5 μm, yellow: 5.8 μm, orange: 8 μm based on *Spitzer* IRAC (InfraRed Array Camera) data while the deep red represents the 24 μm MIPS (Multiband Imaging Photometer for *Spitzer*) data. The inset are images from deep IRSF JHK_s-band observations, combined with the mid infrared images. Figure taken from Jarrett et al. (2007).

The possibility that part of the Great Attractor region remains hidden is supported by the continued galaxy detections in the Zone of Avoidance (e.g., Donley et al., 2006; Jarrett et al., 2007; Marleau et al., 2008; Riad, 2010; Kraan-Korteweg et al., 2010). Galaxy surveys and observations also show a filamentary structure which seems to cross the Galactic Plane, see Figures 1.8 and 1.17. Figure 1.9 shows two recently discovered galaxies in the Great Attractor region by Jarrett et al. (2007), located very close to the Galactic Plane, at $(\ell, b, cz) \sim (317°, -0.^\circ5, 4500 \text{ km s}^{-1})$. At such low Galactic latitudes, the Galactic extinction is extremely high, ~ 20 mag in the Landolt B-filter which is ~ 2 mag in the near-infrared K_s-band.

1.2.4 Shapley Supercluster

The extremely rich Shapley Supercluster lies at $(l, b, v_{\text{hel}}) = (312°, 31°, 14400 \text{ km s}^{-1})$. It was first recognised by Shapley (1930) as a very populous cloud of galaxies, and later highlighted by Oort (1983) in his review of superclusters. With the publication of the southern extension to the Abell cluster catalogue (Abell et al., 1989), a large number of rich clusters in the Shapley Supercluster

was noted (Scaramella et al., 1989). From the analysis of galaxies on the 1.2 m United Kingdom Schmidt Telescope survey plates, Raychaudhury (1989) independently found this remarkable structure.

The role of the Shapley Supercluster in the local dynamics is unclear. While most studies conclude that it only has a modest contribution (≤ 100 km s^{-1}) to the Local Group motion with respect to the CMB, e.g., Ettori et al. (1997); Branchini et al. (1999); Hudson et al. (2004); Bolejko & Hellaby (2008), some studies have concluded a much larger contribution (~ 300 km s^{-1}), see, for example, Marinoni et al. (1998); Plionis et al. (2000); Basilakos & Plionis (2006); Kocevski & Ebeling (2006). The lack of clear evidence for any backside infall into the Great Attractor (Mathewson et al., 1992; Hudson, 1994a) led to the idea that the Shapley Supercluster dominates the motions on the farside of the Great Attractor (Allen et al., 1990). Using the Two Micron All-Sky Redshift Survey, Erdoğdu et al. (2006a) found evidence for a backside infall into the Great Attractor. Lavaux et al. (2010) on the other hand did not detect any backside infall but instead suggested convergence as far as $\sim 200h^{-1}$ Mpc. Extensive redshift surveys (for example, Radburn-Smith et al. 2006) and near-infrared galaxy searches (Kraan-Korteweg et al., 2010; Riad, 2010) have revealed the complex interconnections of the structures in this region.

More recently, Tully et al. (2014) proposed that we live in a supercluster which if approximated as round has a diameter of 12,000 km s^{-1} (with mass $\sim 1 \times 10^{17}\,M_\odot$). They have named it the "Laniakea" supercluster of galaxies (Tully et al., 2014). Their findings show the Great Attractor to significantly influence the local motions, that is, the local flows within the "Laniakea" supercluster converge towards the Norma and Centaurus clusters.

1.3 Redshift-independent Distance Measurements

Redshift-independent distances are measured by relying on sources which have a well defined luminosity. These are referred to as primary distance indicators or standard candles. Examples of such astrophysical objects include RR Lyrae stars (for example, Scowcroft et al., 2013; Klein et al., 2014), Cepheid variables (period-luminosity relationship, for example, Feast & Walker 1987; Macri et al. 2006; Riess et al. 2011; Freedman et al. 2012; Monson et al. 2012) and Type Ia supernovae, for example, the Carnegie Supernova Project (Freedman et al., 2009). The accuracy or reliability of most primary distance indicators is limited to nearby sources ($\lesssim 30$ Mpc for Cepheids, for example, Riess et al. 2011).

Supernovae (Type Ia supernovae) are very useful standard candles since they are very luminous and can be observed to much greater distances (up to $z \sim 0.7$), see for example Freedman et al. (2009) and Folatelli et al. (2010). These provide the most precise and accurate distance measurements with uncertainties as small as 5% for single objects (Riess et al., 1996). Their occurrences are, however, very rare and only last a short period of time. Therefore, extragalactic distance measurements to distant galaxies/groups/clusters employ secondary distance indicators in the so-called *"cosmic distance ladder"* (Rowan-Robinson, 1985; Rowan-Robinson & Harrison, 1985). These depend on primary distance indicators for calibration purposes, implying that the error arising from the lower rung on the ladder will propagate on to the distance measured using a method on the next higher rung, that is calibrated based on distance measurements from the lower rung. Nonetheless, distance measurements to galaxy clusters have been measured with uncertainties less than 10% using secondary distance indicators, some of which are discussed hereafter. Note also that the uncertainties in the extragalactic distance calibration have reduced over the years due to improved and increased data. A good example are the Cepheid detections

from the Hubble Space Telescope Key Project (Freedman et al., 2001), whose main goal was to measure the Hubble constant (H_0) to an accuracy of 10% (also see, Riess et al. 2011 who used optical and infrared data for ~ 600 Cepheid variables and measured H_0 to within 3%).

1.3.1 Distance Measures for Early-type Galaxies

In galaxy formation and evolution, elliptical galaxies represent the advanced stages of galaxy evolution and merging processes (see e.g., Kormendy et al. 2009), with minimal or no ongoing star-formation (Donas et al., 2007; Skibba et al., 2011). The effect of internal extinction (due to absorption by gas and dust internal to the galaxy) can thus be assumed to be negligible in early-type galaxies. Spiral galaxies on the other hand, contain considerable amounts of cold gas and dust, and therefore, ongoing star formation (Skibba et al., 2011; Martini et al., 2013). The elliptical and lenticular galaxies are, together, referred to as early-type galaxies. The early-type galaxies are dominated by an old population of low mass stars.

The structural parameters for early-type galaxies have been well studied. Their central velocity dispersion (σ) is related to their luminosity (L); this is popularly known as the Faber-Jackson relation (Faber & Jackson, 1976). Since the relation correlates a distance-independent (central velocity dispersion) and a distance-dependent (apparent brightness) variable, it is used as a distance indicator for early-type galaxies. However, the relation shows large scatter, leading to suggestions that there was a missing parameter. Soon after, Kormendy (1977) observed that the effective radius of an elliptical galaxy correlates with the effective surface brightness; popularly known as the Kormendy relation. Like the Faber-Jackson relation, the Kormendy relation showed large residuals, and attracted more interest in searching for the missing parameter.

The large scatter in both the $L-\sigma$ and Kormendy relations led to the observation that the central velocity dispersions, the effective radii and the mean effective surface brightnesses for early-type galaxies form a plane, now known as the Fundamental Plane (Djorgovski & Davis, 1987; Dressler et al., 1987). At around the same time, Dressler (1987) introduced a power law of the form $\mathrm{D}_n \propto \sigma^\kappa$ to describe early-type galaxies. This is known as the $\mathrm{D}_n - \sigma$ relation, where D_n is the diameter within which the mean surface brightness reaches a fiducial value. For example, Lynden-Bell et al. (1988) defined D_n to correspond to the angular diameter of a circle within which the integrated B-band surface brightness is 20.75 mag arcsec^{-2}.

1.3.1.1 The Fundamental Plane

The Fundamental Plane (Djorgovski & Davis, 1987; Dressler et al., 1987), describes a special relation for early-type galaxies where they are found to be concentrated on a plane in a three-dimensional space defined by the galaxy's size (effective radius), mean effective surface brightness, and the central velocity dispersion. For a virialised system of radius R:

$$G\mathscr{M} = R\,\langle\sigma_0^2\rangle\,, \tag{1.10}$$

where G is a gravitational constant, $\mathscr{M}$ and $\langle\sigma_0^2\rangle$ are the mass (within R) and mean square velocity dispersion of the stellar system, respectively. Further assuming that early-type galaxies form a homologous family, that is, they have the same mass distribution and structural properties, the observed and theoretical parameters are related by

$$r_e = k_R R, \tag{1.11}$$

and

$$\sigma^2 = k_v \langle\sigma_0^2\rangle. \tag{1.12}$$

Here, k_v and k_R are constants, r_e is the effective radius (the radius of a circle containing half the total luminosity of the galaxy) while σ is the central velocity dispersion. Equation 1.10 then becomes:

$$\mathscr{M} = \frac{1}{Gk_vk_R}\sigma^2 r_e = c_1\sigma^2 r_e, \tag{1.13}$$

where $c_1 = (Gk_vk_R)^{-1}$ is a constant. The mean effective surface brightness, $\langle I\rangle_e$, in flux units and the total luminosity, L, are related via:

$$\langle I\rangle_e = \frac{L}{2\pi r_e^2} \qquad \text{or} \qquad L = c_2\langle I\rangle_e r_e^2. \tag{1.14}$$

From Equations 1.13 and 1.14, the mass-to-light ratio is given by

$$\frac{\mathscr{M}}{L} = \frac{c_1\sigma^2 r_e}{c_2\langle I\rangle_e r_e^2}. \tag{1.15}$$

Equation 1.15 implies that

$$r_e = c_1c_2^{-1}\left(\frac{\mathscr{M}}{L}\right)^{-1}\sigma^2\langle I\rangle_e^{-1}. \tag{1.16}$$

Assuming a constant mass-to-light ratio, Equation 1.16 implies that

$$r_e \propto \sigma^2\langle I\rangle_e^{-1}. \tag{1.17}$$

The Fundamental Plane relation is written in the form:

$$\log r_e = a\log\sigma + b\langle\mu_e\rangle + c, \tag{1.18}$$

where $\langle\mu_e\rangle \propto -2.5\log\langle I_e\rangle$ is the mean effective surface brightness (the mean surface brightness within r_e) in mag arcsec^{-2}, a, b, and c are the Fundamental Plane fit parameters (a and b are often referred to as the 'slopes') while c is the intercept or the Fundamental Plane zero point.

For a virialised system (as seen in Equation 1.17), with the assumption of homology and constant mass-to-light ratio, $(a,b) = (2, 0.4)$. However, the observed Fundamental Plane fit parameters have been found to deviate from those expected from the virial theorem (Bernardi et al., 2003; La Barbera et al., 2008, 2010; Magoulas et al., 2012; Saulder et al., 2013). This deviation is often referred to as the 'Fundamental Plane tilt'. The origin of this tilt has been debated since the invention of the Fundamental Plane and it is thought to result from a break in homology or mass-to-light ratio, or both (Pahre et al., 1998b; Trujillo et al., 2004). The slope, a, has been found to depend on the wavelength of the filter used (e.g., Bernardi et al., 2003; Hyde & Bernardi, 2009; La Barbera et al., 2010), systematically increasing from the optical through to near-infrared wavebands while the value of b remains the same or changes only slightly.

Despite the 'tilt' in the Fundamental Plane, the observed scatter is small and hence makes it a suitable method for extragalactic distance measurements. The three dimensional plane, if viewed edge-on, presents a smaller scatter than both the Faber-Jackson and Kormendy relations, attaining an uncertainty in distance measurement of $\sim 20\%$ per galaxy and less than 10% for rich clusters (Lucey et al., 1991a; Hudson et al., 1997). Due to the small scatter, and the availability of a reasonable number of early-type galaxies in galaxy clusters, the Fundamental Plane has been commonly used for redshift-independent distance measurements for galaxy clusters and peculiar velocity measurements, for example, Hudson et al. (1997), the Streaming Motions of Abell Clusters (Hudson et al., 2004) and the 6dF Galaxy Survey (Magoulas et al., 2012; Springob et al., 2014).

Other methods used to measure redshift-independent distances using early-type galaxies, include the Brightest Cluster Galaxies method (Hoessel, 1980; Lauer & Postman, 1992; Postman & Lauer, 1995), the surface brightness fluctuation method (Tonry et al., 2000; Blakeslee et al., 2001, 2009, 2010), and the $D_n - \sigma$ relation (Dressler, 1987; Lucey & Carter, 1988; Lucey et al., 1991b; Bernardi et al., 2002). Both the $D_n - \sigma$ and the Fundamental Plane relations for early-type galaxies, are more reliable for distance measurements to galaxy clusters than the Faber-Jackson relation. This is especially due to the missing parameter in the latter, which subsequently significantly increases the scatter in the $L - \sigma$ relation. For example, Jorgensen et al. (1993) compared the Coma cluster distance measured using both the $D_n - \sigma$ and the Fundamental Plane relations and obtained uncertainties of 17% and 11%, respectively[4]. Similarly, a modified Faber-Jackson relation where aperture magnitudes are used instead of total magnitudes, has been found to present a reduced scatter and uncertainty in the resulting distance (Lucey, 1986).

1.3.1.2 Streaming Motions of Abell Clusters

The Streaming motions of Abell clusters (SMAC) was an All Sky Fundamental Plane survey for $cz < 12{,}000$ km s^{-1}. The survey consists of ~ 699 early-type galaxies in 56 clusters. The SMAC sample revealed a large scale bulk-flow of $\sim 687 \pm 203$ km s^{-1} in the direction $\ell = 260^\circ \pm 13^\circ$, $b = 0^\circ \pm 11^\circ$ (Hudson et al., 2004). From the SMAC project, Smith (1999) obtained a negligibly small peculiar velocity for the Coma cluster ($v_{\rm pec} = -14 \pm 195$ km s^{-1}). In the distance and peculiar velocity measurements for the Norma cluster (see Chapters 3 and 4 of this dissertation), I use the Coma cluster as a calibrator and assume it to be at rest with respect to the cosmic microwave background frame. Thus, the Coma cluster is assumed to be at $z_{\rm CMB} = z_{\rm H} = 0.024$, where $z_{\rm H}$ is the redshift due to the Hubble flow.

1.3.1.3 The Six-degree Field Galaxy Survey

The Six-degree Field Galaxy Survey (6dFGS; Jones et al., 2004, 2005, 2009) was conducted by the Anglo-Australian Observatory. The galaxy sample was selected from the Two-Micron All Sky Survey (2MASS) Extended Source Catalogue (Jarrett et al., 2000; Skrutskie et al., 2006) with a near-infrared K_s-band magnitude limit of 12.75 mag (Jones et al., 2004). The survey resulted in a catalogue of $\sim 125{,}000$ galaxies, 110,256 unique, reliable redshifts and 136,304 spectra (Jones et al., 2004, 2009). The distribution of the galaxies in this survey is shown in Figure 1.10 (for the Southern Galactic hemisphere) and Figure 1.11 (for the Northern Galactic hemisphere). The galaxies are colour coded according to redshift; $z < 0.02$ in blue while red represents galaxies with $z > 0.1$.

Beutler et al. (2011) have used the 6dFGS data to derive, through the baryon acoustic oscillation study, a local Hubble constant with better than 5% precision, that is, $H_0 = 67 \pm 3.2$ km s^{-1} Mpc^{-1}. The survey's spectroscopic and photometric data suitable for 6dFGS Fundamental Plane study (Magoulas et al., 2012) were reported in Campbell et al. (2014). There are several changes made in Campbell et al. (2014) since the publication of the 6dFGS Fundamental Plane in Magoulas et al. (2012). One of these new changes include applying the new Galactic extinction corrections of Schlafly & Finkbeiner (2011) as opposed to Schlegel et al. (1998).

Springob et al. (2014) have incorporated the new changes and utilised this Fundamental

[4]Note that the definition of the angular diameter, D_n in the $D_n - \sigma$ relation incorporates two parameters, that is, the galaxy size and surface brightness. This in return results in a reduced scatter which is comparable to that obtained using the Fundamental Plane relation.

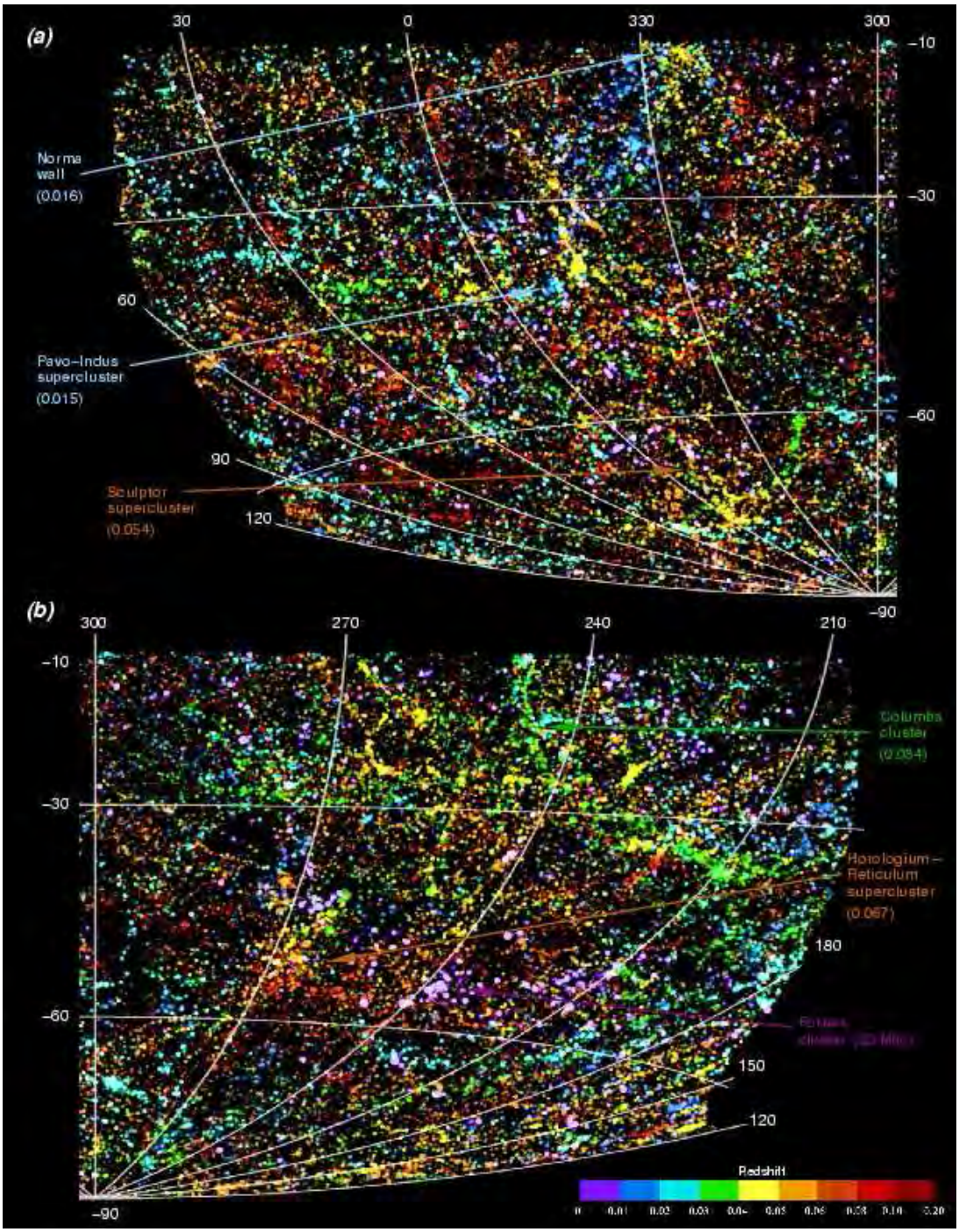

Fig. 1.10: Large scale structures in the nearby Universe as revealed by the 6dFGS, for the Southern Galactic hemisphere. Some of the prominent structures are labelled and their redshifts are given along with their names. Figure taken from Jones et al. (2009).

Plane sample to study the peculiar velocity field and cosmography in the nearby ($z < 0.055$) universe. The 6dFGS subsample used for peculiar velocity studies is the peculiar velocity survey component of 6dFGS (hereafter, 6dFGSv). The 6dFGSv sample was selected from the previously reported Fundamental Plane data (Campbell et al., 2014) using the criteria described in Springob et al. (2014) as follows:

- Heliocentric velocity, $z_{\rm hel} < 0.055$,

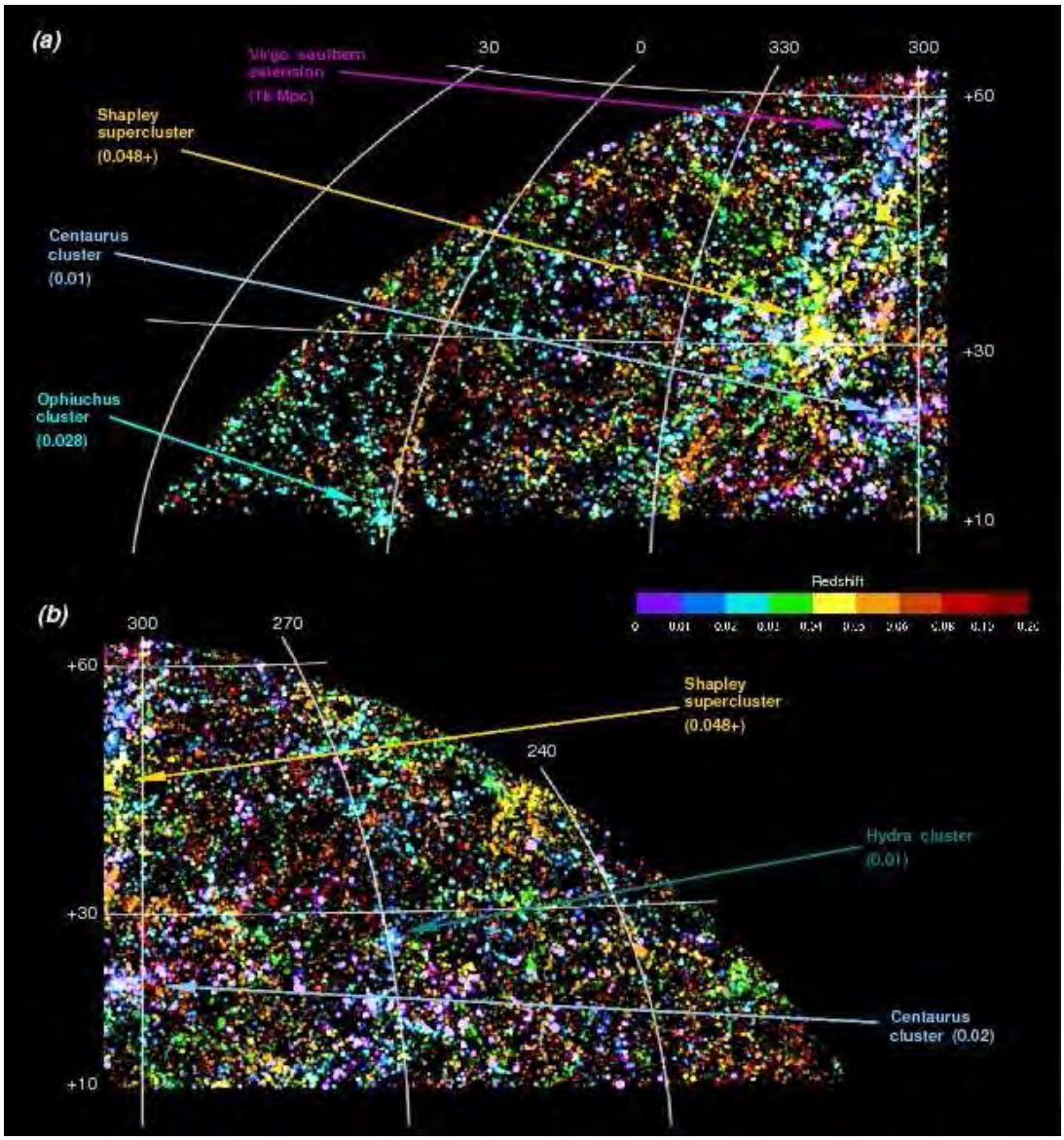

Fig. 1.11: Large scale structures as revealed by the 6dFGS, for the Northern Galactic hemisphere (same as Figure 1.10 but for the Northern hemisphere). Figure taken from Jones et al. (2009).

- Early-type galaxies with spectral signal-to-noise ratios, $S/N > 5$,
- Velocity dispersion greater than $\sigma_{\rm res}$ where $\sigma_{\rm res} = 112$ km s^{-1} is the instrumental resolution limit for the 6dF spectrograph,
- J-band total magnitude brighter than 13.65 mag.

However, galaxies with recessional velocities greater than 16,120 km s^{-1} in the CMB reference frame were excluded from the 6dFGSv sample (Springob et al., 2014). This resulted in a final sample of 8885 early-type galaxies. This is the largest peculiar velocity sample from a single survey to date, with a mean redshift of 11,175 km s^{-1} in the cosmic microwave background reference frame.

Previously, Magoulas (2012) used 6dFGSv and measured a total bulk flow of 337 ± 66 km s^{-1} in the direction $\ell = 313° \pm 9°$ and $b = 15° \pm 10°$. This indeed points towards the Shapley supercluster,

located at $(\ell, b) = (312°, 31°)$, indicating that the Shapley supercluster dominates the motions of the 6dFGSv volume. To incorporate the new changes since their published Fundamental Plane analysis (Magoulas et al., 2012; Springob et al., 2012), Springob et al. (2014) have refitted the J-band Fundamental Plane and found positive peculiar velocities in the direction of Shapley and Vela. The amplitude and direction of the 6dFGSv bulk and residual flow measurements as well as the effect of Galactic extinction corrections on the measured peculiar velocities are being explored in detail and the analysis is still ongoing (Magoulas et al.).

1.3.2 Distance Measures for Late-type Galaxies: The Tully-Fisher Relation

The Tully–Fisher relation or luminosity-linewidth relation (Tully & Fisher, 1977) is the correlation between the maximum observed rotation velocity and absolute luminosity (or observed total flux, absolute magnitude) for spiral galaxies. Assuming the virial theorem holds for spiral galaxies, a virialised system of mass, $\mathscr{M}$, within radius, R, implies that

$$v_{\max}^2 \propto \frac{\mathscr{M}}{R}. \tag{1.19}$$

If spiral galaxies have a uniform mean surface brightness, I_c, the relation between surface brightness and luminosity implies that

$$L \propto I_c R^2. \tag{1.20}$$

If one further assumes a constant mass-to-light ratio ($\mathscr{M}/L$), Equation 1.19 via Equation 1.20 becomes:

$$v_{\max}^2 \propto L \left(\frac{L}{I_c}\right)^{-\frac{1}{2}}. \tag{1.21}$$

The assumption of a constant mean surface brightness I_c (that is, assuming I_c does not significantly change from galaxy to galaxy), implies that:

$$L \propto v_{\max}^4. \tag{1.22}$$

The correlation between luminosity and line width had been observed by Gouguenheim (1969); Roberts (1969); Bottinelli et al. (1971); Balkowski et al. (1973); Sandage & Tammann (1976) but it was Tully & Fisher (1977) who first established it as a linear relation and a distance indicator. Note that a closely related technique, relating rotation velocity and absolute magnitude, had already been used in the early 1920s to measure the distance to the Andromeda galaxy (Opik, 1922).

The relation represented by Equation 1.22 can be written in a linear form such that

$$M = b - a(\log W - 2.5), \tag{1.23}$$

where $M \propto -2.5 \log L$ is the absolute magnitude, b and a are the zero point and slope of the Tully-Fisher relation. The galaxy's maximum rotation velocity, W, can be measured from the Hα emission line through optical spectroscopy (for example, Mathewson et al. 1992; Courteau 1997; Pizagno et al. 2007) or from the neutral hydrogen emission line through 21 cm observations (Haynes et al., 1999a, 1997). Data from the latter are commonly used. The constant value of -2.5 in Equation 1.23 is applied as a normalisation such that the zero point of the Tully-Fisher relation approximates the absolute magnitude of a typical spiral galaxy.

The absolute magnitude which is a measure of the galaxy's luminosity is inferred from the observed apparent (or isophotal) magnitude, m, and systemic velocity, cz, using

$$m - M = \mu = 5 \log(cz) - 5 \log h + 15, \tag{1.24}$$

where μ is the distance modulus (Tully & Fouque, 1985; Aaronson et al., 1986). Note that $m \propto -2.5 \log f$ and $M \propto -2.5 \log L$, where f and L are the galaxy's measured flux and luminosity, respectively. Equation 1.24 implies that

$$M - 5 \log h = m - 5 \log(cz) - 15. \tag{1.25}$$

Equation 1.25 assumes a zero peculiar velocity and the linear Hubble law approximation, hence $cz = H_0 d$. For a galaxy with a peculiar velocity, $v_{\rm pec}$, Equation 1.25 becomes

$$M - 5 \log h = m - 5 \log \left(cz - v_{\rm pec} \right) - 15. \tag{1.26}$$

The relation (Equation 1.23) relates a distance-dependent parameter (absolute magnitude) and a distance-independent parameter (rotation velocity), and is thus used as a distance indicator. The index of 4 in the power law (Equation 1.22) is therefore equivalent to a slope, $a = 10$ of the Tully-Fisher relation (compare Equations 1.22 and 1.23). This is approximately what has been observed at near- and mid-infrared wavelengths (Masters et al., 2008; Lagattuta et al., 2013; Said, 2013; Sorce et al., 2013).

Near-infrared wavelengths are more sensitive to the old stellar population and hence are better tracers of mass, that is, they are less affected by the recent bursts of star formation (Aaronson et al., 1979). In addition, infrared wavelengths are less affected by both Galactic and internal extinction. The Tully-Fisher relation has been calibrated in the near-infrared J, H, and K_s-band using total extrapolated magnitudes from the 2MASS Extended Source Catalogue (Masters et al., 2008) and mid-infrared for example, using the Wide-field Infrared Survey Explorer (WISE) photometry (Lagattuta et al., 2013) and *Spitzer* surface photometry (Sorce et al., 2013). The calibration (to determine the zero point of the relation) is performed using galaxies with known and reliable distances (from, e.g., Cepheids or Supernovae).

Unlike the Fundamental Plane, the Tully-Fisher relation can be used to determine distances to individual spiral galaxies, including field spiral galaxies to an accuracy $\sim 20\%$ (Scodeggio et al., 1997). Note however, that the effect of biases, e.g., the Malmquist bias, are more pronounced for field galaxies than for clusters. Note also that elliptical galaxies make up only 15% of the population of the field galaxies but dominate the cores of rich clusters (Oemler, 1974; Dressler, 1980a,b; Whitmore et al., 1993). The Fundamental Plane is therefore suitable for galaxy clusters.

1.3.2.1 The SFI++ Survey

The Spiral Field I-band ++ (SFI++) survey is an all-sky Tully-Fisher peculiar velocity survey containing 4861 field and cluster galaxies (Masters et al., 2006; Springob et al., 2007). The SFI++ sample was selected from galaxy catalogues compiled in the 1990s, primarily from the Spiral Field I-band (SFI; Giovanelli et al., 1994, 1995; Haynes et al., 1999a,b), Spiral Cluster I-band (SCI; Giovanelli et al., 1997a,b; Haynes et al., 1999a,b) and the Spiral Cluster I-band 2 (SC2; Dale et al., 1999a,c), resulting in the largest Tully-Fisher peculiar velocity sample from a single survey and the largest until the 6dFGSv (Springob et al., 2014). The SFI++ survey covered Galactic latitudes $|b| > 15^\circ$ and used I-band magnitudes for distance and peculiar velocity measurements using the Tully-Fisher relation.

Giovanelli et al. (1998a) measured the bulk flow using the SFI++ sample with a depth of $65h^{-1}$ Mpc and obtained an amplitude of 200 ± 65 km s^{-1} in the direction $\ell = 295^\circ \pm 20^\circ$, $b = 25^\circ \pm 20^\circ$ while Sarkar et al. (2007) obtained an amplitude of 330 ± 101 km s^{-1} in the direction $\ell = 234^\circ \pm 11^\circ$, $b = 12^\circ \pm 9^\circ$ using a sphere with effective radius of $40h^{-1}$ Mpc. Using the

SFI++ survey, Feldman & Watkins (2008) measured a bulk flow motion within $75h^{-1}$ Mpc and obtained an amplitude of 288 ± 71 km s^{-1} in the direction $\ell = 285° \pm 14°$, $b = 11° \pm 10°$. Recently, Nusser & Davis (2011) used the SFI++ sample and measured the bulk flow within a sphere of effective radius of $40h^{-1}$ Mpc and $100h^{-1}$ Mpc. Nusser & Davis (2011) obtained an amplitude of 333 ± 38 km s^{-1} in the direction $(\ell, b) = 276°, 14°$ and 257 ± 44 km s^{-1} in the direction $(\ell, b) = 279°, 10°$ within $40h^{-1}$ Mpc and $100h^{-1}$ Mpc, respectively. These point to or close to the Zone of Avoidance and are all in agreement with predictions from the ΛCDM model.

1.3.2.2 The 2MASS Tully-Fisher Survey

The 2MASS Tully-Fisher (2MTF) Survey aims to map the matter density in the local Universe using distances and peculiar velocities measured using the Tully-Fisher relation. The sample was selected to contain the most inclined bright spiral galaxies in the 2MRS (Huchra et al., 2005a, 2012). The 2MTF survey covers Galactic latitudes as low as $|b| = 5°$ hence providing a good sky coverage despite the remaining part of the Zone of Avoidance which is uncovered at low Galactic latitudes close to the Galactic bulge. The survey includes galaxies selected from the 2MRS which satisfy the following:

- K_s-band magnitude brighter than 11.25 mag,
- Heliocentric velocities, $cz < 10,000$ km s^{-1},
- Galaxy axis ratio, $b/a < 0.5$,
- Galactic latitudes $|b| \geq 5°$.

The photometry for the survey comes from the 2MASS XSC while the HI data were mainly obtained using the 64-m Parkes radio telescope, Green Bank and Arecibo telescopes (Hong et al., 2013; Masters et al., 2014). The survey was first initiated by Masters et al. (2008) who first calibrated the Tully-Fisher relation using the 2MASS J, H and K_s-bands. The measured bulk flow within $40h^{-1}$ Mpc using the K_s-band is of amplitude 292 ± 28 km s^{-1} in the direction $\ell = 296.^{\circ}5 \pm 9.^{\circ}8$, $b = 6.^{\circ}5 \pm 9.^{\circ}2$ (Hong et al., 2014) which, like other previous studies of bulk flows, has direction pointing to the Zone of Avoidance.

1.4 Peculiar Velocity Studies through Redshift Surveys

The concept of peculiar velocities has already been discussed under §1.2 (see Equation 1.5). However, Equation 1.5 describes only the radial (line-of-sight) component which is what is observed. The peculiar velocity field can be determined using

$$cz = H_0 r + \hat{\mathbf{r}} \cdot [\mathbf{v}(r) - \mathbf{v}(0)], \tag{1.27}$$

where $\hat{\mathbf{r}}$ is a unit vector towards the galaxy, $\mathbf{v}(r)$ is the peculiar velocity field or the peculiar velocity at position $\mathbf{r}$, and $\mathbf{v}(0)$ is the peculiar velocity of the observer. For a galaxy/group/cluster with redshift, z, and redshift-independent distance, d, the radial component of peculiar velocity is $v_{\rm pec} \approx cz - H_0 d$. Distance measurements for peculiar velocity studies are usually reported in km s^{-1}, that is, units of $H_0 d$.

Assuming that structure formed from the growth of small perturbations on an initially uniform background (Burstein, 1990; Dekel, 1994), the density field is directly related to the

peculiar velocity field. From the linear perturbation theory, the peculiar velocity is proportional to the gravitational acceleration, that is,

$$\mathbf{v}(\mathbf{r}) = \frac{H_0 f}{4\pi} \int \frac{\mathrm{d}^3\mathbf{r}' \delta_\mathrm{m}\left(\mathbf{r}'\right)\left(\mathbf{r}' - \mathbf{r}\right)}{|\mathbf{r}' - \mathbf{r}|^3}, \tag{1.28}$$

where $\mathbf{v}(\mathbf{r})$ is the velocity field, $\delta\left(\mathbf{r}'\right) = \rho\left(\mathbf{r}'\right)$ is the density contrast in the mass distribution. The other parameters are the linear redshift distortion parameter, $\beta = f(\Omega_0, \Lambda)/b$, where f is the growth factor of linear perturbations, Ω_0 is the cosmological density parameter and Λ is a cosmological constant. The bias parameter, b (Kaiser, 1987) relates the galaxy and dark matter density fields, that is

$$\delta_\mathrm{g}(\mathbf{r}) = b\,\delta_\mathrm{m}(\mathbf{r}), \tag{1.29}$$

where $\delta_\mathrm{g}(\mathbf{r})$ is the galaxy density field. The density contrast, δ_m, at position, $\mathbf{r}$, is given by

$$\delta_\mathrm{m}(\mathbf{r}) = \frac{\rho(\mathbf{r}) - \bar{\rho}}{\bar{\rho}}, \tag{1.30}$$

where $\bar{\rho}$ is the average density of the Universe. In the observed galaxy distribution (measured with galaxy redshift surveys), clustering of galaxies tends to be stronger than the underlying dark matter (Kaiser, 1984; Peacock & Heavens, 1985; Bardeen et al., 1986), that is, galaxies tend to form at the high density peaks of the mass density field, hence the bias. From galaxy redshift surveys, the density field can be estimated while reconstruction of the mass density fluctuations using the linear theory is done using galaxy peculiar velocity surveys. By using galaxy peculiar velocity surveys, the mass density fields have been reconstructed from peculiar velocity measurements by assuming that galaxies trace the velocity field (Bertschinger & Dekel, 1989), that is.

$$\nabla \cdot \mathbf{v} = -\beta\,\delta_\mathrm{g}. \tag{1.31}$$

Examples of such reconstructions include Dekel et al. (1999) who used the MARK III Catalogue of Galaxy Peculiar Velocities (Willick et al., 1997) and revealed the massive nature of the Great Attractor. More recently, Courtois et al. (2012) have reconstructed a three dimensional structure of the local Universe and provided us with a stunning view of the mass densities in the local Universe (for details, see the cosmography of the local Universe by Courtois et al. 2013). Their analysis used data which is part of a larger program: the Extragalactic Distance Database[5] (Tully et al., 2009) whose main aim is to obtain the densest and deepest catalogue of galaxies with distances (and radial peculiar velocities) measured using different, complementary methods (see Tully et al. 2013). Following is a discussion of some of the key redshift surveys that have been conducted.

1.4.1 IRAS Point Source Catalogue Redshift Survey

The infrared astronomical satellite (IRAS) Point Source Catalogue Redshift (PSCz) Survey, consists of ~ 15,411 galaxies with 14,677 redshifts covering 84% of the sky (Saunders et al., 2000). The survey was complete for galaxies to 0.6 Jy but was extended to the Behind the Plane Survey (BPS), covering 93% of the sky. Rowan-Robinson et al. (2000) used the PSCz IRAS galaxy redshift survey (88 nearby groups, 854 clusters and 163 voids), and found convergence at distances $\sim 200h^{-1}$ Mpc.

[5] http://edd.ifa.hawaii.edu/dfirst.php

1.4.2 The REFLEX+eBCS+CIZA Surveys

The Clusters In the Zone of Avoidance (CIZA) survey (Ebeling et al., 2002; Kocevski et al., 2007) is an X-ray flux-limited survey conducted behind the Milky Way. The survey is based on the data from the ROentgen SATellite All Sky Survey (RASS; Voges et al., 1999). The sample was selected to consist of only galaxy clusters with luminosities of $L_X > 5 \times 10^{42}$ erg s^{-1}, and at low Galactic latitudes, i.e., $|b| < 20°$. The survey detected and confirmed (through either imaging or spectroscopic analysis or both), more than 205 galaxy clusters in the Zone of Avoidance, more than 70% of which were newly discovered. The distribution of some of the confirmed galaxy clusters are presented in Figure 1.12. The large circles represent nearby (z<0.075) clusters while the small circles represent more distant clusters.

One of the newly discovered galaxy clusters is CIZA J1324.7-5736, a rich, luminous cluster at $\ell = 307.^\circ4$, $b = 4.^\circ9$, $cz = 5700$ km s^{-1}, that is, $z = 0.019$. This galaxy cluster has since been identified as the second richest cluster in the Great Attractor region (Nagayama et al., 2006). This new cluster along with the Norma cluster (ACO 3627) and the Centaurus cluster (ACO 3526), forms a triangular structure in the Great Attractor region, as shown in the bottom panel of Figure 1.12.

Kocevski & Ebeling (2006) have constructed an All Sky X-ray flux-limited sample of galaxy clusters by combining the ROSAT-ESO Flux-limited X-ray Galaxy Cluster Survey (REFLEX; Böhringer et al., 2001, 2004), the extended ROSAT (ROentgen SATellite) Brightest Cluster Sample catalogue (eBCS; Ebeling et al., 2000) and the Clusters in the Zone of Avoidance data (CIZA; Ebeling et al., 2002). In the analysis of the composite REFLEX+eBCS+CIZA sample, Kocevski & Ebeling (2006) found no convergence (and no backside infall) at the distance of the Great Attractor. They estimated that 44% of the Local Group's peculiar velocity is due to infall into the Great Attractor region, while 56% is due to more distant overdensities at distances between 130 and $180h^{-1}$ Mpc. They further reported that the Shapley Supercluster dominates the distant overdensities and contributes 30.4% of the 56%. Figure 1.13 shows their results; $\mathbf{D}_{\rm cl}$ refers to the dipole vector quantity. This is related to the peculiar velocity vector $\mathbf{v}_{\rm p}$ through:

$$\mathbf{v}_{\rm p} = \beta \mathbf{D}_{\rm cl}, \tag{1.32}$$

where β is related to the biasing parameter, b, via $\beta = \Omega_{\rm m}^{0.6}/b$, where $\Omega_{\rm m}$ is the mass density parameter. The actual velocity dipole is given by $\beta D_{\rm cl}$.

1.4.3 Two Micron All-Sky Redshift Survey

The Two Micron All-Sky Redshift Survey (2MRS), as already described under §1.1.2, is a magnitude-limited sample, selected from the 2MASS Extended Source Catalogue. Using the 2MRS sample (with K_s-band extinction corrected magnitude $< 11.^{\rm m}25$), Erdoğdu et al. (2006a) found convergence within $60h^{-1}$Mpc, indicating that the Local Group's peculiar velocity is generated mainly by the large scale structures within $60h^{-1}$Mpc, of which the Great Attractor is most dominant. Similarly, they detected a backside infall into the Great Attractor (§1.2.4) by reconstructing velocity fields on the 2MRS subsample (Erdoğdu et al., 2006b). On the other hand, Lavaux et al. (2010) recently reconstructed peculiar velocities using the 2MRS and found no convergence of the Local Group's motion within $120h^{-1}$ Mpc. Lavaux et al. (2010) recovered the majority of the amplitude of the Local Group's peculiar velocity within $120h^{-1}$ Mpc, but the direction of motion did not agree – they suggested the convergence lies as far as $200\,h^{-1}$ Mpc (see also Bilicki et al. 2011).

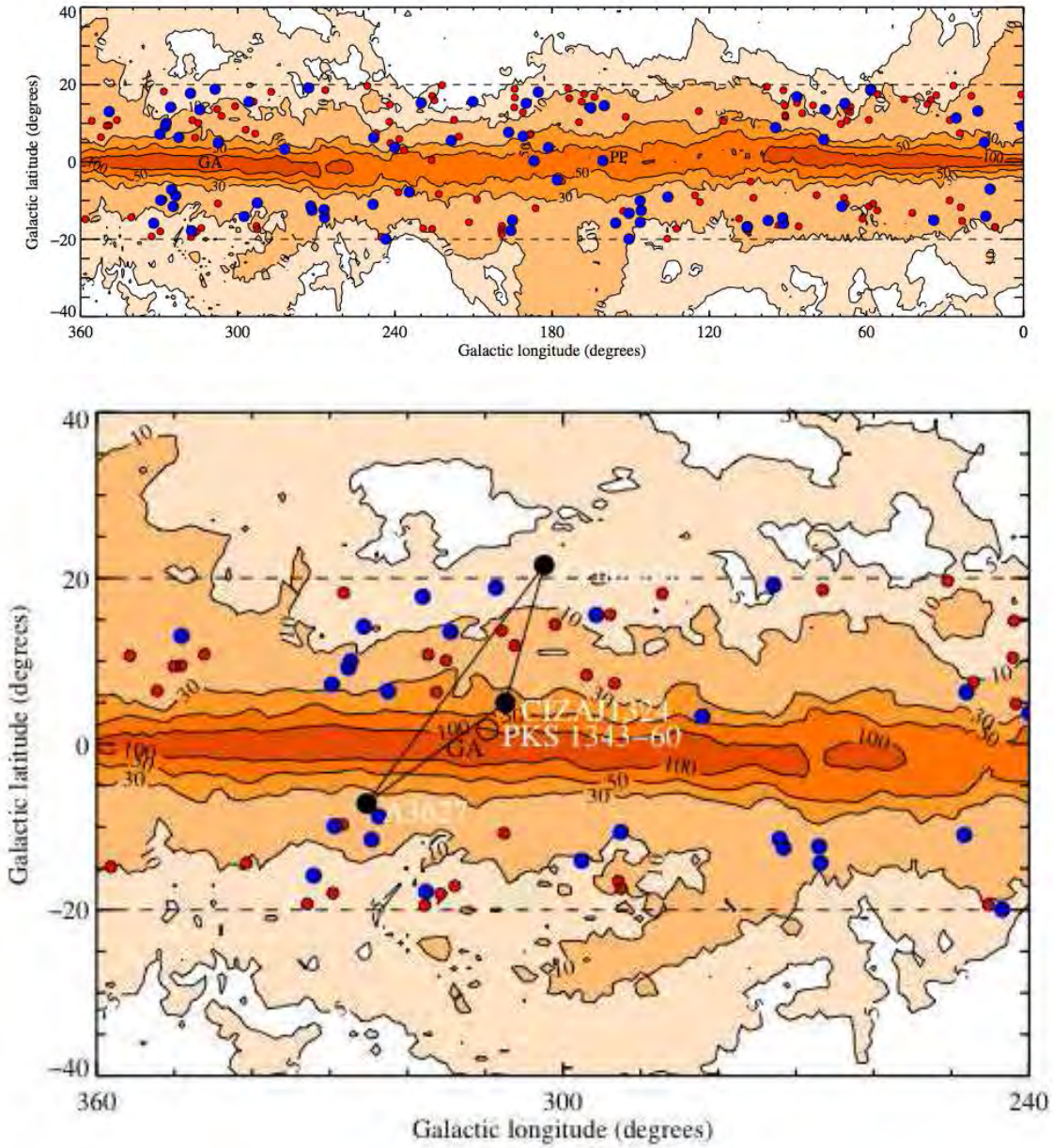

Fig. 1.12: Top panel shows the 191 CIZA clusters with fluxes greater than 2×10^{-12} erg cm^{-2} s^{-1} confirmed by CIZA survey; grey-scale map represents the distribution of Galactic neutral hydrogen. GA and PP represents the Great Attractor and the Perseus–Pisces filaments, respectively. The bottom panel shows the same but only in the Great Attractor region, that is, Galactic longitudes between 240° and 360°. The triangular wall-like structure is marked by the solid black lines joining the three black filled circles which form the vertices of the triangle (the Norma cluster is marked as A3627). Figures taken from Ebeling et al. (2005) — see also Kocevski et al. (2007).

Recently, Nusser et al. (2014) showed that the Local Group motion can not be recovered to better than 150 – 200 km s^{-1} in amplitude and within $\approx 10°$ in direction. Nusser et al. (2014) further show that the main source of uncertainty in their analysis is the limited depth of galaxy surveys like the 2MRS, which prevents a proper sampling of the large scale structure beyond $\sim 100h^{-1}$ Mpc. For an all sky survey like the 2MRS, the contribution to the Local Group motion can be assessed reliably only within $100h^{-1}$ Mpc (Nusser et al., 2014), hence the need for deeper redshift surveys in order to reach the 'convergence scale' of $\sim 250h^{-1}$ Mpc in a ΛCDM universe.

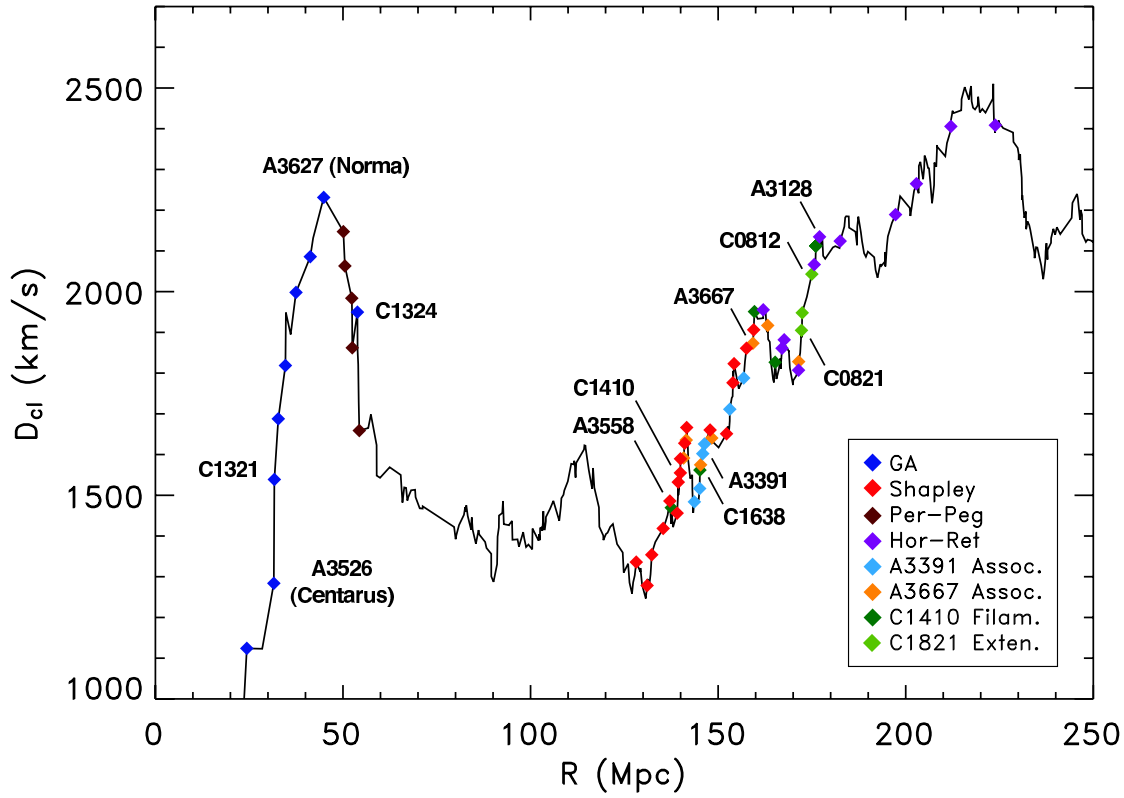

Fig. 1.13: The impact on the Local Group's peculiar motion by the observed large scale structures. Letters "A" and "C" at the beginning of cluster names indicate Abell ("A") and CIZA ("C") clusters, respectively. The clusters have further been grouped into their respective associations and this is indicated by the same colour assigned to the same groupings. The blue and red diamonds represent clusters in the Great Attractor region and Shapley Supercluster, respectively. The acronyms used in the Figure are: GA for Great Attractor, Hor–Ret for Horologium-Reticulum, Per–Peg for Perseus–Pegasus. Figure taken from Kocevski & Ebeling (2006).

1.4.4 The 2M++ Galaxy Redshift Catalogue

The 2M++ galaxy redshift compilation took advantage of the existing data and attempted to map large-scale structures of the Local Universe over nearly the whole sky using high-quality galaxy redshifts from the 2MRS (Erdoğdu et al., 2006a; Huchra et al., 2005b, 2012), the 6dF Galaxy Survey Data Release Three (6dFGS; Jones et al., 2009) and the Sloan Digital Sky Survey Data Release Seven (SDSS-DR7; Abazajian et al., 2009). The 2M++ galaxy redshift catalogue resulted in a total of 69,160 galaxies covering nearly the whole sky reaching depths of about $200h^{-1}$ Mpc after combining the 2MRS, 6dF and SDSS (Lavaux & Hudson, 2011). The photometry for the 2M++ galaxy redshift compilation is from the 2MASS Extended Source Catalogue (Skrutskie et al., 2006).

The near-infrared K_s-band magnitude limit is 11.5 mag for the 2MRS and 12.5 mag for the regions of the sky covered by SDSS or 6dF. These magnitudes were measured using circular isophotes with a surface brightness level of 20 mag arcsec^{-2} in the K_s-band. The magnitude limits were set after applying various corrections to the measured isophotal magnitudes, that is, corrections for Galactic extinction, cosmological dimming, stellar evolution and redshift effects. In the 2M++ redshift compilation, galaxies from the 2MRS were additionally limited to $|b| > 5°$ deep in the Zone of Avoidance and $|b| > 10°$ in the region $-30° < \ell < +30°$ (Erdoğdu et al., 2006a) – this excludes regions covered by SDSS or 6dF (Lavaux & Hudson, 2011). Figure 1.14 shows the 69,160 galaxies in the 2M++ catalogue colour-coded according to redshift. Blue represents

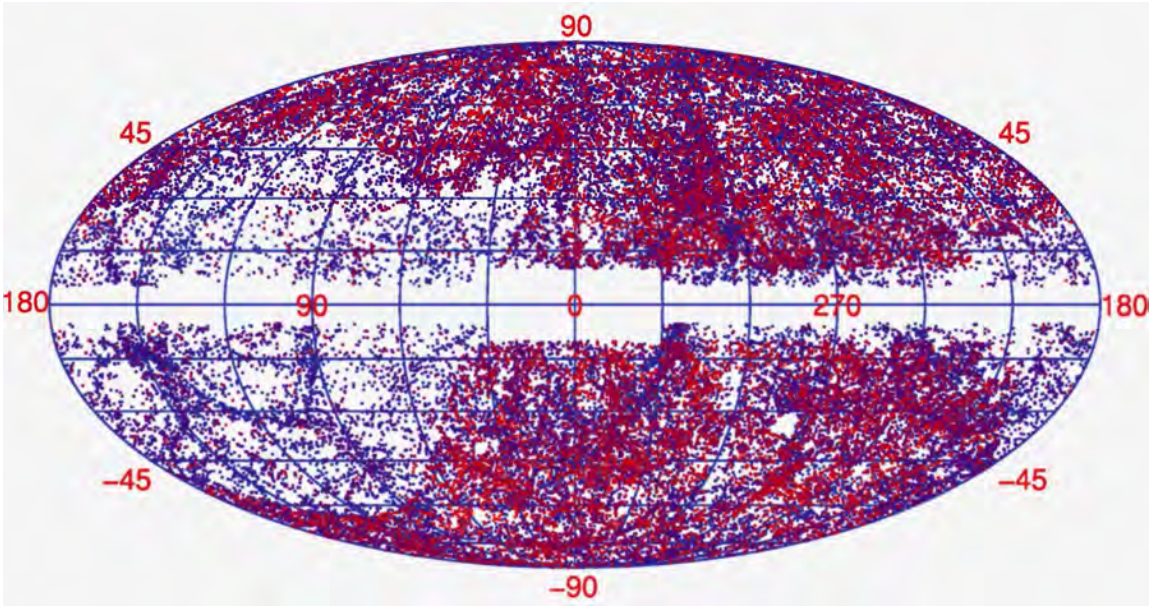

Fig. 1.14: A Molleweide projection in Galactic coordinates showing all the 69,160 galaxies in the 2M++ compilation sample color-coded according to the redshift distance. Nearby galaxies are represented by blue while red represents the farthest galaxies. Figure taken from Lavaux & Hudson (2011) — the bottom right-hand panel of their figure 4.

nearest while red represents farthest galaxies. The 2M++ redshift compilation covers ∼ 90% of the sky (Lavaux & Hudson, 2011).

Carrick (2014) have performed galaxy density reconstructions by utilising the newly compiled 2M++ redshift catalogue. The depth and coverage of the 2M++ sample allows good sampling of relatively distant superclusters such as the Shapley Concentration (Carrick, 2014). Using only the 2M++ coverage, they predicted a Local Group motion of 540±40 km s^{-1} in the direction $\ell = 268.^{\circ}4$, $b = 38.^{\circ}6$. This is so far the best measured alignment with the CMB dipole to date ($\sim 10^{\circ}$ misalignment with the CMB dipole) which supports the earlier suggestion by Lavaux et al. (2010) that the convergence of the observed Local Group motion in both magnitude and direction lies as far as $200h^{-1}$ Mpc.

1.4.5 Bulk Flows

Peculiar velocity measurements and predictions are useful cosmological probes (Koda et al., 2014) since peculiar velocities are sensitive to the matter distribution (including dark matter) on large scales. Using the assumption that the large scale structure we see today formed from the growth of small perturbations on an initially uniform background (Burstein, 1990; Dekel, 1994), the density field is directly related to the peculiar velocity field. From linear perturbation theory, the peculiar velocity is proportional to the gravitational acceleration (Peebles, 1993), that is,

$$\mathbf{v}(\mathbf{r}) = \frac{H_0}{4\pi}\frac{f}{b}\int_0^{\infty} \mathrm{d}^3\mathbf{r}'\delta_{\mathrm{g}}\left(\mathbf{r}'\right)\frac{\left(\mathbf{r}'-\mathbf{r}\right)}{|\mathbf{r}'-\mathbf{r}|^3}, \tag{1.33}$$

where f describes the rate of growth of structure and is approximately given by $f = \Omega_{\mathrm{m}}^{0.55}$ (Wang & Steinhardt, 1998; Linder, 2005) in a flat ΛCDM universe. The bias parameter, b, relates the galaxy and dark matter density fields (Kaiser, 1987), that is, $\delta_{\mathrm{g}}(\mathbf{r}) = b\,\delta_{\mathrm{m}}(\mathbf{r})$.

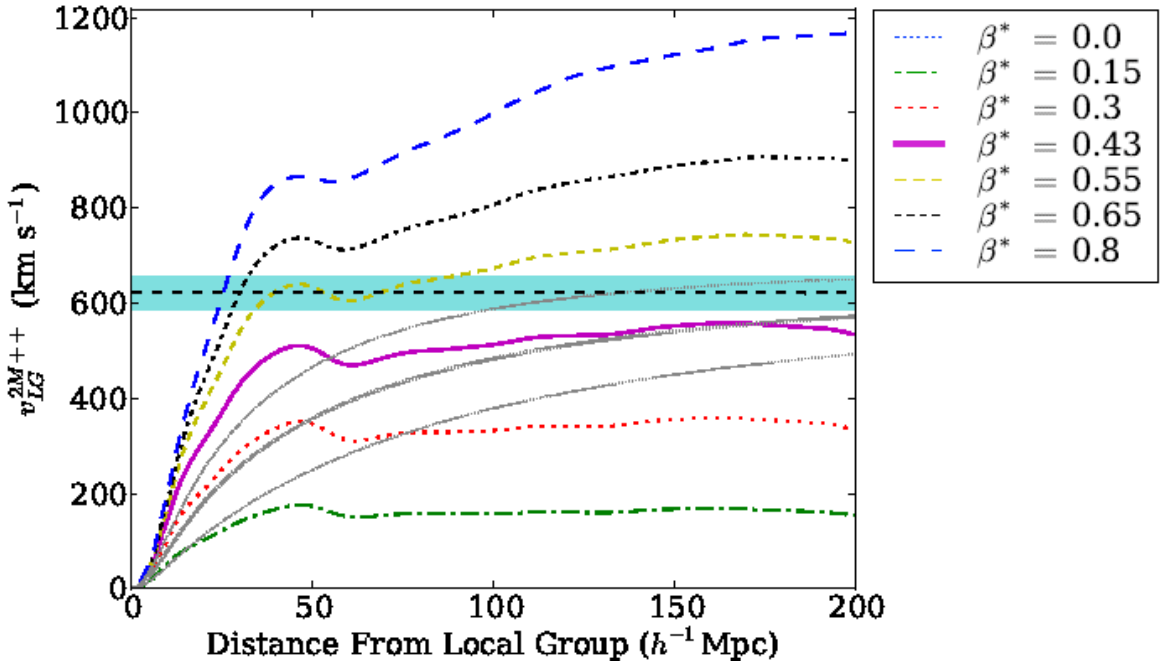

Fig. 1.15: Growth of the Local Group velocity amplitude from linear theory predictions on increasing scales. The 2M++ best fit value ($\beta^* = 0.43$) is represented by the solid purple curve. The grey lines represent the expected growth of the Local Group velocity amplitude $\pm 1\sigma$ in a ΛCDM cosmology with WMAP9 best fit parameters (Hinshaw et al., 2013). The x-axis represents the survey depth. The region shaded in cyan corresponds to the velocity of the Local Group $\pm 1\sigma$ inferred from the CMB dipole. Figure taken from Carrick et al. (2015), their figure 6.

For an all-sky redshift survey extending to a distance $R_{\rm max}$, the peculiar velocity for a galaxy at position r can be obtained by rewriting Equation 1.33 as:

$$\mathbf{v}_{\rm pred}(\mathbf{r}) = \frac{\beta}{4\pi}\int_0^{R_{\rm max}} \mathrm{d}^3\mathbf{r}'\delta_{\rm g}(\mathbf{r}')\frac{(\mathbf{r}'-\mathbf{r})}{|\mathbf{r}'-\mathbf{r}|^3} + \mathbf{U}, \tag{1.34}$$

where $\beta \equiv \frac{f(\Omega_{\rm m})}{b}$ is the linear redshift distortion parameter, $\Omega_{\rm m}$ is the mass density parameter and $\mathbf{U}$ is the residual bulk flow. The first term of $\mathbf{v}_{\rm pred}$ is the peculiar velocity induced by structure within the redshift survey volume ($r < R_{\rm max}$) while the residual bulk flow, $\mathbf{U}$, is the additional velocity of the entire redshift survey volume in the cosmic microwave background reference frame. This additional velocity, $\mathbf{U}$, is presumably due to sources beyond $R_{\rm max}$.

Figure 1.15 (taken from Carrick et al. 2015) shows the linear theory predictions of the growth of Local Group velocity amplitude on increasing scales. The predicted growth of the Local Group velocity amplitude using 2M++ for different values of β^*, where $\beta^* \equiv \Omega_{\rm m}^{0.55}/b^*$, is also shown. The different values of β^* are indicated and the best fit parameter is $\beta^* = 0.43 \pm 0.02$ (Carrick et al., 2015), which is represented by the solid purple curve. The smooth grey lines represent the ΛCDM model predictions ($\pm 1\sigma$) with WMAP9 best fit parameters (Hinshaw et al., 2013). The shaded region (in cyan) is the velocity of the Local Group ($\pm 1\sigma$) as inferred from the CMB dipole, that is, 622 ± 35 km s^{-1} towards Galactic $\ell = 272.^{\circ}3$, $b = 28.^{\circ}5$ (Hinshaw et al., 2009).

Figure 1.16 shows the volume-weighted mean of the predicted velocity field (bulk flow) for a Gaussian window of increasing depth centred on the Local Group. The 2M++ predictions including the residual bulk flow are shown by the dashed grey line with 68% uncertainties in

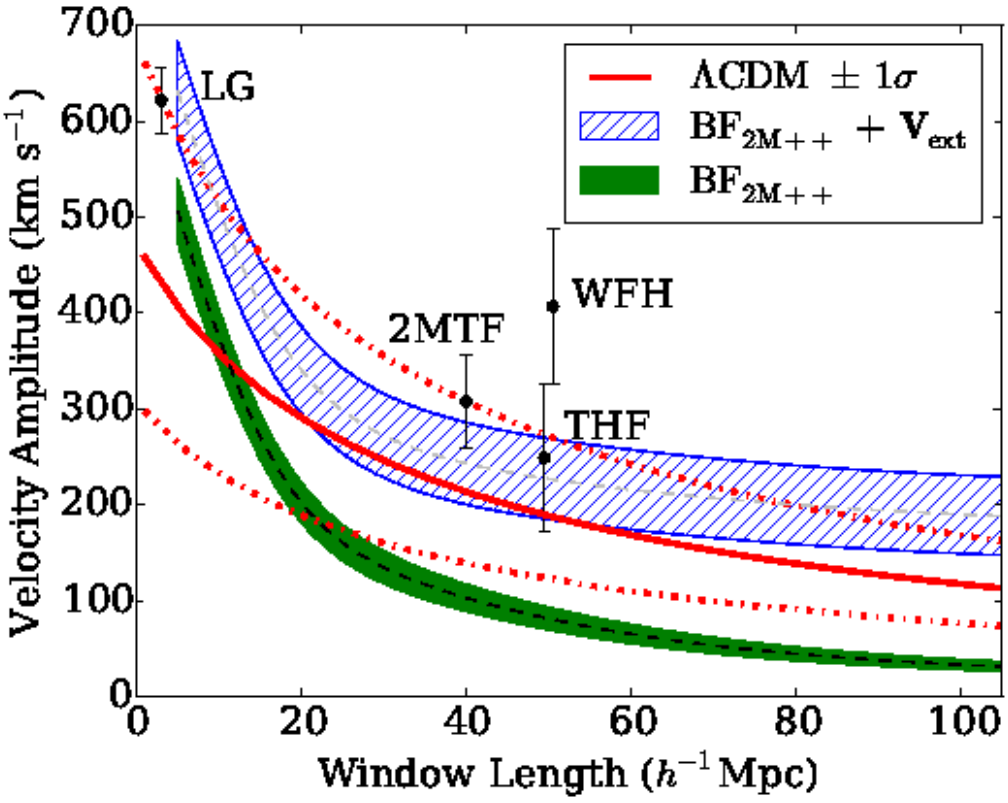

Fig. 1.16: Volume-weighted mean of predicted bulk flow for Gaussian window of increasing depth centred on the Local Group. 2M++ predictions including the residual bulk flow are represented by the dashed grey line with 68% uncertainties in blue hatch. The dashed black line shows the 2M++ predictions without the residual bulk flow (the 68% uncertainties are shown in solid green). The velocity amplitude and its uncertainty ($\pm 1\sigma$) predicted from the ΛCDM universe with WMAP9 best fit parameters (Hinshaw et al., 2013) are represented by the red solid line and red dot-dash lines, respectively. Some of the recent bulk flow measurements are also shown; 2MTF (Hong et al., 2014) who used a radius of $40h^{-1}$ Mpc, THF (Turnbull et al., 2012) and WFH (Watkins et al., 2009) who used a sphere with radius $\sim 50h^{-1}$ Mpc. The Local Group motion is indicated at a radius of $3h^{-1}$ Mpc. Figure taken from Carrick et al. (2015), their figure 9.

blue hatch. The dashed black line shows the 2M++ predictions without the residual bulk flow (the 68% uncertainties are shown in solid green). The predicted velocity amplitude for a ΛCDM WMAP9 cosmology (Hinshaw et al., 2013) is shown as the red solid line while the red dot-dash lines show the cosmic scatter in the velocity amplitude distribution. Some of the recent bulk flow measurements are also shown for: 2MTF (Hong et al., 2014) who used a radius of $40h^{-1}$ Mpc, THF (Turnbull et al., 2012) and WFH (Watkins et al., 2009) who used a sphere with radius $\sim 50h^{-1}$ Mpc. The Local Group motion is also indicated (at a radius of $3h^{-1}$ Mpc). Figure 1.16 was taken from Carrick et al. (2015).

Employing the brightest cluster galaxies as distance indicators, Lauer & Postman (1994) used distances for 432 late spiral galaxies in 119 nearby Abell clusters with $cz_\odot < 15\,000$ km s^{-1} and obtained a bulk flow of 689 ± 178 km s^{-1} in the direction $\ell = 343°$, $b = 52°$ (in Galactic coordinates). This is in strong disagreement with the ΛCDM model predictions (see Figure 1.16 for the expectations from ΛCDM model). The result reported in Lauer & Postman (1994) was immediately challenged by e.g., Riess et al. (1995), Giovanelli et al. (1996), Dale et al. (1999b), Willick (1999). Hudson & Ebeling (1997) used a subsample of 64 clusters and found a bulk flow with a slightly lower amplitude than that reported in Lauer & Postman (1994) and in a

significantly different direction, that is, Hudson & Ebeling (1997) found a bulk flow ~ 494 km s^{-1} towards $\ell = 285°$, $b = 47°$ – see also Hudson et al. (1999). In addition, Hudson et al. (2004) used the Streaming Motions of Abell Clusters sample (SMAC; Hudson et al., 2001), within 12 000 km s^{-1} and found a bulk flow of 687 ± 203 km s^{-1} towards $\ell = 260° \pm 13°$, $b = 0° \pm 11°$. When compared with peculiar velocities predicted from the IRAS Point Source Catalogue redshift (PSCz) survey, the PSCz density field does not fully account for all of the SMAC bulk flow. Hudson et al. (2004) detected a residual bulk flow of 372 ± 127 km s^{-1} towards $\ell = 273°$, $b = 6°$. This residual flow is generated by sources not in the PSCz catalogue, either beyond $200h^{-1}$ Mpc or in the Zone of Avoidance (Hudson et al., 2004). While the amplitude of the bulk flow found by Hudson et al. (2004) is close to that found by Lauer & Postman (1994), the direction of the SMAC flow is $\sim 90°$ away from the flow found by Lauer & Postman (1994). Note that the results obtained by Lauer & Postman (1994) and Hudson et al. (2004) are both in disagreement with the ΛCDM model predictions with WMAP9 best fit parameters (Hinshaw et al., 2013).

Another interesting recent analysis of all major peculiar velocity surveys is by Watkins et al. (2009). They combined the individual peculiar velocity samples (mostly from Tully-Fisher, Fundamental Plane and supernovae) into a 'composite' sample of 4481 peculiar velocity tracers. Using this 'composite' sample, Watkins et al. (2009) found a bulk flow of magnitude 407 ± 81 km s^{-1} towards $\ell = 287° \pm 9°$, $b = 8° \pm 6°$ on the scale of $50h^{-1}$ Mpc radius. Watkins et al. (2009) claim their result is inconsistent with the ΛCDM model at $> 98\%$ confidence level. Feldman et al. (2010) analysed a compilation of all major peculiar velocity surveys, consisting of 4536 measurements and estimated the bulk flow on scales of $\sim 100h^{-1}$ Mpc to be 416 ± 78 km s^{-1} towards Galactic $\ell = 282° \pm 11°$ and $b = 6° \pm 6°$, which is in disagreement with predictions from the ΛCDM model.

The most contraversial bulk flow result is that of the Sunyaev-Zeldovich (Sunyaev & Zeldovich, 1980) flow dipole reported by Kashlinsky et al. (2010) who found a bulk flow ~ 1000 km s^{-1} in the direction $\ell = 296° \pm 28°$, $b = 39° \pm 14°$ over a scale of at least $800h^{-1}$ Mpc. This result strongly conflicts with, and can not be accommodated in the ΛCDM model. It has been suggested that the high amplitude (1005 ± 267 km s^{-1}) bulk flow for $z < 0.25$ clusters found by Kashlinsky et al. (2010), could be due to a tilted universe (Kashlinsky et al., 2008; Ma et al., 2011).

On the other hand, Colin et al. (2011) used the Union2 catalogue (Amanullah et al., 2010) of SNe Ia of which 165 are within 30 000 km s^{-1}. Colin et al. (2011) obtained a bulk flow of 260 ± 150 km s^{-1} based on SNe within 18 000 km s^{-1}. Turnbull et al. (2012) used Type Ia Supernovae (SNe) sample with 245 peculiar velocity measurements, finding a bulk flow of 249 ± 76 km s^{-1} in the direction $\ell = 319° \pm 18°$, $b = 7° \pm 14°$. These are consistent with the ΛCDM model predictions. Turnbull et al. (2012) compared the SNe peculiar velocity predictions of the IRAS Point Source Catalogue Redshift Survey (PSCz; Branchini et al., 1999; Saunders et al., 2000) galaxy density field and found that the PSCz density field fails to account for 150 ± 43 km s^{-1} of the SNe bulk motion. This residual bulk flow is significantly different from zero at the 99.6% confidence level (Turnbull et al., 2012) and may suggest that IRAS PSCz undersamples massive dense superclusters such as the Shapley Concentration.

The First Amendment Supernovae (A1) catalogue used in Turnbull et al. (2012) consists of 245 Type Ia supernovae obtained by merging the data sets of Jha et al. (2007), Hicken et al. (2009), and (Folatelli et al., 2010). Note that 103 of the 108 SNe in Watkins et al. (2009) are also in A1 of Turnbull et al. (2012), yet the bulk flow measured by the latter is consistent with ΛCDM model predictions. It was also recently reported that different statistical methods should not dramatically alter the results from bulk flow measurements (Nusser & Davis, 2011). More over, Nusser & Davis (2011) estimated the bulk flow using the SFI++ Tully-Fisher (TF) catalogue

and obtained results consistent with the ΛCDM model predictions. That is, Nusser & Davis (2011) derived a bulk flow of 333 ± 38 km s^{-1} toward Galactic $(\ell, b) = (276^\circ \pm 3^\circ, 14^\circ \pm 3^\circ)$ using a sphere of radius $40h^{-1}$ Mpc. Within a radius of $100h^{-1}$ Mpc, Nusser & Davis (2011) obtained 257 ± 44 km s^{-1} toward $(\ell, b) = (279^\circ \pm 6^\circ, 10^\circ \pm 6^\circ)$. This is consistent with the ΛCDM model predictions and does not support the large amplitude bulk flow found by Watkins et al. (2009).

A recent analysis by Ma & Scott (2013) suggested potential problems in Watkins et al. (2009) which may result in biased results. These include

- the inhomogeneous Malmquist bias which is not corrected for in most catalogues, for example, the Early-type NEARby galaxies sample (ENEAR; da Costa et al., 2000a; da Costa et al., 2000b; Bernardi et al., 2002); Supernovae sample (SN) from Tonry et al. (2003); SC (Giovanelli et al., 1998b; Dale et al., 1999a); Early-type galaxies FAR away (EFAR; Colless et al., 2000, 2001b) and Willick (Willick, 1999). Inhomogeneous Malmquist bias arises from variations in galaxy number density along the line of sight (Hudson, 1994b; Willick et al., 1997). The uncorrected for inhomogeneous Malmquist bias can significantly bias the distance estimates resulting in more positive peculiar velocities where distances are underestimated and vice-versa.

- for deeper surveys $\gtrsim 100h^{-1}$ Mpc, the errors on the distances measured using the Tully-Fisher and Fundamental Plane relations are comparable to the measured peculiar velocities. This results in noisy data hence making it difficult to accurately measure the bulk flow on large scales (Nusser et al., 2014) since peculiar velocity estimates of distant galaxies are error dominated.

- systematic errors originating from directly combining various catalogues with different calibration methods.

Ma & Scott (2013) have thus, carefully investigated the analysis presented in Watkins et al. (2009) by selecting samples from the SN, ENEAR, Spiral Field I-band Survey (SFI++; Masters et al., 2006; Springob et al., 2007, 2009) and the First Amendment Supernovae (A1SN). Ma & Scott (2013) obtained a bulk flow of 310 km s^{-1} in the direction $\ell = 280^\circ \pm 8$, $b = 5.^\circ 1 \pm 6^\circ$ on scales of $50h^{-1}$ Mpc, which is consistent with the ΛCDM model predictions and bulk flow results from most previous studies, e.g., Nusser & Davis (2011); Turnbull et al. (2012). Both Turnbull et al. (2012) and Ma & Scott (2013) used SFI++ and obtained results consistent with each other, leading to Ma & Scott (2013) questioning whether the high bulk flow amplitude reported by Watkins et al. (2009) is due to the other peculiar velocity surveys used in the 'composite' sample of Watkins et al. (2009). A recent study by Watkins & Feldman (2015) indeed found that the high amplitude bulk flow presented earlier in Watkins et al. (2009) was due to the inclusion of the EFAR (Early-type galaxies FAR away; Colless et al., 2000, 2001b) sample in their compilation. By removing the EFAR sample from the compilation presented in Watkins et al. (2009), Watkins & Feldman (2015) found a small bulk flow with amplitude $\sim 393 \pm 64$ km s^{-1}, within $50h^{-1}$ Mpc. While still inconsistent with the expectations from the ΛCDM, it is consistent with their result ($v_{\rm bulk} = 380 \pm 64$ km s^{-1}) presented in Watkins & Feldman (2015) using *Cosmicflows-2* (Tully et al., 2013) on the same scale and without including the EFAR sample.

Recently, Hong et al. (2014) and Carrick et al. (2015) have, respectively, used the 2MTF and 2M++ to estimate the bulk flow. 2MTF aims at mapping the galaxy peculiar velocity field within $100h^{-1}$ Mpc, with an all sky coverage except $|b| < 5^\circ$. The galaxies in the 2MTF sample were subjected to a K_s-band magnitude cut less than 11.25 mag, $cz < 10\,000$ km s^{-1} and axis ratio $b/a < 0.5$. This resulted in ~ 6000 galaxies although many of them are faint in HI (Hong et al.,

2014). In addition, the 888 cluster spiral galaxies used by Masters et al. (2008) to calibrate the Tully-Fisher template relation were removed from the 2MTF sample used by Hong et al. (2014). This resulted in 2018 spiral galaxies, which in addition, satisfy the following criteria:

- HI spectrum signal-to-noise ratio, $SNR \geq 5$
- $cz \geq 600$ km s^{-1}
- Relative HI width error $\frac{\epsilon_W}{W_{\rm HI}} \leq 10\%$

Using the 2018 spiral galaxies, Hong et al. (2014) combined their bulk flow measurements in the 2MASS J, H and K_s-bands, and found, within radii of 20, 30 and $40h^{-1}$ Mpc, bulk flow amplitudes of 311 ± 34 km s^{-1} in the direction $(\ell, b) = (287.^\circ9 \pm 5.^\circ9, 11.^\circ1 \pm 3.^\circ4)$, 281 ± 25 km s^{-1} in the direction $(\ell, b) = (296.^\circ4 \pm 16.^\circ1, 19.^\circ3 \pm 6.^\circ3)$, 292 ± 28 km s^{-1} in the direction $(\ell, b) = (296.^\circ5 \pm 9.^\circ8, 6.^\circ5 \pm 9.^\circ2)$, respectively. These are consistent with the ΛCDM model predictions.

2M++ compilation combines 2MRS ($K < 11.5$), 6dF ($K < 12.5$) and SDSS ($K < 12.5$), resulting in $\sim 70\,000$ galaxies reaching $200h^{-1}$ Mpc in 6dF and SDSS areas. Carrick (2014); Carrick et al. (2015) have used 2M++ and predicted the Local Group motion arising from 2M++ to be 535 ± 40 km s^{-1} in the direction $(\ell, b) = (268^\circ \pm 4^\circ, 38^\circ \pm 6^\circ)$, only 10° out of alignment with the direction of the Local Group motion inferred from the CMB dipole (Hinshaw et al., 2009). This implies a residual Local Group motion of 100 ± 37 km s^{-1} in the direction $\ell = 303^\circ \pm 36^\circ$, $b = 34^\circ \pm 36^\circ$ (Carrick et al., 2015). Carrick et al. (2015) found a residual bulk flow of 159 ± 23 km s^{-1} in the direction $(\ell, b) = (303^\circ \pm 11^\circ, 6^\circ \pm 13^\circ)$, which is the velocity contribution arising from structures beyond the volume covered by 2M++. Thus, the observed motion of the Local Group is not fully accounted for, with suggestions that structures beyond $150h^{-1}$ Mpc may have considerable contributions (Kocevski & Ebeling, 2006; Nusser & Davis, 2011) while Bilicki et al. (2011) found that the 2MASS dipole had not converged at an effective distance $\sim 300h^{-1}$ Mpc. Some of the recent bulk flow measurements are presented in Table 1.1.

1.5 Multiwavelength Studies of the Norma Cluster

Figures 1.12 and 1.13 show that the Norma cluster is located close to the core of the Great Attractor. Its significance in the dynamics of the local Universe was first realised by Kraan-Korteweg et al. (1996) who identified Norma as the most massive nearby cluster. X-ray observations of the Norma cluster using the ROentgen SATellite (Boehringer et al., 1996) and the Advanced Satellite for Cosmology (Tamura et al., 1998) confirmed ACO 3627 as a massive cluster. It is the sixth brightest cluster in the ROentgen SATellite All Sky Survey (Boehringer et al., 1996). The cluster has also been identified as the most massive cluster in the Great Attractor region: $316^\circ \lesssim \ell \lesssim 338^\circ$, $-10^\circ \lesssim b \lesssim 10^\circ$ (Woudt & Kraan-Korteweg, 2001), with two large cD galaxies at its centre, typical of rich clusters (Woudt et al., 1998). The Norma cluster is however located very close to the Galactic Plane, in the southern Zone of Avoidance, at $(\ell, b, v) = (325.^\circ3, -7.^\circ2, 4871$ km s$^{-1})$, e.g., Woudt et al. (2008). At such low Galactic latitudes, Galactic extinction and star-crowding effects are severe, although the extinction is reduced at near-infrared wavelengths.

In Figure 1.17, the Zone of Avoidance is represented by the region devoid of galaxies, stretching from the right to the left, through the centre, at Galactic latitude 0° (see also Figure 1.8). The position of the Norma cluster is clearly visible as the prominent structure at Galactic coordinates $(\ell, b) \sim (325^\circ, -7^\circ)$. Norma's location in the Zone of Avoidance thus makes it difficult to observe, especially at optical wavelengths. The centre of the Great Attractor proposed by Kolatt et al.

Tab. 1.1: Bulk flow measurements from recent peculiar velocity studies. Column 1 represents the catalogue used, column 2 the depth or the effective radius. Column 3 is the amplitude of the bulk flow while columns 4 and 5 indicate the direction of the flow (in Galactic coordinates). Column 6 represents the author. While there has been conflicting claims regarding the amplitude, and its tension with the expected value in a ΛCDM universe, the vast majority of these surveys have been consistent in their findings for the direction – pointing to or close to the Zone of Avoidance.

Catalogue	Scale (h^{-1} Mpc)	$\|\|v\|\|$ (km s^{-1})	ℓ (°)	b (°)	Reference
COMP1	40	330 ± 101	234 ± 11	12 ± 9	Sarkar et al. (2007)
X-ray/CMB	300 – 800	600 – 1000	283 ± 18	12 ± 14	Kashlinsky et al. (2008)
COMP2	50	407 ± 81	287 ± 9	8 ± 6	Watkins et al. (2009)
COMP3	100	416 ± 78	282 ± 11	6 ± 6	Feldman et al. (2010)
SN	150	188^{+119}_{-103}	290^{+39}_{-31}	20 ± 32	Dai et al. (2011)
SFI++	40	333 ± 38	276 ± 3	14 ± 3	Nusser & Davis (2011)
SFI++	100	257 ± 44	279 ± 6	10 ± 6	Nusser & Davis (2011)
Union 2	100	250^{+190}_{-160}	287^{+62}_{-48}	21^{+34}_{-52}	Colin et al. (2011)
Union 2	160	260 ± 150	298^{+62}_{-48}	8^{+34}_{-52}	Colin et al. (2011)
A1	50	248 ± 87	319 ± 25	7 ± 13	Turnbull et al. (2012)
ENEAR	50	220 ± 60	310 ± 30	-9.8 ± 14	Ma & Scott (2013)
A1SN	50	220 ± 70	290 ± 60	12.1 ± 20	Ma & Scott (2013)
SN	50	370 ± 110	290 ± 30	-0.7 ± 15	Ma & Scott (2013)
SFI++	50	340 ± 40	280 ± 8	5.1 ± 6	Ma & Scott (2013)
ENEAR	49	250 ± 50	314 ± 14	-6^{+11}_{-9}	Ma & Pan (2014)
SFI++	58	290 ± 30	281 ± 7	8^{+6}_{-5}	Ma & Pan (2014)
A1SN	62	230 ± 50	296 ± 16	15^{+13}_{-12}	Ma & Pan (2014)
SC	63	190^{+120}_{-90}	231	-2^{+35}_{-31}	Ma & Pan (2014)
2MTF	20	311 ± 34	288 ± 6	11 ± 3	Hong et al. (2014)
2MTF	30	281 ± 25	296 ± 16	19 ± 6	Hong et al. (2014)
2MTF	40	292 ± 28	297 ± 10	7 ± 9	Hong et al. (2014)
2M++	50	230 ± 30	293 ± 8	14 ± 10	Carrick et al. (2015)

NOTES:
COMP1 is a composite sample consisting six galaxy peculiar velocity surveys. These are ENEAR (da Costa et al., 2000a,b; Bernardi et al., 2002), Spiral Field I-band (SFI; Giovanelli et al., 1994, 1995; da Costa et al., 1996), Revised Flat Galaxy Catalogue (RFGC; Karachentsev et al., 2000), surface brightness fluctuations (SBF; Tonry et al., 2001) and the Mark III singles and group catalogues (Willick et al., 1995, 1996, 1997).
COMP2 is a composite sample of galaxy peculiar velocity surveys; viz SBF, ENEAR, SN (Tonry et al., 2003), SFI++ (Masters et al., 2006; Springob et al., 2007, 2009), SC (Giovanelli et al., 1998b; Dale et al., 1999a), SMAC, LP (Lauer & Postman, 1994), EFAR (Colless et al., 2000, 2001b) and Willick (Willick, 1999).
COMP3 is a composite sample combining SNIa (from Tonry et al. 2003), SC, SMAC, EFAR, SFI++, ENEAR and SBF.
A1 (Turnbull et al., 2012) is the First Amendment Supernovae catalogue obtained by merging the data sets of Jha et al. (2007), Hicken et al. (2009) and Folatelli et al. (2010).
A1SN (Ma & Pan, 2014) is the Type Ia supernovae sample from Turnbull et al. (2012).

(1995) is at $\ell = 320°$, $b = 0°$. At such low Galactic latitudes, it is therefore heavily obscured, with a possibility that the majority of the galaxies within this region remain hidden – refer to the discussion under §1.2.3.

Nonetheless, multiwavelength studies from X-ray to radio observations of the Norma cluster have been conducted in the quest to reveal more about this rich, massive, nearby cluster. These have provided us with rich data and information about Norma and its dynamics. Studies

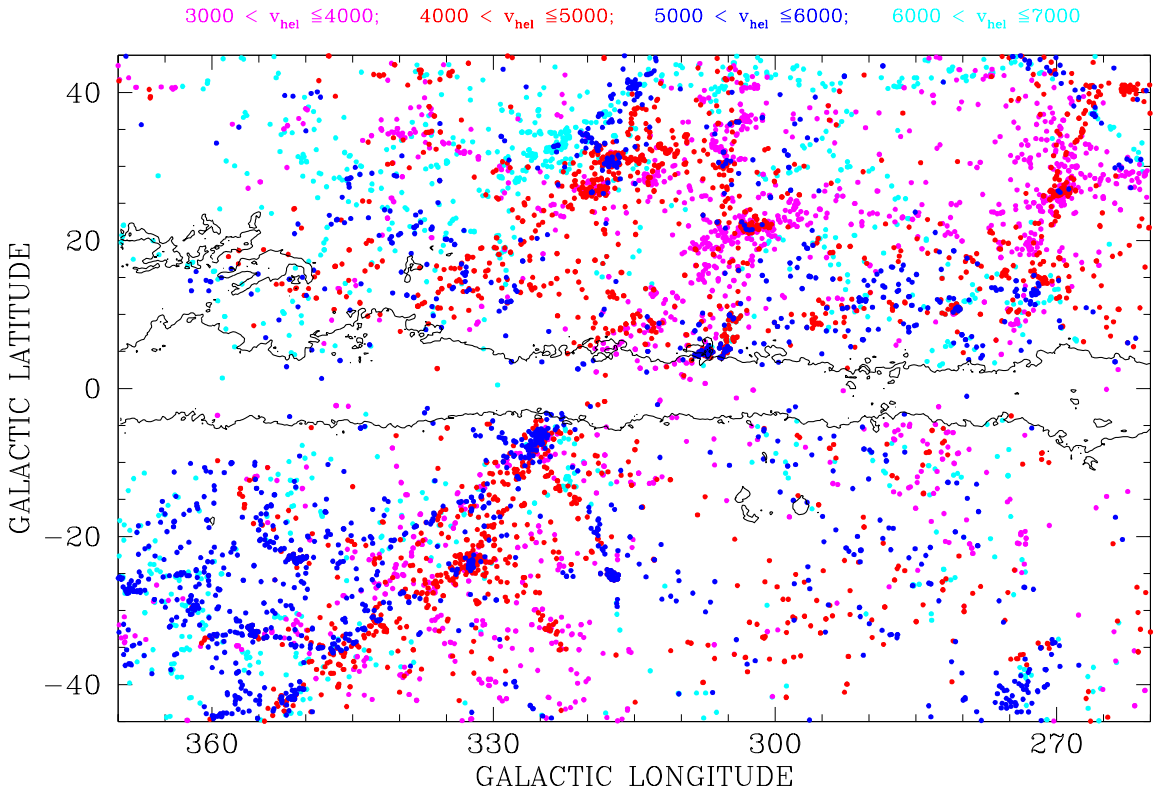

Fig. 1.17: Large-scale structures in the Great Attractor region between $3000 < v_{hel} < 7000$ km s^{-1}. The major structures indicated are: the Norma cluster at $(\ell, b, v) = (325.^\circ3, -7.^\circ2, 4871$ km s$^{-1})$, Pavo II cluster at $(\ell, b, v) = (332.^\circ3, -23.^\circ6, 4167$ km s$^{-1})$, the Centaurus cluster at $(\ell, b, v) = (302.^\circ4, +21.^\circ6, 3418$ km s$^{-1})$, the Hydra cluster at $(\ell, b, v) = (269.^\circ6, +26.^\circ5, 3777$ km s$^{-1})$, CIZA J1324.7–5736 at $(\ell, b, v) = (307.^\circ4, +5.^\circ0, 5700$ km s$^{-1})$ and Cen-Crux cluster at $(305^\circ, +5^\circ, 6214$ km s$^{-1})$. The solid contour marks a line of equal Galactic foreground extinction $A_B = 3.^m0$, from Schlegel et al. (1998). Figure taken from Woudt et al. (2008).

by Woudt et al. (2008) identified Norma as the richest cluster in the Great Attractor region. Woudt et al. (2008) identified 296 cluster member galaxies within the cluster's Abell radius (~ 2 Mpc) and measured a velocity dispersion of 925 km s^{-1}. This implies a dynamical mass $\sim 1 - 1.1 \times 10^{15}\, h_{73}\, M_\odot$ in agreement with the gravitational mass measured through X-ray observations (Boehringer et al., 1996).

The Norma cluster had already been catalogued in the list of Abell clusters as ACO 3627 by Abell et al. (1989). Abell et al. (1989) identified it to be of richness class 1, with "59?" cluster members within m_3 and $m_3 + 2$ where m_3 corresponds to the magnitude of the third brightest cluster member galaxy. It is comparable in both richness and size to the well known and well studied Coma cluster (Kraan-Korteweg et al., 1996), except that the Norma cluster is nearer than the Coma cluster. Skelton et al. (2009) measured the K_s-band luminosity function of the Norma cluster and found it to be comparable to that of the Coma cluster.

Vollmer et al. (2001) studied the neutral hydrogen emission from galaxies in the Norma cluster using the Australian Compact Telescope Array and reported significant HI deficiency in the cluster. The cluster has a considerable number of HI-deficient spiral galaxies, with the HI-deficiency being more pronounced for the central spiral galaxies (Vollmer et al., 2001; Schröder et al., 2009), similar to what has been observed in the Coma cluster (Bravo-Alfaro et al., 2000). More recently, Schröder et al. (2009) reported a detection rate of $\sim 43\%$ and $\sim 53\%$ within

Fig. 1.18: Galaxy transformation in action: ram pressure stripping in WKK 6176 also known as ESO 137–001. This spiral galaxy lies close to the centre of the Norma cluster at $(\ell, b, cz_{\rm hel}) = (325.^\circ25 - 6.^\circ97, 4630 \text{ km s}^{-1})$, that is, ~ 9 arcmin from the cluster's centre. The left-hand, middle and right-hand panels represent X-ray observations (Chandra X-ray Observatory), optical observations (Hubble Space Telescope: red, green and blue) and the composite image, respectively. The image is 1.6 arcmin across. Credit: X-ray: NASA/CXC/UAH/Sun et al., 2006, 2007; Optical: NASA, ESA, & the Hubble Heritage Team (STScI/AURA).

R_A and 1–2R_A, respectively. This is typical of massive rich X-ray-bright clusters where ram pressure stripping is thought to play a significant role in driving galaxy transformation processes (Ebeling et al., 2014). Figure 1.18 shows ram pressure stripping in WKK 6176 (= ESO 137–001), a spiral galaxy located close to the centre of the Norma cluster (separation ~ 9 arcmin). The left-hand panel shows WKK 6176 taken using the Chandra Advanced CCD Imaging Spectrometer (Garmire et al., 2003) showing intense blue streaks (blue "jellyfish-tendrils") due to galaxy-cluster interaction. The blue tail is the stripped interstellar medium of the galaxy mixed with the gaseous intracluster medium (of the Norma cluster) which ultimately turns WKK 6176 into a gas-poor galaxy (Sun et al., 2006, 2007). The middle panel of Figure 1.18 represents the galaxy image as seen by the Hubble Space Telescope while the right-hand panel is the composite image[6]. The latest observations of WKK 6176 with the Multi Unit Spectroscopic Explorer (MUSE, Fumagalli et al., 2014), reveals the kinematic information of the stripped material.

1.6 Project Motivation, Aims and Objectives

The Local Group has a known, measured peculiar velocity of 627 ± 22 km s^{-1} in the CMB rest frame (Kogut et al., 1993), which results from the gravitational influence due to very massive large scale structures, with the Great Attractor and the Shapley Supercluster as prime examples of major attractors in the nearby Universe. Given the central location of Norma in the Great Attractor region and the continued controversy of the dynamical role of Great Attractor versus Shapley Concentration, my aim in this project is to determine the peculiar velocity of the Norma cluster by measuring its redshift-independent distance with special care given to sources of potential systematic uncertainties such as star crowding and Galactic extinction. The Norma cluster forms part of the core of the Great Attractor (Kraan-Korteweg et al., 1996; Woudt, 1998) at a redshift distance of 4871 km s^{-1}. Various studies have placed the peak of the Great Attractor at distances between ~ 3000 km s^{-1} and ~ 5000 km s^{-1} (e.g, Lynden-Bell et al., 1988; Kolatt et al., 1995; Tonry et al., 2000). The Norma cluster therefore lies at or close to the proposed centre of the Great Attractor (Kolatt et al., 1995). By accurately and reliably measuring the redshift-independent distance and peculiar velocity of the Norma cluster, we can infer

[6]CXC: Chandra X-ray Centre, UAH: University of Alabama in Huntsville, ESA: European Space Agency, AURA: Association of Universities for Research in Astronomy, STScI: Space Telescope Science Institute.

whether the Great Attractor partakes in large motions due to other large scale structures, for example, the more massive but distant Shapley Supercluster (Scaramella et al., 1989; Hudson, 1994a; Proust et al., 2006).

In this project, I use two independent methods to derive the redshift-independent distance to the Norma cluster; the Fundamental Plane relation for early-type galaxies and the Tully-Fisher relation for late-types. Due to the Norma cluster's location in the Zone of Avoidance, I performed the photometric analysis with near-infrared data to minimise the effects due to Galactic extinction. The final near-infrared K_s-band Fundamental Plane analysis consists of a total of 41 early-type galaxies within $\frac{2}{3}R_{\rm A}$, where $R_{\rm A}$ is the Abell radius. The Tully-Fisher relation analysis includes a final sample of 12 spiral galaxies whose sky positions lie within $1.5R_{\rm A}$, and with data (near-infrared images) obtained using the 1.4 m IRSF telescope at SAAO. The 21 cm observations were conducted using the 64 m Australian Parkes radio telescope.

1.7 Thesis Outline

Chapter 2 presents the sample selection, observations and data reduction for both the Fundamental Plane and the Tully-Fisher samples. The analysis and results from the Fundamental Plane and Tully-Fisher relations are presented in Chapters 3 and 4, respectively. Finally, the discussion of results and outline for future prospects are given in Chapter 5.

CHAPTER 2

SAMPLE SELECTION AND DATA REDUCTION

This chapter presents the sample selection, observations and the reduction methods for the spectroscopic and near-infrared photometric data used in both the Fundamental Plane and Tully-Fisher analyses of the Norma cluster. The Chapter is divided into two sections: the Fundamental Plane (§2.1) and the Tully-Fisher (§2.2) data. I have adopted, where not stated, standard cosmology with $H_0 = 70.5\,\mathrm{km\,s^{-1}\,Mpc^{-1}}$, $\Omega_\mathrm{m} = 0.27$, and $\Omega_\Lambda = 0.73$ (Hinshaw et al., 2009), where H_0 is the Hubble constant, Ω_m is the density of matter and Ω_Λ is the density of dark energy.

2.1 Fundamental Plane Data

The Fundamental Plane analysis requires a combination of spectroscopic and photometric measurements to determine the central velocity dispersion, effective radius and mean effective surface brightness for each galaxy. The Fundamental Plane analysis of the Norma cluster presented in this work is divided into three parts, namely:

1. The Fundamental Plane analysis of 31 early-type galaxies based on data taken with the 3.6 m New Technology telescope (NTT) at the European Southern Observatory (ESO); the results from this pilot study are also presented in Mutabazi et al. (2014).

2. J and K_s-band Fundamental Plane analysis of 31 early-type galaxies based on data obtained with the 1.4 m Infrared Survey Facility (IRSF) at the South African Astronomical Observatory (SAAO).

3. K_s-band Fundamental Plane analysis of 41 early-type galaxies based on the combined sample (NTT+IRSF).

The spectroscopic data (central velocity dispersions) for the Norma cluster sample were obtained using the Two-degree Field (2dF) facility (Woudt et al., 2008). The spectroscopic data analysis and details about the near-infrared imaging are presented in §2.1.2 and §2.1.3, respectively.

In addition, Coma cluster early-type galaxies were selected for the purpose of calibrating the Fundamental Plane. For the Coma cluster, 2MASS Atlas images were used in the measurement of total extrapolated magnitudes, effective radii and effective surface brightnesses. The criteria used to select the Coma cluster sample are presented in §2.1.6.

The pilot study involved the near-infrared K_s-band Fundamental Plane analysis and pioneered the feasibility of the Fundamental Plane study at low Galactic latitudes. The inclusion of the J-band investigated uncertainties due to Galactic extinction (see §3.2.5). The final sample of 41 early-type galaxies combines all K_s-band data into the largest cluster sample at low Galactic latitudes to date, resulting in the most accurate peculiar velocity of the Norma cluster measured to date.

2.1.1 Norma Cluster Sample

The sample selection for the Norma cluster Fundamental Plane study was based on the dynamical analysis of the Norma cluster by Woudt et al. (2008). Through radial velocity measurements, Woudt et al. (2008) identified 296 galaxies spectroscopically belonging to the Norma cluster. This number includes all galaxy morphologies: elliptical, lenticular, spiral and irregular galaxies. Figure 2.1 shows the location of the galaxies identified by Woudt et al. (2008); the early-type member galaxies are represented by the red filled circles while the late-type member galaxies are represented by blue crosses. The Norma cluster non-member galaxies are marked by the open circles. The vertical dotted line on the far right represents the Abell radius. The Abell radius is defined as $\frac{1.'7}{z}$, where, z is the cluster redshift ($z_{\rm hel} = 0.0162$ for the Norma cluster). Hence, $R_{\rm A} \sim 1.^\circ75$ or ~ 2 Mpc from the centre of the Norma cluster (assuming $H_0 = 73\,{\rm km\,s^{-1}\,Mpc^{-1}}$).

The Norma cluster sample was selected to contain member galaxies with heliocentric velocities, $v_{\rm hel}$, in the range: $2096\ {\rm km\,s^{-1}} < v_{\rm hel} < 7646\ {\rm km\,s^{-1}}$. In Figure 2.1, the horizontal dashed lines show the velocity centroid and the lower and upper $3\sigma_c$ limits to the mean recession velocity. For the 296 galaxies within the Norma cluster, the mean velocity is $\langle v_{\rm hel}\rangle = 4871 \pm 54\ {\rm km\,s^{-1}}$ with dispersion, $\sigma_c = 925\ {\rm km\,s^{-1}}$ (Woudt et al., 2008). The Norma cluster early-type galaxies used in the Fundamental Plane analysis were selected to lie within the velocity range: $\langle v_{\rm hel}\rangle \pm 3\sigma_c$, i.e., $2096\ {\rm km\,s^{-1}} < v_{\rm hel} < 7646\ {\rm km\,s^{-1}}$.

Also available were the central velocity dispersion measurements for 64 of the Norma cluster's early-type galaxies (see Woudt et al. 2008). Only the Norma cluster early-type galaxies within the Abell radius ($R_{\rm A} \sim 1.^\circ75$), whose spectroscopic data are available, were selected for use in the Fundamental Plane analysis.

Prior to the start of this project, near-infrared images were obtained by Patrick Woudt, located within ~ 1/3 of the Norma cluster's Abell radius using the IRSF telescope (see details under §2.1.3). In addition, pointed observations for some of the early-type galaxies were taken by Anja Schröder using the New Technology Telescope (ESO Program 65.N-0242 (A), PI: Woudt). In summary, the Norma cluster early-type member galaxies used in the Fundamental Plane analysis were selected using the following criteria:

- Heliocentric recession velocities in the range: $2096\ {\rm km\,s^{-1}} < v_{\rm hel} < 7646\ {\rm km\,s^{-1}}$.
- Central velocity dispersion measurements available.
- Galaxies lie within the Abell radius.

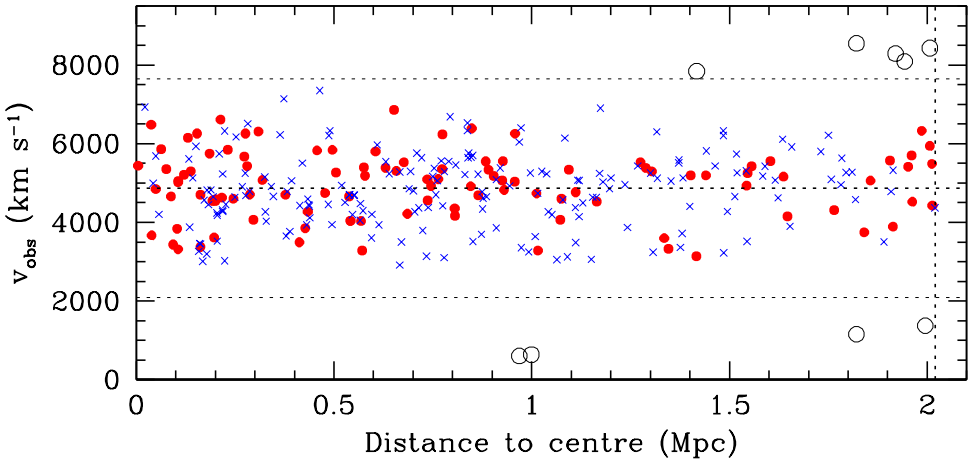

Fig. 2.1: Norma cluster member galaxies; the known redshifts are plotted as a function of distance to the central cD galaxies. The vertical dashed line (far right) represents the Abell radius, while the horizontal dashed lines represent the velocity centroid and the upper and lower $3\sigma_c$ limits. The early-type (E/S0) and the late-type (S/Irr) galaxies in the Norma cluster are represented by the filled circles and crosses, respectively. The open circles represent non-member galaxies. Figure taken from Woudt et al. (2008).

The selection criteria resulted in a total of 31 early-type galaxies with near-infrared images from the New Technology Telescope (K_s-band) and 31 with J- and K_s-band images from the IRSF telescope. There is some overlap in both samples; 21 galaxies are common to both and 10 are unique to each sample. The red filled circles in the left-hand panel of Figure 2.2 shows the positions of the Norma cluster early-type galaxies in the NTT K_s-band Fundamental Plane sample. The open blue circles represent galaxies whose near-infrared images were obtained using the IRSF telescope. The galaxies common to both the NTT and IRSF datasets are therefore represented by the encircled red filled circles. The red dashed, black solid, and the blue dotted circles represent $R_{\rm A}$, $\frac{2}{3}R_{\rm A}$ and $\frac{1}{3}R_{\rm A}$, respectively ($R_{\rm A} \sim 1\overset{\circ}{.}75$ is the Norma cluster's Abell radius). All the selected galaxies lie within $\frac{2}{3}R_{\rm A}$.

The right-hand panel of Figure 2.2 shows the velocity distribution of the total sample ($N = 41$). The light-blue region represents the velocity distribution of the NTT sample while the solid histogram shows the distribution of the combined sample. The dashed line in the right-hand panel corresponds to the mean heliocentric velocity for this combined sample, which is $cz = 4993 \pm 128$ km s^{-1}. This is consistent with the mean velocity of 4979 ± 85 km s^{-1} for the early-type galaxy population in the Norma cluster (Woudt et al., 2008) of which my Fundamental Plane sample is a representative subsample. The blue solid line (right-hand panel of Figure 2.2) represents a Gaussian distribution with mean and standard deviation corresponding to the measured mean heliocentric velocity and velocity dispersion for the Norma cluster, i.e., $v_{\rm hel} = 4871$ km s^{-1} and a standard deviation of 925 km s^{-1}, based on the 296 cluster member galaxies (ellipticals, lenticulars, spirals and irregulars).

2.1.2 Optical Spectroscopy

Fibre spectroscopy for the Norma cluster sample was performed using the Two-degree Field (2dF) facility (Lewis et al., 2002) on the 3.9 m Anglo-Australian Telescope[1]. Three fibre config-

[1]The observations and data reduction presented in this section were performed by S. A. W. Moore and J. R. Lucey (University of Durham, United Kingdom) in 2002, see also Woudt et al. (2008).

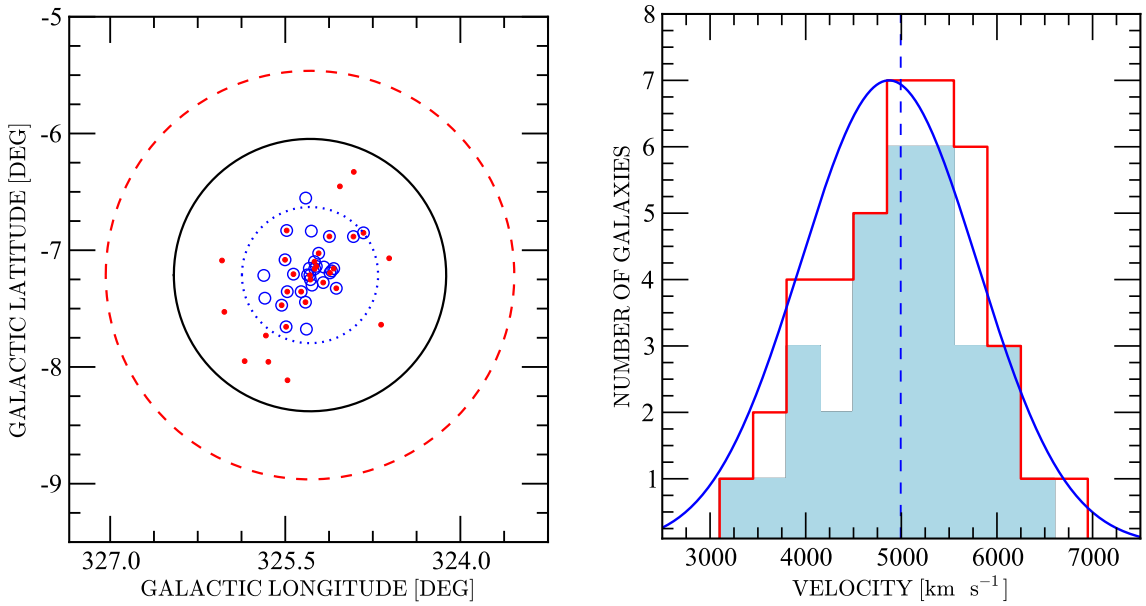

Fig. 2.2: The location and velocity distribution of the Norma cluster early-type galaxies used in the near-infrared Fundamental Plane analysis. Left-hand panel: the red outer dashed circle corresponds to the Abell radius, $R_{\rm A}$. The black solid and the blue dotted circles correspond to $\frac{2}{3}R_{\rm A}$ and $\frac{1}{3}R_{\rm A}$, respectively. The red filled circles indicate the positions of the early-type galaxies in the Norma NTT sample while the open circles represent those whose imaging was done with the IRSF telescope. The 21 galaxies in both the IRSF and NTT datasets are represented by the encircled red filled circles. The right-hand panel shows the velocity distribution for all the 31 galaxies in the NTT sample (light-blue shaded region) and the combined sample (red solid histogram). The blue solid curve represents a Gaussian distribution with mean and deviation corresponding to the values measured for the 296 member galaxies (Woudt et al., 2008).

urations were used, so as to allow repeat observations of the early-type galaxies for the central velocity dispersion measurements as well as an in-parallel redshift survey of the Norma cluster (Woudt et al., 2008). In order to calibrate the measured velocity dispersions on to a standardised system, two fibre configurations centred on the Centaurus cluster (Abell 3526) were immediately observed before the observations of the Norma cluster galaxies. Observations were also made of four K-giant stars along with the Norma cluster observations as well as offset sky and flat-field frames. The K-giant spectra acted as templates for the cross-correlation.

The 2dF fibres are $2\farcs1$ in diameter, which translates into a physical size of 0.70 kpc at the Norma redshift distance. The observations were made with the 1200V gratings which resulted in a wavelength coverage of 4700 — 5840 Å at a FWHM resolution of 125 km s^{-1} at Mgb (Magnesium absorption line); this is sufficient to determine velocity dispersions down to ~ 60 km s^{-1} (see Woudt et al. 2008). The AAO 2DFDR software package[2] was used to reduce the data, by extracting spectra from the raw data frames which were first flat-fielded, wavelength calibrated and sky-subtracted. Redshift measurements were carried out via cross-correlation with the template, after which the spectra were shifted to a rest-frame wavelength and continuum subtracted. Velocity dispersions (σ) were then measured by comparing galaxy spectra to those of the stellar templates, using the Fourier quotient method of Sargent et al. (1977). To estimate the errors, the spectra were re-sampled through bootstrapping.

[2] http://www.aao.gov.au/2df/aaomega/aaomega_2dfdr.html

Tab. 2.1: Aperture corrections for the Centaurus, Norma and Coma cluster central velocity dispersion measurements. The projected fibre diameter (column 4) corresponds to $\sim 2\,r_{\rm ap}\,h^{-1}$ kpc for this work, projected to the corresponding cluster distance/redshift.

Cluster	z	Fibre diameter $['']$	Projected fibre diameter $[h^{-1}\,\mathrm{kpc}]$	Aperture correction [dex]
Centaurus	0.0123	2.1	6.81	−0.0204
Norma	0.0162	2.1	5.05	−0.0152
Coma	0.0240	3	3.51	−0.0027

Systematic offsets in velocity dispersion measurements at the level of ∼0.015 dex exist between different observing systems – telescopes, spectrographs, runs, etc. The Streaming Motions of Abell Clusters (SMAC) survey (Hudson et al., 2001) intercompared measurements from 27 different systems and constructed a standardised system of velocity dispersions. The SMAC survey covered the Centaurus cluster, hence the velocity dispersion measurements of the Centaurus cluster were undertaken along with the Norma cluster measurements to enable the resulting 2dF data to be calibrated on to the SMAC system. Before comparing with SMAC, the measurements were averaged (weighted mean using the measured error as the weight) and corrected to a standardised physical aperture size of $\sim 2\,r_{\rm norm} = 1.19\,h^{-1}$ kpc following the prescription of Jorgensen et al. (1995), that is,

$$\log\sigma_{\rm norm} = \log\sigma + 0.04\,\log\frac{r_{\rm ap}}{r_{\rm norm}}\,; \tag{2.1}$$

where $\sigma_{\rm norm}$ is the normalised velocity dispersion corrected to the standard aperture of radius $r_{\rm norm}$, σ is the measured velocity dispersion and $2\,r_{\rm ap}\,h^{-1}$ kpc for this work is the projected fibre diameter at the cluster distance. This is equivalent to 6.81, 5.05, 3.51 h^{-1} kpc at the redshift distances of Centaurus, Norma, and Coma clusters, respectively. For fibre diameters of $2\farcs1$, $2\farcs1$ and $3''$, the corrections are −0.0204, −0.0152 and −0.0027 dex, respectively. Note that for the Coma cluster reference sample (§2.1.6), I used SDSS DR8 spectroscopic parameters, for which an aperture of $3''$ was used (Aihara et al., 2011). A summary of the projected fibre diameters and the aperture corrections is given in Table 2.1. Table 2.2 presents the velocity dispersion measurements for Centaurus cluster galaxies. The independent measurements from the two different fibre configurations are presented.

A total of 26 velocity dispersion measurements for 18 galaxies were obtained from the two fibre configurations centred on the Centaurus cluster. The observed mean offset ($\mathrm{SMAC}-\mathrm{2dF_{norm}}$) is only $+0.0122 \pm 0.0073$ dex (see the upper panel of Figure 2.3). Thus, there is good agreement between the 2dF measurements and the SMAC standardised values. From the SMAC survey and the more recent fibre velocity dispersion measurements in the northern hemisphere by SDSS-III (Aihara et al., 2011), there are $N = 130$ galaxies which overlap in the two surveys. A comparison between the two surveys shows good agreement with an observed mean offset ($\mathrm{SMAC}-\mathrm{SDSS_{norm}}$) of $+0.0045 \pm 0.0039$ dex (see the lower panel of Figure 2.3). Also, included in this comparison are 38 Coma cluster galaxies. These have an offset of $+0.0035 \pm 0.0067$ dex. Note that the overall correction to the central velocity dispersion measurements for the Norma sample is −0.003 dex.

Table 2.3 presents the velocity dispersion measurements for the Norma cluster galaxies, where the individual measurements from all three fibre configurations are indicated. Also given in Table 2.3 for each galaxy is the averaged (weighted mean) velocity dispersion corrected to the

Tab. 2.2: Velocity dispersions for 18 galaxies in the Centaurus cluster. The σ_1 and σ_2 columns refer to the velocity dispersion measurements made with the two different fibre configurations, err_1 and err_2 are the respective errors. The weighted average of the σ_1 and σ_2 measurements is σ_{norm} (after the aperture correction of –0.0204 dex has been applied). The $\log \sigma_{\mathrm{SMAC}}$ values were taken from Table 7 of Hudson et al. (2001).

Identification	RA (2000.0)	Dec (2000.0)	σ_1	err_1	σ_2	err_2	$\log \sigma_{\mathrm{norm}}$	$\mathrm{err}_{\mathrm{norm}}$	$\log \sigma_{\mathrm{SMAC}}$	$\mathrm{err}_{\mathrm{SMAC}}$
	h m s	° ′ ″	$\mathrm{km\,s^{-1}}$	$\mathrm{km\,s^{-1}}$	$\mathrm{km\,s^{-1}}$	$\mathrm{km\,s^{-1}}$	dex	dex	dex	dex
E322-075	12 46 26.00	–40 45 08.6	139.7	2.6	128.9	2.9	2.110	0.006	2.164	0.038
CCC054	12 48 31.02	–41 18 24.1			83.9	5.0	1.903	0.026	1.893	0.026
CCC089	12 49 18.60	–41 20 08.0	81.0	3.8			1.888	0.020	1.911	0.026
E322-099	12 49 26.27	–41 29 22.6	121.6	2.1			2.065	0.008	2.072	0.026
E322-101	12 49 34.55	–41 03 17.6	165.4	2.7	165.8	2.6	2.199	0.005	2.205	0.019
N4706	12 49 54.17	–41 16 46.0	226.1	2.7			2.334	0.005	2.325	0.014
CCC135	12 50 11.54	–41 13 15.8	113.8	3.2	119.5	2.2	2.050	0.007	2.075	0.009
CCC136	12 50 11.87	–41 17 57.0	66.3	4.8	72.9	4.6	1.823	0.021	1.837	0.018
E323-005	12 50 12.26	–41 30 53.8	219.0	3.2	215.2	2.7	2.316	0.004	2.343	0.026
E323-008	12 50 34.40	–41 28 15.2	137.1	3.0			2.117	0.010	2.134	0.014
E323-009	12 50 42.98	–41 25 49.5	136.4	1.9			2.114	0.006	2.126	0.018
CCC191	12 51 37.33	–41 18 12.3	126.2	3.2			2.081	0.011	2.120	0.025
CCC205	12 51 47.97	–40 59 37.4	74.0	3.5	74.2	3.1	1.849	0.014	1.884	0.025
CCC207	12 51 50.85	–41 11 10.7	65.3	5.2			1.794	0.035	1.720	0.025
CCC210	12 51 56.51	–41 32 20.2	132.9	3.4	132.3	2.7	2.102	0.007	2.095	0.025
N4743	12 52 16.02	–41 23 25.8	135.7	2.3			2.112	0.007	2.107	0.021
CCC231	12 52 22.58	–41 16 55.5			218.4	3.7	2.319	0.007	2.309	0.025
CCC242	12 52 40.86	–41 13 47.3	124.1	5.1	127.3	4.9	2.079	0.012	2.154	0.025

standardised physical aperture size and the SMAC system, that is, a correction of +0.012 dex is applied. The uncertainty in calibrating to the SMAC system is ∼ 0.007 dex. This corresponds to a systematic distance error at the distance of the Norma cluster of ∼ 2%.

2.1.3 Near-infrared Imaging

The near-infrared imaging for the Norma cluster early-type galaxies was conducted using:

- The SOFI[3] instrument mounted on the New Technology Telescope (NTT) at the European Southern Observatory (ESO). The K_s-band observations were conducted over four nights in June 2000.
- Simultaneous J (1.26 μm), H (1.63 μm) and K_s (2.14 μm) band observations were also obtained in June 2001, July 2001, and June 2002 using the 1.4 m InfraRed Survey Facility (IRSF), a Japanese telescope at the Sutherland site of the South African Astronomical observatory; see also Skelton et al. (2009).

The NTT is an alt-azimuth 3.6 m telescope with the capability of adaptive optics, which helps to correct for the deformation of the telescope and the mirror. The telescope is equipped with SOFI which is an infrared spectrograph and imaging camera, with a plate scale of $0\farcs29$ pixel^{-1} covering wavelengths in the range 0.9 — 2.5 μm (Moorwood et al., 1998). The largest field of view is $4\farcm9 \times 4\farcm9$. The gain and read out noise are 5.4 e^- per ADU and 2.1 e^-, respectively.

The IRSF telescope is an alt-azimuth cassegrain telescope, equipped with a three-colour band camera, SIRIUS[4]. The camera has a plate scale of $0\farcs453$ per pixel and a field of view of $7\farcm7 \times 7\farcm7$. The camera is equipped with three 1024×1024 pixels HgCdTe infrared detectors (HAWAII[5] array) and is capable of simultaneously imaging in the J, H and K_s passbands. The gain and readout noise are 5.5 e^- per ADU and 30 e^-, respectively (Nagashima et al., 1999;

[3]SOFI (Son of ISAAC) is the infrared spectrograph and imaging camera on the NTT, covering 0.9 – 2.5 μm

[4]SIRIUS: Simultaneous 3-colour InfraRed Imager for Unbiased Survey

[5]HAWAII – Hawaii Astronomical Wide Area Infrared Imager

Tab. 2.3: Velocity dispersions for 41 galaxies in the Norma cluster. The σ_1, σ_2 and σ_3 columns refer to velocity dispersion measurements made with the three different fibre configurations. In the Table, σ_c is the weighted average of the σ_1, σ_2 and σ_3 measurements with both the aperture correction equivalent to −0.0152 dex and the run offset of +0.0122 dex applied.

Identification	RA (2000.0)	Dec (2000.0)	σ_1	err_1	σ_2	err_2	σ_3	err_3	$\log \sigma_c$	err_c
	h m s	° ′ ″	km s^{-1}	km s^{-1}	km s^{-1}	km s^{-1}	dex	dex	dex	dex
WKK5920	16 07 52.618	–60 31 12.95	206.8	4.6					2.312	0.010
WKK5972	16 09 16.053	–60 31 51.00	254.8	4.8			277.8	7.5	2.414	0.007
WKK6012	16 10 12.103	–61 16 01.15	151.3	5.2			147.1	6.4	2.172	0.012
WKK6019	16 10 17.131	–60 57 32.44	269.7	6.2	250.9	5.0			2.409	0.007
WKK6047	16 10 58.873	–60 55 24.51	96.8	3.7			120.9	6.3	2.010	0.013
WKK6075	16 11 32.671	–60 24 15.77	129.3	5.8	122.7	6.7			2.099	0.015
WKK6116	16 12 11.560	–60 47 00.00	230.6	6.3			212.9	6.8	2.344	0.009
WKK6148	16 12 50.814	–60 38 36.13	110.7	7.2			94.7	5.3	1.998	0.018
WKK6180	16 13 32.141	–61 00 22.69	212.4	6.5	200.6	4.9			2.308	0.008
WKK6183	16 13 32.930	–60 49 23.71	240.3	5.0					2.377	0.009
WKK6193	16 13 45.900	–61 00 29.54	166.0	4.2			172.7	3.9	2.226	0.007
WKK6198	16 13 54.073	–61 37 57.00	81.0	5.1			81.1	5.1	1.905	0.019
WKK6204	16 13 56.206	–61 00 40.92	314.4	4.8			322.3	5.4	2.499	0.005
WKK6207	16 13 57.471	–60 56 23.98	175.5	3.6					2.241	0.009
WKK6221	16 14 02.807	–60 29 41.07	116.0	5.8	105.3	5.2			2.038	0.015
WKK6229	16 14 10.410	–60 51 01.34	163.3	5.0					2.210	0.013
WKK6233	16 14 18.007	–60 53 25.87	176.1	5.0					2.243	0.012
WKK6235	16 14 22.561	–61 08 38.17					139.3	5.1	2.141	0.016
WKK6242	16 14 30.538	–60 53 46.35			280.5	6.8	249.6	7.8	2.424	0.008
WKK6250	16 14 45.228	–61 01 50.68	219.4	6.2	210.0	3.8			2.324	0.007
WKK6252	16 14 45.420	–60 51 41.76	126.9	5.0	115.6	3.5			2.073	0.010
WKK6269	16 15 03.833	–60 54 25.61	381.9	6.9					2.579	0.008
WKK6275	16 15 09.830	–60 53 27.59					147.2	4.2	2.165	0.012
WKK6282	16 15 15.440	–60 56 15.54	183.0	5.7			194.1	4.9	2.274	0.009
WKK6297	16 15 26.992	–60 58 49.95	70.3	4.0					1.844	0.025
WKK6305	16 15 32.922	–60 39 55.27	220.3	4.0	207.9	3.8			2.327	0.006
WKK6318	16 15 50.163	–60 48 10.67	227.8	5.9					2.354	0.011
WKK6342	16 16 18.929	–60 57 23.60	234.9	6.0	206.7	3.4			2.326	0.006
WKK6360	16 16 36.915	–61 02 45.90	323.4	4.7	330.0	6.6	310.2	7.8	2.505	0.005
WKK6383	16 17 00.358	–60 52 24.96	165.3	4.9			147.9	5.7	2.195	0.010
WKK6402	16 17 22.032	–60 38 03.50	187.4	5.4			166.2	4.2	2.238	0.008
WKK6429	16 17 54.934	–61 12 58.56	120.2	4.6	123.4	3.6			2.084	0.010
WKK6431	16 17 57.345	–60 55 22.98	191.8	4.9			197.0	4.2	2.286	0.007
WKK6459	16 18 26.899	–60 46 47.12	212.7	5.1			210.3	4.6	2.322	0.007
WKK6473	16 18 41.300	–60 17 38.00	112.6	4.6			130.5	8.3	2.064	0.015
WKK6477	16 18 48.612	–61 04 47.79	128.6	5.2					2.106	0.018
WKK6555	16 20 15.031	–61 00 44.75	161.6	3.3			162.9	3.9	2.207	0.007
WKK6600	16 21 06.095	–60 37 08.90	221.9	4.7			215.2	6.6	2.338	0.008
WKK6620	16 21 26.857	–61 11 06.12	57.1	9.9			64.2	10.9	1.777	0.053
WKK6615	16 21 26.940	–61 24 42.51			129.1	5.8			2.108	0.020
WKK6679	16 22 34.872	–61 02 14.19	141.4	3.4			155.0	5.5	2.159	0.009

Nagayama et al., 2003; Nagayama, 2012). The IRSF telescope thus enables deep and wide-field imaging. In addition, the dithering mode increases the size of the field depending on the dithering radius and the dithering pattern. Dithering refers to shifting of the telescope pointing by a few pixels so as to allow the different exposures of the same image to fall on different parts of the detector. In the image reduction process, the resulting dither frames for each target galaxy are combined into a single final image.

While the effect of Galactic extinction is significantly lower at NIR wavelengths than optical, the sky is also brighter at the NIR wavelengths. The NIR sky brightness also varies significantly over short time intervals. To avoid background saturation, NIR observations employ short exposures with a dithering pattern. Such short exposures ensure accurate sky determination, while the dithering mode minimises the effect of bad (dead, faulty) pixels. For the IRSF observations, a total integration time of 600 s was used, split over 20 short exposures of

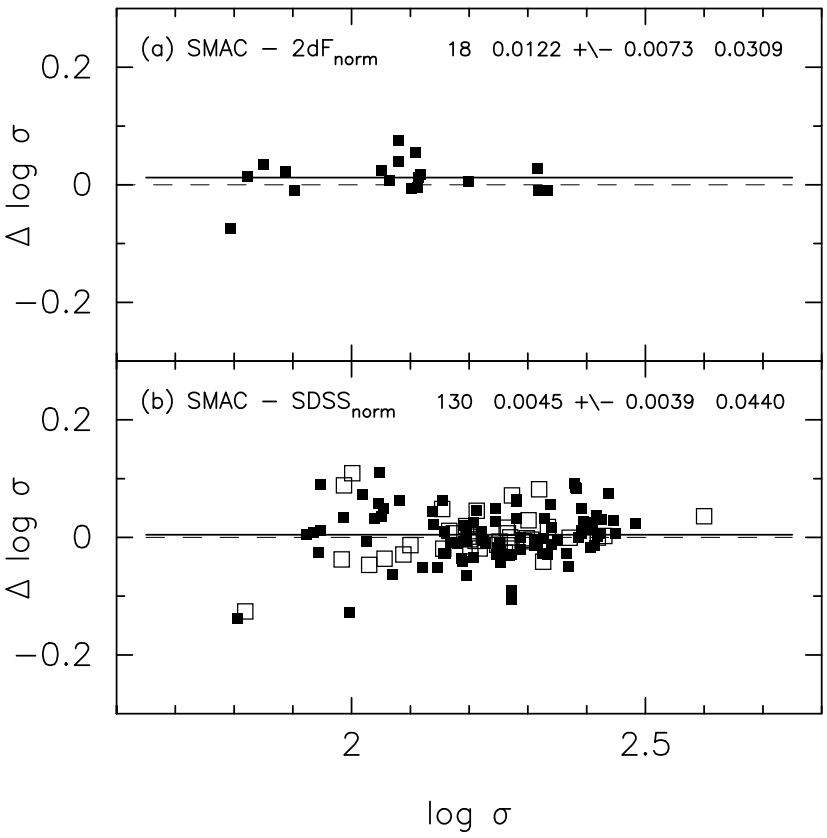

Fig. 2.3: Comparison of the velocity dispersion measurements from SMAC, 2dF (aperture corrected) and SDSS (aperture corrected). The upper panel is the comparison of the 2dF Centaurus measurements with the SMAC values. The lower panel is the comparison of the SMAC and the SDSS values. The open squares represent the Coma cluster galaxies. Credit: J. R. Lucey; figure 2 of Mutabazi et al. (2014).

30 s each. For the imaging using the 3.6 m NTT, a total integration time of 300 s was used, split over 40 short exposures each of 7.5 s exposure time. With such deep observations, coupled with the small pixel scale of these imaging instruments, reliable photometry is achievable at the low Galactic latitudes despite the high stellar density.

The small pixel scale and improved angular resolution of the IRSF and NTT (relative to 2MASS) make them better suited for observations at low Galactic latitudes, where stellar density is high. The foreground sources are better resolved compared to, e.g., 2MASS (pixel scale=$2''$ pixel^{-1}). Reliable and accurate photometry in such high stellar density regions requires that the foreground sources are well resolved so that they can easily be subtracted before the photometric analysis, see also §3.1 and §3.2.

In the photometric calibration of both the NTT and IRSF data, the 2MASS Point Source Catalogue (Cutri et al., 2003; Skrutskie et al., 2006) was used. This allows direct comparisons of the NTT and IRSF photometric data as well as the combination of the NTT and IRSF K_s-band data (for the combined K_s-band Fundamental Plane analysis). In addition, 2MASS Atlas images were used in the photometric analysis of the Coma cluster galaxies (reference sample presented in §2.1.6 of this dissertation). It was therefore necessary to have both the reference and Norma cluster samples on the same photometric system for direct comparisons. The transformation to the 2MASS photometric system was done via photometric calibration (this is explained further in §2.1.4).

Tab. 2.4: Summary table for telescope parameters, showing the telescope size, pixel scale, the total exposure time (per image), and the seeing conditions (average full width at half maximum).

	NTT	IRSF	2MASS
Telescope size	3.6 m	1.4 m	1.3 m
Filters	K_s	J,H,K_s	J,H,K_s
Field of view	$4\farcm9 \times 4\farcm9$	$7\farcm8 \times 7\farcm8$	$8\farcm5 \times 8\farcm5$
Pixel scale	$0\farcs29$ pixel^{-1}	$0\farcs45$ pixel^{-1}	$2\farcs0$ pixel^{-1}
Total Exp. time	300 s	600 s	7.8 s
Mean FWHM	$1\farcs1$	$1\farcs4$	$2\farcs7$

2.1.4 Data Reduction and Image Calibration

Standard near-infrared data reduction techniques were applied to both the IRSF and NTT data. These include dark subtraction, flat-fielding (to minimise the effect of pixel-to-pixel response variations), sky-subtraction, and combining the dither frames for each target into a single science image (see §2.2.5 for a detailed explanation). For the Fundamental Plane analysis, the fully reduced images were already available at the beginning of this project. I performed the astrometric and photometric calibrations using the 2MASS Point Source Catalogue (2MASS PSC; Cutri et al., 2003; Skrutskie et al., 2006). This was done in such a way that both the reference sample (Coma cluster early-type galaxies) and the Norma cluster early-type galaxies are on the same photometric system. The process of coordinate conversion utilised the Optimistic Pattern Matching algorithm implemented by Tabur (2007) and compiled by Dr. N. Matsunaga (Priv. Com.). The point sources within each image were matched with the corresponding 2MASS point sources before the conversion from pixel (image) to world coordinate system.

The photometric calibration was performed following a procedure by Riad et al. (2010). Only 2MASS point sources with reliable photometry (with photometric quality flag AAA) were used in the calibration. In addition, the 2MASS point sources used in determining the zero-point magnitudes were restricted to have a measurement error on the $(J-H)$, and $(J-K_s)$ colour not exceeding 0.1 mag. These point sources were then identified within the image to be calibrated. Aperture photometry (instrumental magnitudes) for these sources were measured using a combination of IRAF[6] tasks and SExtractor (Bertin & Arnouts, 1996). The instrumental magnitude is given by

$$m_\lambda^i = -2.5 \log\left(\frac{F_\lambda}{t_{\rm exp}}\right), \tag{2.2}$$

where F_λ is the sky-subtracted counts in a given filter and $t_{\rm exp}$ is the exposure time (in seconds) for each dither frame. The subscript λ is used for wavelength dependence, in this case representing the J, H and K_s-bands. The process of converting the measured instrumental magnitudes to standard magnitudes is the photometric calibration, and was achieved using the 2MASS Point Source Catalogue. The instrumental magnitude m_λ^i and the global (standard) magnitude m_λ are related via:

$$m_\lambda = ZP_\lambda + m_\lambda^i + c_1\chi + c_2 m_{\rm col}, \tag{2.3}$$

where m_λ is the magnitude in a standard system, ZP_λ is the zero-point magnitude for a given filter of observations, c_1 is the airmass extinction coefficient, $m_{\rm col}$ is a colour term and c_2 is the

[6]Image Reduction and Analysis Facility; written and supported by the IRAF programming group at the National Optical Astronomy Observatories which are operated by the Association of Universities for Research in Astronomy, Inc. under cooperative agreement with the National Science Foundation: `http://iraf.noao.edu/`

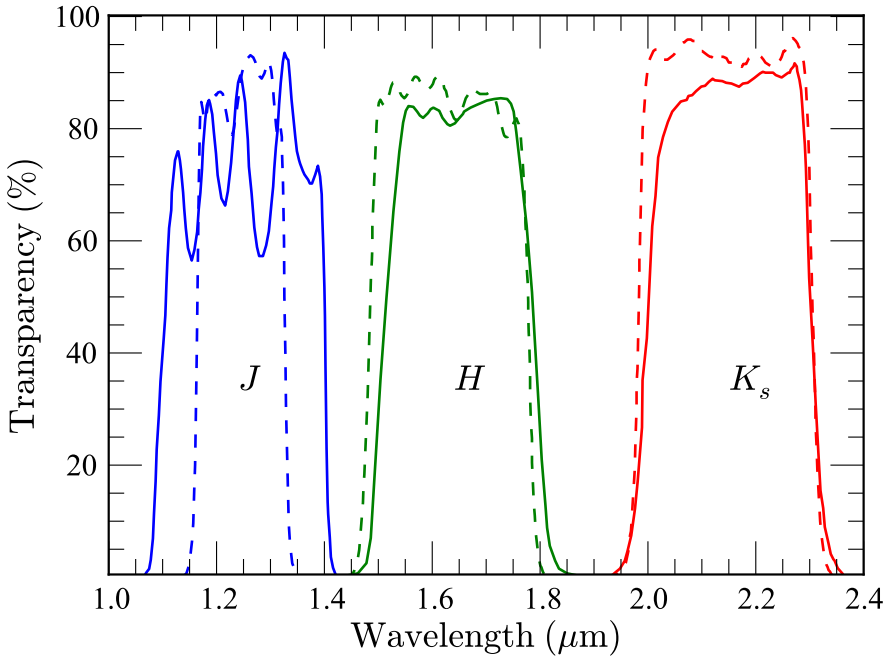

Fig. 2.4: Differences in the transmission curves between the IRSF (dashed curves) and 2MASS (solid curves). The three filters are; J (in blue), H (in green) and K_s (in red).

colour coefficient. For the IRSF and NTT filters, there is no colour dependence and hence $c_2 = 0$. Equation 2.3 then becomes

$$ZP_\lambda = m_\lambda - m^i_\lambda - c_1\chi. \tag{2.4}$$

The measurements, m^i_λ, using Equation 2.2 were carried out for individual stars per galaxy field for each of the individual filter systems (IRSF and NTT). Suitable stars were selected from my IRSF and NTT images after which the corresponding stars were identified from the 2MASS Point Source Catalogue. The zero-point, ZP_λ, for each selected star was calculated using Equation 2.4. The zero-point for each galaxy field was finally computed as the median value over as many stars as possible (provided these stars had reliable and high quality photometry). However, the near-infrared filters used by 2MASS slightly differ from the IRSF (Nagashima et al., 1999; Jarrett et al., 2000; Nagayama et al., 2003; Skrutskie et al., 2006) and NTT filters (see e.g, Figure 2.4 for the IRSF and 2MASS filter transmission curves). The transmission equations relating these two instruments (NTT/SOFI and IRSF/SIRIUS) with the 2MASS system are:

$$J_{\rm SIRIUS} = J_{\rm 2MASS} + (-0.045 \pm 0.008)(J-H)_{\rm 2MASS} - 0.001 \pm 0.008 \tag{2.5}$$

$$K_{s,\rm SIRIUS} = K_{s,\rm 2MASS} + (-0.015 \pm 0.008)(J-K_s)_{\rm 2MASS} - 0.001 \pm 0.008 \tag{2.6}$$

$$K_{s,\rm 2MASS} = K_{s,\rm ESO} + (0.005 \pm 0.011)(J-K_s)_{\rm ESO} + (-0.045 \pm 0.004) \tag{2.7}$$

$$(J-K_s)_{\rm 2MASS} = (0.956 \pm 0.017)(H-K)_{\rm ESO} + (-0.008 \pm 0.006) \tag{2.8}$$

$$(H-K_s)_{\rm 2MASS} = (0.956 \pm 0.126)(H-K)_{\rm ESO} + (0.034 \pm 0.006). \tag{2.9}$$

Equations 2.5 — 2.6, as given by Yasushi Nakajima (Priv. Com.), relate the 2MASS filters and those of the IRSF. These equations were used to transform the IRSF magnitudes on to the 2MASS system. Equations 2.7 — 2.9 (Carpenter, 2001) show the transformation equations between the NTT/SOFI (ESO) data and the 2MASS system.

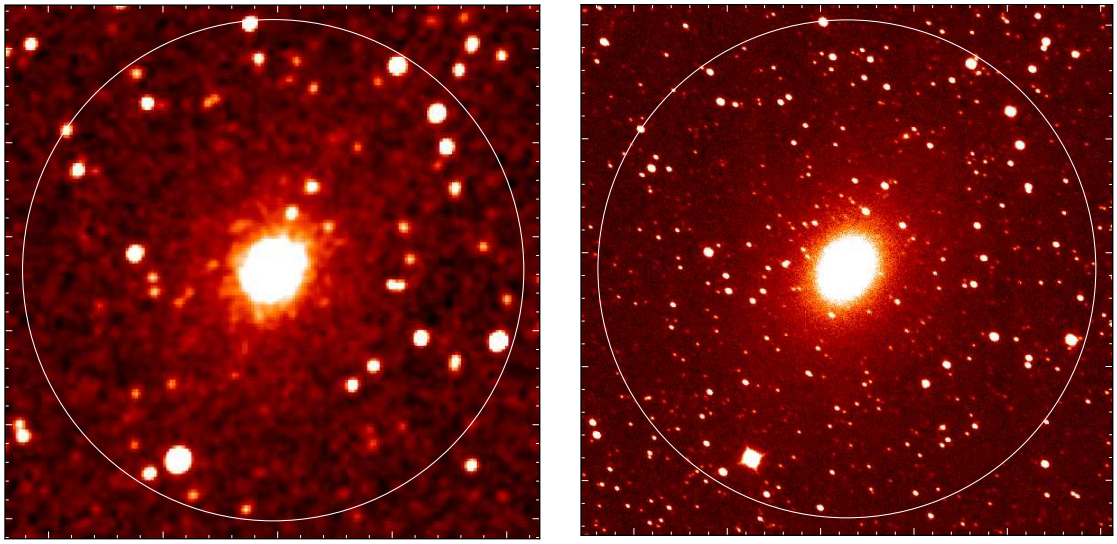

Fig. 2.5: Images of WKK 6318, one of the Norma cluster galaxies in the Norma NTT K_s-band Fundamental Plane sample. These images were obtained from 2MASS (left-hand panel) and ESO/NTT (right-hand panel). In both images, the white circle represents $80''$. It is very clear that the small pixel scale of the SOFI imaging instrument coupled with deep imaging yields a higher resolution and improved signal-to-noise ratio, compared to 2MASS.

2MASS Atlas images are used for the Coma cluster early-type galaxies used in the Fundamental Plane reference sample (see §2.1.6). While the 2MASS data provide such a uniform all-sky coverage with excellent photometric calibration, the 2MASS Atlas images are not suitable for the Norma cluster sample used in the Fundamental Plane analysis due to the low spatial resolution and shallow pointings (small exposure/integration time). Such low resolution images may not be reliable for the high stellar density Norma cluster region. Figure 2.5 shows a comparison between 2MASS and NTT data; shown is an example of a Norma cluster galaxy WKK 6318 taken from the 2MASS data (left-hand panel) and NTT/SOFI observations (right-hand panel). The white circle represents a radius of $80''$. The 2MASS co-add image was taken from the final 2MASS products (fully reduced and calibrated). Note the significant improvement in the data quality in the right-hand panel; the foreground stars are well resolved, hence enabling more reliable star-subtraction and photometry.

2.1.5 Star-subtraction

To derive accurate photometric parameters (total apparent magnitudes and effective radii), an accurate estimation of the sky background level is necessary. Over-estimating the sky value results in the galaxies appearing fainter and vice-versa. In addition, there is also a significantly high stellar density (star-crowding) in the Norma region due to its location at low Galactic latitudes $\sim 35^\circ$ away from the Galactic bulge. The average stellar density in the Norma region as measured from my near-infrared images taken using the IRSF telescope is $\sim 10^{4.0}$ stars deg^{-2}. This was obtained using only stars brighter than 14.0 mag in the K_s-band (see also Jarrett et al., 2000; Riad, 2010). There is therefore a need to carefully subtract the foreground stars in order to achieve reliable photometric results. The photometric analysis (extraction of the total magnitudes and the effective radii) for both the Norma and Coma samples was processed in the same way so as to minimise the effect of possible systematic errors arising from different photometric analyses.

Star-subtraction for the Norma cluster galaxies was performed using a star-subtraction algorithm that uses various IRAF tasks especially under the package DAOPHOT (Stetson, 1987). The most important step in foreground star subtraction is an accurate determination of the point spread function (PSF) which is used to fit and subtract the stars in the field. To locate and subtract the foreground stars in each field, both the IRAF task DAOFIND and an independent software package – SEXTRACTOR (Bertin & Arnouts, 1996), were used. The detected sources were thereafter subtracted using the model PSF image. To identify any underlying stars at the position of the target galaxy, the galaxy was modelled using the IRAF task BMODEL under STSDAS-ANALYSIS-ISOPHOTE. The model galaxy was then subtracted so as to add the underlying stars to the detected star catalogue. The star-subtraction process was thereafter repeated on the original galaxy field using this newly created star catalogue. It is important to note that the subtraction of the galaxy model was performed so as to obtain a good and reliable estimate of the sky background for all stars in the catalogue.

In some cases where there were saturated stars in the field, which could not easily and properly be fitted by the PSF, the IRAF task IMEDIT was used to clean the residuals by replacing with the average sky value. However, if such a saturated star lay far from the target galaxy, it was left out during the star-subtraction process and masked out during the photometric analysis. Figure 2.6 shows an example of a star-subtracted image. The images (WKK 6360 and WKK 6318) are two examples of early-type galaxies from the NTT data. The left and right-hand panels represent the original and star-subtracted images, respectively. The images shown are of size $86\farcs4$ by $86\farcs4$. The extraction of the photometric parameters (total extrapolated magnitude, effective radius and mean effective surface brightness) as well as the applied corrections are presented in Chapter 3.

2.1.6 Coma Cluster Reference Sample

The Coma cluster sample was taken from Dressler (1980a), who classified galaxies in 55 rich galaxy clusters. Dressler (1980a) includes the morphological classification of 247 galaxies in the Coma cluster. The spectroscopic data (central velocity dispersions) for the early-type galaxies in the Coma cluster were taken from the Sloan Digital Sky Survey Data Release 8 (first data from SDSS-III, Aihara et al., 2011). The calibration sample (the Coma cluster early-type galaxies) used in the Fundamental Plane analysis were restricted to the following criteria:

- Classified by Dressler (1980a) as early-type,
- Central velocity dispersion measurements are available in SDSS DR8,
- Have reliable and accurate photometry (measured using the 2MASS Atlas images).

The first two criteria resulted in a total Coma sample of 130 early-type galaxies. After performing photometric analysis on these galaxies, the results for 9 galaxies were deemed unreliable (see §3.3 for details). Thus, the final calibration sample consisted of 121 early-type galaxies. The spectroscopic data for all the Coma galaxy sample have a signal-to-noise ratio $S/N > 20$, except for 3 galaxies with $S/N = 16.4, 18.1, 16.9$. Aperture corrections and a run offset were applied as described in §2.1.2.

For the calibration/reference sample (Coma cluster early-type galaxies), the 2MASS Atlas images were used in the photometric analysis. In the Two Micron All Sky Survey, observations were conducted using two dedicated 1.3 m telescopes (equatorial Cassegrain) located at Mount

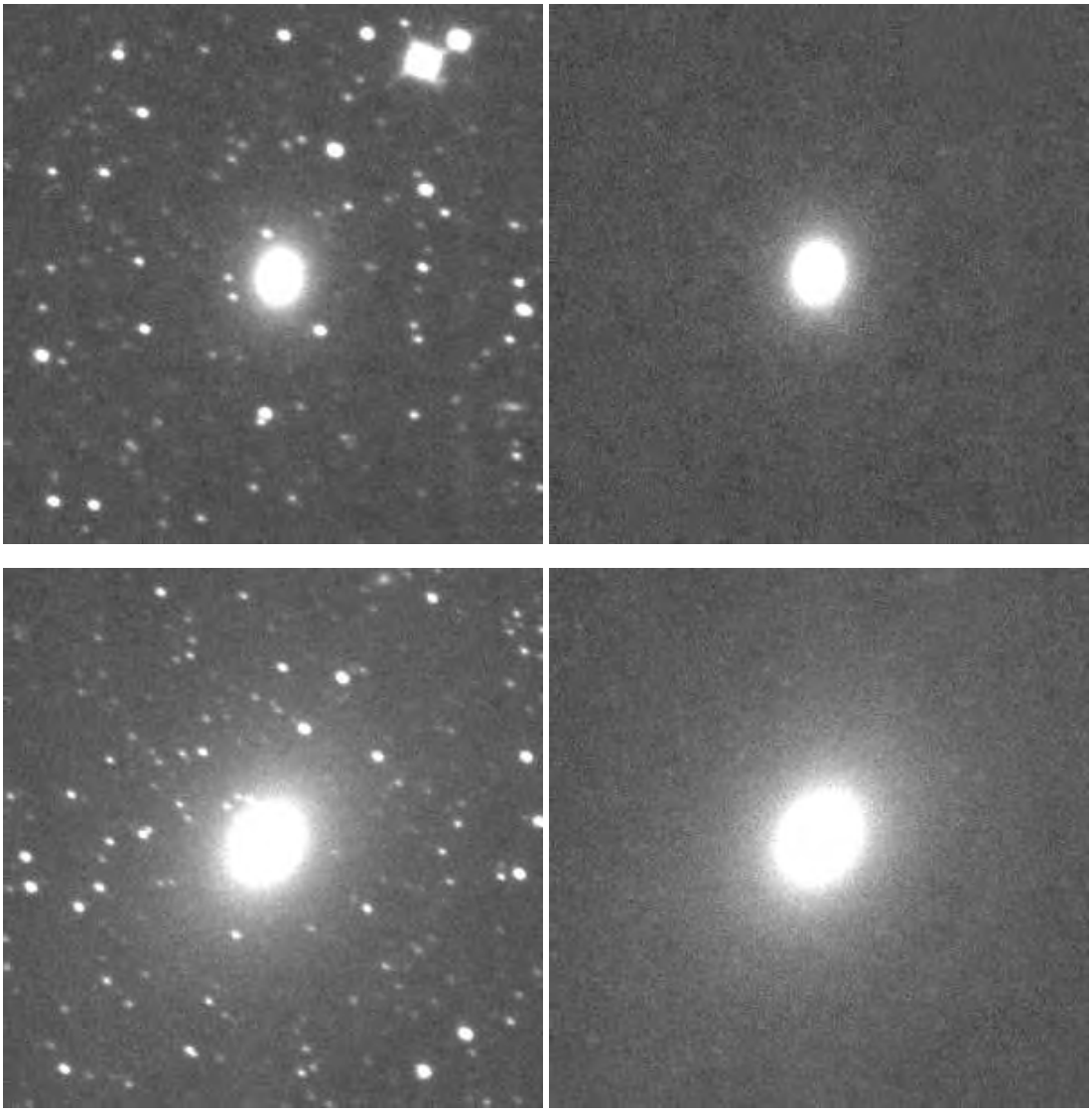

Fig. 2.6: Two of the Norma cluster galaxies in the Fundamental Plane sample (NTT data). Top panels represent WKK 6360 while the bottom panels represent WKK 6318. The original and star-subtracted images are shown on the left and right-hand panels, respectively.

Hopkins (Arizona) and Cerro Tololo (Chile), with simultaneous J (1.25 μm), H (1.65 μm) and K_s (2.16 μm) band imaging equipped with 256×256 NICMOS3 (HgCdTe) arrays (Skrutskie et al., 2006). The observations employed a total of 6 sky exposures each with 1.3 s. This implies a total integration time of ~ 7.8 s. In the 2MASS data reduction process, the six sets of images were combined and normalised to a pixel scale of $1''$ per pixel. Note that, the raw 2MASS data has a pixel scale of $2''$ per pixel. The average FWHM for the 2MASS K_s-band data is ~ $2\farcs7$. Table 2.4 presents the parameters of the telescopes used in the near-infrared imaging.

2.2 Tully-Fisher Data

The Tully-Fisher analysis requires a combination of spectroscopic data (for example, line width from HI observations) and photometric data (total or isophotal magnitudes) for late-type galaxies. Masters et al. (2008) calibrated the Tully-Fisher relation based on the 2MASS total

extrapolated magnitudes for ~ 888 bright inclined spiral galaxies. However, recently, Said (2013) found the axial ratios of galaxies to significantly change from edge-on to face-on when the Galactic extinction is severe. This is due to the Galactic extinction effects where the faint outer parts of galaxies tend to be lost, resulting in the galaxy appearing more circular than it really is (Said et al., 2015). Thus, galaxies at low Galactic latitudes appear to be less inclined than they really are, and ultimately bias the Tully-Fisher relation. For the Norma cluster sample, $A_{K_s} < 0^{\mathrm{m}}.15$ and hence the bias is not significant.

For low Galactic latitudes, not only should the measured magnitudes be corrected for Galactic extinction effects but also the semi-major and semi-minor axes. In addition, the outer-most parts of galaxies are likely to be missed, as a result of the effect of gas and dust in the plane of the Milky Way. Said (2013) therefore favoured the use of isophotal magnitudes as opposed to total apparent magnitudes in the Tully-Fisher analysis and peculiar velocity measurements within the Zone of Avoidance. Said (2013) have re-calibrated the 2MASS Tully-Fisher relation using isophotal magnitudes, while following closely the steps by Masters et al. (2008) who first calibrated the universal NIR J, H, and K_s-band Tully-Fisher relation (using the total extrapolated magnitudes from the 2MASS XSC). Since the Norma cluster lies at low Galactic latitudes, the measured peculiar velocities for the late-type galaxies in the cluster, as presented in this work (§4.3.1), made use of the K_s-band near-infrared images to perform the photometric analysis, before applying the K_s-band isophotal Tully-Fisher template of Said (2013).

2.2.1 Sample Selection

The sample selection for the Tully-Fisher relation was based on spiral galaxies within $1.5R_{\mathrm{A}}$, where $R_{\mathrm{A}} \sim 1.^{\circ}75$ is the Abell radius of the Norma cluster. The redshifts and sky positions were taken from Woudt & Kraan-Korteweg (2001) and Woudt et al. (1999, 2004) who performed optical galaxy searches within the Great Attractor region. The galaxy searches were complete to magnitude limits of $B_J \lesssim 15.5$ mag and diameter $D \gtrsim 0.'2$. While selecting the Norma cluster sample, the velocity range was restricted to within $2096\ \mathrm{km\,s^{-1}} < v_{\mathrm{hel}} < 7646\ \mathrm{km\,s^{-1}}$ (Woudt et al., 2008) – see §2.1 for details regarding this choice of the velocity range. The late-type galaxies within $0.27R_{\mathrm{A}}$ were excluded from the sample because they are HI-deficient (Vollmer et al., 2001; Schröder et al., 2009). This resulted in a final sample of 99 late-type galaxies within $1.5R_{\mathrm{A}}$ of the Norma cluster.

Figure 2.7 shows the location of the 99 late-type galaxies in the Norma cluster. The symbol meanings are: small blue open circles correspond to 99 late-type galaxies in the Norma cluster with measured redshifts (Woudt & Kraan-Korteweg, 2001; Woudt et al., 1999, 2004). The galaxy redshifts were taken from Woudt et al. (1999) who conducted measurements (spectroscopy) at the South African Astronomical Observatory (SAAO) and spectroscopic measurements by Woudt et al. (2004) who used the Meudon ESO Fibre Optical Spectrograph (MEFOS). The black filled squares are 26 HI detected galaxies by Schröder et al. (2009) – these were re-observed in order to get higher resolution spectra and hence more reliable line widths (see §2.2.2 for details). While Woudt et al. (2008) found the early-type galaxy population to appear relaxed, they identified subclustering in the late-type galaxies. They identified two major subclusters, Norma A and Norma B. The filled and open triangles represent the location of the two dynamical spiral-rich subgroups: Norma A and Norma B, respectively. The spiral galaxies within these two infalling subgroups were excluded from my final Tully-Fisher analysis. Excluding such galaxies was done following Woudt et al. (2008) who identified galaxies belonging to the two dynamically rich subgroups as: Norma A (WKK 6071, WKK 6078, WKK 6125, WKK 6135 and ZOAJ16113352), Norma B (WKK 5718, WKK 5751, WKK 5779, WKK 5783, WKK 5796 and WKK 5813).

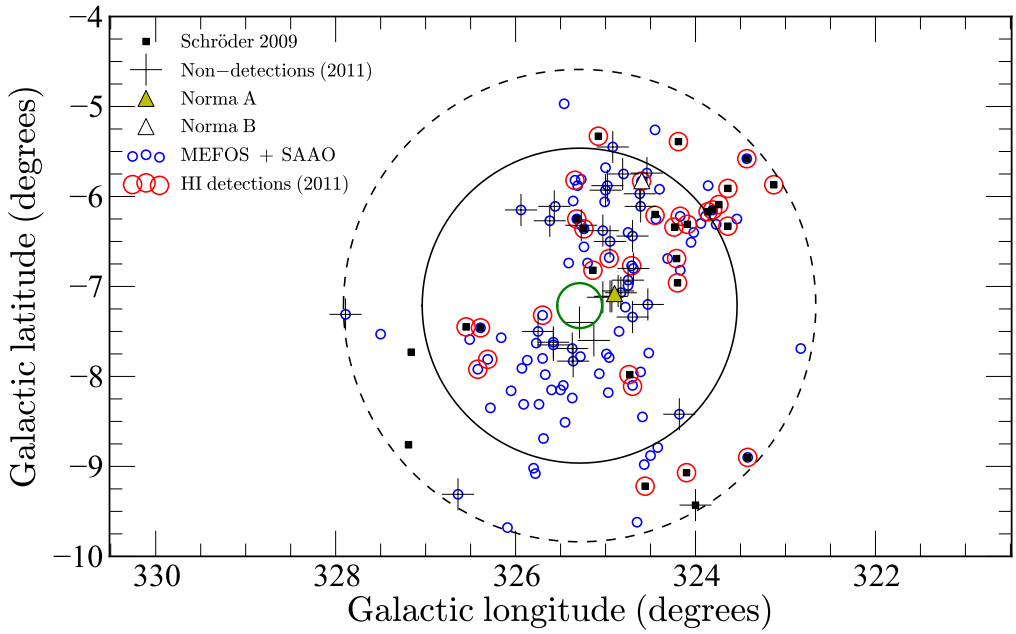

Fig. 2.7: Location of the late-type galaxies within the Norma cluster. The symbol meanings are; small open circles: spiral galaxies in the Norma cluster with measured redshifts, filled squares: HI detected galaxies by Schröder et al. (2009). The large open and filled triangles represent the location of the dynamical spiral-rich subgroups Norma A (filled triangle) and Norma B (open triangle). The inner green solid circle covers the region with radius $\sim 0.27 R_{\rm A}$ (spiral galaxies within this circle are HI deficient and were excluded from the sample). The black solid and dashed circles indicate the Abell radius ($R_{\rm A} \sim 1.^{\circ}75$) and $1.5 R_{\rm A}$, respectively.

2.2.2 HI *Data — Observations and Data Reduction*

Narrow-band 21 cm pointed observations were obtained by me in September 2011. These observations used the 21 cm multibeam receiver (Staveley-Smith et al., 1996) installed at the prime focus of the Parkes 64 m radio telescope[7]. The receiver has 13 beams, each with two linear polarisations, and system temperatures of ~ 20 K. During the HI observations, 7 of the available 13 beams were used (the 7 beams used are the inner and most sensitive; see Figure 2.8). The correlator has a bandwidth of 64 MHz divided into 1024 channels, covering a velocity range of -1200 km s^{-1} $< cz <$ $+12700$ km s^{-1} at a channel spacing of 13.2 km s^{-1}. For these observations, a narrow bandwidth of 8 MHz was used. This corresponds to a channel separation of 1.6 km s^{-1}. The velocity resolution was ~ 2 km s^{-1} after Hanning smoothing. The observations were carried out in a beam switching mode, that is, the target galaxy was tracked in turn by each of the 7 beams. Each beam was set on the target for a total of 512 s, implying a total integration time of ~ one hour per galaxy. During the observing run, the radio galaxy PKSB 1934-638 (Sadler et al., 2006) was observed regularly for calibration purposes.

Due to limited observing time, the priority sample was picked from known HI-detected galaxies (Schröder et al., 2009). The reason for re-observing these galaxies ($N = 26$) was so that I get a higher resolution for reliable line width measurements by observing each target for an hour (Schröder et al. 2009 used a total integration time ~ 30 minutes). A total of 66 late-type galaxies were observed using the Parkes radio telescope in September 2011. The data analysis resulted in a total of 32 HI-detections and 34 non-detections. These are represented by the

[7]The Parkes telescope is part of the Australia Telescope, which is funded by the Commonwealth of Australia for operation as a National Facility managed by CSIRO.

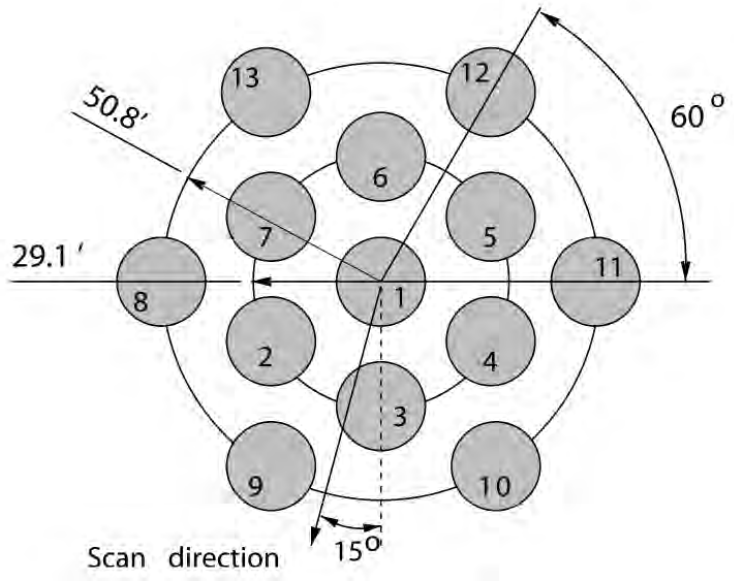

Fig. 2.8: The configuration of the Parkes multibeam receiver on the sky. The HI observations of the Norma cluster galaxies utilised only the inner 7 of the available 13 beams. Figure taken from Barnes et al. (2001).

open red circles (HI detections) and the black crosses (non-detections) shown in Figure 2.7. This implies a detection rate of 48.5% which is similar to that obtained by previous observers in this region (Schröder et al., 2009). However, the majority of the new HI-detections had a low signal-to-noise ratio while some had poor baselines. The HI-detected galaxies ($N = 32$) have an average signal-to-noise ratio, S/N, in the range $1.7 - 18$ (69% of these have $S/N > 3$). As expected, the average signal-to-noise ratio was always smaller than the peak signal-to-noise ratio (peak signal-to-noise ratio is the ratio of the measured peak flux and the noise level or rms).

In Figure 2.7, the large red open circles represent my HI detections while the black crosses represent the HI non-detections in this work. The green solid circle represents the inner $0.27R_{\rm A}$ within which the spiral galaxies are HI-deficient (this region is approximately $0.^{\circ}46$ or ~ 0.5 Mpc from the cluster centre). The black solid circle indicates the Abell radius, $R_{\rm A}$, while the black dashed circle represents $1.5R_{\rm A}$.

2.2.3 HI *Parameterisation*

The data were bandpass-corrected and calibrated within LIVEDATA, which is part of the Astronomical Image Processing System, AIPS[8] program (van der Bliek et al., 1996). The spectra were then gridded into data cubes using GRIDZILLA[9] with a weighted median statistic. The weighted median gridding statistic was adopted since it is robust against possible sources of RFI and other artifacts (see for example, McClure-Griffiths et al. 2009; Freudling et al. 2011; Calabretta et al. 2014). The HI parameters were thereafter extracted using the task MBSPECT in MIRIAD (Sault et al., 1995).

[8] AIPS is produced and maintained by the National Radio Astronomy Observatory, a facility of the National Science Foundation operated under cooperative agreement by Associated Universities, Inc.

[9] Note that GRIDZILLA is provided in the same package as LIVEDATA which is available via `ftp://ftp.atnf.csiro.au/pub/software/livedata`.

We used standard procedures to optimally extract w_{50}. For each source, the gridded data cube was used in measuring the HI parameters. The HI spectrum was inspected and the size of the HI emission profile was determined manually. A baseline fit was then performed excluding the line profile using the MIRIAD task MBSPECT. Different orders were tried during the fitting process with a first-order polynomial given a higher priority if it reasonably fitted the baseline. The fitted baseline was then subtracted with Hanning smoothing applied once. The velocity range of the HI emission was thereafter determined manually and the HI parameters were estimated using MBSPECT. The measured parameters include the peak and integrated flux densities, the systemic velocity, signal-to-noise ratio, and the velocity widths (measured at 20% and 50% of the peak flux). The measurement errors were obtained by following Koribalski et al. (2004) and this is presented in §4.3.2 (see Chapter 4.3.2 on page 126).

Figure 2.9 shows some of the examples of the HI spectra where the baseline has been fitted and subtracted. The x-axis represents the optical velocity, $VOPT$. The velocity range over which the HI line profile was parameterised is shown by the vertical dashed lines. Thus, the data in the velocity range outside the two vertical dashed lines were used in fitting the baseline. The width-maximised 50% and 20% points are indicated with a circle, while the width-minimised points are labelled with a cross. The peak flux density is marked by the filled circle. The line width measurement (w_{50}) adopted for the Tully-Fisher analysis is the width-maximised 50%. These are represented by the open solid circles in Figure 2.9 and they correspond to the width measured at 50% of the peak flux.

Using the near-infrared and optical counterparts, the HI spectra were checked for possible galaxy confusion. In Figure 2.10, possible galaxies in the target galaxy field which lie within the redshift range of my galaxy sample are marked with small circles. The target galaxy is shown at the centre of the galaxy field. The large magenta circle corresponds to a radius of $7\farcm0$ which is the approximate beam size for these HI observations, that is, the full width half power of Parkes beam is $14\farcm3$ across; the central beam has FWHM of $14'$. In a few cases, there was confusion in the HI profile arising from neighbouring galaxies. An example is WKK 5993 whose HI profile is dominated by WKK 5999 as shown in Figure 2.11. The target galaxy (WKK 5993) and the neighbouring galaxy (WKK 5999) have measured heliocentric velocities of 3487 km s^{-1} and 3246 km s^{-1}, respectively. The two galaxies are separated by only $8'$ and WKK 5999 dominates the HI profile. The high confusion makes it difficult to measure the line width for WKK 5993. However, in this case, the line profile for WKK 5999 has been accurately measured (see the top panel of Figure 2.9 on page 54). Therefore, the neighbouring galaxy (WKK 5999) was masked out using the measured widths for WKK 5999 so as to get better estimate for the HI parameters of WKK 5993. In a few other cases where the HI profile had very poor baselines and/or very low signal-to-noise ratio, the HI parameters were taken from Schröder et al. (2009).

In addition to the 26 galaxies detected by Schröder et al. (2009), I have six more HI detections in my observations. These new HI detections include WKK 6801 which was previously observed and detected by Vollmer et al. (2001) but not observed by Schröder et al. (2009). Table 2.5 shows my HI-detections. Presented in Table 2.5 are the galaxy name, equatorial coordinates (right ascension and declination), Galactic coordinates (longitude and latitude), line widths (w_{20} and w_{50} measured at 20% and 50% of the peak flux), systemic velocity ($V_{\rm sys}$), intensity, rms and the average signal-to-noise ratio (S/N) for each galaxy. The HI non-detections are presented in Table 2.6.

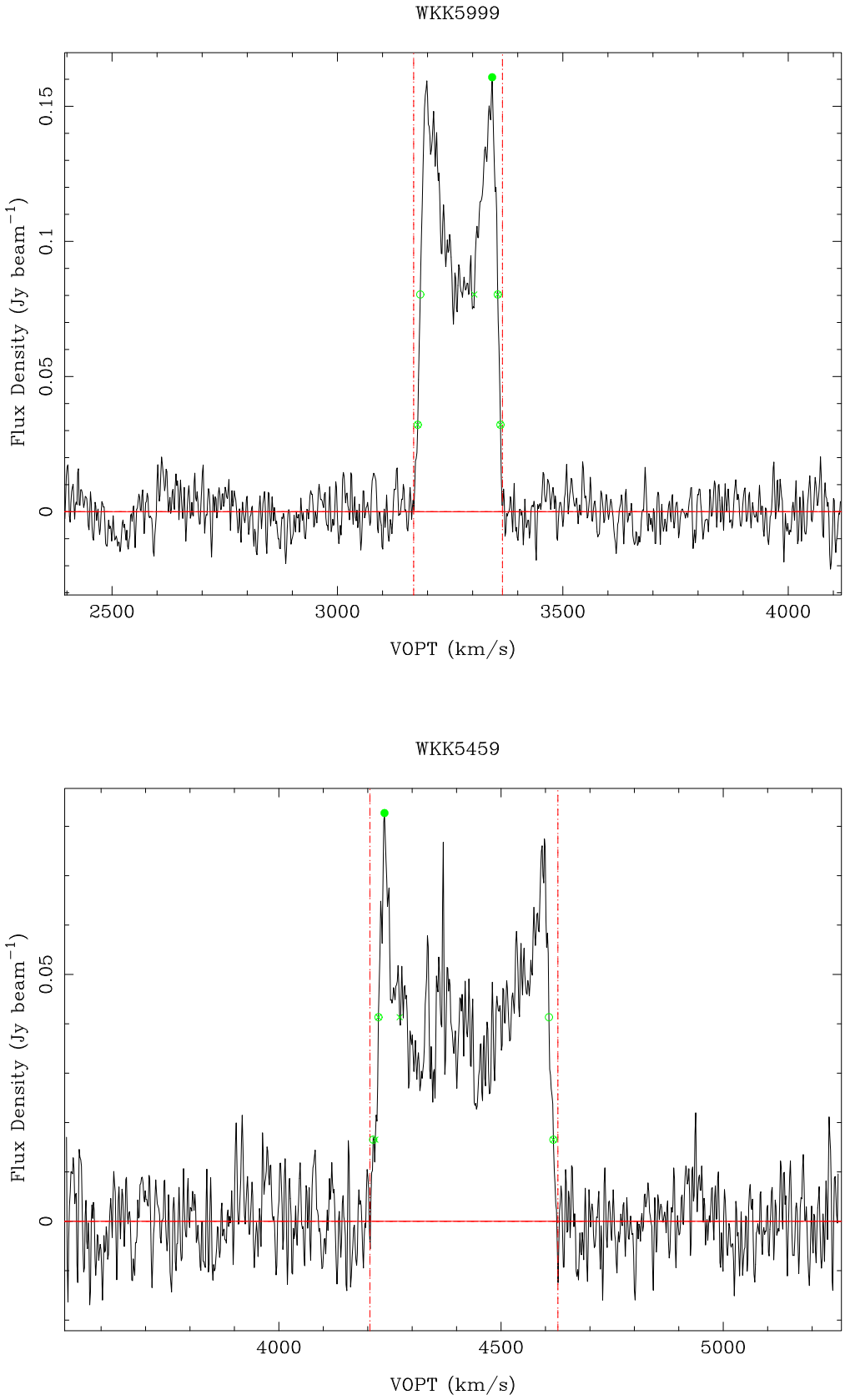

Fig. 2.9: Parkes HI data reduction: the top and bottom panels represent WKK 5999 and WKK 5459, two of the HI profiles for the late-type galaxies in my Tully-Fisher sample. Hanning smoothing has been applied, and the baseline fit has been subtracted. $VOPT$ (on the x-axis) is the optical velocity.

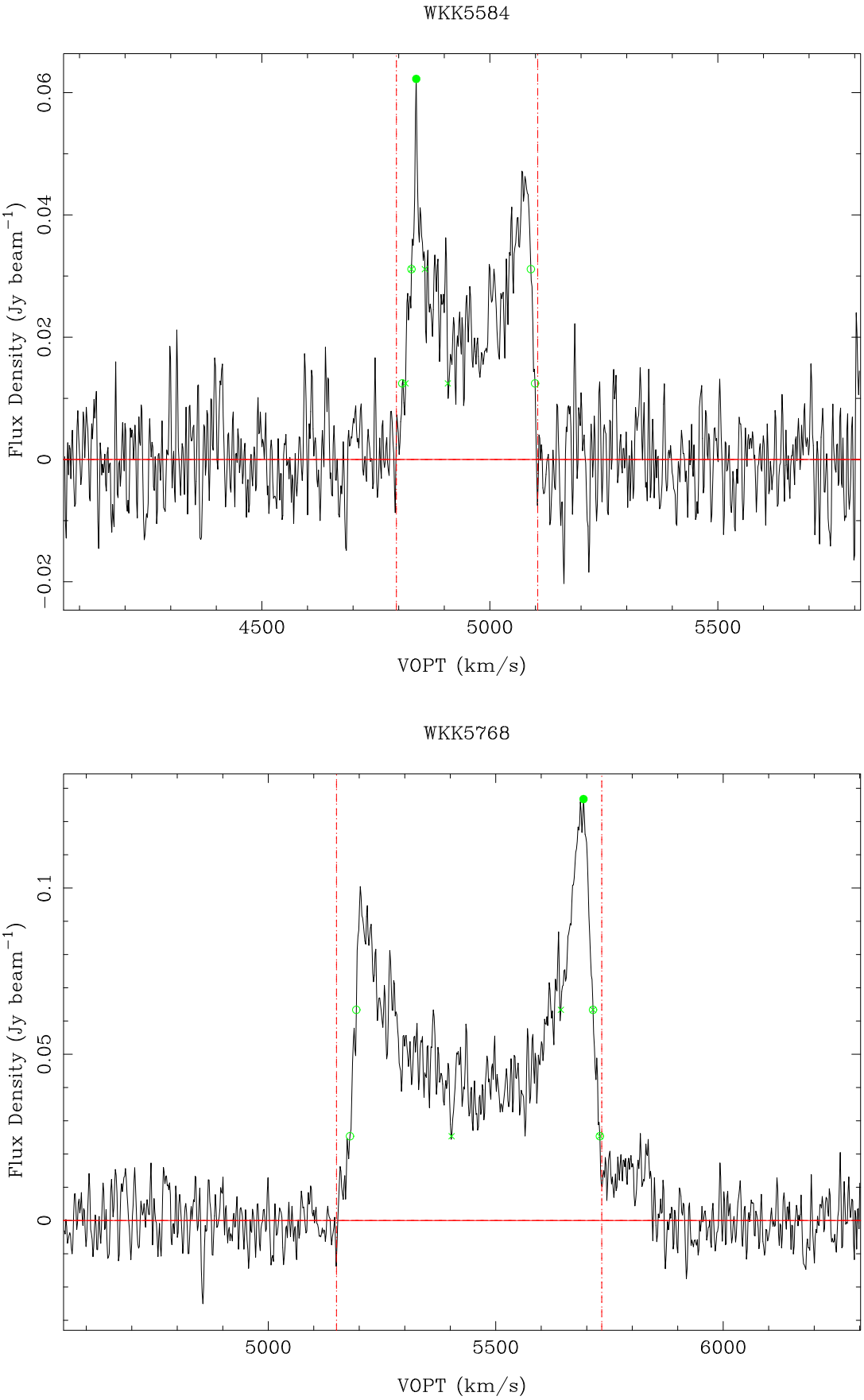

Fig. 2.9: Continued . . . for WKK 5584 (top panel) and WKK 5768 (bottom panel).

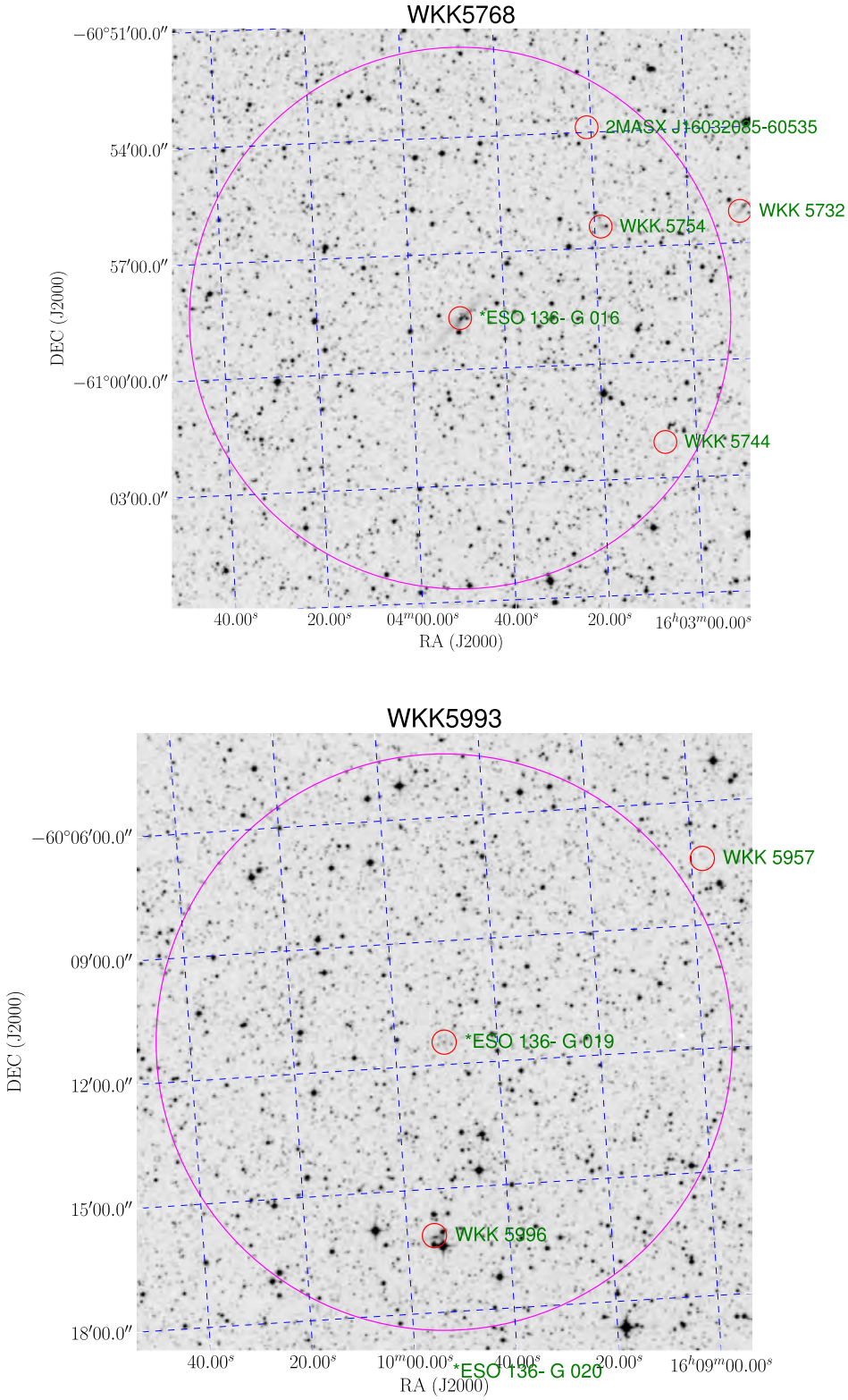

Fig. 2.10: Identifying and searching for the neighbouring galaxies (close to the target galaxy both in position and redshift) that may lead to contamination of the observed HI profile or detected signal. The small red circles indicate the location of the identified galaxies; the target galaxy lies at the centre. The large magenta circle corresponds to a radius of 7.′0 (the mean Parkes beam is 14.′3 across). WKK 5768 (ESO 136-G016) is shown in the top panel, WKK 5993 (ESO 136-G019) is shown in the bottom panel.

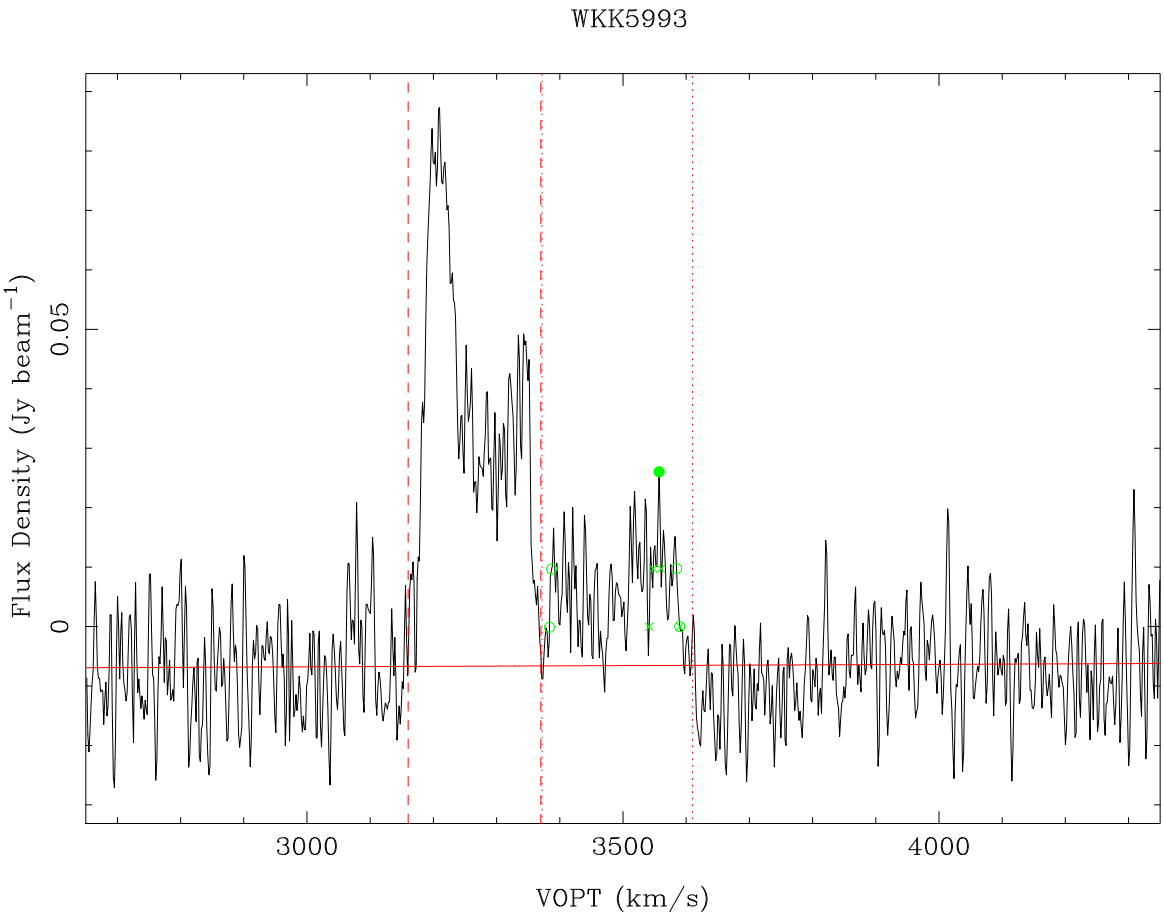

Fig. 2.11: Parkes HI data reduction for WKK 5993 (also known as ESO 136-G 019), an example of a contaminated HI profile. The HI profile for this galaxy is dominated by WKK 5999 (also known as ESO 136-G 020). The two galaxies are separated by $\sim 8'$. The line profile for WKK 5999 (cz = 3246 km s^{-1}) is clearly seen on the left-hand side of WKK 5993 (cz = 3487 km s^{-1}). The masked region is indicated by the dashed lines while the dotted lines represent the profile of WKK 5993 (the HI parameters were estimated within the region shown by the dotted lines).

The final Tully-Fisher sample consists of 12 spiral galaxies after applying inclination cuts and an additional cut on the final corrected line widths (see Chapter 4 on page 113 for a detailed information). Note also that of the 12 spiral galaxies used in the final Tully-Fisher analysis, 11 are marked with $*$ in Column 12 of Table 2.5 while WKK 6570, one of the 12 galaxies in my final Tully-Fisher sample, is not, since its line width measurement was not made in this work, but taken from Schröder et al. (2009).

2.2.4 Near-infrared Imaging

Near-infrared images for the HI-detected galaxies were obtained using the InfraRed Survey Facility (IRSF). These observations were obtained by me in May 2012. For details regarding the IRSF telescope, I refer to §2.1.3. A total integration time of 600 s was used for each target galaxy. As mentioned earlier, such high exposure times result in saturation by both bright stars and the infrared sky background. To avoid saturation of the detector arrays, the total exposure time was split into small 24 s exposures using dithering mode. This implies a total of 25 dither frames for each target. The choice of the exposure time used here was based on the experience of past observers in the same region (e.g., Nagayama et al., 2004, 2006; Williams et al., 2014) and the previous observations of the early-type galaxies used in the IRSF J and K_s-band Fundamental

Tab. 2.5: HI detections ($N = 32$). The different columns correspond to the galaxy name, equatorial coordinates (right ascension and declination), Galactic coordinates (longitude and latitude), line widths (w_{20} and w_{50} measured at 20% and 50% of the peak flux), systemic velocity ($V_{\rm sys}$), intensity, rms noise and the average signal-to-noise ratio (S/N). The galaxies used in the final Tully-Fisher analysis are indicated using $*$ in Column 12.

Identification	RA (2000.0)	Dec (2000.0)	G. lon	G. lat	w_{20}	w_{50}	$V_{\rm sys}$	Intensity	rms	S/N	
	h m s	° ′ ″	°	°	km s^{-1}	km s^{-1}	km s^{-1}	Jy km s^{-1}	mJy		
WKK5459	15 54 22.9	–61 20 24	323.13	–5.87	405	383	4418	17.7	5.6	7.4	*
WKK5470	15 54 44.8	–60 56 06	323.43	–5.58	372	294	5151	6.5	3.1	5.3	*
WKK5562	15 57 52.7	–61 02 53	323.64	–5.91	147	139	4431	4.5	5.6	5.1	
WKK5584	15 58 29.4	–60 17 43	324.19	–5.39	291	261	4957	7.8	4.8	5.2	*
WKK5616	15 59 27.3	–61 07 03	323.74	–6.09	65	44	4186	3.8	5.6	8.8	
WKK5636	16 00 04.0	–61 21 51	323.64	–6.33	105	88	5888	6.9	5.5	10.3	
WKK5642	16 00 10.8	–61 06 54	323.81	–6.15	420	367	5969	3.9	3.6	2.4	*
WKK5659	16 00 38.0	–61 06 03	323.86	–6.17	159	139	4428	4.6	4.8	5.7	*
WKK5729	16 02 47.6	–61 03 14	324.09	–6.31	107	56	5689	4.4	5.9	6.6	
WKK5732	16 02 48.9	–60 56 11	324.17	–6.22	102	97	5802	2.2	4.4	4.6	
WKK5751	16 03 15.4	–60 21 27	324.60	–5.83	136	87	5184	1.6	3.9	2.9	
WKK5760	16 03 29.2	–59 39 47	325.08	–5.33	383	364	5165	9.2	3.9	6.0	*
WKK5768	16 03 49.2	–60 58 41	324.24	–6.34	549	520	5466	31.7	5.9	9.2	*
WKK5796	16 04 25.0	–60 44 14	324.45	–6.21	250	219	5345	4.9	4.5	4.1	
WKK5829	16 05 34.8	–61 15 28	324.21	–6.69	182	163	4431	7.4	4.7	8.1	
WKK5891	16 07 04.2	–61 27 56	324.20	–6.96	99	61	5319	0.8	4.0	1.7	
WKK5912	16 07 35.1	–59 51 35	325.34	–5.82	145	125	5240	3.1	7.6	2.4	
WKK5964	16 09 06.3	–60 59 08	324.71	–6.77	395	270	4801	4.2	3.5	2.6	
WKK5993	16 09 50.4	–60 11 27	325.32	–6.25	206	197	3510	2.9	6.8	1.8	*
WKK5999	16 09 56.0	–60 19 18	325.24	–6.36	183	171	3266	19.9	5.6	18.0	*
WKK6006	16 10 06.4	–60 45 07	324.96	–6.69	152	93	5717	1.2	3.3	2.2	
WKK6100	16 11 55.8	–60 43 33	325.14	–6.82	414	373	4897	10.4	5.2	4.7	
WKK6181	16 13 44.6	–63 24 26	323.42	–8.90	261	229	3385	4.0	2.9	5.0	*
WKK6331	16 16 14.4	–61 50 49	324.74	–7.98	186	160	4415	3.0	3.5	4.2	
WKK6366	16 16 47.3	–61 57 04	324.70	–8.11	142	122	3863	1.2	3.4	2.4	
WKK6439	16 18 04.0	–60 41 41	325.70	–7.32	179	121	3677	3.9	6.2	2.2	
WKK6483	16 19 01.2	–63 03 11	324.10	–9.07	171	148	3293	5.6	4.1	6.8	*
WKK6680	16 22 46.0	–62 50 05	324.56	–9.22	93	64	6490	1.1	3.5	3.2	
WKK6689	16 22 47.6	–60 18 56	326.39	–7.46	152	120	3200	6.2	6.0	6.3	
WKK6732	16 23 36.1	–60 11 29	326.55	–7.45	106	91	3246	6.7	4.7	11.6	
WKK6760	16 24 24.1	–60 36 46	326.31	–7.81	107	103	3520	1.1	3.8	2.4	
WKK6801	16 25 36.2	–60 36 19	326.42	–7.92	165	143	3513	4.2	3.9	6.4	

Plane analysis. The exposure time should not be too high to cause saturation by bright foreground stars or the sky background but should also not be too short to result in images with very low signal-to-noise ratio.

2.2.5 Near-infrared Data Reduction

The process of data reduction and image calibration followed the same steps as described in §2.1.4 for the IRSF observations of early-type galaxies used in the J and K_s-band Fundamental Plane analyses. The procedures used to reduce the data include dark subtraction, flat-fielding, sky subtraction and finally, combining the dither frames for each target galaxy into a single science image. These were performed using the SIRIUS data reduction pipeline (SIRIUS09) developed and maintained by Yasushi Nakajima[10]. The SIRIUS09 package was built as an IRAF package, with various tasks dedicated for automated reduction of images taken using the SIRIUS imaging camera on the IRSF.

Among the tasks used is SETPAR09 which creates the initial files required before executing the pipeline using the PIPE09 task. After executing PIPE09, the major steps in the reduction of the raw images include:

[10]Center of Information and Communication Technology, Hitotsubashi University, Japan

Tab. 2.6: HI non-detections ($N = 34$). The different columns represent the galaxy name, equatorial coordinates (right ascension and declination), Galactic coordinates (longitude and latitude) and the heliocentric recession velocity from optical observations (Woudt & Kraan-Korteweg, 2001; Woudt et al., 1999, 2004). In column 7, I present the status of the HI data/profile; PSN for poor signal-to-noise ratio, PB for poor baseline.

Identification	RA (2000.0)	Dec (2000.0)	G. lon	G. lat	$v_{\rm hel}$	
	h m s	° ′ ″	°	°	km s^{-1}	
WKK5718	16 02 27.6	–60 19 42	324.54	–5.74	5326	PSN
WKK5749	16 03 09.2	–59 51 47	324.92	–5.45	5373	PSN
WKK5779	16 04 05.2	–60 09 50	324.81	–5.75	5632	PSN
WKK5783	16 04 10.8	–60 26 46	324.62	–5.97	6114	PSN
WKK5813	16 04 54.3	–60 33 40	324.61	–6.11	4276	PSN
WKK5840	16 05 49.0	–60 08 43	324.98	–5.88	5177	PSN
WKK5859	16 06 13.7	–60 10 17	325.00	–5.93	5736	PB
WKK5899	16 07 14.7	–60 44 51	324.70	–6.44	5062	PSN
WKK5951	16 08 48.1	–60 28 42	325.03	–6.38	4741	PSN
WKK5961	16 09 03.2	–60 37 20	324.95	–6.50	5088	PB
WKK5967	16 09 08.1	–61 01 11	324.69	–6.80	5631	PSN
WKK5996	16 09 54.8	–60 16 08	325.27	–6.32	5230	PSN
WKK6016	16 10 15.1	–61 03 58	324.75	–6.93	4271	PB
WKK6026	16 10 27.8	–61 24 41	324.53	–7.20	4617	PSN
WKK6029	16 10 29.1	–59 55 03	325.57	–6.11	5123	PB
WKK6071	16 11 34.2	–61 07 05	324.83	–7.07	4693	PSN
WKK6078	16 11 36.9	–61 04 53	324.86	–7.05	4510	PB
WKK6086	16 11 42.4	–59 59 55	325.62	–6.27	4638	PSN
WKK6118	16 12 17.5	–61 24 10	324.70	–7.34	4648	PB
WKK6125	16 12 22.2	–61 04 47	324.93	–7.11	3937	PB
WKK6135	16 12 26.4	–61 03 50	324.95	–7.11	4426	PB
WKK6152	16 12 56.6	–61 01 03	325.03	–7.12	4266	PB
WKK6156	16 12 54.5	–59 41 32	325.94	–6.15	5814	PB
WKK6290	16 15 31.2	–62 32 29	324.18	–8.42	4815	PSN
WKK6330	16 16 08.9	–61 02 34	325.29	–7.40	6324	PB
WKK6340	16 16 19.5	–61 17 45	325.13	–7.60	6330	PB
WKK6451	16 18 17.1	–61 11 42	325.37	–7.69	4475	PB
WKK6489	16 19 03.6	–61 17 47	325.36	–7.83	3794	PB
WKK6493	16 19 04.4	–60 59 34	325.58	–7.62	5184	PSN
WKK6503	16 19 17.1	–61 01 11	325.58	–7.65	3939	PSN
WKK6508	16 19 23.2	–60 47 27	325.75	–7.50	5624	PB
WKK6570	16 20 40.1	–63 22 45	324.00	–9.43	2938	PSN †
WKK6986	16 30 06.2	–59 07 47	327.89	–7.31	4869	PSN
WKK7157	16 35 16.4	–61 23 37	326.64	–9.31	5328	PSN

† My HI observations resulted in a non-detection for WKK 6570 although this galaxy was detected by Schröder et al. (2009). I therefore adopted the measurements obtained by Schröder et al. (2009).

- dark current subtraction,
- flat-fielding or flat correction,
- sky subtraction,
- frame to frame offset determination and combination.

2.2.5.1 Dark Subtraction

Detectors used for near-infrared observations are susceptible to thermal noise. When a detector is non-illuminated, there is a build-up of charge although the shutter is closed. This build-up of charge in the absence of light is often referred to as dark current. The thermal noise is a function of exposure time, that is, it increases with exposure time. To correct for this effect, ten dark frames were taken at the end of each observing night with the shutter closed. The same exposure time was used as for the images to be corrected. This implies 10 dark frames for the 5 second sky exposures (flat fields, see §2.2.5.2) and then after, 10 dark frames for the target galaxies taken with an exposure time of 24 seconds.

The ten dark frames for each exposure time were pixel-by-pixel median combined to create a master dark. Combining the ten dark frames reduces the noise. In the data reduction pipeline, the master dark frames were subtracted from all raw images, including twilight or flat-field frames (see §2.2.5.2). The resulting object frames after dark-subtraction are hereafter referred to as $\text{self}_{\text{no dark}}$.

2.2.5.2 Flat-fielding

Not all the pixels across the near-infrared array/detector will respond uniformly when exposed to the same amount of light. Flat-fielding helps correct for pixel-to-pixel response variations across the near-infrared array. In addition to correcting the effect of the pixel-to-pixel sensitivity variations across the array, flat fielding also removes the effect of dust and scratches on the detector window. To create a flat-field frame, a uniform source of light is often used. In my observations, 100 flat-field frames were taken using the twilight sky with exposure times of 5 seconds per frame. These were, weather permitting, taken at evening and morning. A separate task, AUTOTWFLAT, within the SIRIUS package was used to create a master flat field for my observing run. This was done through pixel-by-pixel median combining of the different flat frames. Note that the twilight frames were also first corrected for the dark current (dark subtraction).

Variations in the pixel-to-pixel response are not significant on scales of less than one month (Riad, 2010). I therefore created and used one master flat-field for each of the J, H, and K_s filters used in my observing run. In order to correct for the individual object frames for the pixel-to-pixel variations in sensitivity, the frames $\text{self}_{\text{no dark}}$ were divided by the master flat-field. The resulting new frames are hereafter referred to as $\text{self}'_{\text{no dark}}$.

2.2.5.3 Sky Determination and Subtraction

Visual patterns due to imperfections, dirt or dust in the telescope's optical system as well as emission from the atmosphere will imprint on the observed frames. The effect is usually not visible in the J-band as compared to H and K_s-bands. Diffraction patterns from OH emission in the atmosphere dominate these visual patterns in the H-band while dust is hot enough to radiate in the K_S-band. These sky-background effects were corrected for through sky subtraction.

Not only is the sky brighter in the near-infrared than optical, but also, there is a higher proportion of faulty/hot pixels in the near-infrared than in optical. To overcome the effect of faulty pixels, a procedure known as dithering was used. This effectively ensures that the observed objects/sources fall on different parts of the detector. The effect of faulty pixels is then averaged out when the dither frames are aligned and combined. In my observations, I used 25 dither frames per target galaxy with a dithering radius of $20''$. This resulted in $9\farcm24$ by $9\farcm24$ images although the central field is about $7\farcm7$ by $7\farcm7$. The total exposure time is 600 seconds per target galaxy, which implies an exposure time of 24 seconds per dither frame.

For a given set of dither frames corresponding to a given observed object/source, the mean flux of the dithered frames was scaled to the mean flux of the central frame (first frame) by adding or subtracting a value equal to the difference of their mean flux. This was done to ensure that all frames in the given set have the same mean flux value. These images were thereafter pixel-by-pixel median combined. Due to the applied dithering, astronomical sources were shifted around the detector while the sky patterns always occupied the same regions on the detector. When the images were pixel-by-pixel median combined, the astronomical

sources in the combined frame were removed leaving only the sky patterns. I refer to this new image as SKY. It is important to note that these sky frames were also corrected for the pixel-to-pixel variations in sensitivity across the array (flat-fielding). To remove the sky patterns, the sky frame (SKY) was subtracted from each of the $\text{self}'_{\text{no dark}}$ frames. To ensure the sky background level of the resultant frames remained unchanged, the mean value of the sky background, $\langle \text{sky} \rangle$, was added back. This resulted in the final images which I refer to as $\text{image}_{\text{self}}$.

The final science image was created from the corrected dithered images by aligning and combining the dithered frames denoted by $\text{image}_{\text{self}}$. The aligned frames were pixel-by-pixel average combined into a single final science image. This science image has an enhanced gain of $G \times N$ and a reduced noise which scales as $1/\sqrt{N}$, where N is the number of dithered frames and G refers to the gain for a single frame (single exposure).

The reduced images from the SIRIUS pipeline require astrometric calibration to transform image/pixel coordinates to the World Coordinate System and photometric calibration to measure zero-point magnitudes which in turn help convert instrumental magnitudes to a standard magnitude system. In this analysis, I used the 2MASS Point Source Catalogue (Skrutskie et al., 2006) to perform both the astrometric and photometric calibrations. For a detailed description about astrometric and photometric calibration of the IRSF data/images, see §2.1.4 on page 45.

2.2.6 Star-subtraction

Star-subtraction was performed in the same way to that used for the Fundamental Plane data. However, star-subtraction in spiral galaxies is more difficult than in elliptical galaxies due to for example, star-forming regions or bars that may be present in spiral galaxies. This may lead to the removal of parts of a galaxy by the algorithm. However, this can be avoided by identifying such areas/parts and remove them from the star catalogue before subtracting stars on the original galaxy image.

Figure 2.12 shows an example where parts that seem to belong to the galaxy were subtracted (see the middle panel). The left-hand panel shows the original galaxy image while the middle panel shows the star-subtracted image. In the right-hand panel, the stars in the catalogue that seem to be part of the galaxy were removed from the star catalogue so as not to subtract them from the original image. The difference in the measured isophotal magnitude (measured at the 20 mag arcsec^{-2} level in the K_s-band) using the galaxy images shown in the middle and right-hand panels is not significant, that is, ~ 0.009 mag. The difference in the total extrapolated magnitude is 0.011 mag.

Figure 2.13 shows the original and star-subtracted images for 12 spiral galaxies in my Tully-Fisher sample. The star-subtracted image is shown on the right-hand side of the corresponding original galaxy image. Each image is of size $68'' \times 68''$. The determination of the isophotal magnitudes and the applied corrections are presented in Chapter 4.

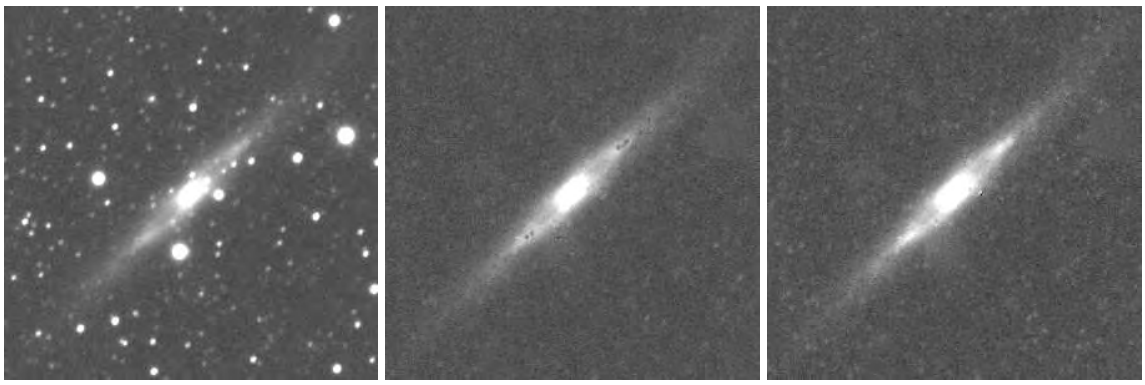

Fig. 2.12: Star-subtraction for WKK 5768. The left-hand panel shows the original image. The middle and right-hand panels represent the star-subtracted images. In the right-hand panel, parts which seem to belong to the galaxy were removed from the star catalogue before performing star-subtraction. This resulted in the star-subtracted image shown in the right-hand panel. The images are of size $136'' \times 136''$.

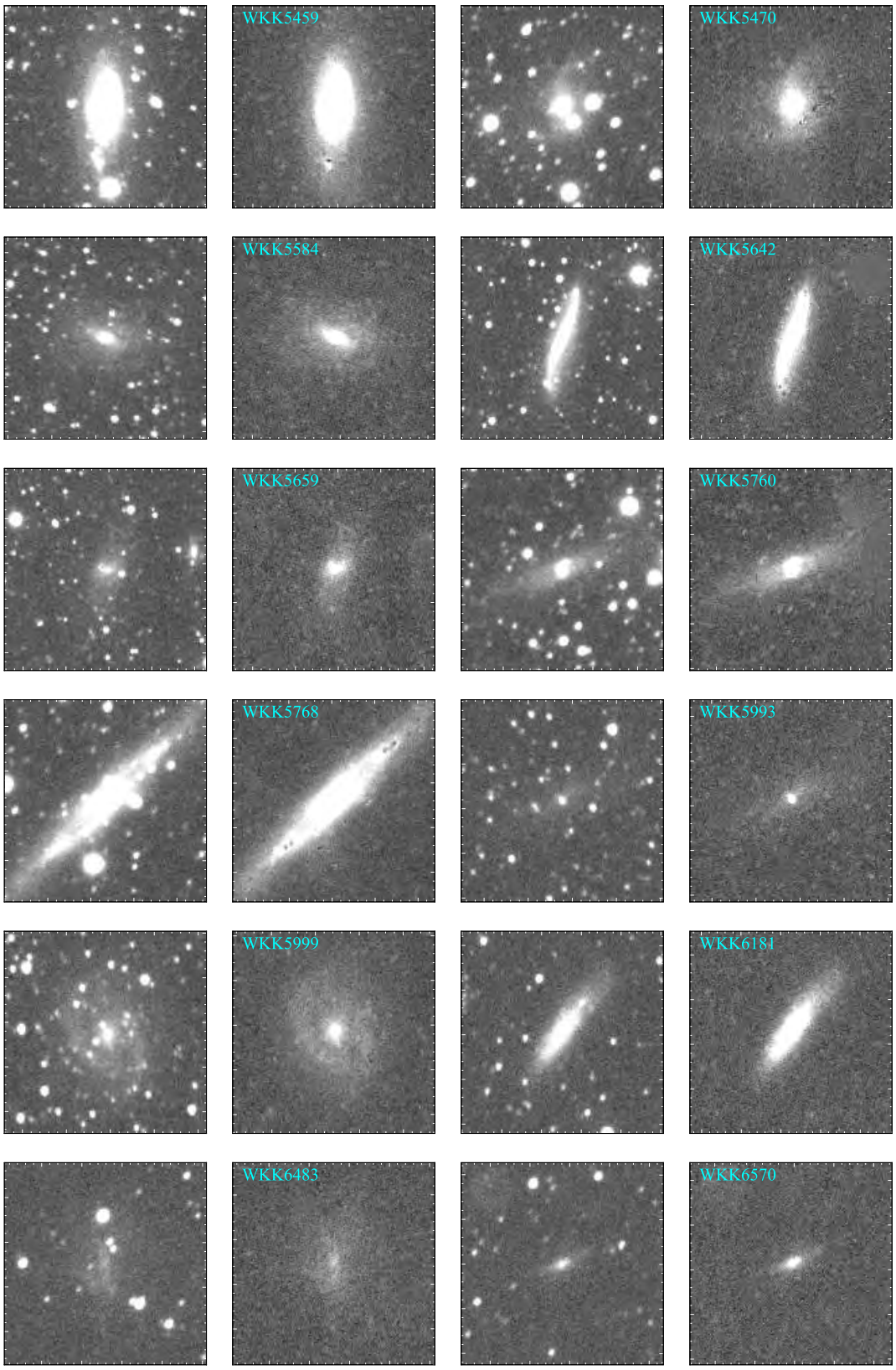

Fig. 2.13: IRSF NIR images (original and star-subtracted) for 12 spiral galaxies used in the Tully-Fisher analysis. From top to bottom (starting from left to right) are the K_s-band images for: WKK 5459, WKK 5470, WKK 5584, WKK 5642, WKK 5659, WKK 5760, WKK 5768, WKK 5999, WKK 5993, WKK 6181, WKK 6483, WKK 6570. For each galaxy, the star-subtracted image is on the right-hand side of the corresponding original image (embedded with stars). The above images are of size $68'' \times 68''$.

CHAPTER 3

THE NORMA CLUSTER FUNDAMENTAL PLANE

The abundance of early-type galaxies in galaxy clusters makes the Fundamental Plane relation ideal for distance measurements to galaxy clusters. Although the error in distance to individual early-type galaxies measured using the Fundamental Plane has been found to be as high as $\sim 30\%$ (Magoulas et al., 2012), this decreases to below 5% for rich galaxy clusters since the error scales as $1/\sqrt{N}$ and the majority of galaxy clusters are rich in early-type galaxies (N is the number of galaxies in the sample). The measured parameters which enter into the Fundamental Plane are the central velocity dispersion (σ), the effective radius (r_e) and the mean effective surface brightness ($\langle\mu_e\rangle$), that is,

$$\log r_e = a \log \sigma + b \langle \mu_e \rangle + c. \tag{3.1}$$

The effective radii and mean effective surface brightnesses were measured through near-infrared photometric analysis while the central velocity dispersions were measured through optical spectroscopy (see §2.1.2 for the spectroscopic data analysis).

The Fundamental Plane relation has been used for distance measurements and peculiar velocity studies by, for example, the NOAO Fundamental Plane Survey (NFPS; Smith et al., 2004), Early-type NEARby survey project (ENEAR; da Costa et al., 2000b), Ellipticals Far away survey (EFAR; Colless et al., 2001b), the Streaming Motions of Abell Clusters (SMAC; Hudson et al., 2004), and more recently the 6dF Galaxy Survey (Magoulas et al., 2012; Campbell et al., 2014; Springob et al., 2014). In this chapter, I present the methods used to extract the photometric variables that go into the Fundamental Plane. I then present an investigation into possible systematic uncertainties and bias corrections, leading to a reliable measurement of the peculiar velocity of the Norma cluster (in the rest frame of the cosmic microwave background).

3.1 Near-infrared Surface Photometry

Near-infrared observations are dominated by the counts from the background sky. It is therefore necessary to accurately measure and subtract the sky background before measuring the galaxy flux (counts per second).

Surface photometry was performed on both the Norma and Coma samples through galaxy surface brightness profile fitting. The surface brightness profiles were derived by fitting isophotes to the 2MASS, NTT/SOFI and IRSF/SIRIUS images using the IRAF task ELLIPSE. The galaxy position, ellipticity and position angle were determined using GALFIT (version 3.0.5; Peng et al., 2002, 2010). These were kept fixed while fitting the isophotes. The surface brightness in mag arcsec^{-2} is given by

$$\mu(r) = \mathrm{ZPO} - 2.5\log\left(\frac{\text{average counts per pixel} - \text{sky background}}{\text{exptime} \times \text{area}}\right), \tag{3.2}$$

where ZPO is the magnitude zero point, exptime is the exposure time per dither frame and area=(pixel scale)^2. The total magnitudes were measured from fitting and extrapolating the galaxy surface brightness profiles. The effective radius was then measured to be the radius of the circle containing half the total flux. This was obtained through interpolation. The mean effective surface brightness (mean surface brightness within the effective radius) was calculated using the measured effective radius and the total extrapolated magnitude. Note that an overestimate in the sky background will result in the galaxies appearing fainter than they really are, and conversely (as can be seen in Equation 3.2). It is therefore crucial to reliably and accurately measure the sky background (or sky value).

3.1.1 Determining the Sky Background

The sky background used in Equation 3.2 was determined in an annulus around each galaxy. The width of the annulus varied according to the initial estimate of the galaxy size, i.e., the galaxy size was approximated to be ~ three times the measured effective radius (r_e) and the inner and outer radii were set to $3.5r_e$ and $6r_e$, respectively. The initial effective radius was measured using GALFIT (Peng et al., 2010). In cases (only for some of the Coma 2MASS Atlas images) where the outer radius ($6r_e$) was greater than the image size, the outer radius was set to match the image size but excluded the pixels on the edges. For accurate measurements of the sky background, an iterative procedure was applied using a $2\sigma_s$-clipping where σ_s is the standard deviation in the sky background within the annulus used.

Figure 3.1 shows an example of the pixel value distribution within the annulus. The annulus used is represented by the white circles (see the top panels). The vertical blue dotted lines (bottom panels) represent the median pixel values (sky values) while the red solid lines represent the $\pm2\sigma_s$-clipping. After iteratively applying the $\pm2\sigma_s$-clipping, I adopted the median pixel value as the sky background. By using simulated data, I further investigated the effect of sky gradients and unresolved stars on the sky brightness determination, based on simulated data. The details of the simulation and results are presented in §3.2.8.2 on page 86. The results show no significant effects from sky gradients, and hence, the adopted iterative method used to measure the sky value is robust to small sky gradients.

The same procedure used in the NTT K_s-band data analysis was adopted for the J and K_s-band Fundamental Plane analysis using the IRSF data. Figure 3.2 shows an example of the sky background estimation for the J (left-hand panels) and the K_s-band images (right-hand panels). The top panels represent WKK 6429 while the bottom panels represent WKK 6047.

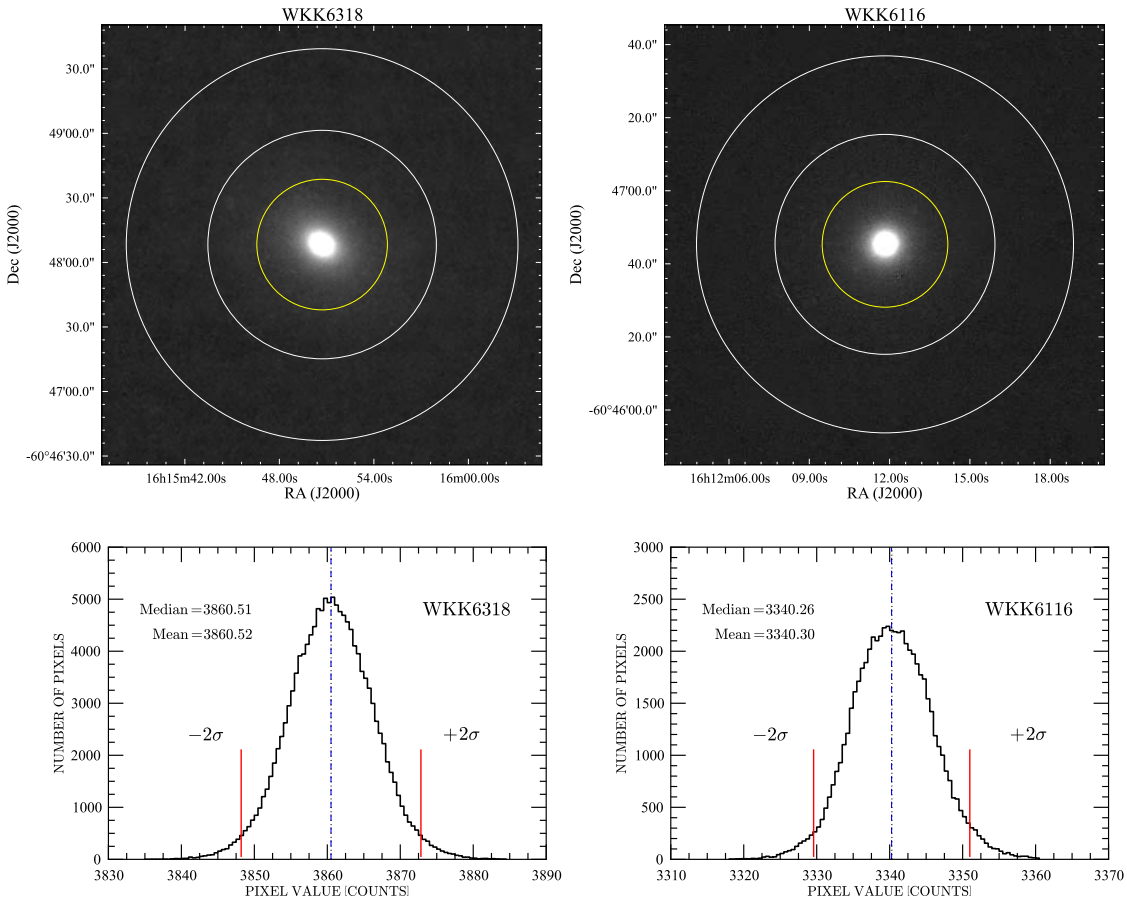

Fig. 3.1: Sky background estimation using an annulus, the white circles in the top panels represent the annulus used while the bottom panels show the distribution of the pixel values within the annulus. The sky value is the median value after applying a $2\sigma_s$-clipping (only points within the two red solid vertical lines were used to calculate the median sky value and the deviation in the sky background — see the bottom panels). The examples of galaxies in the Norma cluster, shown here are: top left-hand panel: WKK 6318 (image size $\sim 203''$ by $203''$) and top right-hand panel: WKK 6116 (image size $\sim 60''$ by $60''$). The yellow circles represent approximately twice the effective radius.

3.1.2 Fitting Galaxy Surface Brightness Profiles

Surface brightness profiles for galaxies can be fitted using a Sérsic $1/n$ law, of the form

$$I(r) = I_0 \exp\left[-\left(\frac{r}{r_0}\right)^{\frac{1}{n}}\right], \tag{3.3}$$

where I_0 and r_0 refer to the central intensity and scaling radius (where for $n = 1$, is the radius at which intensity drops by a factor e^{-1}), respectively. The Sérsic index, n, is also known as the concentration index or shape parameter. Special surface brightness profiles, where $n = 0.5$, $n = 1$, $n = 4$ are referred to as Gaussian, exponential and de Vaucouleurs profiles, respectively. Equation 3.3, can also be re-written as

$$I(r) = I_e \exp\left\{-b_n\left[\left(\frac{r}{r_e}\right)^{\frac{1}{n}} - 1\right]\right\}, \tag{3.4}$$

where I_e is the intensity at the effective radius, r_e. The choice of the value of b_n (which also depends on the shape parameter, n) is such that half the total flux is enclosed within r_e. This

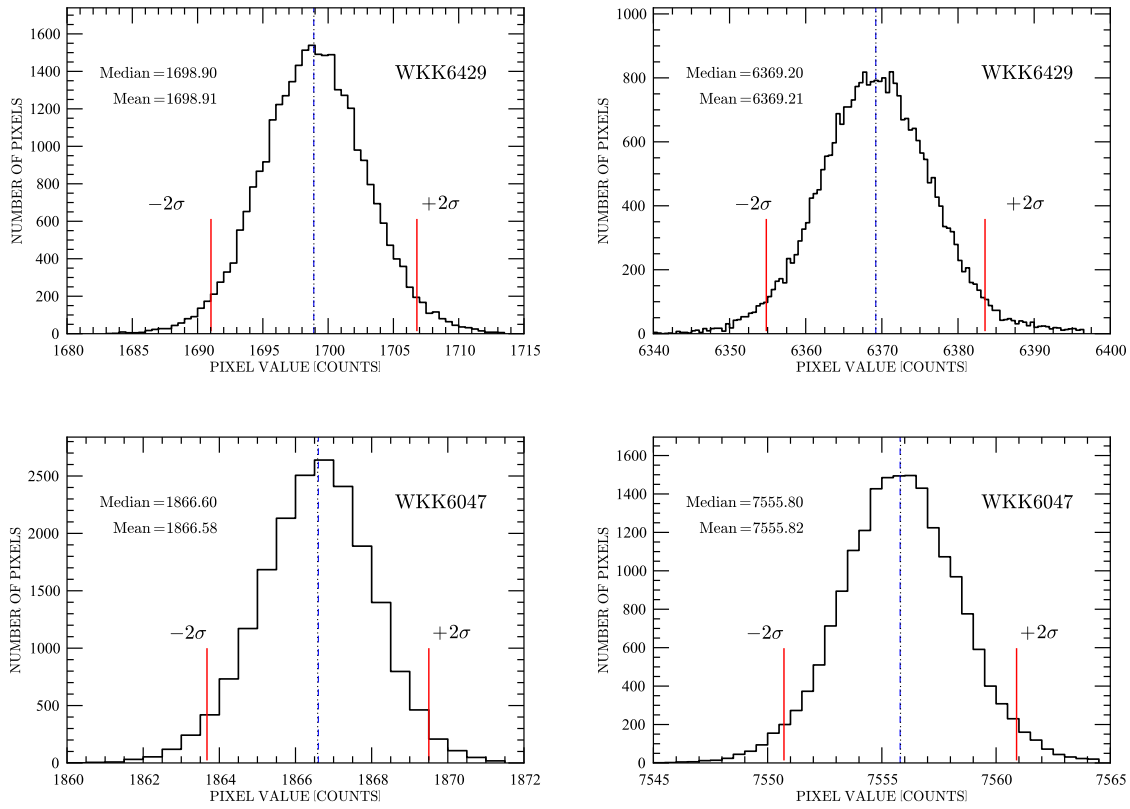

Fig. 3.2: Distribution of pixel values (within an annulus) in the J-band (left-hand panels) and the K_s-band (right-hand panels). The blue dashed and black dotted lines represent the median and mean sky values, respectively. The vertical red solid lines represent $\pm 2\sigma_s$. The possible effect of outliers is reduced through sigma-clipping, whereby only pixel values within the two left and right red solid lines were used to determine the median sky value.

then implies that,

$$\int_0^{\infty} 2\pi r I(r)\,\mathrm{d}r = 2\int_0^{r_e} 2\pi r I(r)\,\mathrm{d}r. \tag{3.5}$$

The intensity in flux units is related to the surface brightness (in mag arcsec^{-2}) via

$$\mu(r) \propto -2.5\log(I(r)). \tag{3.6}$$

Equation 3.6 when used in Equations 3.3 and 3.4 results in:

$$\mu(r) = \mu_0 + 1.08574\left[\left(\frac{r}{r_0}\right)^{\frac{1}{n}}\right]; \tag{3.7}$$

$$\mu(r) = \mu_e + 1.08574\left\{b_n\left[\left(\frac{r}{r_e}\right)^{\frac{1}{n}} - 1\right]\right\}; \tag{3.8}$$

where the surface brightness is now in the units of magnitudes, i.e., mag arcsec^{-2}. For $n \gtrsim 1$, the numerical approximation to Equation 3.5, is $b_n \sim 2n - 0.332$; see e.g., Ciotti (1991); Ciotti & Bertin (1999); MacArthur et al. (2003); Graham & Driver (2005). A more precise estimate of b_n is;

$$b_n \sim 2n - \frac{1}{3} + \frac{4}{405n} + \frac{46}{25515n^2} + \frac{131}{1148175n^3} - \frac{2194697}{30690717750n^4}. \tag{3.9}$$

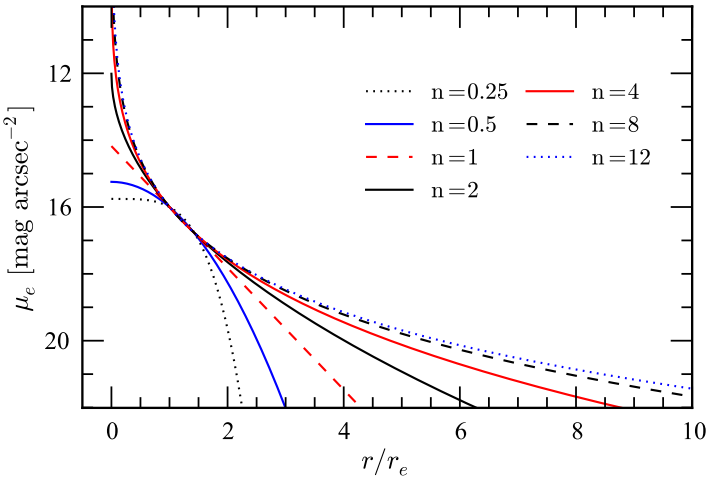

Fig. 3.3: Analytic single Sérsic galaxy surface brightness profile models for a galaxy with an effective surface brightness of 16 mag arcsec^{-2}. The profiles are normalised at 16 mag arcsec^{-2}, the effective radius is unity for all different values of n ($n = 0.25, 0.5, 1, 2, 4, 8, 12$). Clearly, there is more flux in the outer parts of the galaxy profile for galaxies with higher Sérsic indices ($n > 4$).

Note that Equation 3.9 diverges for $n \lesssim 0.36$ (MacArthur et al., 2003). Figure 3.3 shows the derived analytical surface brightness profiles using Equation 3.8 and the expression for b_n given in Equation 3.9. One can clearly see in Figure 3.3, that the effect of the sky background is more pronounced for galaxies with higher Sérsic indices. This is due to the fact that these galaxies are more extended and hence more flux from their faint outer parts tend to get lost within the background noise. On the other hand, the effect is smaller for galaxies with relatively small Sérsic indices.

The central surface brightness, μ_0, is also significantly dependent on the seeing conditions. To overcome the seeing effects on the surface brightness profile fit, a combined double Sérsic profile, each of the form shown in Equation 3.7 was used. The two Sérsic components were used to simultaneously fit the galaxy surface brightness profiles through simple least-squares fitting. The best fit is the combination of the two components. Figure 3.4 shows an example of the fitted galaxy surface brightness profiles, for four Coma galaxies (first top two left and right-hand panels) and four Norma galaxies (last bottom two left and right-hand panels). A few of the inner central pixels were excluded to reduce the seeing effects on the surface brightness profile fit parameters. That is, the data used to fit the galaxy surface brightness profile were restricted to radii ranging from twice the seeing value (for the Norma sample) which is indicated by the small vertical dashed lines on the extreme left, and where the galaxy flux is $1\sigma_s$ above the sky background (vertical dashed lines on the extreme right).

For the Coma sample, the minimum radius was set to $0\farcs5$, that is, the inner $0\farcs5$ pixels were excluded from the fit. The maximum radius was set to match the radius of the isophote whose surface brightness was equivalent to the standard deviation in the sky background (at $1\sigma_s$). The choice of the inner radius (minimum radius) for the Coma sample is due to the large pixel scale of the 2MASS Atlas images and the fact that some of the smaller galaxies in my Coma sample had effective radii slightly less than or equal to the seeing (FWHM).

The subscripts α and β denote the fit parameters for the two separate Sérsic components (represented by the blue dotted and blue dot-dashed curves in Figure 3.4) which were ob-

tained through a simultaneous fit to each galaxy surface brightness profile. The red solid line represents the best fit, which is the sum of the two Sérsic components. This was extrapolated to infinity to determine the galaxy flux that would otherwise get lost within the background noise.

The same procedures were used to extract the photometric parameters for the IRSF J and K_s-band images. As a pilot study, the Fundamental Plane analysis was first performed using only the K_s-band images from the NTT data. For consistency, the galaxy parameters (position, position angle and ellipticity) used in the IRAF task ELLIPSE for the IRSF J and K_s-band images were measured using GALFIT on the IRSF K_s-band images. These same parameters were adopted for the corresponding J-band images. In summary, the following steps were used to measure the total extrapolated magnitudes and effective radii used for the J and K_s-band Fundamental Plane analysis:

- Subtract foreground stars
- Derive the galaxy surface brightness profiles using the IRAF task ELLIPSE
- Fit the resultant surface brightness profiles using two Sérsic components
- Measure the total extrapolated magnitude by extrapolating the best fit (sum of the two Sérsic components) to infinity
- Use the measured total magnitude to determine the radius of the circle which encloses half the total light (through interpolation)

Figure 3.5 shows the fitted galaxy surface brightness profiles for WKK 6235 (top panels) and WKK 6402 (bottom panels). The left and right-hand panels represent the galaxy surface brightness profiles in the J- and K_s-bands, respectively. The arrows on the left and right-hand side of each plot represent the range of the radius and hence the data used to fit the galaxy surface brightness profile. This was selected in the same manner as for the NTT K_s-band photometric analysis. The inset in Figure 3.5 shows the residuals. Both the NTT and IRSF data are deeper than 2MASS (see e.g., Kato et al. 2007; Skrutskie et al. 2006) due to the longer exposure times for the IRSF and NTT observations (refer to Table 2.4 on page 45 for a summary of the telescope parameters – IRSF, NTT and 2MASS).

3.1.3 Total Extrapolated Magnitudes

The total luminosity, L, can be approximated by extrapolating the surface brightness profile to infinity. In this section, I derive and present the quantity dm which is the magnitude corresponding to the galaxy flux that would otherwise get lost in the sky background noise. For simplicity, I have ignored the ellipticity term[1], i.e.,

$$L = \int_0^\infty 2\pi r I(r)\,\mathrm{d}r. \tag{3.10}$$

Defining the gamma function as

$$\Gamma(n) = \int_0^\infty t^{n-1} e^{-t}\,\mathrm{d}t;$$

[1]For convenience, the factor $(1-e)$; where e is the galaxy ellipticity, has been left out since it does not affect the final expression for the magnitude correction, dm. The full expression should be: $L_{\mathrm{tot}} = \int_0^\infty 2\pi(1-e)rI(r)\mathrm{d}r$

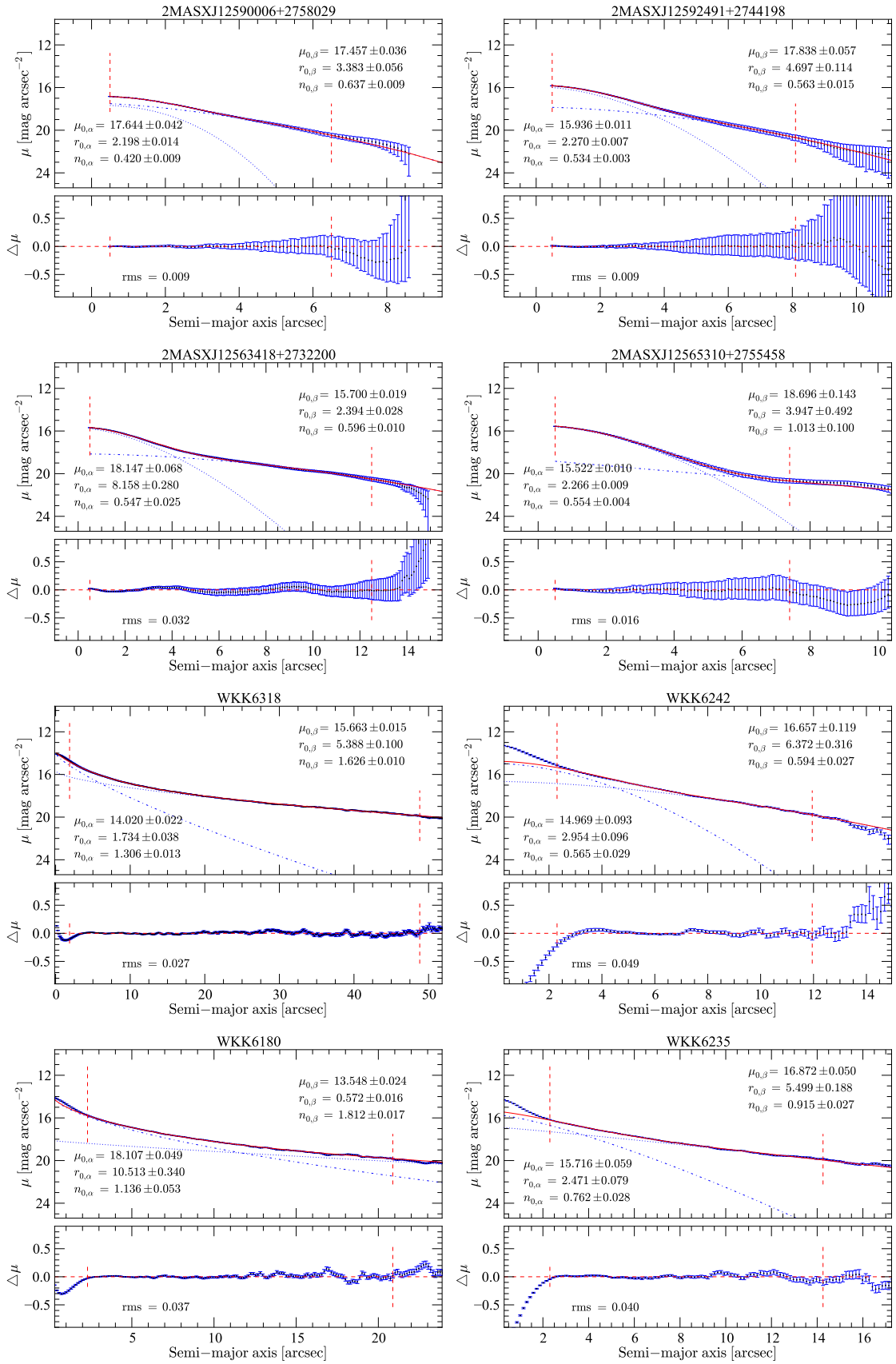

Fig. 3.4: Double Sérsic component fits to the galaxy surface brightness profiles for four Coma galaxies (top two left and right-hand panels) and four Norma galaxies (bottom two left and right-hand panels) in the K_s-band Fundamental Plane sample (from the NTT data for Norma). The dashed and dot-dashed blue lines represent the individual Sérsic components while the red solid line represents the combined fit. The small vertical dashed lines represent the range of the data points used to fit the galaxy surface brightness profiles.

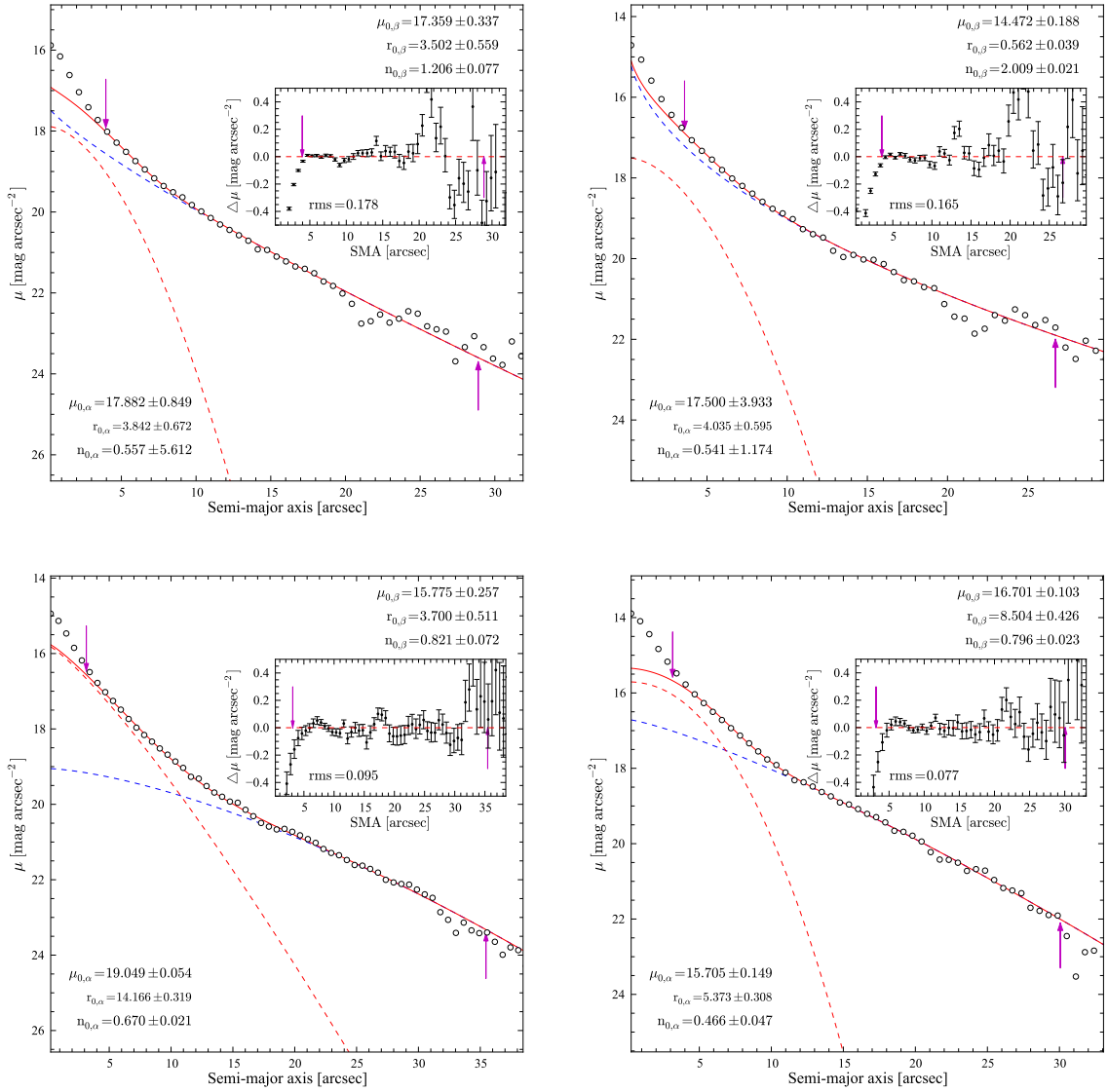

Fig. 3.5: Galaxy surface brightness profiles for the J-band (left-hand panels) and the K_s-band (right-hand panels). The top panels represent WKK 6235 while the bottom panels are for WKK 6402. The two small magenta arrows on the extreme left and right of each panel represent the range of the data used in fitting the galaxy surface brightness profile. The x-axis represents the semi-major axis, SMA. The two Sérsic components used to fit the galaxy profile are represented by the dashed lines (in red and blue). The red solid line represents the best fit, which is a combination of the two Sérsic components. The inset shows the residuals; the y-axis is the difference between the measured galaxy surface brightness (in mag arcsec^{-2}) and the galaxy surface brightness obtained from the best fit (double Sérsic components).

and setting $\int_0^\infty t^n\, e^{-t}\, \mathrm{d}t = F_n$, yields

$$\begin{aligned} n F_{n-1} &= F_n \\ (n-1) F_{n-2} &= F_{n-1}. \end{aligned}$$

Thus,

$$\begin{aligned}\int_0^\infty t^n e^{-t}\,\mathrm{d}t &= \prod(n) = n!;\ n \text{ a positive integer}\\ \Gamma(n+1) &= n!\\ \Gamma(n+1) &= n\,\Gamma(n);\end{aligned} \tag{3.11}$$

where $\prod(n)$ is the Pi–function. From Equations 3.4 and 3.10, the total integrated luminosity, L, is given by

$$\begin{aligned}L &= \int_0^\infty 2\pi r I_e \exp\left\{-b_n\left[\left(\frac{r}{r_e}\right)^{\frac{1}{n}}-1\right]\right\}\mathrm{d}r\\ &= 2\pi r I_e \exp(b_n)\int_0^\infty r\exp\left(-b_n\, {r_e}^{-1/n}\, r^{1/n}\right)\mathrm{d}r.\\ \text{Let: } a &= b_n\, {r_e}^{-1/n}\\ \text{and: } t &= a\, r^{1/n}\\ \Rightarrow L &= 2\pi I_e \exp(b_n)\int_0^\infty n\, a^{-2n}\, t^{2n-1} e^{-t}\,\mathrm{d}t\end{aligned}$$

$$\begin{aligned}L &= 2\pi I_e \exp(b_n)\, n\, a^{-2n}\int_0^\infty t^{2n-1} e^{-t}\,\mathrm{dt}\\ &= 2\pi I_e \exp(b_n)\, n\, a^{-2n}\,\Gamma(2n)\\ &= \frac{2\pi I_e\, e^{b_n}\, n\, r_e^2}{(b_n)^{2n}}\,\Gamma(2n) \qquad (3.12)\\ &= \frac{\pi I_e\, e^{b_n}\, r_e^2}{(b_n)^{2n}}\,\Gamma(2n+1). \qquad (3.13)\end{aligned}$$

Thus, the total luminosity integrated to infinity (L_{tot}) and the luminosity within a radius, $r_{\max}$ ($L_{r_{\max}}$) are given by:

$$L_{\mathrm{tot}} = \int_0^\infty 2\pi r I(r)\,\mathrm{d}r = \frac{2\pi I_e\, e^{b_n}\, n\, r_e^2}{(b_n)^{2n}}\,\Gamma(2n) \tag{3.14}$$

$$L_{r_{\max}} = \int_0^{r_{\max}} 2\pi r I(r)\,\mathrm{d}r = \frac{2\pi I_e\, e^{b_n}\, n\, r_e^2}{(b_n)^{2n}}\,\gamma\left[2n, b_n\left(\frac{r_{\max}}{r_e}\right)^{1/n}\right]. \tag{3.15}$$

$\Gamma(n) = \int_0^\infty t^n e^{-t}\,\mathrm{d}t$ is the complete gamma function, $\gamma(s,x) = \int_0^x t^{s-1}e^{-t}\,\mathrm{d}t$ is the lower incomplete gamma function, and $\Gamma(s,x) = \int_x^\infty t^{s-1}e^{-t}\,\mathrm{d}t = \Gamma(s) - \gamma(s,x)$ is the upper incomplete gamma function.

For the two Sérsic components, the combined total luminosity integrated to infinity ($L_{\rm tot}$) and the luminosity within a radius, $r_{\rm max}$ ($L_{r_{\rm max}}$) are given by:

$$\begin{aligned} L_{\rm tot} = {} & 2\pi I_{0,\alpha}\, n_\alpha \left(r_{0,\alpha}\right)^2 \Gamma(2n_\alpha) + \\ & 2\pi I_{0,\beta}\, n_\beta \left(r_{0,\beta}\right)^2 \Gamma(2n_\beta) \end{aligned} \tag{3.16}$$

$$\begin{aligned} L_{r_{\rm max}} = {} & 2\pi I_{0,\alpha}\, n_\alpha \left(r_{0,\alpha}\right)^2 \gamma\left[2n_\alpha, \left(\frac{r_{\rm max}}{r_{0,\alpha}}\right)^{1/n_\alpha}\right] + \\ & 2\pi I_{0,\beta}\, n_\beta \left(r_{0,\beta}\right)^2 \gamma\left[2n_\beta, \left(\frac{r_{\rm max}}{r_{0,\beta}}\right)^{1/n_\beta}\right]. \end{aligned} \tag{3.17}$$

The correction, which is subtracted from the magnitude measured within $r_{\rm max}$ is:

$$\mathrm{d}m = 2.5 \log\left[\frac{L_{\rm tot}}{L_{r_{\rm max}}}\right], \tag{3.18}$$

where $r_{\rm max}$ is the radius at which the galaxy counts fall to $1\sigma_s$ (σ_s is the standard deviation in the sky background). $r_{\rm max}$ therefore, corresponds to the maximum radius used to fit the galaxy surface brightness profile (the vertical dashed lines to the extreme right of Figures 3.4 and 3.5). Thus, the correction ($\mathrm{d}m$) corresponds to the flux that would otherwise be missed out due to the background noise in the outer parts of the galaxy profile, beyond $r_{\rm max}$.

3.1.4 Effective Radius and Effective Surface Brightness

As mentioned earlier, the effective radius is the radius of the circle which encloses half the total flux. A galaxy's effective radius can therefore be measured once the total magnitude is known. The effective surface brightness, I_e (in flux units) is related to both the effective radius, r_e, and the total luminosity, L, via:

$$\langle I_e \rangle = \frac{L/2}{\pi r_e^2} = \frac{L}{2\pi r_e^2}\,.$$

Using $m \propto -2.5 \log L$, results in

$$\langle \mu_e \rangle = m_{_{\rm tot}} + 2.5 \log(2\pi) + 5 \log(r_e)\,. \tag{3.19}$$

Hence, the mean effective surface brightness, $\langle \mu_e \rangle$, was calculated from the measured total extrapolated magnitude and the effective radius for each galaxy in the sample.

3.1.5 External Photometry Comparison: NTT and IRSF K_s-band Data

For consistency and internal checks regarding my photometric analysis, I compared the K_s-band total extrapolated magnitudes for 21 early-type galaxies which have both NTT/SOFI and IRSF/SIRIUS photometry. It was necessary to compare these two datasets before combining them for use in the final K_s-band Fundamental Plane analysis. The comparison shows a very good agreement between the two datasets with a median difference of 0.009 ± 0.022 mag. Figure 3.6 shows the photometry comparison, the red dashed lines in the upper panels represent a one-to-one relation while those in the lower sub-panels represent the median difference. The figure shows comparisons of the total extrapolated magnitudes (no corrections applied except the background and star-subtraction effects), the PSF-corrected effective radii ($\log r_e$) and the X-component ($X_{\rm FP} = \log r_e - 0.32\langle \mu_e \rangle$) of the Fundamental Plane. For a detailed analysis and description of the photometric corrections, see §3.2.

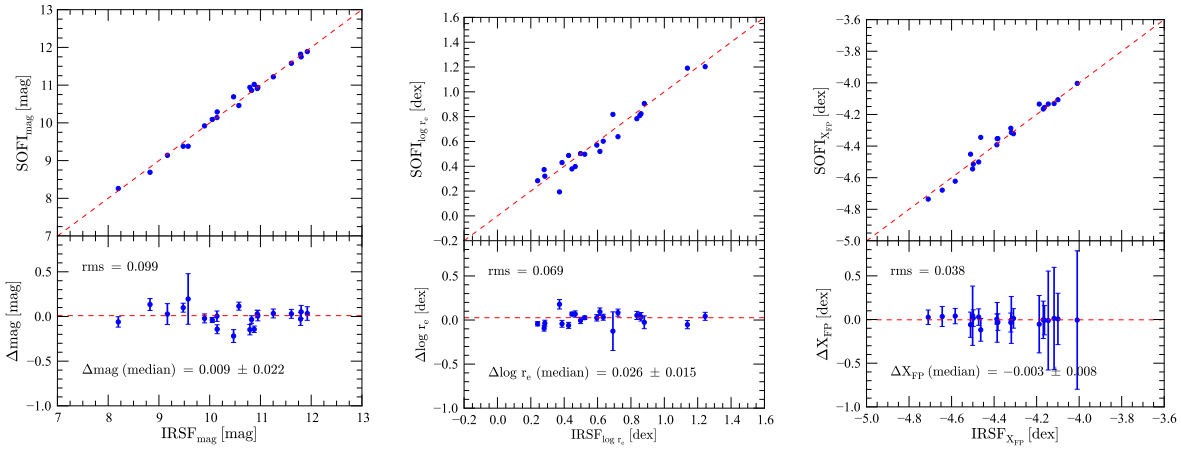

Fig. 3.6: Photometric comparison for the 21 Norma cluster early-type galaxies with near-infrared photometry from both the NTT and IRSF telescopes. The left-hand, middle and right-hand panels represent the comparisons of the total extrapolated magnitudes, $\log r_e$ and the X-component of the Fundamental Plane, respectively. The red dashed lines in the upper panels represent a one-to-one relation while the red dashed lines in the lower sub-panels represent the median difference. In all the three panels (left-hand, middle and right-hand panels), the rms and median difference (NTT – IRSF) are shown in the lower sub-panel.

3.2 Photometric Corrections

Various corrections must be applied to the measured photometric parameters (the effective radii and the mean effective surface brightnesses) before they, together with the central velocity dispersions, can be used in the Fundamental Plane. These include a seeing correction, correction for star-subtraction effects, Galactic extinction correction, k-correction, and cosmological dimming correction. A small correction due to the background effect was also applied. The small correction for the background effect was measured through simulations and was applied to correct for the effect on the measured total extrapolated magnitude resulting from small sky background variations across the galaxy/image field. For a summary of the various applied corrections and their magnitude (or size), see Table 3.5 on page 96.

3.2.1 Effect of Star-subtraction

To quantify the effect of star-subtraction on the measured photometric parameters, two methods were used. In the first approach (hereafter referred to as Method I), 12 early-type galaxies from the Centaurus cluster were used. In the second approach (hereafter Method II), IRSF images for the Norma cluster early-type galaxies in my Fundamental Plane sample were used.

3.2.1.1 Method I

This approach was used for the NTT data used in the K_s-band Fundamental Plane analysis. Here, a simulation was performed to quantify the effect of star-subtraction on the photometric results of the Norma sample by using 12 galaxies from the Centaurus cluster observed with the NTT (ESO Program 65.N-0242 (A), PI: Woudt). The choice of these galaxies is due to the fact that they lie at higher Galactic latitudes, hence the very low star-density makes them suitable for the simulation. In the simulation, stars from a typical, randomly chosen Norma field were superimposed on to the Centaurus galaxies and a photometric analysis was performed on the original image and the star-subtracted test image. Different star-fields that were used in the simulation were randomly selected from the Norma sample. Figure 3.7 shows the original Centaurus galaxy

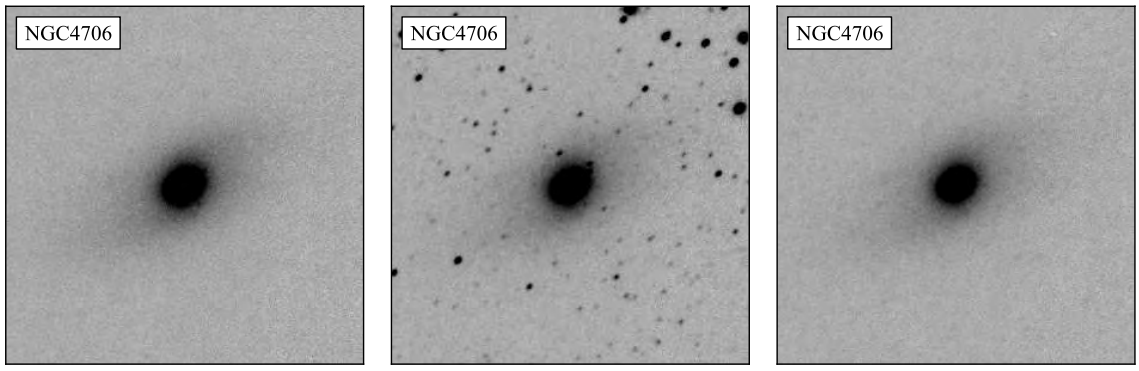

Fig. 3.7: NGC 4706, one of the 12 sample galaxies from the Centaurus cluster. The left-hand panel shows the original image before adding stars, the middle panel shows the original image superimposed with stars from a typical Norma field. The resultant star-subtracted image is shown in the right-hand panel. The images are of size $\sim 86'' \times 86''$.

image (left-hand panel) while the middle panel shows the original image superimposed with stars from a typical Norma field. The right-hand panel shows a star-subtracted image using the same star-subtraction algorithm that was used to subtract the foreground stars from the Norma galaxy images.

In Figure 3.8, I compared the photometry from the original and the star-subtracted test image. Aperture radii of 5, 7, 10, 15, and 20 arcsec were used to compare the aperture photometry. The difference in aperture magnitudes, $\triangle m$, is the aperture magnitude of the star-subtracted test image subtracted from the aperture magnitude of the corresponding original image (image before adding stars from a typical Norma field) – refer to Figure 3.8 for the star-subtraction effect for individual aperture radii of $5''$, $7''$, $10''$, $15''$, $20''$.

To estimate the mean correction to be applied to correct for the star-subtraction effect, the average difference per aperture radius was used. In other words, the difference in aperture magnitude for each aperture radius was averaged over all the 12 Centaurus galaxies used in the simulation. Figure 3.9 shows the difference in aperture magnitude averaged over all the 12 Centaurus galaxies; the red dashed line represents the mean difference ($\langle\widetilde{\triangle \mathrm{mag}}\rangle$), i.e., the correction which is -0.0106 ± 0.0003 mag. After correcting for the star-subtraction effect, the target galaxies are consistently brighter by 0.0106 mag. The simulation results show no trend with radius which may indicate that the process of star-subtraction slightly increases the measured sky value which in turn makes the galaxies look fainter than they really are.

3.2.1.2 Method II

In this alternative approach, the Norma cluster J- and K_s-band images (from the IRSF data) with and without star-subtraction were used. Using the star-subtracted images, galaxy models were created using GALFIT. To simulate the effect of star-subtraction, these galaxy models were added to the star fields around the Norma cluster where no star-subtraction had been performed. While adding the galaxy models, the positions occupied by any extended sources in the observed field were avoided. This implies that this method works best when a large size of the observed field is available ($\sim 7\farcm8 \times 7\farcm8$ for the IRSF J- and K_s-band images). The stars in the Norma field where the galaxy model was added were then subtracted. Aperture photometry was performed on the galaxy model before adding it to a starry Norma field and on the same model after subtracting the

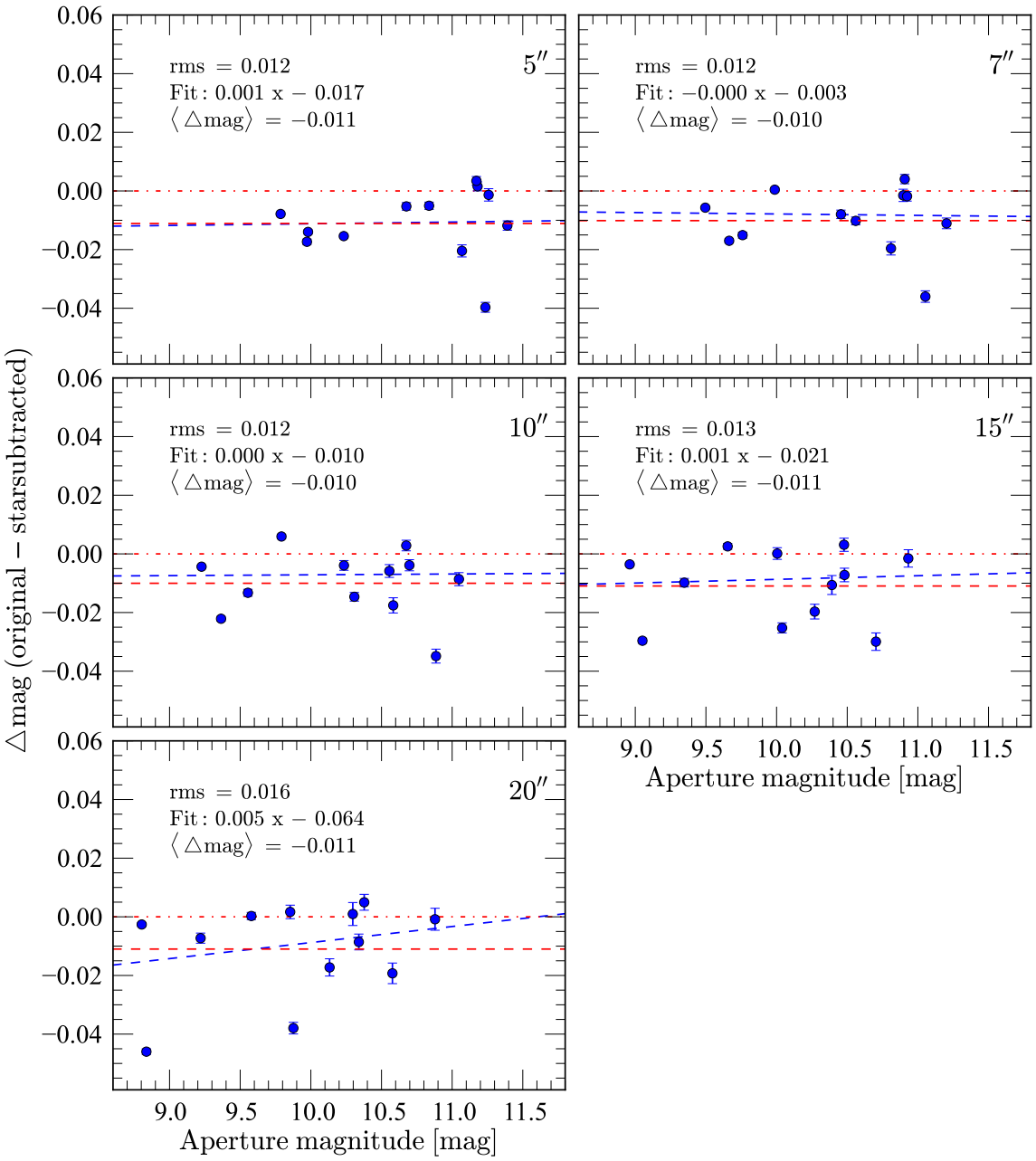

Fig. 3.8: The effect of star-subtraction, a comparison through aperture photometry. The y-axis is the difference in magnitude, i.e, the aperture magnitude measured on the star-subtracted test image was subtracted from the aperture magnitude measured from the corresponding original image. The x-axis is the aperture magnitude from the original galaxy (before adding stars). Top: left-hand panel is for an aperture radius of 5″, right-hand panel for 7″. Middle: left-hand panel is for an aperture radius of 10″, right-hand panel for 15″. The bottom left-hand panel corresponds to an aperture radius of 20″. The blue and red dashed lines represent the best least-squares fit and the mean difference, respectively. The average rms is 0.012 mag using linear fits and 0.013 mag for the constant offsets. Thus, the linear fits do not significantly improve the goodness of fit relative to a constant offset and average offsets were therefore used.

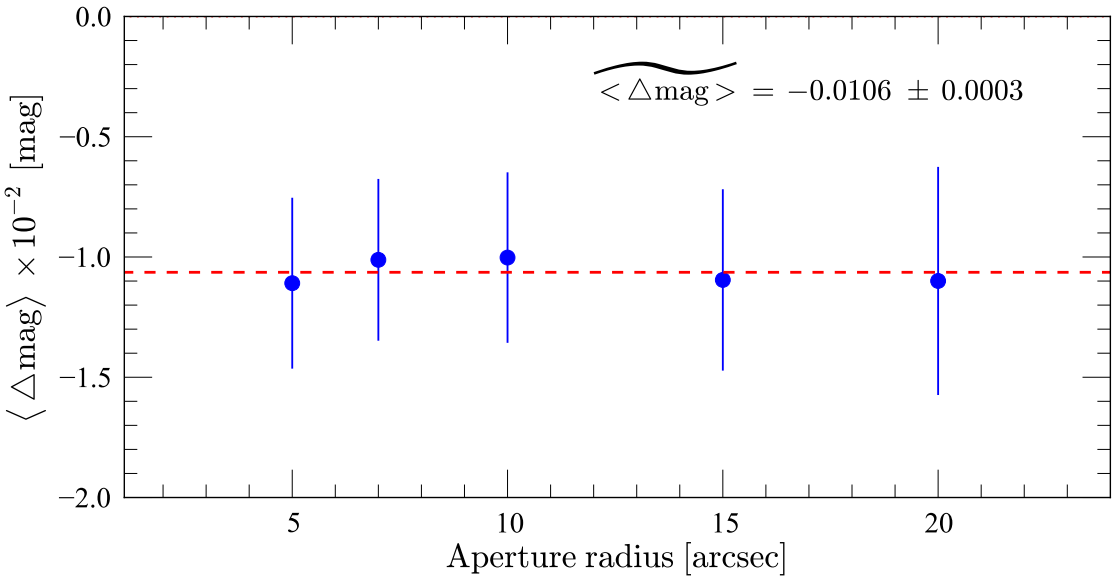

Fig. 3.9: Comparison of the average difference in aperture magnitudes for a given aperture radius for the 12 galaxies from the Centaurus cluster, plotted against the aperture radius to determine the average overall correction to be applied for the effect of star-subtraction. The red dashed line represents the mean value (-0.0106 ± 0.0003 mag). The rms is 0.0005 mag.

stars in the star field where the model was added. Aperture radii of 3, 5, 7, 10, 12 and 15 arcsec were used. Below is the summary of the steps followed:

1. Use GALFIT to create models of the IRSF/SIRIUS J and K_s-band images. These galaxy models were created using the star-subtracted galaxy fields
2. Perform aperture photometry on the galaxy models
3. Add the model to the original fully reduced IRSF/SIRIUS data image, i.e., the original galaxy field where no star-subtraction has been performed
4. Subtract the foreground stars
5. Measure aperture magnitudes after star-subtraction
6. Compare the aperture magnitudes in steps 2 and 5

Figure 3.10 shows the results of the star-subtraction simulation. These values were obtained by averaging the differences in each aperture radius. The measured mean value which was later applied to correct for the effect of star-subtraction is -0.0143 mag and -0.0135 mag in the J and K_s-band, respectively.

The two methods (Method I and Method II) give comparable results, that is, the final average correction applied to the measured K_s-band total extrapolated magnitudes is -0.0106 ± 0.0003 mag (Method I) versus -0.0135 ± 0.0003 mag (Method II) — see Figures 3.9 and 3.10 for the K_s-band. The star-subtraction effect is a small but systematic offset, consistently making the target galaxies fainter by ~ 0.01 mag. The effect is such that the target galaxies become brighter after applying the correction. This systematic effect due to star-subtraction seems to originate from systematic differences in the sky background determined before and after star-subtraction.

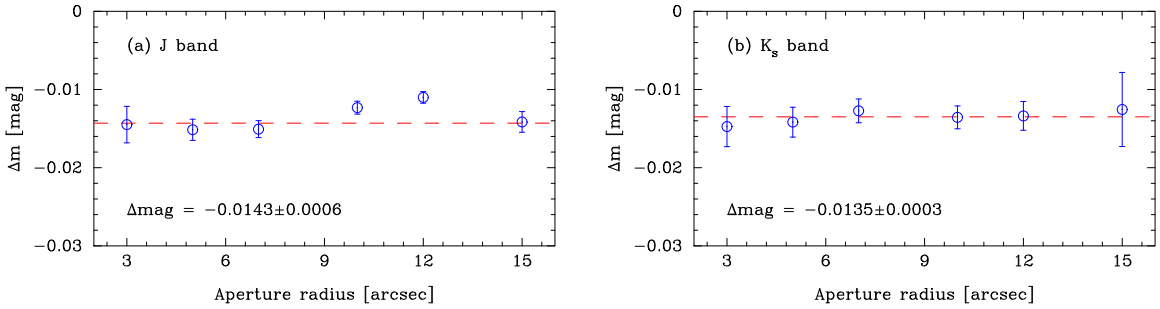

Fig. 3.10: The effect of star-subtraction through aperture photometry for the J-band (left-hand panel) and the K_s-band (right-hand panel). The y-axis is the average difference in aperture magnitude for each aperture radius. The x-axis is the aperture radius used. The overall correction is represented by the red dashed lines. The rms is 0.0015 mag in the $J-band$ and 0.0008 mag for the K_s-band.

3.2.2 *Effect of Galactic Extinction on Effective Radius (using the NTT Data)*

Gas and dust within the Milky Way absorb extragalactic light and this results in galaxies appearing fainter than they really are. A simulation was conducted to determine the effect of Galactic extinction on the measured effective radius. The same sample of 12 galaxies from the Centaurus cluster was used. Extinction values in the range of $\triangle\text{mag} = 0 \rightarrow 2.8$ mag were applied to the Centaurus galaxies. The zero mag in this range therefore, corresponds to the original Centaurus galaxy, i.e., no extinction. The extinction factor is given as $\frac{f_1}{f_2} = 10^{-\triangle m/2.5}$, that is,

$$A_{K_s} = m_1 - m_2 = -2.5 \log \frac{f_1}{f_2}. \tag{3.20}$$

The extinction factor applied to the 12 Centaurus galaxies is such that the effect of sky-subtraction is minimised. This was done by estimating the sky and subtracting it from the image before introducing the extinction factor (extinction factor multiplied by the image) after which the sky was added back. The multiplication factor varies according to the value of extinction used, that is, the different values of $A_{K_s} = \triangle\text{mag}$; where $A_{K_s} = m_1 - m_2$ and f_1, f_2 correspond to the flux associated with m_1 and m_2, respectively. Figure 3.11 shows the results of the simulation for two of the 12 Centaurus galaxies. The y-axis shows the difference between the measured effective radius when there is no extinction ($A_{K_s} = 0$) and the measured effective radius in the presence of extinction (the K_s-band extinction values are shown on the x-axis of the left-hand panel). The simulation results show no significant effect of the Galactic extinction on the measured effective radius for small values of A_{K_s} for all the 12 sample galaxies from the Centaurus cluster. Note that, for the Norma cluster sample, $A_{K_s} < 0.15$ mag while the average value is $A_{K_s} \approx 0.003$ mag for the Coma cluster sample. The effect of Galactic extinction on the measured effective radius is therefore negligibly small in the near-infrared. This quantifies one of the reasons why the J and K_s-bands where the Galactic extinction is relatively small are preferred compared to optical bands – the Galactic extinction is much larger in the optical and this would therefore lead to significant bias in the measured effective radii.

3.2.3 *Redshift Effects: k-correction*

For a galaxy emitting radiation at a wavelength, λ_e, in its rest frame, the combined effects of its motion and the expansion of the Universe will lead to an observed wavelength, λ_o, that is usually shifted to longer values. This redshift, z, is calculated through the simple relation

$$z = \frac{\lambda_o - \lambda_e}{\lambda_e}. \tag{3.21}$$

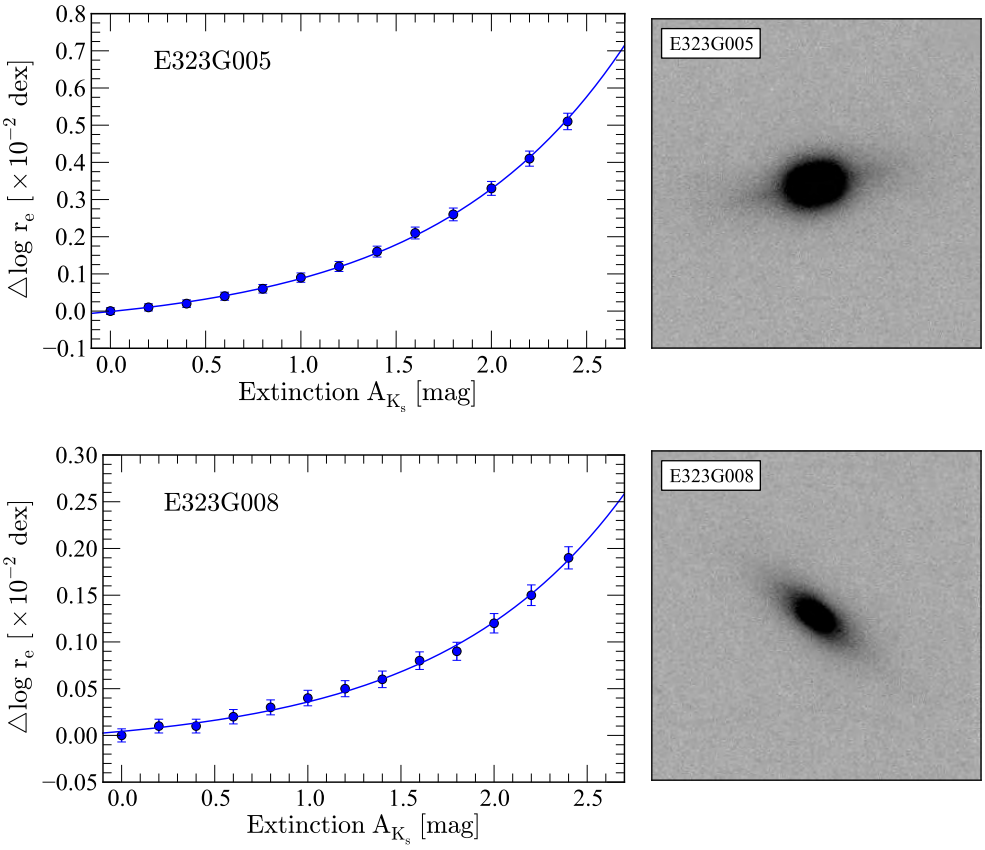

Fig. 3.11: The extinction effect on the effective radius. The left-hand panel shows the result of the simulation while the right-hand panel shows the galaxy image (size $\sim 86'' \times 86''$). The y-axis (on the left-hand panels) is the difference in the effective radius, Δr_e. This difference (Δr_e) is the effective radius measured from the original image subtracted from the effective radius measured using the corresponding image after applying the extinction values shown on the x-axis.

Due to the expansion of the Universe, the observed wavelengths differ from the rest-frame wavelengths (Humason et al., 1956; Oke & Sandage, 1968). A redshift implies that the wavelength in the galaxy's rest frame is shifted to longer wavelength at the time when it is observed. The process of transforming between the observed and rest-frame frequencies is called k-correction. Oke & Sandage (1968) define the k-correction as

$$k_\lambda = 2.5\log(1+z) + 2.5\log\left\{\frac{\int_0^\infty F(\lambda_o)S_\lambda(\lambda)d\lambda}{\int_0^\infty F\left(\frac{\lambda_o}{(1+z)}\right)S_\lambda(\lambda)d\lambda}\right\}, \tag{3.22}$$

where, S_λ is the transmission function of the instrument, k_λ (in magnitudes) is the k-correction in a given band/filter (see also Poggianti 1997). The denominator for the second term in Equation 3.22 is due to the shift in wavelength (i.e., $\lambda_e = \lambda_o(1+z)^{-1}$) due to redshift. The k-correction is therefore the difference in the observed magnitude taken at the emitted wavelength, λ_e, and the observed wavelength, λ_o.

Since the k-correction is a function of redshift (and also varies between filters), the correction plays a significant role for high redshift galaxies. Various redshift corrections exist, for example, Bell et al. (2003); Blanton & Roweis (2007); Chilingarian et al. (2010). For the NTT

K_s-band photometry, I adopted a k-correction from Pahre (1999), which is given by:

$$k_{K_s} = 21.9\,z^2 - 3.83\,z. \tag{3.23}$$

In the nearby universe (at low redshifts), the different k-correction methods do not differ significantly. For example, the mean difference between the k-correction by (Bell et al., 2003) and (Pahre, 1999) is 0.02 mag and 0.03 mag for the Norma and Coma samples, respectively. Note that, the distance to the Norma cluster was measured relative to the Coma cluster. Thus, the magnitude difference due to different k-correction techniques will affect both the Norma and Coma galaxies resulting in a reduced effect on the measured distance as compared to, for example, an equal magnitude difference due to star-subtraction effect on the Norma sample.

The k-corrections applied in the near-infrared J- and K_s-band Fundamental Plane analysis for the IRSF data are from Glass (1999). These are given by:

$$k_J = 0.7\,z; \tag{3.24}$$

$$k_{K_s} = -3.3\,z. \tag{3.25}$$

The k-corrections by Glass (1999) were adopted for consistency in the J and K_s-band photometry since the previously-used correction by Pahre (1999) only applied to the K_s band and not the J-band. The difference between the K_s-band k-correction by Pahre (1999) and Glass (1999) is very small, that is, a mean difference of ~ 0.0028 mag and ~ 0.0001 mag for the Norma and Coma galaxy samples, respectively. While combining the IRSF/SIRIUS and the NTT/SOFI K_s-band data, the k-corrections were normalised to be the same in both datasets before the final combined K_s-band Fundamental Plane analysis. The k-correction applied to the combined K_s-band Fundamental Plane sample was adopted from Glass (1999) and is given by Equation 3.25.

3.2.4 Galactic Extinction Corrections: Schlafly & Finkbeiner Versus Schlegel et al.

Since the Norma cluster is located in the Zone of Avoidance, it is of particular importance to correct for Galactic extinction. Typically, this has been corrected for using the DIRBE/IRAS reddening maps of Schlegel et al. (1998). It has been found however, that the NIR reddening maps by Schlegel et al. (1998), over-estimate the extinction at low Galactic latitudes where they are uncalibrated — see e.g., Bonifacio et al. (2000), Schröder et al. (2007) and Yasuda et al. (2007).

To correct for the Galactic extinction for the NTT K_s-band total extrapolated magnitudes, the new Galactic extinction corrections from Schlafly & Finkbeiner (2011), which is a modification of the Schlegel et al. (1998) maps, were applied. These are $\sim 14\%$ less than the extinction values from the original Schlegel et al. values, that is, Schlafly & Finkbeiner (2011) measured an extinction correction factor of ~ 0.86. The Galactic extinction values in the Landolt B filter were obtained through the NASA/IPAC Extragalactic Database (NED) queries[2] and converted to the near-infrared K_s-band using $A_{K_s} = 0.085\,A_B$ (Pahre, 1999). The differences between the applied corrections (Schlafly & Finkbeiner, 2011) and those of Schlegel et al. (1998), Bonifacio et al. (2000) and Schröder et al. (2007) are -0.0110 mag, 0.0041 mag and 0.0007 mag, respectively.

3.2.5 Extinction and NIR *Colours:* IRSF *J and K_s-band Data*

Since the Schlegel et al. (1998) NIR reddening maps have been found to over-estimate the Galactic extinction especially at low Galactic latitudes, a re-calibration of the NIR reddening

[2]The NASA/IPAC Extragalactic Database (NED) is operated by the Jet Propulsion Laboratory, California Institute of Technology, under contract with the National Aeronautics and Space Administration.

maps based on the $J-K_s$ colour for the Norma and Coma galaxies is presented here. This closely follows the re-calibration done by Schröder et al. (2007) and more recent Galactic extinction corrections by Schlafly & Finkbeiner (2011). The re-calibration is especially appropriate for the Norma region. The Galactic extinction effect on the Coma sample is very small (mean ~ 0.003 mag in the K_s-band). Schröder et al. (2007) obtained an extinction correction factor of 0.87. Their work focussed on the region around the highly obscured bright radio galaxy PKS 1343 – 601 which lies at very low Galactic latitudes at $(\ell, b) = (309.^{\circ}7, +1.^{\circ}8)$. Their result implies that the NIR reddening maps (Schlegel et al., 1998) over-estimate the extinction by $\sim 13\%$. This is in good agreement with Schlafly & Finkbeiner (2011) who found an extinction correction factor of ~ 0.86.

In view of the above, the extinction correction for the Norma cluster sample using the NIR $J-K_s$ colour has been investigated. The challenge is that this sample covers a very small range of extinction values (see the left-hand panel of Figure 3.28). The extinction in the J and K_s bands, assuming the Fitzpatrick (1999) reddening law, with $R_{\rm v} = 3.1$ is given by

$$A_J = 0.937E(B-V) \tag{3.26}$$

$$A_{K_s} = 0.382E(B-V). \tag{3.27}$$

The k- and extinction-corrected $(J-K_s)$ colour is thus given by

$$(J-K_s)^o = (J-K_s) - 0.555E(B-V) + 4.0z, \tag{3.28}$$

where, $(J-K_s)$ is the measured NIR colour with no corrections applied while $(J-K_s)^o$ is the NIR colour, corrected for both redshift (k-correction) and Galactic extinction effects. To minimise any systematic effects which may arise from galaxy surface brightness profile fitting, PSF-corrected J and K_s-band magnitudes measured within an aperture radius of $5''$ were used. Equation 3.28 can be expressed in the form

$$C^o = aA_{K_s} + b\,; \tag{3.29}$$

where A_{K_s} is the extinction in the K_s-band, a and b are parameters which were measured through simple least-squares regression. The reddening equation is given by

$$C = C^o + \left(\frac{E}{A_{K_s}}\right) A_{K_s}. \tag{3.30}$$

The true extinction-corrected colour denoted by $\widetilde{C^o}$ is therefore given by

$$\widetilde{C^o} = C - \left(\frac{\widetilde{E}}{A_{K_s}}\right) \widetilde{A}_{K_s}. \tag{3.31}$$

Using Equations 3.29 and 3.30 in Equation 3.31 results in

$$\widetilde{C^o} = \left(A_{K_s} - \widetilde{A}_{K_s}\right)\left(\frac{E}{A_{K_s}}\right) + aA_{K_s} + b. \tag{3.32}$$

Since $\widetilde{C^o}$ is not independent of A_{K_s}, then $\widetilde{A}_{K_s} = f\,A_{K_s}$, which implies:

$$\widetilde{C^o} = \left[a + (1-f)\left(\frac{E}{A_{K_s}}\right)\right] A_{K_s} + b. \tag{3.33}$$

For the true extinction-corrected colour to be independent of A_{K_s}, the slope in Equation 3.33 must be zero. This then implies that,

$$f = 1 + a\left(\frac{E}{A_{K_s}}\right)^{-1}. \tag{3.34}$$

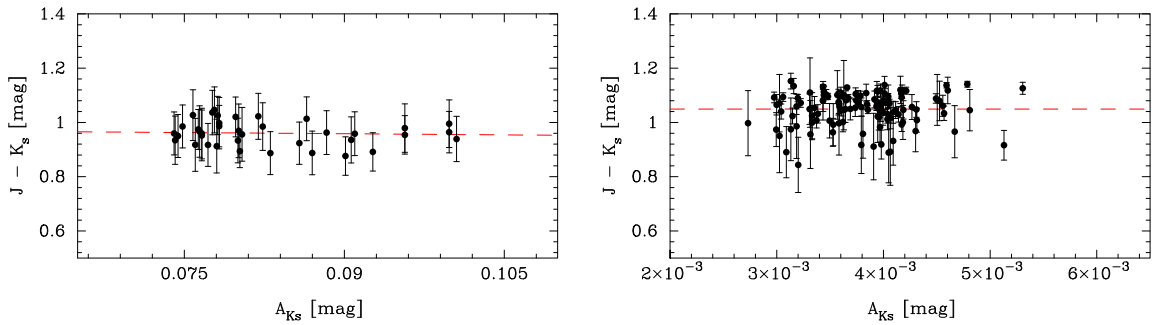

Fig. 3.12: Measuring the extinction correction factor using the $J-K_s$ colour for the Norma (left-hand panel) and the Coma (right-hand panel) samples. The y-axis is the $J-K_s$ colour which has been corrected for Galactic extinction and k-correction effects as given in Equation 3.28. For the Norma cluster, the effect from star-subtraction was applied (the net effect on the $J-K_s$ colour is very small, ~ 0.008 mag).

The extinction correction factor was computed by using a simple linear least-squares fit using Equations 3.28 and 3.29 so as to determine the slope, a, which is then used to compute the extinction correction factor by applying Equation 3.34. Figure 3.12 shows the fit to the Norma sample (left-hand panel) and Coma sample (right-hand panel). The red dashed lines represent the best fit to the data. From the fit parameter a, the extinction correction factor using the Norma and Coma samples is 0.81 ± 0.06 and 0.93 ± 0.05, respectively. The results are summarised in Table 3.1. The $\langle J-K_s\rangle$ and σ_{J-K_s} values quoted in this table were measured from the near-infrared $J-K_s$ colour, corrected for the extinction effect by applying the measured extinction correction factor shown in column 4. These are the expected near-infrared $(J-K_s)$ values for typical early-type galaxies (Jarrett, 2000; Jarrett et al., 2003).

Tab. 3.1: Re-calibrating the NIR reddening maps for the extinction values using the $J-K_s$ colour for the early-type galaxies in the Norma and Coma cluster samples. PSF-corrected aperture magnitudes measured within an aperture radius of $5''$ were used. These were used in the Galactic extinction corrections for the J and K_s-band Fundamental Plane analysis using the IRSF data and also in the final K_s-band Fundamental Plane analysis.

	a	b	f	N	σ	$\langle J-K_s\rangle$	σ_{J-K_s}
Norma	-0.283 ± 0.087	0.984 ± 0.037	0.81 ± 0.06	38	0.05	0.98	0.04
Coma	-0.096 ± 0.056	1.050 ± 0.067	0.93 ± 0.05	118	0.06	1.05	0.06

3.2.6 Seeing Corrections

To correct for the seeing (PSF) effects, the GALFIT algorithm was used with and without a PSF convolution to measure the difference in the obtained effective radius. This same approach was used in the 6dFGS Fundamental Plane study (Magoulas et al., 2012; Campbell et al., 2014). From the GALFIT output model images (with and without PSF), the effective radius was measured through interpolation. The difference between the effective radius measured from the GALFIT model with and without PSF convolution is the seeing correction (denoted by Δr). This implies that,

$$\Delta r = r_{\rm e,psf} - r_{\rm e,o}, \tag{3.35}$$

where $r_{\rm e,psf}$ and $r_{\rm e,o}$ are the effective radii measured from the GALFIT model with and without using a PSF image, respectively. To apply the seeing correction, Δr was subtracted from the effective radius measured from the star-subtracted galaxy image as described under §3.1.4. That is,

$$r_{\rm e,corr} = r_{\rm e,m} - \Delta r, \tag{3.36}$$

where $r_{\rm e,m}$ is the effective radius which corresponds to the measured total extrapolated magnitude, that is, the radius of the circle within which half the total flux is contained. Note that, $r_{\rm e,m}$ was measured from the original galaxy image and not the GALFIT model. $r_{\rm e,corr}$ is the seeing or PSF-corrected effective radius that finally enters the Fundamental Plane.

Figure 3.13 shows the seeing effects as measured using GALFIT on the Coma cluster 2MASS Atlas images (for the K_s-band). The top panel shows the seeing correction (y-axis) plotted against the measured effective radius. J. Lucey (Priv. Com.) measured the PSF-corrected effective radius for the Coma cluster galaxies based on the 2MASS total extrapolated magnitudes as given in the 2MASS Extended Source Catalogue (2MASS XSC; Jarrett et al., 2000; Skrutskie et al., 2006). The measurements based on my ELLIPSE fitting are represented by "ELLIPSE" (e.g., ELLIPSE $\log r_e$) while those adopted from the 2MASS Extended Source Catalogue (J. Lucey) are represented by "2MASS" (e.g., 2MASS $\log r_e$). The difference (on the y-axis of each sub-panel) is represented by 2MASS – ELLIPSE. Also shown in Figure 3.13 are: the comparisons between the effective radius (middle left and right-hand panels) and the mean effective surface brightness (bottom left and right-hand panels). The left-hand panels (middle and bottom) show the comparison before I applied the seeing correction to my measurements while the right-hand panels (middle and bottom) show the comparison after the PSF-corrections were applied. There is a significant effect of the PSF-correction, especially for the relatively small galaxies. It is therefore important to measure and correct for the seeing effects before fitting the Fundamental Plane to minimise possible bias in the fit parameters.

3.2.7 Cosmological Dimming Correction

The cosmological dimming correction is necessary due to the fact that light from a distant galaxy is distributed over ever increasing area, as it travels through space. The expansion of the universe therefore results in a dimming effect on the measured galaxy surface brightness. This was corrected for using the $(1+z)^4$ term, that is, the cosmological dimming correction is $-10\log(1+z)$. The average cosmological dimming corrections are ~ 0.07 mag arcsec^{-2} and ~ 0.10 mag arcsec^{-2} for the Norma and Coma clusters, respectively.

3.2.8 Measurement Errors and Analysis

The three photometric parameters: total extrapolated magnitude, effective radius and the mean effective surface brightness are correlated. This implies that the errors on the total extrapolated magnitude and the effective radius (and hence $\langle\mu_e\rangle$) are also correlated.

3.2.8.1 The Coma Cluster Sample

The measurement errors on the total magnitude for the Coma cluster galaxies were determined following the description given in the 2MASS All-Sky Data Release Explanatory Supplement[3]. The error on the total magnitude was calculated using:

$$\triangle\,\mathrm{mag} = 1.087\,\frac{\left[(S/g_{\rm av}) + n\,(2k\sigma_s)^2 + (0.024n\sigma_s)^2\right]^{1/2}}{S}. \tag{3.37}$$

$g_{\rm av} = G \times N$ where $G = 10$ is the gain, $N = 6$ is the total number of co-added frames, S is the total flux, $k \approx 1.7$ is the kernel smoothing factor, σ_s is the co-added noise, and n is the total number of pixels within an aperture. The aperture size was set to four times the effective radius, so that the aperture magnitude within that radius would be a good approximation of the galaxy's total

[3] http://www.ipac.caltech.edu/2mass/releases/allsky/doc/sec6_8a.html

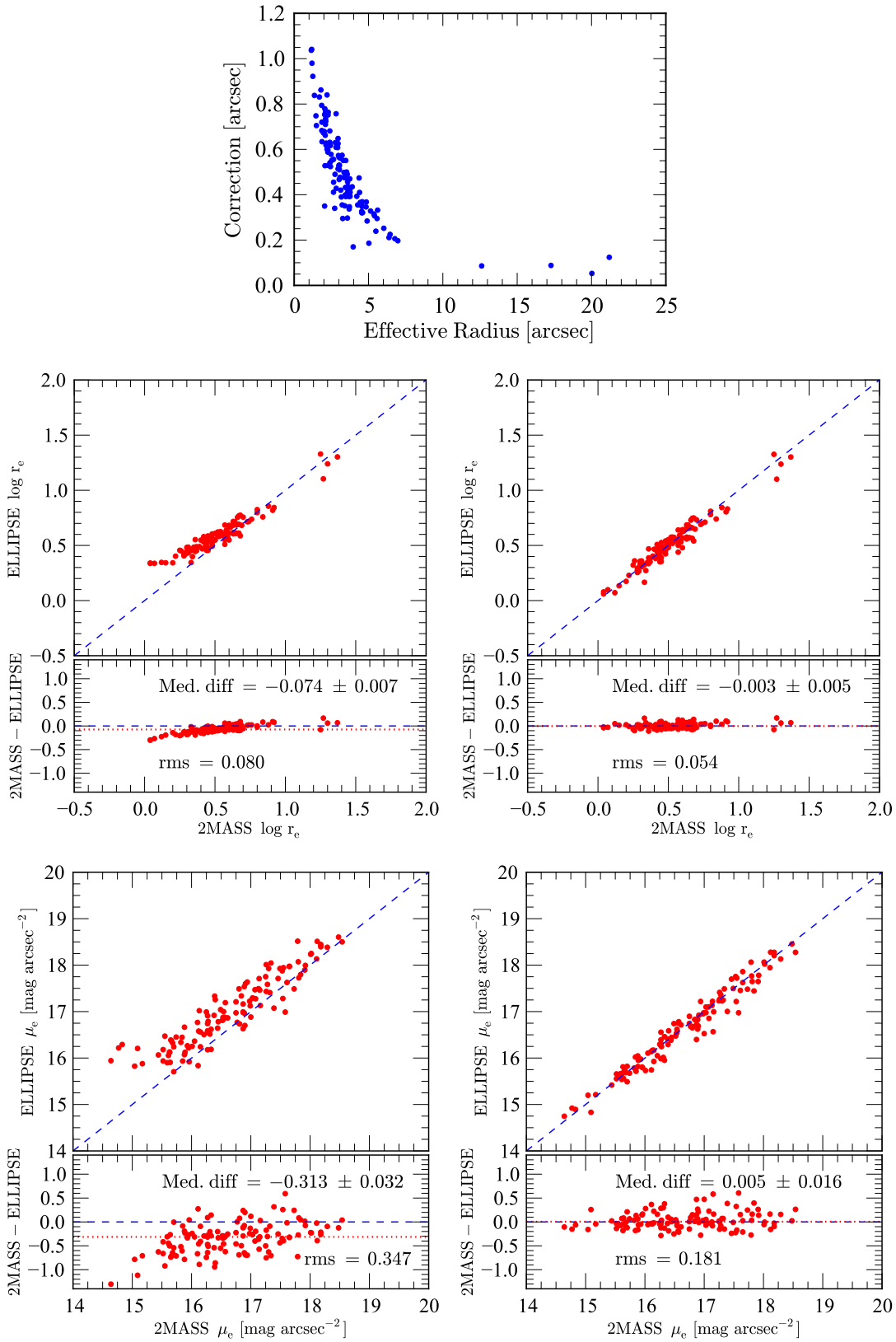

Fig. 3.13: Effect of seeing. The top panel shows the seeing correction (y-axis) plotted against the PSF-corrected effective radius (x-axis). Clearly, the effect of seeing is more significant for relatively small size galaxies (see the top panel). The middle and bottom panels represent $\log r_e$ and the mean effective surface brightness, $\langle \mu_e \rangle$ with (right-hand panels) and without (left-hand panels) the seeing correction. The blue dashed lines are a one-to-one relation and not a best fit to the data.

extrapolated magnitude.

Figure 3.14 is a comparison of the errors on the total extrapolated magnitude from the 2MASS XSC (for the Coma cluster sample), with the measured errors in this work. The difference in the measured errors is due to the differences in the sky background noise (σ_s). The sky background in this work was iteratively measured within an annulus, using 2σ-clipping resulting in a standard deviation in the sky which was usually lower than that of the 2MASS XSC. Note that the 2MASS XSC was used to compare with my measurements for the Coma sample. The Fundamental Plane analysis therefore uses my own measurements for both the Norma and Coma samples and not the data taken from the 2MASS XSC.

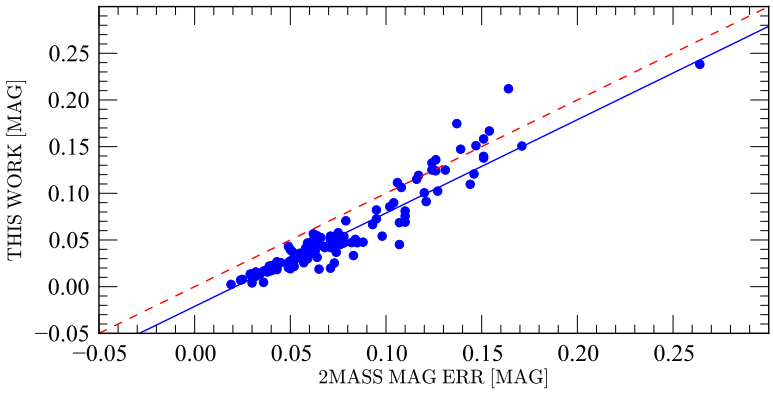

Fig. 3.14: Comparison between 2MASS XSC errors on the total magnitude for the Coma cluster sample, with the photometric errors in this work. The red dashed line is a one-to-one relation. There is a median difference of $\sim 0\overset{\mathrm{m}}{.}02$ with the 2MASS XSC errors being larger. The blue solid line represents the one-to-one relation corrected for the offset equal to the median difference (i.e., ~ 0.02 mag).

3.2.8.2 The Norma Cluster Sample

For the Norma cluster sample, measurement errors were estimated using galaxy models created using GALFIT. Input parameters (i.e., the total magnitude, the effective radius along the semi-major axis, the axial ratio, the position angle, and the Sérsic index) the same as the parameters measured from the Norma cluster galaxy images were used to create the galaxy models. Mock images were then created by adding the galaxy models to various positions across the original star-subtracted galaxy fields. Each of the galaxy models was first convolved with the PSF image for the respective galaxy field. The centres or the positions of the original observed galaxies were avoided. A total of 1103 mock images were created, with a minimum of 30 mock images per galaxy field.

Figure 3.15 shows a comparison of the input parameters and the recovered parameters after performing photometry on the PSF-convolved images. The left and right-hand panels show the difference in the magnitude and effective radius, respectively. In both panels, the y-axis represents the output subtracted from the input parameter. This was performed as a check before photometric analysis on all the mock images.

Photometry was then performed on each of the added model galaxies and the output was compared with the input GALFIT parameters. Figure 3.16 shows some of the results from the simulation, for the individual galaxies (distribution of the difference in the total magnitude) while Figure 3.17 shows the simulation results for all the 31 galaxy fields combined, i.e., the

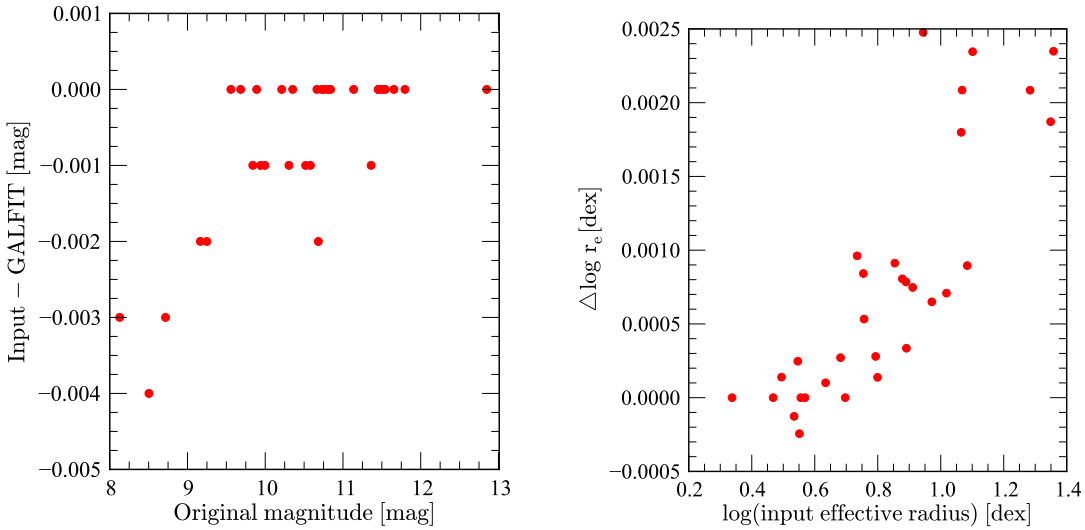

Fig. 3.15: Comparison of the difference between the real and simulated data for the NTT K_s-band GALFIT models and the mock images convolved with the respective PSF model. The left-hand panel is for the total magnitude while the right-hand panel shows the comparison of the effective radius. The y-axis is the measurement from the PSF-convolved model subtracted from the original GALFIT model input parameter.

distribution over all the 1103 simulated images. The difference between the simulated and true magnitude is negligible, with a median difference of −0.008 mag, and rms of $0\overset{\mathrm{m}}{.}039$. This indicates that the photometry is not affected by sky gradients or faint unresolved stars in the field. Note that, the statistics were conducted through an iterative procedure involving σ-clipping (robust statistics). These quoted values were computed from the resulting 1076 out of the 1103 data points, after the iterative procedure. These 1076 data points (98%) lie within the two small vertical red solid lines. By using the median value for each individual galaxy field shown in Figure 3.16, the measurement error on the total magnitude for the 31 galaxy fields is $\sim 0\overset{\mathrm{m}}{.}02 \pm 0\overset{\mathrm{m}}{.}01$.

In addition, the error on the magnitude measured within an aperture whose size is four times the measured effective radius (taking into consideration the photometric zero point error as well) was estimated. The total error on the total extrapolated magnitude is the quadrature sum of the error obtained through the simulation and the aperture photometry error within the $4r_e$ aperture radii. For both Norma and Coma sample galaxies, the error in effective radii were measured based on the measured error in the total magnitude. A simple standard propagation of errors was applied to compute the error in the mean effective surface brightnesses by combining the error on the effective radii, δr_e, and total extrapolated magnitudes, δm, using

$$\delta\langle\mu_e\rangle = \left[\left(\frac{5\delta r_e}{r_e \ln(10)}\right)^2 + (\delta m)^2\right]^{\frac{1}{2}}. \tag{3.38}$$

Equation 3.38 assumes insignificant error contribution from the galaxy's redshift, Galactic extinction and k-corrections, that is, the error is dominated by the measurement errors associated with the total extrapolated magnitudes and effective radii.

3.3 Coma Cluster Photometry Comparison

The photometric analysis for the Coma sample was performed on 2MASS Atlas images using the same method as for the Norma cluster. I therefore similarly used the IRAF task ELLIPSE to

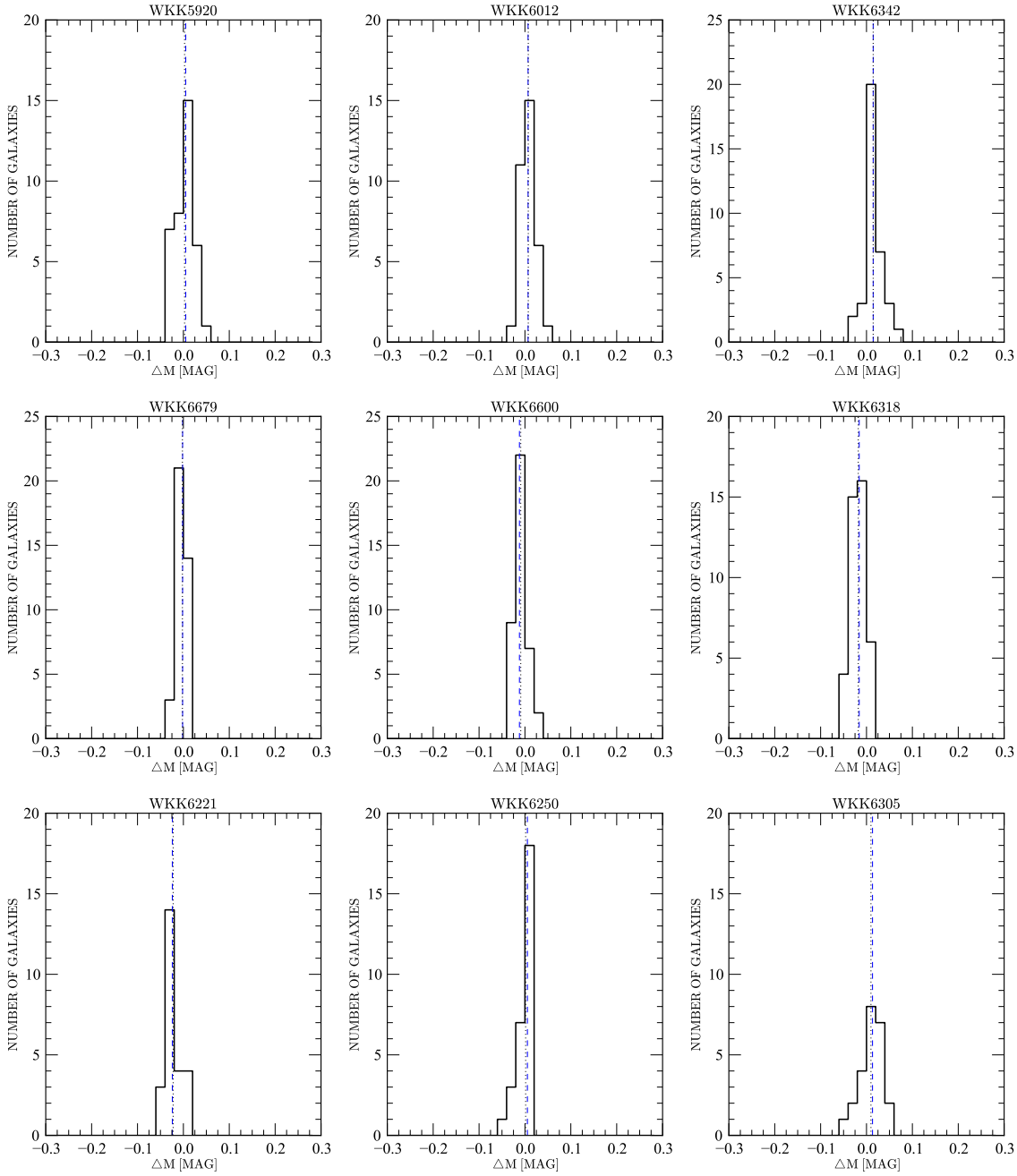

Fig. 3.16: GALFIT output for individual galaxy simulations, showing the distribution of the difference between the original total magnitude (observed data) and the simulated data, for some of the individual galaxy fields in the simulated sample.

derive and fit galaxy surface brightness profiles of the 2MASS Coma early-type galaxies in the Fundamental Plane sample. Like the Norma sample, two Sérsic functions were used to fit the galaxy surface brightness profiles. The total extrapolated magnitude (and thereafter the effective radius) was determined through extrapolating the best fit to infinity and applying interpolation to accurately measure the radius of the circle containing half the total flux. Figure 3.18 shows a comparison between my measurements and the 2MASS total extrapolated magnitudes. The circular effective radii that I have compared with, were provided by J. Lucey (Priv. Com.) and these were measured such that half the total flux is contained within r_e, where the total flux

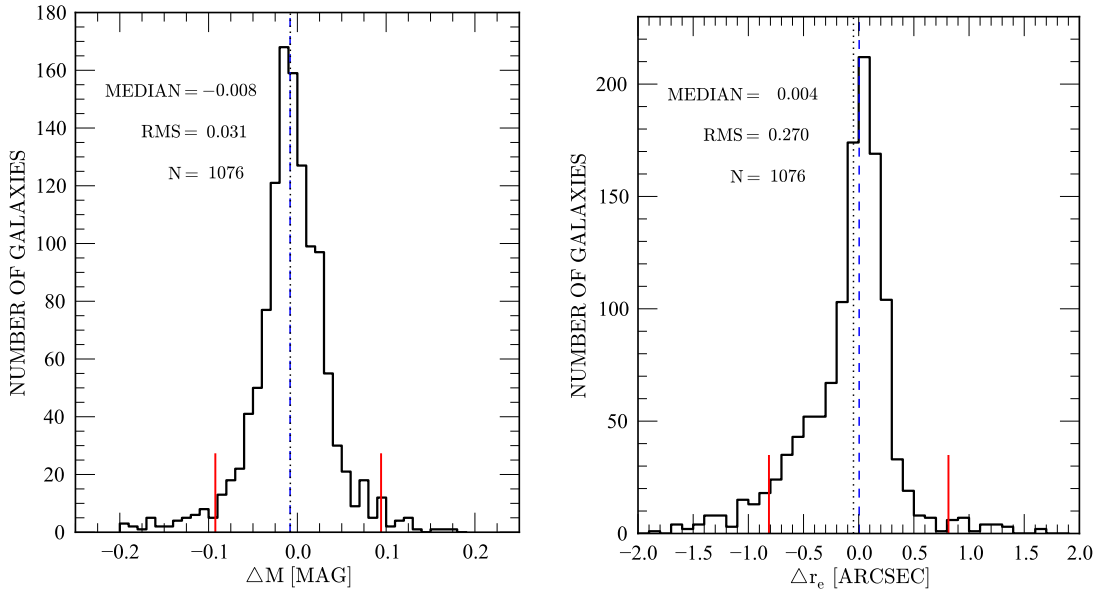

Fig. 3.17: Results from the simulation for a total of 1076 mock images created using the image fields for the whole Norma sample (31 individual galaxy fields). The 1076 data points are within the vertical red solid lines, which represent a 2σ-clipping.

corresponds to the 2MASS total extrapolated magnitude (J. Lucey measured the effective radii for the Coma cluster galaxies based on the total extrapolated magnitudes from the 2MASS XSC). Both datasets were PSF-corrected using GALFIT.

The comparisons of total extrapolated magnitudes, effective radii, mean effective surface brightnesses and the X-component of the Fundamental Plane ($X_{\rm FP} = \log r_e - 0.32\langle\mu_e\rangle$) shown in Figure 3.18 show that the parameters extracted using my method are in good agreement with the 2MASS values. The median difference in the total extrapolated magnitude is -0.014 ± 0.009 mag. The difference between the X-component of the Fundamental Plane as shown in the bottom right-hand panel is also very small, i.e., a median value of -0.005 dex and an rms of 0.012. In the top left-hand panel, the blue stars represent the Coma cluster galaxies whose magnitude difference is > 0.26 mag. There is a total of 9 such galaxies and these were excluded from both these statistical comparisons and the final Fundamental Plane analysis. The reason for these Coma cluster galaxies being 'outliers' is most likely a result of sky background issues with the possibility that I over-estimated the sky value. There may also be possible errors associated with the processing of the original raw data for these galaxies. These 9 galaxies are presented in the appendix (Table C.1).

3.4 Variables for the Fundamental Plane Analysis: $\log r_e$, $\langle\mu_e\rangle$ and $\log\sigma$

The $\langle\mu_e\rangle$ values were first corrected for Galactic extinction, cosmological dimming effects, as well as redshift effects (k-corrections). The fully corrected mean effective surface brightness which finally goes into the Fundamental Plane is

$$\langle\mu_e\rangle = m_{\rm tot} + 2.5\log\left(2\pi r_e^2\right) - A_{K_s} - k_{\rm corr} - 10\log(1+z), \tag{3.39}$$

where $m_{\rm tot}$ is the measured total extrapolated apparent magnitude (corrected for the star-subtraction and sky background effects in the case of the Norma cluster sample), A_{K_s} is the

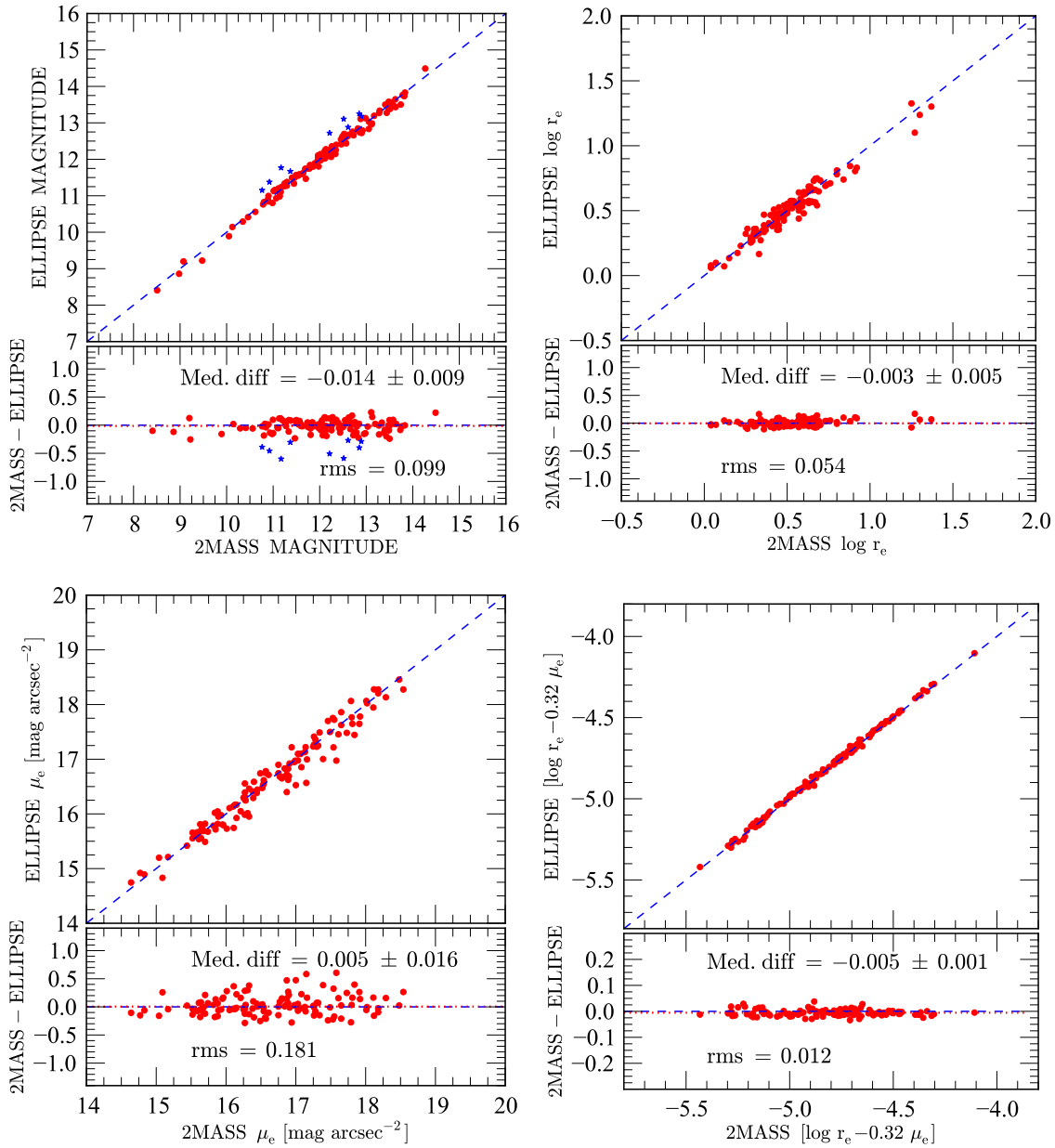

Fig. 3.18: K_s-band photometry for the Coma cluster, showing a comparison between this work and the 2MASS XSC for the Fundamental Plane calibration sample. The top left and top right-hand panels show the comparison between the total extrapolated magnitude and the effective radius, respectively. The blue stars represent the nine galaxies which were excluded from the final Fundamental Plane analysis. The bottom left and right-hand panels show the comparison between the mean effective surface brightness and the X-component ($\log r_e - 0.32\langle\mu_e\rangle$) of the Fundamental Plane.

Galactic extinction, $k_{\rm corr}$ is the k-correction and r_e is the PSF-corrected effective radius. The final K_s-band Fundamental Plane data (r_e, $\langle\mu_e\rangle$ and $\log\sigma$) are presented in Table 3.2 (for the Norma sample based on the NTT K_s-band images).

The J and K_s-band Fundamental Plane data for the Norma cluster (from photometry measurements using the IRSF data) are presented in Table 3.3. For the Coma cluster, the Fundamental Plane data are presented in Table 3.4. In all the three tables (for the Norma

Tab. 3.2: Norma cluster photometry results (NTT) obtained by fitting and extrapolating the galaxy surface brightness profiles. The total magnitudes presented here have been corrected for only the star-subtraction and sky background effects by adding −0.0106 mag and −0.008 mag, respectively. The values presented in columns 3, 4 and 7 are fully-corrected and these are the variables which finally go into the Fundamental Plane.

Identification	Tot. mag	r_e	$\langle\mu_e\rangle$	A_{K_s}	$z_{\rm helio}$	$\log\sigma$
(1)	(2)	(3)	(4)	(5)	(6)	(7)
WKK5920	9.93±0.04	4.63±0.43	15.03±0.21	0.086	0.0159	2.312±0.012
WKK5972	9.64±0.05	6.72±0.76	15.54±0.25	0.079	0.0185	2.414±0.010
WKK6012	10.89±0.05	4.48±0.38	15.94±0.19	0.080	0.0146	2.172±0.014
WKK6019	9.94±0.04	3.72±0.26	14.56±0.15	0.070	0.0186	2.409±0.010
WKK6047	11.90±0.07	3.07±0.21	16.11±0.16	0.070	0.0180	2.010±0.015
WKK6116	9.39±0.03	6.66±0.56	15.33±0.19	0.066	0.0129	2.344±0.012
WKK6180	10.15±0.05	6.07±0.59	15.87±0.22	0.065	0.0153	2.308±0.011
WKK6183	10.30±0.04	4.35±0.30	15.27±0.16	0.063	0.0198	2.377±0.012
WKK6198	11.71±0.09	4.29±0.58	16.67±0.31	0.056	0.0158	1.905±0.020
WKK6204	9.39±0.04	6.58±0.64	15.28±0.21	0.065	0.0154	2.499±0.009
WKK6221	10.70±0.06	6.44±0.48	16.51±0.17	0.066	0.0195	2.038±0.017
WKK6229	11.59±0.04	1.92±0.07	14.78±0.09	0.063	0.0177	2.210±0.015
WKK6233	11.77±0.06	2.36±0.16	15.42±0.16	0.062	0.0171	2.243±0.014
WKK6235	10.95±0.05	3.31±0.30	15.36±0.21	0.069	0.0135	2.141±0.018
WKK6242	10.92±0.03	2.09±0.09	14.31±0.10	0.061	0.0175	2.424±0.011
WKK6250	10.47±0.04	3.18±0.24	14.74±0.17	0.064	0.0206	2.324±0.010
WKK6269	8.27±0.05	15.95±1.44	16.07±0.20	0.060	0.0182	2.579±0.011
WKK6282	11.23±0.04	1.56±0.17	14.00±0.24	0.060	0.0165	2.274±0.012
WKK6305	9.15±0.04	8.05±0.61	15.45±0.17	0.080	0.0165	2.327±0.009
WKK6318	8.70±0.06	15.52±1.46	16.48±0.21	0.073	0.0114	2.354±0.013
WKK6342	11.04±0.03	2.39±0.06	14.72±0.06	0.062	0.0162	2.326±0.009
WKK6360	10.11±0.02	3.14±0.08	14.35±0.06	0.063	0.0208	2.505±0.009
WKK6383	10.95±0.05	4.00±0.27	15.74±0.15	0.071	0.0185	2.195±0.012
WKK6431	10.87±0.03	2.50±0.16	14.68±0.14	0.075	0.0118	2.286±0.010
WKK6473	11.94±0.07	2.00±0.16	15.23±0.19	0.067	0.0186	2.064±0.017
WKK6477	11.84±0.06	2.69±0.21	15.79±0.18	0.073	0.0135	2.106±0.019
WKK6555	11.04±0.06	2.79±0.38	15.05±0.30	0.067	0.0165	2.207±0.010
WKK6600	10.07±0.05	5.15±0.58	15.41±0.25	0.068	0.0168	2.338±0.011
WKK6615	12.04±0.08	2.22±0.21	15.59±0.22	0.060	0.0139	2.108±0.021
WKK6620	12.94±0.21	2.83±0.56	16.97±0.48	0.062	0.0208	1.777±0.054
WKK6679	10.79±0.04	3.19±0.20	15.10±0.14	0.074	0.0155	2.159±0.012

NOTES: The columns refer to (1) galaxy name (2) the measured total extrapolated magnitude corrected for the star-subtraction and background effects (3) effective radius in arcsec corrected for the seeing effect (4) mean effective surface brightness in mag arcsec^{-2}, corrected for Galactic extinction, redshift, and the cosmological dimming effects (5) Galactic extinction from Schlafly & Finkbeiner (2011): $A_{K_s} = 0.085 A_B$ (6) galaxy redshift (heliocentric) (7) central velocity dispersion in dex, with both aperture correction and run offset applied.

and Coma cluster galaxies), the column for the $\log\sigma$ represents the aperture corrected and normalised values (see the description of the spectroscopic data reduction and corrections presented in Chapter 2, §2.1.2). No corrections have been applied to the total magnitude presented in the tables except the star-subtraction and sky background effects for the Norma cluster galaxies.

Table 3.5 shows the measurement errors and corrections applied to the NTT K_s-band photometry data before performing the Fundamental Plane analysis. The Malmquist bias correction was determined from the Fundamental Plane scatter and the Fundamental Plane fit parameter, a (see §3.7.1.1). All the other corrections given in this table (except the Malmquist bias correction) were applied prior to fitting the Fundamental Plane. For the J and K_s-band Fundamental Plane analysis, the measurement errors and applied corrections are presented in Table 3.6. Note that the measurement errors and corrections presented in Table 3.6 are for the J and K_s-band Fundamental Plane analysis which is based only on the IRSF/SIRIUS data. For clarity, the K_s-band Fundamental Plane analysis where the NTT/SOFI and IRSF/SIRIUS datasets were

Tab. 3.3: Norma cluster J and K_s-band photometry results (IRSF) from fitting and extrapolating the galaxy surface brightness profiles, using the IRSF/SIRIUS galaxy images. The total magnitudes presented here have been corrected for only the star-subtraction and sky background effects.

Identification	Total magnitude		Effective radius		Mean eff. surf. brightness		Extinction		$\log\sigma$
	J	K_s	J	K_s	J	K_s	A_J	A_{K_s}	
(1)	(2)	(3)	(4)	(5)	(6)	(7)	(8)	(9)	(10)
WKK6019	10.87±0.06	9.82±0.03	4.56±0.50	4.22±0.23	15.98±0.24	14.81±0.12	0.172	0.070	2.409±0.010
WKK6047	12.81±0.06	11.83±0.03	3.07±0.22	2.92±0.13	17.09±0.16	16.04±0.10	0.173	0.070	2.010±0.015
WKK6075	12.95±0.06	11.92±0.03	2.32±0.27	2.14±0.06	16.56±0.26	15.38±0.07	0.181	0.074	2.099±0.017
WKK6116	10.50±0.06	9.47±0.04	7.48±1.00	7.59±0.70	16.71±0.30	15.71±0.21	0.163	0.066	2.344±0.012
WKK6148	12.67±0.05	11.69±0.03	3.84±0.18	3.33±0.14	17.39±0.11	16.13±0.10	0.155	0.063	1.998±0.019
WKK6180	11.16±0.06	10.13±0.03	6.84±0.69	7.18±0.37	17.12±0.23	16.24±0.12	0.159	0.065	2.308±0.011
WKK6183	11.13±0.06	10.06±0.03	5.32±0.82	5.58±0.42	16.68±0.34	15.66±0.17	0.155	0.063	2.377±0.012
WKK6193	11.10±0.07	10.00±0.03	6.48±0.68	6.60±0.28	16.97±0.24	15.99±0.10	0.159	0.065	2.226±0.010
WKK6204	10.35±0.07	9.63±0.28	6.87±1.12	5.22±3.16	16.37±0.36	14.98±1.34	0.160	0.065	2.499±0.009
WKK6207	11.05±0.07	9.90±0.03	4.38±0.83	6.39±0.52	16.21±0.42	15.78±0.18	0.152	0.062	2.241±0.012
WKK6221	11.31±0.06	10.47±0.04	9.14±1.05	7.47±0.38	17.89±0.26	16.62±0.11	0.164	0.067	2.038±0.017
WKK6229	12.56±0.07	11.59±0.03	2.30±0.25	1.97±0.09	16.19±0.24	14.88±0.11	0.156	0.063	2.210±0.015
WKK6233	12.73±0.07	11.91±0.04	2.69±0.22	2.14±0.07	16.66±0.19	15.26±0.08	0.152	0.062	2.243±0.014
WKK6235	11.91±0.06	10.96±0.03	4.73±0.42	4.39±0.21	17.07±0.20	15.99±0.11	0.170	0.069	2.141±0.018
WKK6242	11.82±0.07	10.90±0.03	2.74±0.24	2.16±0.15	15.86±0.20	14.41±0.15	0.151	0.061	2.424±0.011
WKK6250	11.56±0.05	10.55±0.02	3.58±0.31	3.41±0.13	16.15±0.20	15.01±0.08	0.159	0.065	2.324±0.010
WKK6252	13.00±0.06	12.18±0.03	2.80±0.24	2.44±0.16	17.04±0.19	15.88±0.14	0.153	0.063	2.073±0.012
WKK6269	8.97±0.06	8.14±0.03	20.40±2.47	17.57±1.03	17.44±0.27	16.22±0.13	0.148	0.060	2.579±0.011
WKK6275	11.40±0.06	10.22±0.03	7.74±0.78	8.39±0.60	17.62±0.23	16.68±0.16	0.149	0.061	2.165±0.014
WKK6282	12.17±0.06	11.22±0.03	3.05±0.33	2.60±0.17	16.42±0.24	15.14±0.15	0.147	0.060	2.274±0.012
WKK6297	12.69±0.05	11.78±0.02	4.38±0.25	4.01±0.18	17.72±0.14	16.71±0.10	0.149	0.061	1.844±0.026
WKK6305	10.23±0.05	9.24±0.11	6.77±0.79	7.93±1.49	16.25±0.26	15.45±0.42	0.198	0.081	2.327±0.009
WKK6318	9.61±0.06	8.73±0.03	15.84±1.76	13.75±0.79	17.49±0.25	16.35±0.13	0.180	0.073	2.354±0.013
WKK6342	12.08±0.05	10.86±0.02	2.59±0.13	3.05±0.15	15.98±0.12	15.11±0.11	0.152	0.062	2.326±0.009
WKK6360	10.92±0.06	10.02±0.02	4.19±0.66	3.60±0.15	15.91±0.35	14.61±0.10	0.154	0.063	2.505±0.009
WKK6383	11.94±0.06	10.78±0.03	4.04±0.26	4.59±0.22	16.77±0.15	15.88±0.11	0.176	0.072	2.195±0.012
WKK6402	11.56±0.05	10.62±0.02	3.70±0.29	3.23±0.15	16.20±0.18	14.98±0.10	0.190	0.077	2.238±0.011
WKK6429	12.30±0.04	11.63±0.04	5.04±0.37	5.56±0.17	17.73±0.16	16.91±0.09	0.159	0.065	2.084±0.012
WKK6431	11.74±0.05	10.78±0.03	3.56±0.24	3.18±0.19	16.28±0.16	15.17±0.13	0.184	0.075	2.286±0.010
WKK6459	11.37±0.06	10.45±0.04	6.18±0.85	6.25±0.21	17.09±0.31	16.13±0.08	0.200	0.081	2.322±0.010
WKK6477	12.67±0.05	11.73±0.04	3.02±0.32	2.68±0.13	16.90±0.23	15.76±0.11	0.179	0.073	2.106±0.019

NOTES: The columns refer to (1) galaxy name, (2) and (3) are respectively, the J and K_s-band total extrapolated magnitude, (4) and (5) are respectively, the J and K_s-band effective radius in arcsec corrected for the seeing effect, (6) and (7) are respectively, the J and K_s-band mean effective surface brightness in mag arcsec^{-2}, corrected for the Galactic extinction, redshift, and the cosmological dimming effects, (8) and (9) the Galactic extinction from the re-calibration presented under §3.2.5, where, $A_J = 0.937\,f\,E(B-V)$ and $A_{K_s} = 0.382\,f\,E(B-V)$, (10) the central velocity dispersion in dex, with both aperture correction and run offset applied (see §2.1.2 of this dissertation).

combined is what I refer to as the "combined K_s-band Fundamental Plane analysis".

3.5 The Coma Cluster Calibration Sample: Comparing the J and K_s-band Total Extrapolated Magnitudes with the 2MASS Extended Source Catalogue

As stated earlier, the Fundamental Plane calibration sample consists of 121 early-type galaxies within the Coma cluster. The photometric analysis for these galaxies was performed using the 2MASS Atlas images. *The analysis was conducted in exactly the same way as for the Norma cluster early-type galaxies*. The photometry results from this work were compared with the values taken from the 2MASS XSC. The left and right-hand panels of Figure 3.19 represent the J- and K_s-band, respectively. There is a good agreement between these and the total extrapolated magnitudes taken from the 2MASS XSC, with a median difference of -0.023 ± 0.014 mag and -0.014 ± 0.009 mag, in the J and K_s-band, respectively. These are represented by the red dashed lines in the lower sub-panel. The red dashed lines in the upper panels represent a one-to-one relation (refer to Table 3.7 for a summary of the photometry comparison for the J and K_s-band).

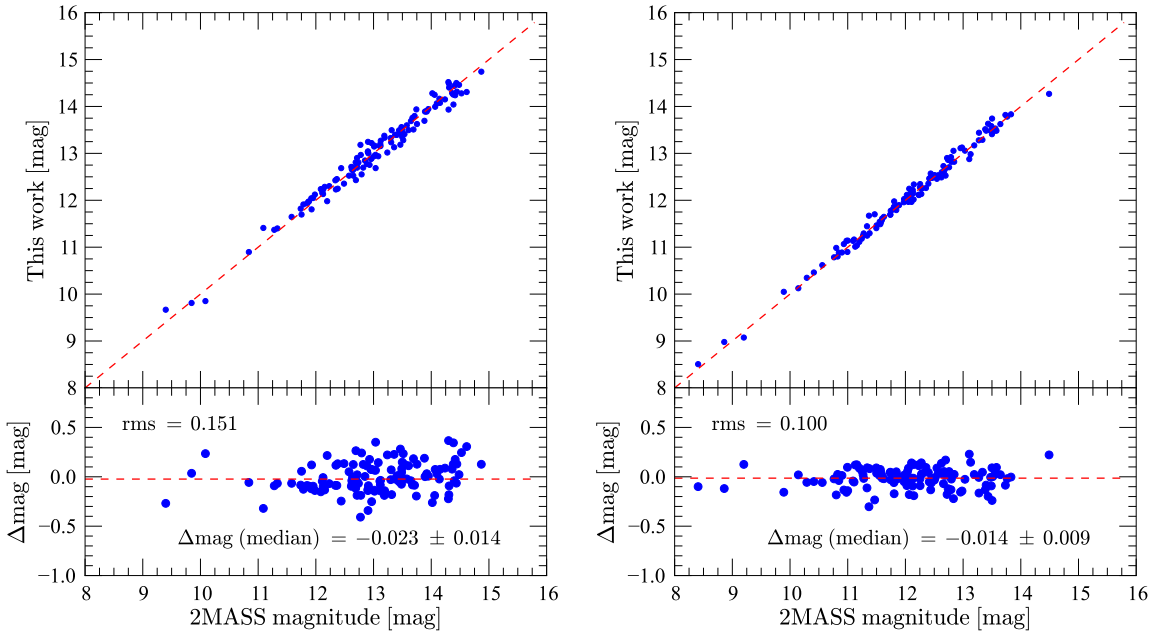

Fig. 3.19: Comparison of the total extrapolated magnitudes in this work with the 2MASS XSC for the Coma J and K_s-band. The left and right-hand panels represent the J and K_s-band, respectively. The red dashed lines in the lower sub-panels represent the median difference between the total magnitudes from the 2MASS XSC and this work, that is, Δm = (2MASS XSC – THIS WORK).

Tab. 3.4: Coma cluster J and K_s photometry results from fitting and extrapolating the galaxy surface brightness profiles using the 2MASS Atlas images.

Identification	Total magnitude		Effective radius		Mean eff. surf. brightness		$\log\sigma$
	J	K_s	J	K_s	J	K_s	
(1)	(2)	(3)	(4)	(5)	(6)	(7)	(8)
2MASXJ13023273+2717443	14.15±0.08	13.48±0.15	3.98±0.21	3.23±0.59	19.05±0.14	17.83±0.42	1.709±0.055
2MASXJ13020552+2717499	13.93±0.06	13.51±0.14	4.19±0.08	2.21±0.52	18.95±0.07	17.04±0.53	1.836±0.033
2MASXJ13000623+2718022	13.63±0.04	12.82±0.07	4.59±0.18	4.46±0.46	18.83±0.09	17.86±0.23	1.748±0.038
2MASXJ12593730+2720097	14.74±0.11	14.27±0.24	2.25±0.17	2.29±0.58	18.41±0.20	17.89±0.60	1.640±0.076
2MASXJ13010615+2723522	14.31±0.09	13.83±0.17	3.26±0.44	2.15±0.41	18.76±0.31	17.28±0.45	1.809±0.041
2MASXJ12564777+2725158	14.25±0.10	13.48±0.12	3.11±0.33	2.24±0.27	18.61±0.25	17.03±0.29	1.618±0.042
2MASXJ12583209+2727227	13.38±0.05	12.57±0.05	2.00±0.10	1.87±0.20	16.78±0.11	15.74±0.23	2.056±0.014
2MASXJ12573614+2729058	13.15±0.03	12.15±0.04	1.97±0.04	2.05±0.04	16.53±0.05	15.52±0.06	2.210±0.009
2MASXJ12570940+2727587	12.24±0.02	11.16±0.02	2.55±0.32	3.02±0.02	16.17±0.27	15.37±0.02	2.304±0.008
2MASXJ13002689+2730556	13.49±0.05	12.52±0.05	1.86±0.09	2.40±0.21	16.74±0.11	16.21±0.20	2.023±0.014
2MASXJ12580974+2732585	14.25±0.08	13.28±0.10	3.48±0.30	2.95±0.27	18.87±0.20	17.45±0.22	1.727±0.042
2MASXJ12573584+2729358	11.97±0.02	10.90±0.02	3.07±0.05	3.57±0.02	16.31±0.04	15.47±0.02	2.321±0.009
2MASXJ12572435+2729517	9.85±0.00	9.07±0.00	27.31±0.05	21.19±0.20	18.93±0.00	17.51±0.02	2.431±0.008
2MASXJ12570431+2731328	14.24±0.08	13.63±0.15	4.32±0.48	3.17±0.49	19.31±0.25	17.92±0.37	1.872±0.041
2MASXJ12563418+2732200	12.71±0.03	11.61±0.03	2.80±0.08	3.59±0.07	16.85±0.07	16.20±0.05	2.208±0.009
2MASXJ13014841+2736147	13.51±0.04	12.82±0.07	3.21±0.16	2.41±0.14	17.94±0.12	16.51±0.15	1.846±0.022
2MASXJ13011224+2736162	13.76±0.06	12.53±0.05	3.09±0.15	4.37±0.31	18.11±0.12	17.53±0.16	1.729±0.039
2MASXJ13001914+2733135	12.88±0.03	11.79±0.03	3.28±0.08	3.90±0.24	17.37±0.06	16.59±0.14	2.030±0.013
2MASXJ12585812+2735409	13.16±0.06	12.06±0.04	1.37±0.22	2.12±0.10	15.76±0.35	15.53±0.11	2.166±0.011
2MASXJ12573284+2736368	11.65±0.01	10.62±0.01	3.47±0.06	3.76±0.09	16.27±0.04	15.33±0.05	2.379±0.008
2MASXJ13020106+2739109	13.41±0.03	12.70±0.07	4.01±0.19	3.02±0.24	18.32±0.11	16.91±0.19	1.805±0.026
2MASXJ13015375+2737277	10.90±0.01	10.05±0.01	6.76±0.20	5.49±0.07	16.94±0.06	15.54±0.03	2.423±0.008
2MASXJ12591030+2737119	13.28±0.04	12.34±0.05	2.76±0.18	2.75±0.25	17.40±0.15	16.38±0.20	2.078±0.014
2MASXJ12571682+2737068	13.51±0.06	12.48±0.05	1.12±0.28	1.18±0.33	15.65±0.55	14.64±0.61	2.208±0.009
2MASXJ12594713+2742372	12.05±0.05	11.14±0.02	4.04±0.27	3.66±0.04	16.97±0.15	15.74±0.03	2.130±0.010
2MASXJ12584742+2740288	11.97±0.01	11.07±0.02	7.20±0.15	6.77±0.11	18.14±0.05	17.00±0.04	2.273±0.009
2MASXJ12583157+2740247	13.94±0.06	12.90±0.07	1.27±0.15	1.80±0.15	16.37±0.26	15.99±0.20	2.104±0.012
2MASXJ12563420+2741150	14.28±0.07	13.82±0.21	3.54±0.37	2.09±0.53	18.93±0.24	17.24±0.59	1.798±0.029
2MASXJ13000626+2746332	12.97±0.03	11.98±0.04	4.29±0.25	4.21±0.15	18.04±0.13	16.94±0.09	2.061±0.013
2MASXJ12592491+2744198	13.15±0.04	12.27±0.04	1.65±0.76	1.96±0.13	16.15±1.00	15.58±0.15	2.159±0.012
2MASXJ12591348+2746289	12.65±0.02	11.90±0.03	4.39±0.20	3.41±0.11	17.77±0.10	16.38±0.08	2.071±0.014
2MASXJ12590821+2747029	12.12±0.03	11.13±0.02	3.38±0.09	3.45±0.08	16.67±0.07	15.63±0.06	2.314±0.009
2MASXJ12590745+2746039	12.90±0.05	11.98±0.04	2.13±0.10	2.25±0.06	16.45±0.11	15.57±0.07	2.223±0.010
2MASXJ12585766+2747079	13.69±0.05	13.12±0.09	4.24±0.40	3.41±0.37	18.73±0.21	17.60±0.25	1.582±0.055
2MASXJ12585208+2747059	12.43±0.02	11.65±0.03	4.01±0.24	3.34±0.09	17.37±0.13	16.11±0.06	2.175±0.011
2MASXJ12581922+2745437	14.28±0.08	13.48±0.13	2.41±0.12	1.86±0.40	18.12±0.13	16.68±0.49	1.872±0.031
2MASXJ12574616+2745254	12.75±0.02	12.15±0.04	7.93±0.20	5.02±0.34	19.17±0.06	17.49±0.15	1.696±0.042
2MASXJ13011761+2748321	11.91±0.02	10.88±0.01	3.38±0.03	3.69±0.03	16.46±0.02	15.53±0.02	2.274±0.009
2MASXJ13003334+2749266	14.46±0.11	13.53±0.12	3.25±0.41	3.44±0.31	18.91±0.30	18.00±0.23	1.625±0.060
2MASXJ13000551+2748272	12.55±0.02	11.89±0.03	4.75±0.16	3.30±0.10	17.84±0.08	16.31±0.07	2.067±0.013
2MASXJ12595489+2747453	14.40±0.11	13.74±0.13	2.07±0.35	1.47±0.35	17.87±0.39	16.36±0.53	1.658±0.041
2MASXJ12593697+2749327	14.50±0.12	13.62±0.15	1.08±0.10	1.36±0.41	16.57±0.23	16.13±0.68	1.927±0.023
2MASXJ12592936+2751008	12.35±0.03	11.41±0.02	2.87±0.26	2.29±0.02	16.55±0.20	15.02±0.03	2.387±0.009
2MASXJ12580349+2748535	12.85±0.04	12.03±0.04	2.44±0.10	2.03±0.14	16.69±0.10	15.37±0.15	2.216±0.009
2MASXJ12574728+2749594	12.89±0.03	12.11±0.04	2.25±0.15	2.16±0.05	16.57±0.14	15.63±0.06	2.118±0.012
2MASXJ12571778+2748388	13.89±0.07	12.86±0.08	2.98±0.25	3.62±0.25	18.16±0.19	17.46±0.17	1.710±0.038
2MASXJ13025272+2751593	12.25±0.02	11.29±0.02	3.10±0.35	2.82±0.10	16.59±0.25	15.33±0.08	2.186±0.009
2MASXJ13015023+2753367	12.52±0.02	11.67±0.03	3.09±0.08	2.64±0.02	16.88±0.06	15.58±0.03	2.290±0.010
2MASXJ12594610+2751257	13.22±0.04	12.08±0.04	1.97±0.04	2.48±0.08	16.58±0.06	15.84±0.08	2.090±0.011
2MASXJ12593789+2754267	12.64±0.03	11.49±0.03	2.36±0.02	2.93±0.11	16.40±0.04	15.61±0.09	2.261±0.009
2MASXJ12592016+2753098	13.41±0.04	12.48±0.05	3.28±0.20	3.12±0.35	17.90±0.14	16.78±0.25	1.831±0.021
2MASXJ12590459+2754389	13.33±0.04	12.73±0.08	2.94±0.14	2.06±0.13	17.58±0.11	16.13±0.16	2.044±0.012
2MASXJ12590791+2751179	12.45±0.03	11.46±0.03	3.11±0.20	2.78±0.11	16.82±0.15	15.51±0.09	2.258±0.009
2MASXJ12575059+2752454	13.49±0.03	12.50±0.05	2.82±0.65	3.03±0.10	17.65±0.50	16.72±0.08	2.013±0.017
2MASXJ12572169+2752498	13.89±0.06	12.92±0.09	2.38±0.06	2.44±0.30	17.67±0.08	16.66±0.28	1.685±0.037
2MASXJ13004285+2757476	13.25±0.07	12.11±0.04	2.21±0.25	3.05±0.22	16.85±0.25	16.31±0.17	2.060±0.012
2MASXJ13004737+2755196	13.02±0.03	12.54±0.06	5.33±0.25	3.09±0.20	18.54±0.11	16.76±0.15	1.944±0.016
2MASXJ13003975+2755256	12.29±0.02	11.18±0.02	3.37±0.09	4.40±0.03	16.82±0.06	16.20±0.02	2.240±0.009
2MASXJ13002798+2757216	13.24±0.04	12.26±0.05	2.29±0.06	2.28±0.06	16.94±0.07	15.86±0.08	2.121±0.011

NOTES: The columns refer to (1) 2MASS galaxy name, (2) and (3) are the measured total extrapolated magnitude in J and K_s-bands, (4) and (5) are respectively, the J and K_s-band effective radius in arcsec corrected for the seeing effect, (6) and (7) are respectively, the J and K_s-band mean effective surface brightness in mag arcsec^{-2}, corrected for Galactic extinction, redshift, and the cosmological dimming effects, (8) central velocity dispersion in dex, with both aperture correction and run offset applied. The applied Galactic extinction correction is from the re-calibration presented under §3.2.5, i.e., $A_J = 0.937\,f\,E(B-V)$ and $A_{K_s} = 0.382\,f\,E(B-V)$.

Tab. 3.4: Continued ...

Identification	Total magnitude		Effective radius		Mean eff. surf. brightness		$\log\sigma$
	J	K_s	J	K_s	J	K_s	
(1)	(2)	(3)	(4)	(5)	(6)	(7)	(8)
2MASXJ12595670+2755483	13.44±0.04	12.49±0.05	4.16±0.32	3.76±0.33	18.43±0.17	17.16±0.20	2.001±0.016
2MASXJ12594438+2754447	12.30±0.02	11.25±0.02	3.44±0.03	3.74±0.09	16.89±0.02	15.93±0.06	2.207±0.009
2MASXJ12594234+2755287	13.56±0.07	12.53±0.05	1.07±0.21	1.20±0.15	15.62±0.42	14.74±0.27	2.238±0.011
2MASXJ12594423+2757307	13.60±0.05	12.68±0.07	2.99±0.12	3.10±0.25	17.88±0.10	16.95±0.19	1.819±0.025
2MASXJ12593570+2757338	9.81±0.00	8.98±0.00	26.13±0.03	20.02±0.12	18.80±0.00	17.30±0.01	2.426±0.009
2MASXJ12590414+2757329	14.08±0.10	12.98±0.11	1.74±0.31	2.10±0.32	17.18±0.39	16.40±0.35	2.112±0.014
2MASXJ12565310+2755458	13.27±0.09	12.26±0.04	1.21±0.08	1.25±0.01	15.60±0.17	14.59±0.05	2.272±0.009
2MASXJ12562984+2756240	12.81±0.03	11.70±0.03	2.48±0.68	3.47±0.15	16.69±0.60	16.23±0.10	2.266±0.009
2MASXJ13012713+2759566	13.69±0.08	12.60±0.05	0.87±0.15	1.15±0.16	15.29±0.39	14.70±0.31	2.198±0.010
2MASXJ13005445+2800271	11.40±0.01	10.46±0.01	7.55±0.03	6.97±0.18	17.72±0.01	16.54±0.06	2.371±0.009
2MASXJ13003877+2800516	13.03±0.04	11.97±0.03	3.86±0.08	4.58±0.16	17.86±0.06	17.07±0.08	2.026±0.014
2MASXJ13000809+2758372	9.67±0.00	8.51±0.00	14.79±0.15	17.27±0.06	17.43±0.02	16.52±0.01	2.570±0.008
2MASXJ13000643+2800142	12.94±0.03	12.02±0.04	3.25±0.06	3.22±0.23	17.40±0.05	16.37±0.16	2.081±0.013
2MASXJ12594681+2758252	12.70±0.02	11.53±0.02	3.55±0.09	4.60±0.11	17.33±0.06	16.60±0.05	2.116±0.012
2MASXJ12593827+2759137	13.80±0.05	13.11±0.10	3.80±0.27	3.70±0.48	18.60±0.16	17.77±0.30	1.909±0.022
2MASXJ12592657+2759548	14.28±0.10	13.06±0.09	1.77±0.23	2.27±0.13	17.43±0.30	16.66±0.16	1.904±0.018
2MASXJ12592136+2758248	14.44±0.13	13.48±0.14	2.26±0.22	2.53±0.53	18.13±0.24	17.34±0.47	1.713±0.050
2MASXJ12590603+2759479	12.23±0.02	11.30±0.02	4.68±0.25	4.83±0.24	17.48±0.12	16.52±0.11	2.179±0.010
2MASXJ12583023+2800527	11.81±0.01	11.14±0.02	5.87±0.19	3.71±0.03	17.55±0.07	15.80±0.03	2.282±0.009
2MASXJ13025659+2804133	13.00±0.03	12.22±0.05	4.59±0.25	4.45±0.10	18.21±0.12	17.26±0.07	1.753±0.030
2MASXJ13024442+2802434	12.04±0.01	10.98±0.02	5.22±0.08	6.38±0.26	17.55±0.04	16.84±0.09	2.254±0.010
2MASXJ13004867+2805266	11.93±0.02	10.89±0.01	3.28±0.04	3.60±0.02	16.42±0.03	15.48±0.02	2.321±0.008
2MASXJ13002215+2802495	12.68±0.03	11.54±0.03	3.48±0.09	4.56±0.17	17.29±0.06	16.62±0.08	2.087±0.011
2MASXJ13001702+2803502	13.35±0.05	12.35±0.04	2.68±0.26	2.40±0.23	17.40±0.21	16.09±0.21	2.070±0.013
2MASXJ13001475+2802282	12.80±0.03	11.80±0.03	1.91±0.05	2.11±0.03	16.13±0.07	15.27±0.04	2.206±0.010
2MASXJ13001286+2804322	13.20±0.04	12.35±0.05	2.15±0.10	1.85±0.10	16.77±0.11	15.48±0.12	2.075±0.011
2MASXJ13000803+2804422	12.66±0.04	11.57±0.02	1.83±0.04	2.13±0.07	15.88±0.07	15.02±0.08	2.263±0.008
2MASXJ12595601+2802052	12.13±0.02	11.04±0.02	3.99±0.13	4.85±0.15	17.03±0.07	16.25±0.07	2.206±0.010
2MASXJ12593141+2802478	12.70±0.03	11.86±0.04	3.29±0.13	2.88±0.13	17.18±0.09	15.98±0.10	2.108±0.011
2MASXJ12591389+2804349	12.78±0.02	12.11±0.05	6.60±0.11	5.36±0.26	18.77±0.04	17.55±0.12	2.150±0.014
2MASXJ12564585+2803058	14.52±0.09	13.51±0.12	2.70±0.18	2.83±0.48	18.59±0.17	17.59±0.39	1.669±0.048
2MASXJ12563890+2804518	13.94±0.07	13.17±0.11	4.35±0.32	4.55±0.61	19.03±0.17	18.25±0.31	1.625±0.062
2MASXJ13014700+2805417	12.23±0.02	11.11±0.02	2.67±0.02	3.47±0.03	16.28±0.02	15.66±0.02	2.257±0.008
2MASXJ13004459+2806026	13.18±0.04	12.46±0.05	4.14±0.28	2.92±0.20	18.18±0.15	16.61±0.16	1.891±0.017
2MASXJ13003552+2808466	13.04±0.03	11.96±0.03	3.91±0.22	4.56±0.16	17.92±0.13	17.11±0.08	1.885±0.020
2MASXJ12595511+2807422	13.33±0.05	12.25±0.04	2.32±0.27	2.98±0.23	17.05±0.26	16.42±0.17	2.096±0.014
2MASXJ12590392+2807249	11.37±0.01	10.35±0.01	4.77±0.13	4.90±0.12	16.65±0.06	15.59±0.05	2.422±0.008
2MASXJ12585341+2807339	13.39±0.06	12.52±0.05	2.34±0.11	2.10±0.09	17.14±0.12	15.95±0.11	2.062±0.013
2MASXJ12583636+2806497	11.98±0.01	11.25±0.02	5.19±0.09	3.53±0.07	17.46±0.04	15.80±0.04	2.239±0.009
2MASXJ12574670+2808264	14.04±0.07	13.41±0.14	4.16±0.45	3.76±0.83	19.04±0.24	18.11±0.50	1.607±0.066
2MASXJ13021025+2811309	13.90±0.07	13.05±0.11	3.95±0.39	3.01±0.43	18.80±0.23	17.30±0.33	1.834±0.025
2MASXJ13012280+2811456	12.97±0.03	12.12±0.04	4.00±0.53	3.35±0.22	17.88±0.29	16.55±0.15	2.109±0.013
2MASXJ13001795+2812082	11.41±0.01	10.12±0.01	4.26±0.02	6.45±0.13	16.44±0.02	15.95±0.04	2.369±0.008
2MASXJ12592021+2811528	13.99±0.06	12.88±0.05	2.32±0.10	2.94±0.18	17.69±0.11	16.97±0.14	1.949±0.022
2MASXJ12581382+2810576	12.94±0.02	12.13±0.05	6.46±0.11	5.57±0.30	18.89±0.04	17.67±0.12	1.869±0.019
2MASXJ12574866+2810494	12.70±0.03	11.69±0.03	2.72±0.11	2.65±0.22	16.77±0.09	15.62±0.18	2.159±0.011
2MASXJ12572841+2810348	13.18±0.11	11.69±0.03	2.71±0.20	4.54±0.14	17.24±0.19	16.76±0.07	2.021±0.015
2MASXJ12563516+2816318	12.69±0.02	12.03±0.04	4.67±0.24	3.04±0.20	17.93±0.11	16.26±0.15	2.090±0.013
2MASXJ12592611+2817148	14.31±0.08	13.58±0.12	2.02±0.12	1.86±0.35	17.73±0.15	16.72±0.42	1.695±0.039
2MASXJ12584394+2816578	14.49±0.18	13.78±0.17	2.26±0.38	1.49±0.36	18.15±0.41	16.45±0.55	1.629±0.046
2MASXJ12582949+2818047	14.16±0.09	13.29±0.12	2.76±0.25	2.44±0.50	18.28±0.21	17.07±0.46	1.844±0.027
2MASXJ13024079+2822163	12.42±0.02	11.45±0.03	5.40±0.15	5.14±0.24	17.99±0.06	16.81±0.11	1.941±0.020
2MASXJ13021434+2821099	13.50±0.04	12.62±0.08	5.46±0.19	5.40±0.56	19.07±0.09	18.05±0.24	1.855±0.032
2MASXJ13020865+2823139	12.16±0.01	11.01±0.02	4.61±0.11	5.61±0.17	17.37±0.05	16.56±0.07	2.213±0.020
2MASXJ13010904+2821352	13.13±0.03	12.51±0.05	4.88±0.39	2.65±0.39	18.48±0.18	16.44±0.33	1.879±0.018
2MASXJ13005207+2821581	11.82±0.01	10.80±0.01	3.89±0.10	4.27±0.10	16.67±0.06	15.75±0.05	2.240±0.010
2MASXJ13004423+2820146	12.52±0.02	11.78±0.03	3.41±0.03	2.82±0.20	17.08±0.02	15.82±0.16	2.098±0.010
2MASXJ13003074+2820466	11.70±0.01	10.78±0.01	6.63±0.08	6.03±0.15	17.72±0.03	16.53±0.06	2.205±0.009
2MASXJ13023199+2826223	14.07±0.13	13.44±0.16	5.11±0.84	3.70±0.76	19.53±0.38	18.12±0.48	1.776±0.064
2MASXJ12575392+2829594	13.40±0.07	12.46±0.06	1.15±0.28	1.69±0.21	15.60±0.54	15.42±0.28	2.121±0.012
2MASXJ12593568+2833047	13.16±0.05	12.25±0.04	2.07±0.42	2.26±0.11	16.64±0.44	15.82±0.11	2.113±0.012
2MASXJ12565652+2837238	12.75±0.03	11.97±0.03	4.05±0.19	2.95±0.16	17.70±0.11	16.14±0.13	2.036±0.013

Tab. 3.5: Corrections, measurement and systematic errors for the Norma cluster early-type galaxies. The photometric measurements were obtained using the NTT/SOFI K_s-band images. The extinction correction presented in this table is from Schlafly & Finkbeiner (2011) — refer to §3.2.4 for details.

	Correction	Error	S/M
(1)	(2)	(3)	(4)
Star-subtraction [mag]	−0.0106	0.0003	M
Sky background [mag]	−0.008	0.020	M
σ-aperture correction [dex]	−0.015	-	M
σ-run offset [dex]	0.012	0.007	M
Seeing correction [″]	0.001 – 2.607	-	M
Malmquist bias [%]	0.587	-	S
Extinction correction [mag]	0.057 – 0.088	-	S
k-correction [mag]	0.042 – 0.071	-	S
Cosmological dimming [mag]	0.051 – 0.091	-	S

NOTES:
Column 1 represents the different corrections applied to the spectroscopic and photometric measurements for the Norma sample. Column 2 is the mean value of the correction. Where the correction was applied to individual galaxies, the range is given. Column 3 is the error on the mean value. M and S given in column 4 refer to the type, i.e., measurement and systematic errors, respectively. For the measurement errors and the corrections applied to the J and K_s-band photometric parameters, refer to Table 3.6.

Tab. 3.6: Corrections, measurement and systematic errors for the Norma cluster early-type galaxies. The extinction correction presented in this table is from the re-calibration presented in §3.2.5 i.e., using the extinction correction factor of 0.81 for the Norma sample.

	Applied correction for each band		Type: S/M
	J	K_s	
(1)	(2)	(3)	(4)
Star-subtraction [mag]	−0.0143	−0.0135	M
Sky background [mag]	−0.011	−0.008	M
Seeing correction [″]	0.134 – 2.418	0.085 – 2.227	M
Malmquist bias [%]	0.652	0.589	S
Extinction correction [mag]	0.147 – 0.200	0.060 – 0.081	S
k-correction [mag]	0.008 – 0.016	0.037 – 0.076	S
Cosmological dimming [mag]	0.049 – 0.099	0.049 – 0.099	S

Tab. 3.7: Summary of the comparison between the total extrapolated magnitude from the 2MASS XSC and this work. The Δm is the difference between the 2MASS XSC and this work, where, Δm = (2MASS XSC – THIS WORK).

Band	Δm (mean)	Δm (median)	σ	N
J	–0.003	–0.023	0.151	121
K_s	–0.015	–0.014	0.100	121

3.6 The Fundamental Plane Projections

The results presented in this section have been published in the Monthly Notices of the Royal Astronomical Society, see Mutabazi et al. (2014). Before discussing the procedure used to fit the Fundamental Plane, I first present here, the various projections of the Fundamental Plane for both the Norma and Coma samples used in the K_s-band Fundamental Plane analysis based on the NTT/SOFI data for the Norma cluster. The top left-hand panel of Figure 3.20 shows the Kormendy relation (Kormendy, 1977) which relates the effective surface brightness and effective radius for early-type galaxies (see e.g., Longhetti et al. 2007; Nigoche-Netro et al. 2008). The Norma cluster sample galaxies are represented by the red filled squares. The Coma cluster sample, which I have used as a calibrator, has been subdivided into two; the galaxies with central velocity dispersions less than 100 km s^{-1} are represented by the blue empty circles, while the filled black circles represent galaxies in the Coma sample with $\sigma \geq 100$ km s^{-1}. There are 79 galaxies in the Coma sample with $\log \sigma \geq 2$. This constitutes $\sim 65\%$ of the total Coma cluster sample while 94% of the galaxies in the Norma cluster sample have $\log \sigma \geq 2$, that is, only two galaxies in the Norma cluster sample have $\sigma < 100$ km s^{-1}.

The projections were to check the distribution of the Fundamental Plane data (effective radii, mean effective surface brightnesses and the central velocity dispersions) for both the Norma and Coma cluster samples. The three panels clearly show that there are more faint early-type galaxies (low central velocity dispersions represented by the blue open circles) from the Coma cluster sample than there are from the Norma cluster sample. I therefore conducted simulations to study the effect of the low central velocity dispersion galaxies on the Fundamental Plane results (see §3.7.1.4).

3.7 Relative Distances — Norma and Coma Clusters

In measuring the distance to the Norma cluster, the Coma cluster sample was used as a calibrator, on the assumption that the Coma cluster has a zero peculiar velocity, that is, the Coma cluster is at rest with respect to the CMB frame. Various measurements support this assumption, for example, the SMAC survey (Smith, 1999; Bernardi et al., 2002; Hudson et al., 2004) and the SFI++ survey (Springob et al., 2007). The relative distance between the Norma and Coma clusters was computed from the measured zero point offset (see §3.7.5). This was done using three slightly different techniques:

- fitting the Fundamental Plane using the simultaneous inverse regression method,
- fitting the Fundamental Plane using the MIST algorithm, and
- using a modified Faber-Jackson relation.

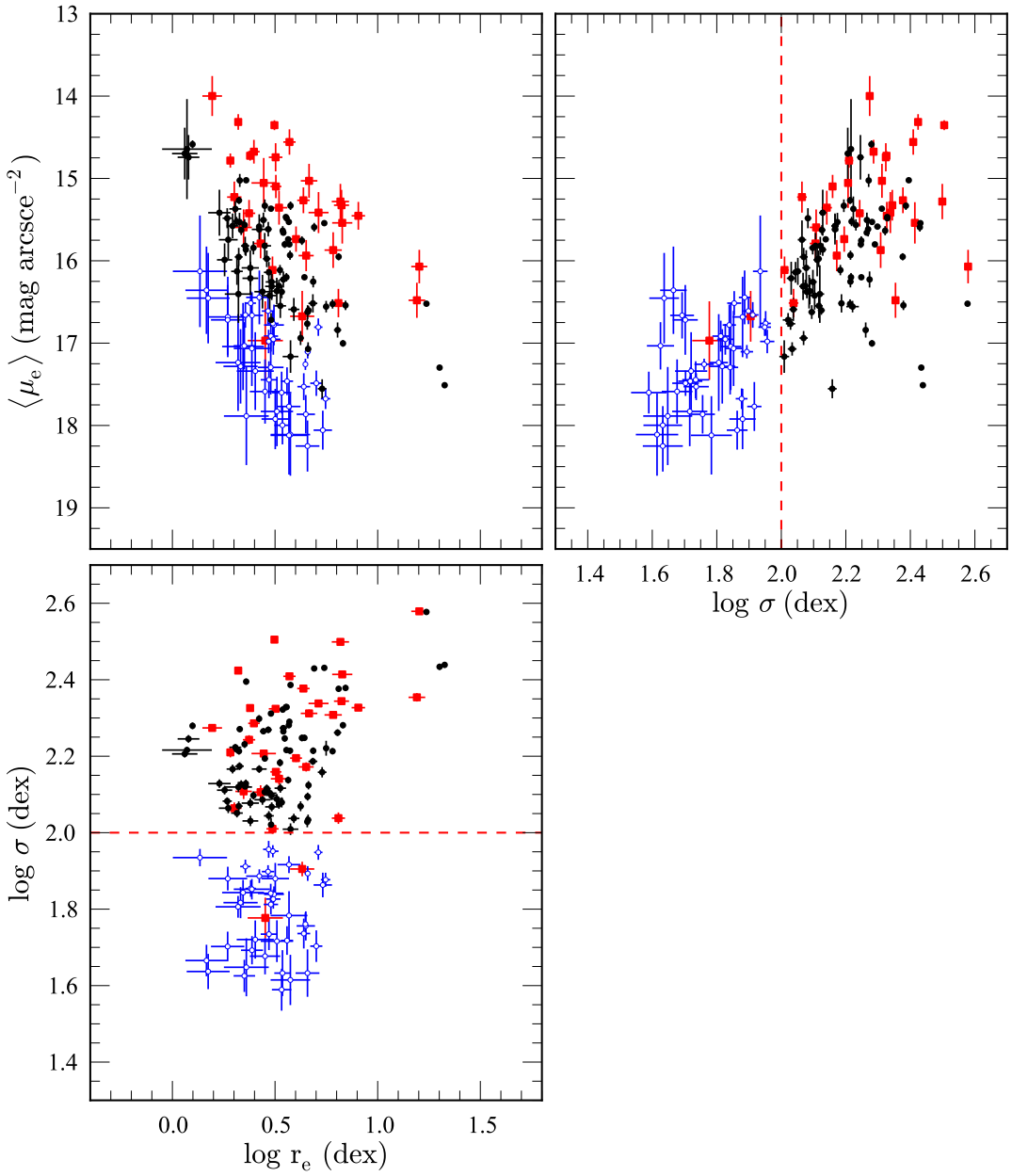

Fig. 3.20: Fundamental Plane projections; the top left-hand panel shows the Kormendy relation. The galaxies in the Norma cluster sample (only the NTT/SOFI data) are represented by the red filled squares. The open blue and the black filled circles represent, respectively, the Coma cluster galaxies with central velocity dispersions less than 100 km s^{-1} and those with $\log\sigma \geq 2$. The vertical and horizontal red dotted lines represent $\log\sigma = 2$.

3.7.1 K_s-band Fundamental Plane Results using the NTT/SOFI Data

The above three methods were applied while using the NTT/SOFI K_s-band data and showed excellent agreement (see Table 3.8). However, the simultaneous inverse regression method was associated with a reduced scatter and was therefore adopted as the best method to measure the distance and peculiar velocity for the Norma cluster. Having tested the three methods on the NTT/SOFI K_s-band data, I adopted the best method (simultaneous inverse regression) for the J and K_s-band Fundamental Plane analyses as well as the combined K_s-band data.

3.7.1.1 Fitting the Fundamental Plane: the Inverse Regression Method

As shown earlier in Chapter 1 (Equation 1.18), the Fundamental Plane relation can be written in the form

$$\log r_e = a \log\sigma + b \langle\mu_e\rangle + c, \tag{3.40}$$

where r_e is the effective radius, $\langle\mu_e\rangle$ is the mean effective surface brightness, σ is the central velocity dispersion and a, b, and c are the Fundamental Plane fit parameters.

To minimise the effect of sample selection biases and the effect of outliers, the Fundamental Plane fit parameters were obtained by minimising the absolute residuals along the $\log\sigma$ direction (Jorgensen et al., 1996; La Barbera et al., 2010). A simultaneous fit was therefore performed by constraining the Fundamental Plane parameters a and b to be the same for both the Norma and Coma clusters. Since the Fundamental Plane intercept, c is a measure of distance and given the fact that Norma and Coma clusters lie at different distances, the intercepts were allowed to vary between the two clusters.

From the simultaneous fit performed by minimising the absolute residuals along the $\log\sigma$ direction, the measured Fundamental Plane parameters are $a = 1.465 \pm 0.059$, $b = 0.326 \pm 0.020$, and an rms scatter, Δ_σ, of ~ 0.083 dex in $\log\sigma$. The zero point offset between the two clusters is 0.154 ± 0.014 dex in $\log r_e$ (see Table 3.11 for a summary of results from the Fundamental Plane analyses). Figure 3.21 shows the projected Fundamental Plane; the Norma cluster which is represented by the red filled circles has been shifted to the Coma distance. Note that this is based on high quality NTT/SOFI data for the Norma cluster sample. The error in the individual galaxy distances is given by $\Delta_g = a\ln(10)\Delta_\sigma$. For cluster distances, the error decreases according to the number of galaxies (N) in the sample, and is given by $\Delta_g/\sqrt{N}$. The measured rms therefore implies an uncertainty of $\sim 28\%$ in distances measured to the individual Norma cluster galaxies. This reduces to an error of $\sim 5\%$ for the distance to the Norma cluster. However, one needs to correct for the effect of Malmquist bias.

3.7.1.2 Malmquist Bias Correction

In order to obtain reliable peculiar velocities using distance indicators, the Malmquist bias correction is necessary. The Malmquist bias was originally used to describe the bias which results from the fact that the mean luminosity of the observable galaxies in any magnitude or flux limited survey will be brighter than the mean luminosity of the underlying population (Malmquist, 1920, 1922, 1924). The term was later used to refer to the bias associated with the use of distance indicators when the galaxy distribution along the line of sight is not constant (Lynden-Bell et al., 1988).

For true distance, r, the number of galaxies along the line of sight increases as r^2 (assuming a homogeneous distribution of galaxies in the Universe). However, distance indicators are associated with a significant error. For a given distance, d, measured using a distance indicator with uncertainty, δd, the range of distances are $d - \delta d$ to $d + \delta d$. Since the number density along the line of sight increases as r^2, more galaxies are likely to "scatter in" from greater true distances that they "scatter out" from lower true distances. This implies that the average d will underestimate the true distance, r. For a constant density field, the measured distance, d, can be rescaled by a constant factor to yield the expected true distance (Lynden-Bell et al., 1988). This is the homogeneous Malmquist bias (see for example, Hudson, 1994b; Giovanelli et al., 1998b).

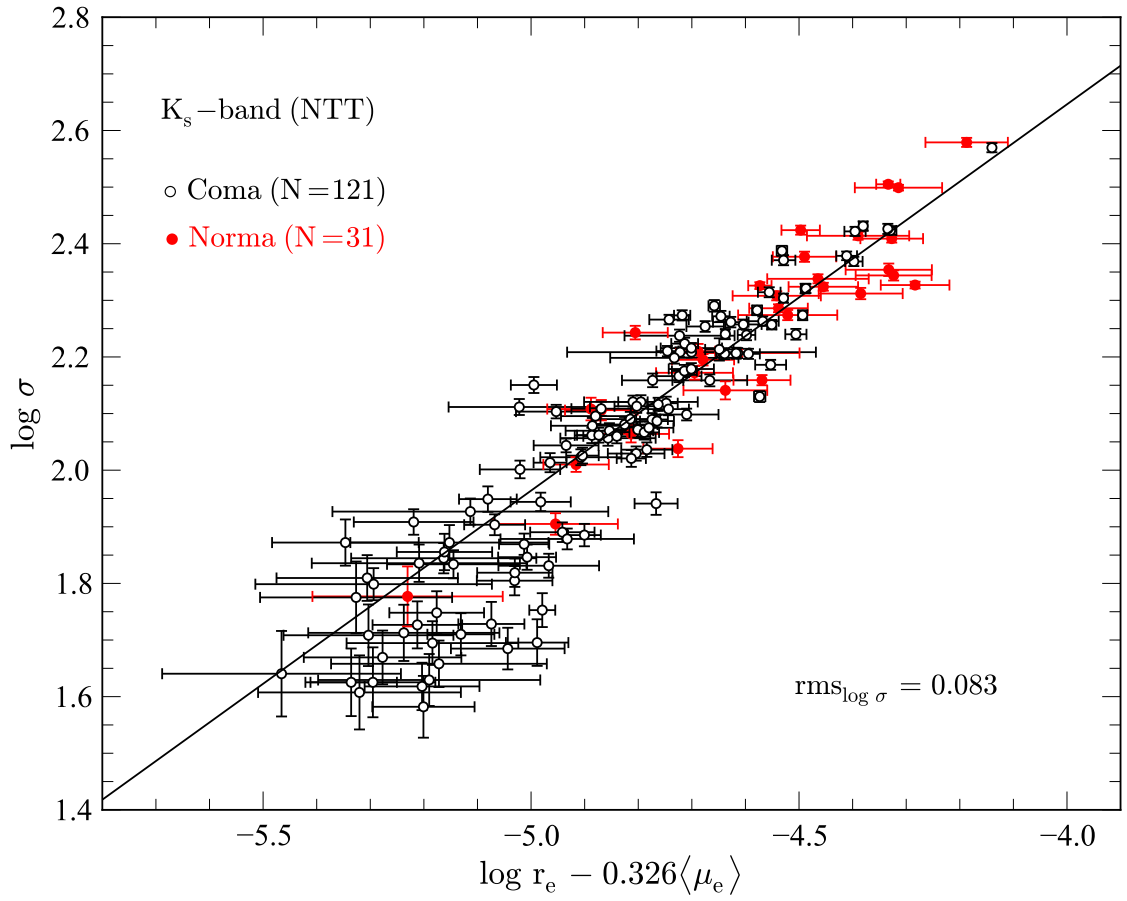

Fig. 3.21: K_s-band Fundamental Plane projection, obtained by simultaneously minimising absolute residuals along $\log\sigma$; for the Coma cluster (empty circles), and the Norma cluster (red filled circles). The Norma cluster has been shifted by applying the Fundamental Plane zero point offset so that the Norma cluster lies at the Coma cluster's distance.

I have therefore only corrected for the homogeneous Malmquist bias whose effect is a rescaling of the cluster distance by a multiplicative factor. This correction thus depends on the uncertainty associated with the distance indicator and the measured cluster distance; the effect increases with distance but also reduces with the number of galaxies in the cluster sample. For a measured distance d, the distance corrected for the homogeneous Malmquist bias is given by $d\exp(3.5\Delta_g^2/N)$ (Lynden-Bell et al., 1988; Hudson et al., 1997). For the measured distance to the Norma cluster, this bias correction is only 0.59% (equivalent to 29 km s^{-1} at the measured Norma cluster distance). Note that I obtained a Malmquist bias correction of 0.59% by considering the rms for only the Norma cluster galaxies . This is smaller than the 0.083 dex for the Norma+Coma samples.

Inhomogeneous Malmquist bias arises from variations in galaxy number density along the line of sight. The effect is such that, if the galaxy distribution peaks at true distance, $r_{\rm peak}$, along the line of sight, distances inferred from $d < r_{\rm peak}$ will underestimate the true distance while distances inferred from $d > r_{\rm peak}$ will be overestimated. Note that the existence of such a peak in the number density does not affect the observed recessional velocity. This results in more positive peculiar velocities where distances are underestimated and vice versa. A correction for the inhomogeneous Malmquist bias therefore requires a model for the density field (Willick et al.,

1997). The effect is more significant for field galaxies than galaxy clusters (see for example, Dekel, 1994; Hudson, 1994b; Strauss & Willick, 1995). The inhomogeneous Malmquist bias in my analysis was assumed to be negligible for galaxy clusters.

3.7.1.3 Fundamental Plane using the MIST Algorithm

For comparison, I fitted the Fundamental Plane using the MIST (Measurement errors and Intrinsic Scatter Three dimensional) algorithm (La Barbera et al., 2000). The MIST algorithm is a bisector least-squares fit, used to determine the Fundamental Plane parameters a, b, and c. The statistical errors on the Fundamental Plane coefficients are computed through an inbuilt bootstrap procedure. The MIST algorithm can also be used to fit the Fundamental Plane by regressing along any of the three directions ($\log\sigma$, $\log r_e$ or $\langle\mu_e\rangle$). The average of the fit parameters obtained by regressing along the three directions approximates to those obtained using the bisector fit. For the MIST algorithm, I fitted the Coma cluster Fundamental Plane (by regressing along the $\log\sigma$-direction) and fixed the slopes a and b to determine the median value of the intercept, $c_{\rm N}$, for the Norma cluster. The individual errors on the Fundamental Plane intercept for Norma and Coma samples were each computed as

$$\frac{\rm rms}{\sqrt{(N-1)}}, \tag{3.41}$$

where N is the number of galaxies in the sample and rms is the scatter on the Fundamental Plane. The error in the Fundamental Plane zero point offset was computed using a simple propagation of the individual errors on the intercepts for Norma and Coma clusters. The Fundamental Plane zero point offset measured using this method is 0.154 ± 0.019 dex in $\log r_e$, corresponding to a distance ratio of 1.426 ± 0.062 (that is, an uncertainty of 4.4%).

3.7.1.4 Distribution of Fundamental Plane Fit Parameters

Using the MIST algorithm, I checked the consistency of the Fundamental Plane fit parameters obtained by regressing along the $\log\sigma$ direction. By re-sampling the Coma cluster (with replacement) 10000 times, I analysed the distribution of the Fundamental Plane parameters a, b, and c. Figure 3.22 (left-hand panels) shows the bootstrap results when all the 121 Coma early-type galaxies were used in the bootstrap procedure while the right-hand panels show the results for only Coma early-type galaxies brighter than $12^{\rm m}.5$ ($N = 78$, only 9% of these have $\log\sigma < 2$). The Fundamental Plane fit parameters in either case, are consistent with each other. The red solid curve is a Gaussian fit to the data. The mean value from the Gaussian fit of each of the Fundamental Plane parameters is indicated at the top part in each panel. The difference between the Fundamental Plane parameter from the original Coma data and that from the fitted distribution of the bootstrap results, is also indicated (as Δa, Δb, and Δc). The blue dotted curve shows the small shift in the Gaussian fit due to this difference, i.e., Δa, Δb, and Δc. The reason for imposing the magnitude cut of 12.5 mag is because such a cut results in a sub-sample dominated by Coma cluster early-type galaxies with $\log\sigma > 2$, thus making it possible to determine the effect of including early-type galaxies with central velocity dispersions less than 100 km s^{-1}, on the measured Norma distance. There is no significant change in the zero point offset with and without the magnitude cut, that is, the small shift Δc in Figure 3.22 (larger in the left-hand panels than the right-hand panels) is accompanied by small changes in the Fundamental Plane fit parameters Δa, and Δb, which in turn affect the intercept of Norma, thereby leaving no significant changes in the zero point offset.

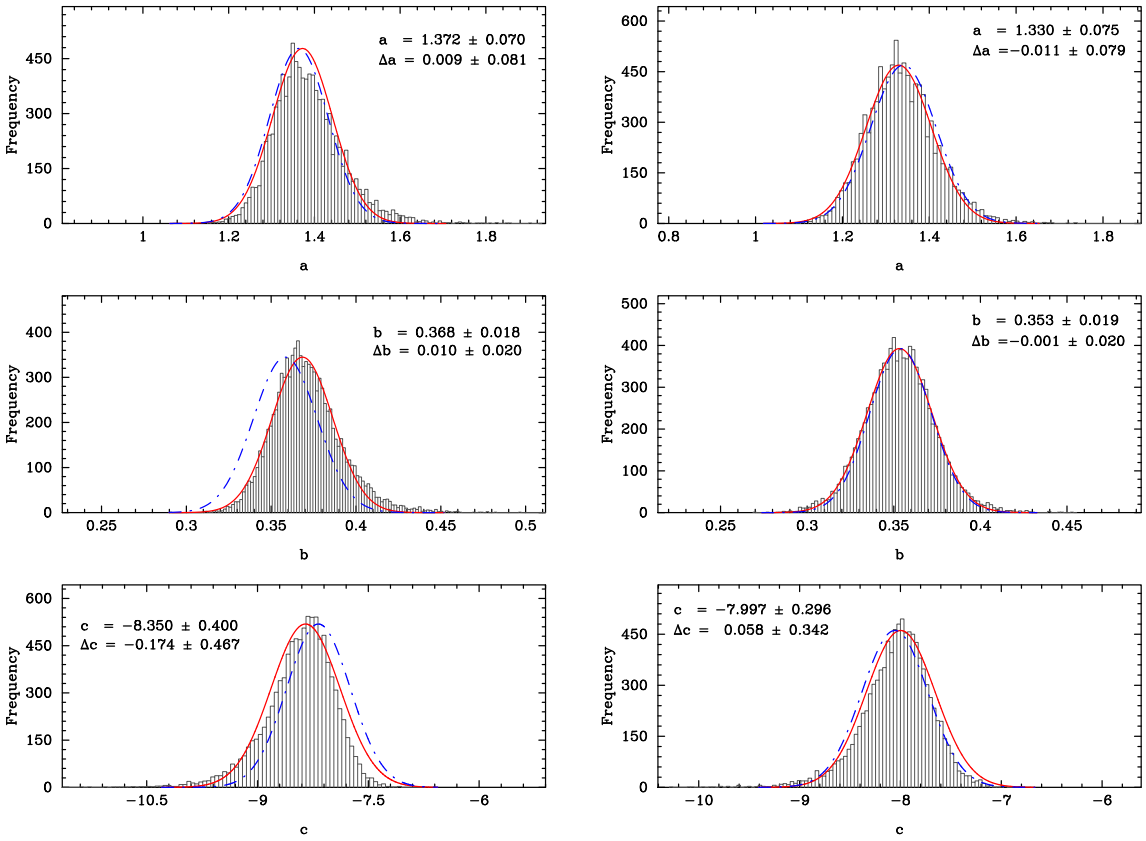

Fig. 3.22: The distribution of the Fundamental Plane fit parameters through bootstrap re-sampling. The MIST algorithm was used to determine the fit parameters a, b and c, by minimising along the $\log\sigma$- direction. The Coma cluster galaxies were randomly selected, with replacement 10000 times. The panels (top to bottom) show the distribution of the Fundamental Plane parameters (a, b, and c). The red curve is the Gaussian fit to the data. The blue curve represents the shift when the Gaussian fit parameters (mean and standard deviation) are replaced by Fundamental Plane fit parameters (fit parameter and its bootstrap error) obtained by fitting the original Coma data using the MIST algorithm. The difference is indicated by Δa, Δb, and Δc. These values are shown in the top right-hand corner (for Δa and Δb; see the top and middle panels) and in the left top corner (for Δc; see the bottom panel). In the right-hand panels, only the Coma early-type galaxies brighter than 12.5 mag were used in the re-sampling procedure (only 9% of the early-type galaxies in this subsample have $\log\sigma < 2$).

3.7.1.5 Fixed Metric Aperture Magnitudes: the Modified Faber-Jackson Relation

Relative distances can also be measured using the Faber-Jackson relation (Faber & Jackson, 1976) with galaxy magnitudes measured within a fixed and relatively small aperture radius (Lucey, 1986). Lucey (1986) found this approach to present a relatively smaller scatter compared to when total galaxy magnitudes were used in the $L_{\rm total}-\sigma$ relation. I have therefore adopted Lucey's approach for the $L-\sigma$ relation, using aperture magnitudes within a physical size of 2 kpc. For the Coma cluster distance, this corresponds to an aperture radius of 4.16 arcsec. The measured aperture magnitudes were PSF-corrected using GALFIT. If Norma has zero peculiar velocity then the 2 kpc radius corresponds to a size of 5.99 arcsec. For each galaxy in the Norma sample, I determined a set of PSF-corrected aperture magnitudes that spanned a range of possible Norma cluster distances, given r = 5.99 arcsec corresponds to a zero peculiar velocity for the Norma cluster. Galactic extinction and k-corrections were applied to the PSF-corrected aperture magnitudes of both Coma and Norma galaxies. A simultaneous fit was performed by minimising the absolute residuals along the $\log\sigma$ direction. In the fitting process, the slope and intercepts were determined and constrained so that both the Norma and Coma clusters have

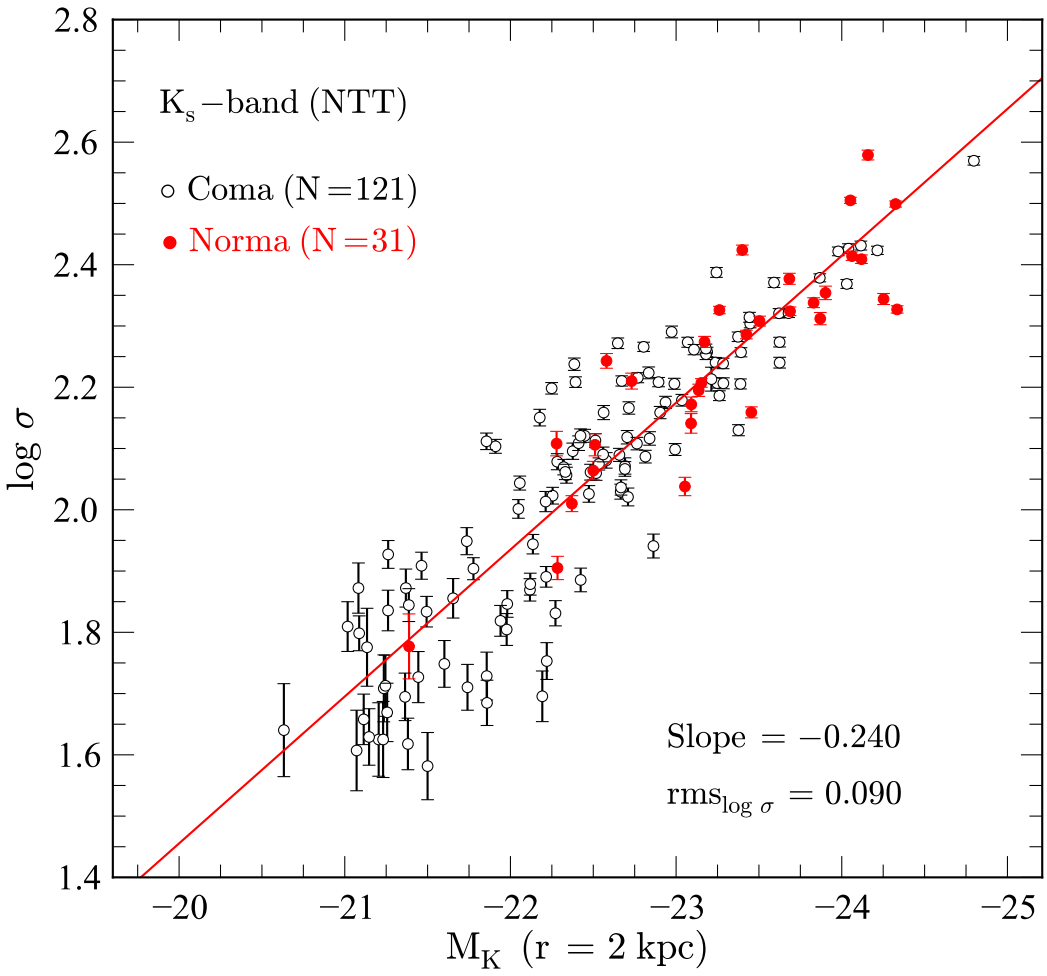

Fig. 3.23: The Faber-Jackson relation, based on aperture photometry using an aperture radius equal to 2 kpc. The black open circles represent the Coma cluster. The Norma cluster (red filled circles) has been shifted to the Coma distance.

the same slope. Figure 3.23 shows the fit results; the Norma cluster is represented by the red solid circles while the Coma cluster is represented by the black open circles. The measured zero point offset using this approach is 0.159 ± 0.022, which is in very good agreement with the values measured using the Fundamental Plane. Table 3.8 presents a summary of the measured zero point offset between the Norma and Coma clusters using the three different methods. The measured zero point offsets are consistent with each other. Note that the results presented in Table 3.8 are based on the photometry data from the NTT/SOFI images for the Norma cluster. For the J and K_s-band Fundamental Plane results, and the results from the combined K_s-band data, refer to Table 3.11.

From Table 3.8, the best method is the inverse least-squares fit since it is associated with the least measurement error on the zero point offset. I therefore applied this method to perform the J and K_s-band Fundamental Plane analyses using the IRSF/SIRIUS data and the combined K_s-band sample (see §3.7.2 and §3.7.3).

Tab. 3.8: Summary: zero point offset between Coma and Norma clusters by regressing along $\log \sigma$ using the MIST algorithm (FP: MIST), simultaneous least-squares Fundamental Plane fit (FP: SLS), and the modified Faber-Jackson relation ($L-\sigma$).

Method	Δc
FP: SLS	0.154 ± 0.014
FP: MIST	0.154 ± 0.019
$L-\sigma$	0.159 ± 0.022

NOTES: $L-\sigma$ is the modified Faber-Jackson relation, where aperture magnitudes within 2 kpc were used. The derivation of the ratio of angular diameter distance and the peculiar velocity is described under §3.7.5.

3.7.2 J and K_s-band Fundamental Plane – Fit Results

The photometric data for the Norma cluster sample used in the J- and K_s-band Fundamental Plane analyses presented in this section, are based only on the IRSF/SIRIUS NIR imaging. A total of 31 early-type galaxies in the Norma cluster were used in this analysis along with 121 early-type galaxies within the Coma cluster. The Fundamental Plane was fitted using the inverse least-squares fitting method as described earlier (see §3.7.1.1). The left- and right-hand panels of Figure 3.25 show the Fundamental Plane projection for the J- and K_s-band, respectively. The Norma cluster galaxies, which have been shifted to the Coma cluster distance, are represented by the red filled circles. A summary of the Fundamental Plane fit parameters is presented in Table 3.9.

The Fundamental Plane zero point offset measured using the J-band is comparable to that measured using the K_s-band, that is, 0.149 ± 0.016 dex versus 0.145 ± 0.014 dex. This is expected given the good comparison between the J and K_s-band PSF-corrected effective radii (see Figure 3.24). For the 31 Norma cluster early-type galaxies with IRSF photometry, the average difference is 0.023 dex with a scatter of 0.061 dex. The J-band effective radii are on average, 4% larger than those measured in the K_s-band. For comparison, the Coma cluster (reference sample) is shown in the right-hand panel. However, including the J-band in this analysis made it possible to investigate the Galactic extinction correction at low Galactic latitudes where the Schlegel et al. (1998) reddening maps are uncalibrated (see §3.2.5 on page 81).

3.7.3 Combined K_s-band Fundamental Plane

The combined K_s-band Fundamental Plane analysis was performed using the combined IRSF/SIRIUS and NTT/SOFI data. In combining the two datasets, the NTT/SOFI data were given preference, that is, a galaxy from the IRSF/SIRIUS dataset was added only if such a galaxy did not exist in the NTT/SOFI sample, and if a given galaxy existed in both the NTT/SOFI and IRSF/SIRIUS samples, the NTT/SOFI data were used[4]. The combined sample resulted in a total of 41 early-type galaxies within the Norma cluster. As for the K_s-band Fundamental Plane analysis using only the SOFI data, the Fundamental Plane for the combined SOFI and SIRIUS data was fitted using a simple inverse least-squares fit by simultaneously fitting both the Norma and Coma samples (refer to §3.7.1.1 for details). Figure 3.26 shows the Fundamental Plane projection of the combined IRSF/SIRIUS and NTT/SOFI K_s-band data. A summary of results from this combined K_s-band Fundamental Plane analysis is included in Table 3.9.

[4]SOFI has a pixel scale of $0\farcs29$ while SIRIUS has a pixel scale of $0\farcs45$. The effect of seeing for the NTT/SOFI observations is also lower than that for the IRSF/SIRIUS observations. Hence the NIR images for the former have a higher resolution (hence high signal-to-noise ratio) than the latter.

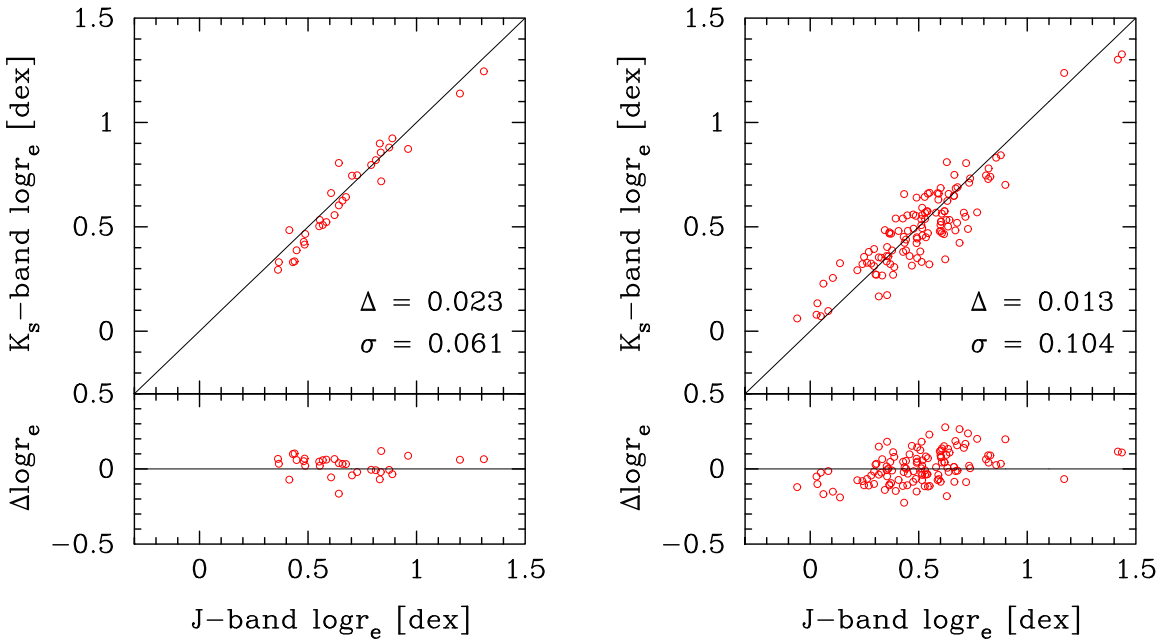

Fig. 3.24: Comparison of the PSF-corrected effective radii for the Norma cluster (left-hand panel) and the Coma cluster (right-hand panel). The J and K_s-band measured effective radii corrected for the seeing effects are shown on the x-axis and y-axis, respectively. The black solid lines in the upper subpanels represents a one-to-one relation.

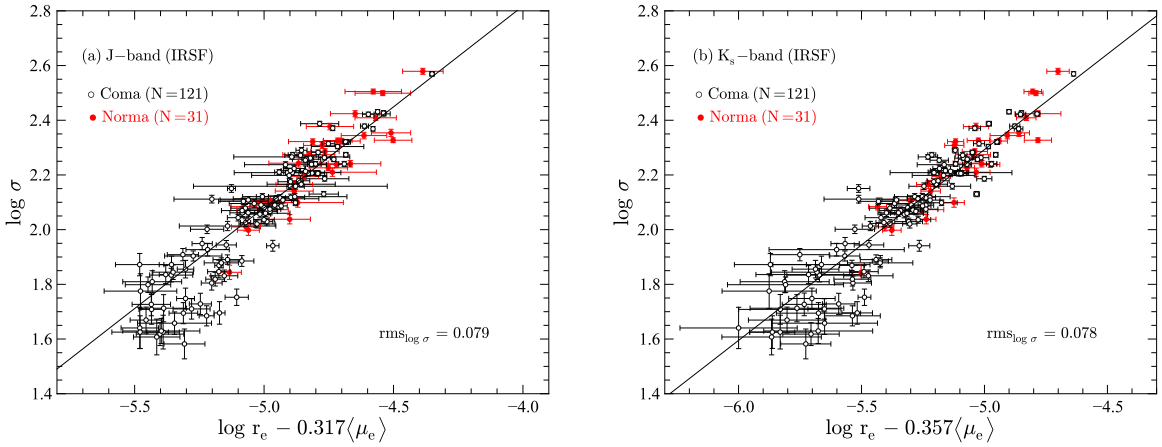

Fig. 3.25: The J and K_s-band Fundamental Plane based on 31 early-type galaxies from the IRSF data (for the Norma cluster). For the Coma cluster, 121 early-type galaxies were used. The left- and right-hand panels represent the J- and K_s-band Fundamental Plane projections, respectively. The Norma cluster which is represented by the red filled circles has been shifted to the Coma cluster's distance.

3.7.4 Fundamental Plane from Literature

The observed Fundamental Plane fit parameters have been found to not only deviate from the virial expectation but also differ depending on the type of fitting method used. For example, D'Onofrio et al. (2008) measured Fundamental Plane fit parameters for early-type galaxies in 59 clusters at redshifts $0.04< z <0.07$ and obtained $a = 1.239$, $b = 0.342$, $c = -9.15$, rms = 0.080 for 80 galaxies within the Coma cluster (using the MIST algorithm) but obtained different parameters using the orthogonal fit, i.e., $a = 1.439$, $b = 0.345$, $c = -9.67$, rms = 0.077. The slope, a, is usually higher when the minimisation is performed along the $\log\sigma$ direction (La Barbera et al., 2000).

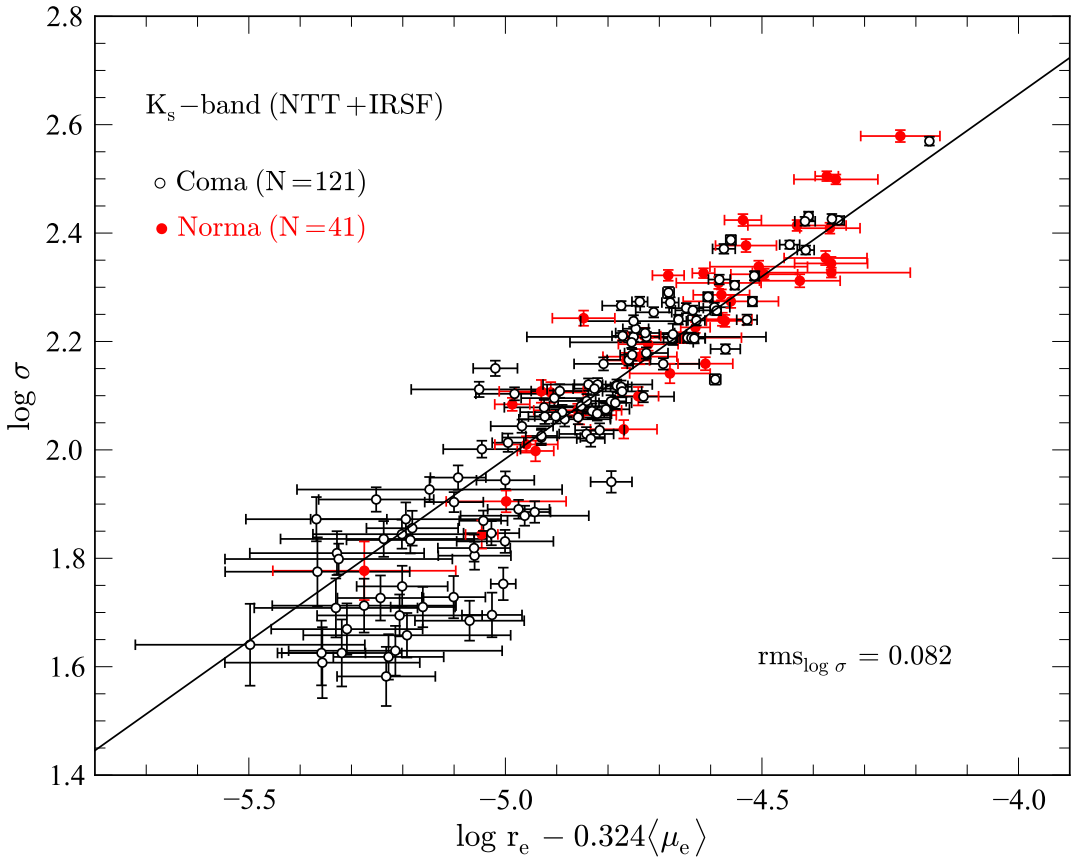

Fig. 3.26: The combined K_s-band Fundamental Plane projection. The analysis was performed on 41 Norma cluster early-type galaxies from the IRSF/SIRIUS and NTT/SOFI data and 121 galaxies from the Coma cluster (black open circles). The Norma cluster galaxies (red filled circles) have been shifted to the Coma cluster distance.

Tab. 3.9: The J- and K_s-band Fundamental Plane fit parameters and the corresponding uncertainty in distance measurements to individual galaxies in the Norma cluster. The first column indicates the source of the data (photometry) used. Column 5 represents the Fundamental Plane zero point offset. Column 6 represents the rms scatter in $\log\sigma$ while column 7 represents the percentage uncertainty in the distance to the individual Norma cluster galaxies, given by $[a \times \ln(10) \times \mathrm{rms}]$. Column 8 indicates the number of Norma cluster galaxies used in the analysis; this is 121 for the Coma cluster. The Fundamental Plane parameters a, b and Δc were obtained using a simultaneous fit performed by minimising the absolute residuals along the $\log\sigma$ direction.

Sample	Filter	a	b	Δc	rms	% err	N
(1)	(2)	(3)	(4)	(5)	(6)	(7)	(8)
IRSF	J	1.356 ± 0.058	0.317 ± 0.018	0.149 ± 0.016	0.079	25	31
IRSF	K_s	1.470 ± 0.053	0.357 ± 0.019	0.145 ± 0.014	0.078	26	31
NTT+IRSF	K_s	1.551 ± 0.053	0.324 ± 0.017	0.150 ± 0.013	0.082	29	41

In addition, the fit parameters have been found to be wavelength dependent (Recillas-Cruz et al., 1990; Hyde & Bernardi, 2009; La Barbera et al., 2010) with the slope, a, steepening from the optical to near-infrared wavelengths (see Figure 3.27, which was taken from La Barbera et al. 2010). In Figure 3.27, the dashed dark-grey line corresponds to a Fundamental Plane projection with slope, a, measured in the r-band. Using this as a reference, the variation in the slope from the g-band through to the K-band is clearly indicated by the light-grey solid lines which represent the Fundamental Plane slope, a, measured in each of the filters. The measured fit

parameters (a and b) however, still differ from those expected from the virial theorem. This deviation of the observed Fundamental Plane fit parameters a and b from the expected, is referred to as the 'Fundamental Plane tilt'.

The tilt in the Fundamental Plane has been, and is still, a subject of debate with suggestions that it partly results from a break in structural homology (Busarello et al., 1997; Pahre et al., 1995, 1998a, 1998b). The break in structural homology implies that early-type galaxies slightly differ in their dynamical structure. For example, their surface brightness profiles are best fit with $r^{1/n}$ rather than the simple de Vaucouleurs $r^{1/4}$ profile (Caon et al., 1993; Bertin et al., 2002). La Barbera et al. (2010) argued that the Fundamental Plane tilt in the near-infrared is not due to stellar population variation while Hyde & Bernardi (2009) argue that if low luminosity objects are missing in the Fundamental Plane analysis, then, a and b are both biased low. They also argue that when low/small velocity dispersion galaxies are missing, the slope, a, is biased high — and that these affect the orthogonal fit more than the direct fitting method. Such low velocity dispersion measurements (less than 100 km s^{-1}) can have large systematic and random errors and hence bias Fundamental Plane results (Jorgensen et al., 1995; Gargiulo et al., 2009). However, the inverse Fundamental Plane fit parameters where the regression is performed along the $\log \sigma$ direction, are less affected (Hudson et al., 1997).

Bernardi et al. (2003) have argued in support of the direct fit as a better method of fitting if the Fundamental Plane is to be used to measure relative distances (also see Saulder et al. 2013). In this case, the residuals along the distance dependent parameter, r_e, are minimised. This however biases the Fundamental Plane fit parameters unless a proper correction for sample incompleteness and selection bias (magnitude limits) is applied (Hudson et al., 1997). In Table 3.10, I summarise some of the Fundamental Plane studies by different authors (author reference indicated in column 1). Table 3.10 covers the majority of the past Fundamental Plane studies, where the author list is in chronological order starting with the earlier to the more recent studies. The corresponding filter used for observations is indicated in column 2. The total number of galaxies used in the study and the Fundamental Plane fit parameters a and b are, respectively indicated in columns 3, 4, and 5. Column 6 gives, where available, the percentage error on the distance to individual galaxies from their Fundamental Plane analysis. Column 7 shows the method used to determine the Fundamental Plane fit parameters. Note that the photometric variable $\langle \mu_e \rangle$ in mag arcsec^{-2} can also be replaced with $\langle I_e \rangle$ in flux units, that is, $L_\odot$ pc^{-2} where $\langle \mu_e \rangle \sim -2.5 \times \log(\langle I_e \rangle)$. This implies that the virial expectation would be $(a, b) = (2, -1)$. Therefore, the value of b presented in the table both from this work and other studies where $\langle \mu_e \rangle$ was used have been rescaled using $b' = -2.5 \times b$. Clearly, the Fundamental Plane parameters vary between the choice of the fitting method (see e.g., direct versus orthogonal method by Hyde & Bernardi 2009). Higher values for the slope, a, seem to be more associated with the orthogonal, inverse least-squares and the maximum likelihood fitting methods. The origin of the biases due to different fitting methods has been explored and explained in more detail by Magoulas et al. (2012).

3.7.5 Distance and Peculiar Velocity of the Norma Cluster

In the previous section (§3.7), different approaches were used to measure the zero point offset between the Coma and Norma clusters. It was found out that, the simultaneous inverse least-squares has the least scatter on the measured zero point offset compared to the MIST algorithm and the modified Faber-Jackson relation. I hereafter, adopt the best measured (least scatter/measurement error) zero point offset of 0.150 ± 0.013 dex from the simultaneous inverse least-squares fit to the combined K_s-band Fundamental Plane. The ratio of the angular diameter

Tab. 3.10: Fundamental Plane studies taken from literature, the source or author is given in column 1, the Fundamental Plane best fit parameters a and b' as well as the method used to obtain the fit parameters are given. Columns 2 and 3 represent the different observation filter and the total number of galaxies used in fitting the Fundamental Plane, respectively. Also presented in column 6 is, where available, the percentage uncertainty in the individual galaxy distances resulting from the rms or scatter on the Fundamental Plane in their study.

Source	Band	N	a	b'	σ_d	Method (fit)
			2	−1		Virial theorem
Dressler et al. (1987)	B	97	1.33±0.05	−0.83±0.03	20	Inverse regression
Djorgovski & Davis (1987)	$r+G$	106	1.39±0.14	−0.90±0.09	20	2-step inv. regression
Lucey et al. (1991a)	V	66	1.26±0.07	−0.82±0.09	17	Forward regression
Guzman et al. (1993)	V	37	1.14	−0.79	17	Forward regression
Jorgensen et al. (1996)	r	226	1.24±0.07	−0.82±0.02	17	Orthogonal regression
Hudson et al. (1997)	R	352	1.38±0.04	−0.82±0.03	21	Inverse regression
Scodeggio et al. (1997)	I	109	1.25±0.02	−0.79±0.03	20	Direct/mean regression
Pahre et al. (1998b)	K	251	1.53±0.08	−0.79±0.03	21	Orthogonal regression
Müller et al. (1998)	R	40	1.25	−0.87	19	Orthogonal regression
Mobasher et al. (1999)	K	48	1.38±0.26	−0.75±0.05	17	-
Kelson et al. (2000)	V	30	1.31±0.13	−0.86±0.10	14	Orthogonal regression
Gibbons et al. (2001)	R	428	1.37±0.05	−0.84±0.03	21	Inverse regression
Colless et al. (2001b)	R	255	1.22±0.09	−0.84±0.03	20	Maximum Likelihood
Bernardi et al. (2003)	g	5825	1.45±0.06	−0.74±0.01	20	Maximum Likelihood
Bernardi et al. (2003)	r	8228	1.49±0.05	−0.75±0.01	20	Maximum Likelihood
Bernardi et al. (2003)	i	8022	1.52±0.05	−0.78±0.01	20	Maximum Likelihood
Bernardi et al. (2003)	z	7914	1.51±0.05	−0.77±0.01	20	Maximum Likelihood
Hudson et al. (2004)	$V+R$	694	1.43±0.03	−0.84±0.02	21	Inverse regression
D'Onofrio et al. (2008)	V	-	1.21±0.05	−0.80±0.01	-	Orthogonal regression
La Barbera et al. (2008)	K	1430	1.53±0.04	−0.77±0.01	28	Orthogonal regression
La Barbera et al. (2008)	r	1430	1.42±0.05	−0.76±0.01	29	Orthogonal regression
Gargiulo et al. (2009)	R	91	1.35±0.11	−0.81±0.03	21	Orthogonal regression
Hyde & Bernardi (2009)	g	46410	1.40±0.05	−0.76±0.02	31	Orthogonal regression
Hyde & Bernardi (2009)	r	46410	1.43±0.05	−0.79±0.02	30	Orthogonal regression
Hyde & Bernardi (2009)	i	46410	1.46±0.05	−0.80±0.02	29	Orthogonal regression
Hyde & Bernardi (2009)	z	46410	1.47±0.05	−0.83±0.02	29	Orthogonal regression
Hyde & Bernardi (2009)	g	46410	1.12±0.05	−0.74±0.02	-	Direct regression
Hyde & Bernardi (2009)	r	46410	1.17±0.05	−0.76±0.02	-	Direct regression
Hyde & Bernardi (2009)	i	46410	1.20±0.05	−0.76±0.02	-	Direct regression
Hyde & Bernardi (2009)	z	46410	1.23±0.05	−0.78±0.02	-	Direct regression
Fraix-Burnet et al. (2010)	R	699	1.13±0.03	−0.84±0.01	-	Direct regression
La Barbera et al. (2010)	g	4589	1.38±0.02	−0.79±0.003	-	Orthogonal regression
La Barbera et al. (2010)	r	4589	1.39±0.02	−0.79±0.003	-	Orthogonal regression
La Barbera et al. (2010)	J	4589	1.53±0.02	−0.80±0.003	26	Orthogonal regression
La Barbera et al. (2010)	H	4589	1.56±0.02	−0.80±0.005	27	Orthogonal regression
La Barbera et al. (2010)	K	4589	1.55±0.02	−0.79±0.005	28	Orthogonal regression
Magoulas et al. (2012)	J	8901	1.52±0.03	−0.89±0.01	30	Maximum Likelihood
Magoulas et al. (2012)	H	8568	1.47±0.02	−0.88±0.01	29	Maximum Likelihood
Magoulas et al. (2012)	K	8573	1.46±0.02	−0.86±0.01	29	Maximum Likelihood
Saulder et al. (2013)	u	92953	0.80±0.03	−0.70±0.01	17	Direct regression
Saulder et al. (2013)	g	92953	0.97±0.03	−0.74±0.01	16	Direct regression
Saulder et al. (2013)	r	92953	1.03±0.03	−0.75±0.01	15	Direct regression
Saulder et al. (2013)	i	92953	1.06±0.03	−0.76±0.01	15	Direct regression
Saulder et al. (2013)	z	92953	1.11±0.03	−0.76±0.01	15	Direct regression
This work †	J	152	1.36±0.06	−0.79±0.04	25	Inverse regression
This work ††	K	152	1.47±0.06	−0.82±0.05	28	Inverse regression
This work †††	K	162	1.55±0.05	−0.81±0.04	29	Inverse regression

† Analysis using Norma cluster sample of 31 early-type galaxies (IRSF data) + 121 Coma cluster galaxies (calibration sample).
†† Analysis using Norma cluster sample of 31 early-type galaxies (NTT data) hence $N = 152$, calibration sample inclussive.
††† Analysis using Norma cluster sample of 41 early-type galaxies (IRSF+NTT data). Adding the calibration sample of 121 Coma cluster early-type galaxies implies that $N = 162$.

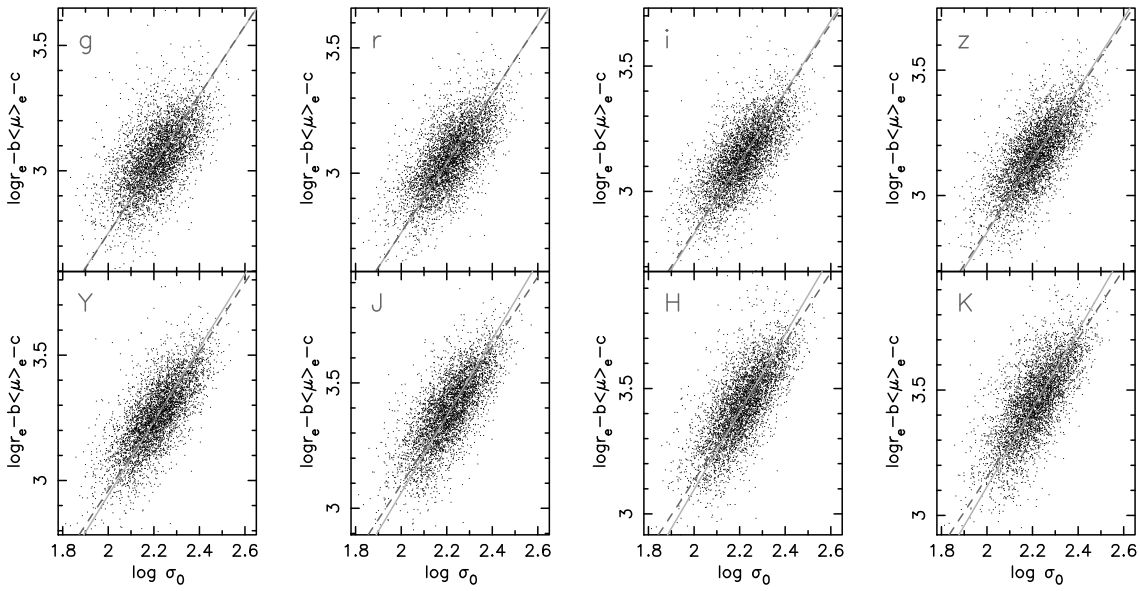

Fig. 3.27: The dependence of the Fundamental Plane on wavelength; shown is the edge-on projection of the Fundamental Plane in different filters: $grizYJHK$. The dashed dark-grey line corresponds to a Fundamental Plane projection with slope, a, measured in the r-band. This acts as a reference and shows the variation in the slope from the g-band through to the K-band. The light-grey solid lines represent the Fundamental Plane slope, a, measured in each of the filters. Figure reproduced from La Barbera et al. 2010, their figure 16.

distance is given by

$$\frac{D_A(\text{Coma})}{D_A(\text{Norma})} = 10^{\Delta c}. \tag{3.42}$$

Δc is the measured zero point offset between the Norma and Coma clusters and is given by $\Delta c = C_{\text{Norma}} - C_{\text{Coma}}$ where C_{Norma} and C_{Coma} are the Norma and Coma Fundamental Plane intercepts, respectively. Using Equation 3.42, this implies that the adopted zero point offset of 0.150 ± 0.013 dex results in an angular diameter distance ratio $\sim 1.414 \pm 0.042$.

The measured peculiar velocity is the line-of-sight component and is reported with respect to the cosmic microwave background. Therefore, the measured velocities must be transformed into the CMB rest frame. In the Local Group and CMB rest frame, the conversion of the heliocentric velocity adopted from Yahil et al. (1977) is

$$cz_{\text{LG}} = cz_{\odot} - 79\cos\ell\cos b + 296\sin\ell\cos b - 36\sin b\,; \tag{3.43}$$

$$cz_{\text{CMB}} = cz_{\text{LG}} + v_{\text{LG}}\left[\sin(b)\sin\left(b_{\text{CMB}}\right) + \cos(b)\cos\left(b_{\text{CMB}}\right)\cos\left(\left|\ell_{\text{CMB}} - \ell\right|\right)\right]. \tag{3.44}$$

$cz_{\odot} = 4871 \pm 54$ km s^{-1} (Woudt et al., 2008) is the Norma cluster's heliocentric velocity, $v_{\text{LG}} = 627$ km s^{-1} is the Local Group's peculiar velocity with respect to the CMB dipole, $(\ell_{\text{CMB}}, b_{\text{CMB}}) = (276°, 30°)$ is the Local Group's direction of motion in Galactic coordinates, and $(\ell, b) = (325.^{\circ}3, -7.^{\circ}2)$ is the central position of the Norma cluster in Galactic coordinates. For the Norma cluster, $cz_{\text{hel}} = 4871$ km s^{-1} translates into $cz_{\text{CMB}} = 4954 \pm 54$ km s^{-1} which is the same as the value taken from the NASA/IPAC Extragalactic Database (NED)[5]. In addition, it also agrees with the value obtained using the model by Fixsen et al. (1996), that is,

$$cz_{\text{CMB}} = v_{\text{hel}} + v_{\text{apex}}\left[\sin(b)\sin\left(b_{\text{apex}}\right) + \cos(b)\cos\left(b_{\text{apex}}\right)\cos\left(\left|\ell_{\text{apex}} - \ell\right|\right)\right]; \tag{3.45}$$

[5]The NASA/IPAC Extragalactic Database (NED) is operated by the Jet Propulsion Laboratory, California Institute of Technology, under contract with the National Aeronautics and Space Administration.

where $v_{\rm hel} = 4871$ km s^{-1}, $v_{\rm apex} = 371$ km s^{-1} is the peculiar velocity of the Sun, and the dipole direction is $(\ell_{\rm apex}, b_{\rm apex}) = (264.^{\circ}14, 48.^{\circ}26)$.

The peculiar velocity was derived from the measured relative angular diameter distance following Wright (2006). The measured zero point offset was used to measure the angular diameter distances (D_A) of the two clusters using

$$\log D_A\,(\text{Coma}) - \log D_A\,(\text{Norma}) = \Delta c = 0.150 \pm 0.013. \tag{3.46}$$

The assumption that the Coma cluster has zero peculiar velocity (Smith, 1999; Bernardi et al., 2002) implies that Coma's Hubble flow redshift is equal to the observed redshift in the local CMB rest frame, that is, $z_{\rm H} = z_{\rm CMB}$. For the Coma cluster, $z_{\rm CMB} = 0.02400 \pm 0.00016$ (Hudson et al., 2004) which for the adopted cosmology with $H_0 = 70.5\,{\rm km\,s^{-1}Mpc^{-1}}$, $\Omega_{\rm m} = 0.27$, and $\Omega_\Lambda = 0.73$, results in $\log D_A\,(\text{Coma}) = 1.996 \pm 0.003$ where the angular diameter distance is in Mpc. From Equation 3.46, $\log D_A\,(\text{Norma}) = 1.846 \pm 0.013$ which implies a Hubble flow redshift for Norma $\left(z_{\rm H}\right)$ of 0.01680 ± 0.00052 (Wright, 2006). The peculiar velocity redshift, $z_{\rm pec}$, for the Norma cluster was derived following Harrison (1974), that is,

$$1 + z_{\rm CMB} = \left(1 + z_{\rm H}\right)\left(1 + z_{\rm pec}\right), \tag{3.47}$$

where,

$$v_{\rm pec} \equiv c z_{\rm pec} \tag{3.48}$$

At low redshifts,

$$c z_{\rm pec} \approx c z_{\rm CMB} - c z_{\rm H} \approx c z_{\rm CMB} - H_0\, d. \tag{3.49}$$

The above approximation (Equation 3.49) has been found to overestimate the peculiar velocity by ~ 100 km s^{-1} at $z \sim 0.04$ (Davis & Scrimgeour, 2014). I therefore used Equation 3.47 to measure $z_{\rm pec}$ and thereafter applied $v_{\rm pec} = c z_{\rm pec}$.

For the Norma cluster, $z_{\rm CMB} = 0.01652 \pm 0.00018$. Using this in Equation 3.47 results in a peculiar velocity for Norma of -83 ± 157 km s^{-1}. Applying the homogeneous Malmquist bias correction which is 0.52% or 26 km s^{-1} (see Table 3.11) lowers this value to -109 ± 157 km s^{-1}. Thus, the Norma cluster has a small and insignificant peculiar velocity which within errors, is consistent with zero or at least consistent with it being at rest with respect to Coma.

Tab. 3.11: The J- and K_s-band Fundamental Plane fit parameters and the corresponding peculiar velocity measurements for the Norma cluster. The first column is the source of the data (photometry) used. Columns 5 and 6 represent the Fundamental Plane zero point offset and the resulting Hubble flow redshift, respectively. Column 7 is the measured peculiar velocity for the Norma cluster. The homogeneous Malmquist bias correction shown in column 10 has been applied. Columns 8 and 9 are the scatter and the resulting measured distance error to individual galaxies, respectively. Column 11 indicates the number of Norma cluster galaxies used in the analysis. Note that, for the Coma cluster, N=121.

Sample	Filter	a	b	Δc	$z_{\rm H}$	$v_{\rm pec}$ km s^{-1}	rms	% err	Malm. bias	N
(1)	(2)	(3)	(4)	(5)	(6)	(7)	(8)	(9)	(10)	(11)
NTT	K_s	1.465 ± 0.059	0.326 ± 0.020	0.154 ± 0.014	0.01667 ± 0.00055	-72 ± 170	0.083	28	29	31
IRSF	J	1.356 ± 0.058	0.317 ± 0.018	0.149 ± 0.016	0.01684 ± 0.00062	-128 ± 187	0.079	25	33	31
IRSF	K_s	1.470 ± 0.053	0.357 ± 0.019	0.145 ± 0.014	0.01704 ± 0.00058	-182 ± 173	0.078	26	30	31
NTT+IRSF	K_s	1.551 ± 0.053	0.324 ± 0.017	0.150 ± 0.013	0.01680 ± 0.00052	-109 ± 157	0.082	29	26	41

A summary of results for the J- and K_s-band and the combined K_s-band Fundamental Plane results is presented in Table 3.11. Norma's distance measured from the combined K_s-band Fundamental Plane analysis and corrected for the homogeneous Malmquist bias is

5063 ± 147 km s^{-1} ($\sim 71.8 \pm 2.1$ Mpc assuming $H_0 = 70.5$ km s^{-1} Mpc^{-1}). The resulting peculiar velocity is -109 ± 157 km s^{-1} (see Table 3.11). Since the combined K_s-band Fundamental Plane analysis has the least measurement error, I will hereafter adopt the corresponding derived distance and peculiar velocity for Norma as the 'overall' results obtained from the Fundamental Plane analysis. Therefore, in the section that follows, I will refer to Norma's peculiar velocity measured using the combined K_s-band Fundamental Plane analysis (i.e., $v_{\rm pec} = -109 \pm 157$ km s^{-1}) as the final result from my Fundamental Plane distance measurements.

3.7.6 Comparison with PSCz and 2MRS Models

The availability of data from all-sky galaxy redshift surveys has made it possible to reconstruct density and peculiar velocity fields. From the reconstruction of the IRAS Point Source Catalogue redshift survey (PSCz), Branchini et al. (1999) provided a data cube of the predicted peculiar velocity components v_x, v_y and v_z at grid positions x, y, z. Furthermore, peculiar velocity predictions by Lavaux et al. (2010) using the 2MASS Redshift Survey (2MRS) are available at the Extragalactic Distance Database[6] (Tully et al., 2009). These two reconstructions have therefore been applied to estimate the radial component of Norma's peculiar velocity (Lucey et al., Priv. Com.).

Figure 3.28 shows the model predictions for the radial component of the peculiar velocity from the 2MRS and PSCz surveys. The squares are non-grouped galaxies while the circles represent groups with the size of the circle reflecting the number of galaxies in the group. Positions within a cone were averaged in line-of-sight radial bins (green curve). The crosses shown at the bottom show the redshifts of the PSCz galaxies in the cone. The velocity flow as predicted from 2MRS is represented by the red curve while the green curve represents the PSCz predictions in the Norma direction. The red curve is the smoothed version of the black points including the groups weighted appropriately. The Norma cluster is represented by the large bold circle. The velocity reconstruction from the PSCz survey gives under-estimated peculiar velocities as compared to the 2MRS. This may be due to the former being less sensitive to galaxy clusters (Branchini, Priv. Com) and the larger smoothing scale in the PSCz model. However, both the 2MRS and PSCz models predict a small peculiar velocity for Norma, that is, less than ± 100 km s^{-1} which is in good agreement with the peculiar velocity for Norma of -109 ± 157 km s^{-1} measured using the Fundamental Plane. It should be noted that, Lavaux & Hudson (2011) assigned galaxies to groups using the standard percolation or 'friends-of-friends' algorithm developed by Davis et al. (1982), using galaxy distances estimated from redshifts. This does not hold when peculiar velocities are significant (Lavaux & Hudson, 2011). This may explain why the model predictions of the grouped galaxies seem to be at odds with those for the ungrouped/field galaxies.

Woudt et al. (2008) performed a dynamical analysis of the Norma cluster and measured a cluster mean velocity of 4871 ± 54 km s^{-1}. This value was obtained using radial velocities of 296 Norma cluster member galaxies, which includes all galaxy morphologies, that is, ellipticals and lenticulars (E/S0 or early-type) as well as spirals and irregulars (S/Irr or late-type)[7]. Woudt et al. (2008) further showed that the E/S0 and S/Irr galaxy populations have mean velocities of 4979 ± 85 km s^{-1} and 4812 ± 70 km s^{-1}, respectively. This implies that the E/S0 and S/Irr populations are offset from the mean cluster velocity by $\Delta v \approx 108$ km s^{-1} and $\Delta v \approx 59$ km s^{-1}, respectively. While Woudt et al. (2008) identified two spiral-rich subclusters (Norma A and Norma B), they found the E/S0 population to appear relaxed. In my Tully-Fisher analysis and

[6] `http://edd.ifa.hawaii.edu/dfirst.php`

[7] In the Norma cluster's dynamical analysis, Woudt et al. (2008) identified 107 early-type and 189 late-type galaxies as members of the Norma cluster. All the 296 galaxies lie within the Abell radius of the Norma cluster.

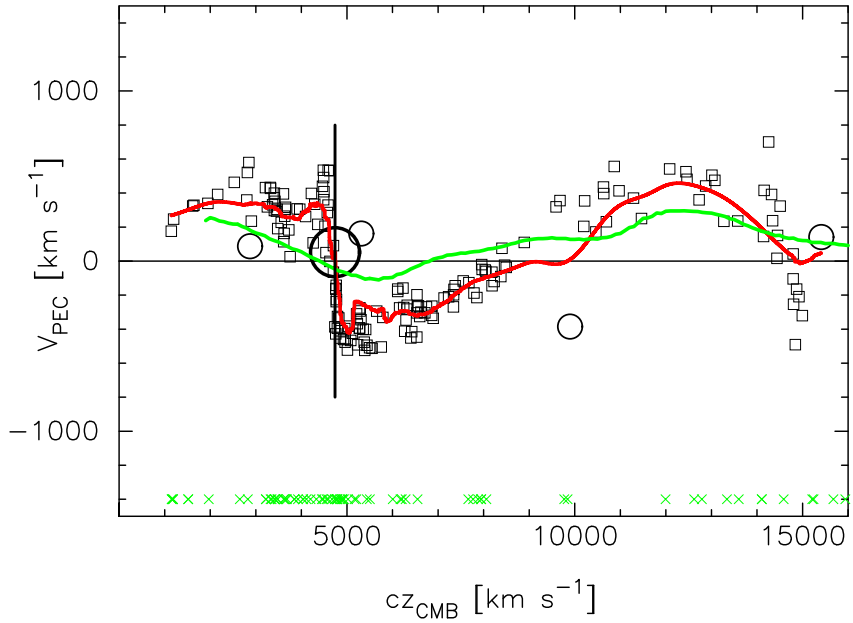

Fig. 3.28: Model predictions for the line-of-sight component of peculiar velocity in the direction of the Norma cluster. The green and red curves represent PSCz and 2MRS predictions, respectively. The crosses shown at the bottom of each panel show the redshifts of the PSCz galaxies in the cone. The black squares show the 2MRS predictions for non-grouped galaxies while the circles represent grouped galaxies. The size of the circle reflects the number of galaxies in the group. The Norma cluster is represented by the large bold circle. Credit: J. Lucey; figure 8 of Mutabazi et al. (2014).

results presented in Chapter 4 for 12 spiral galaxies, I find six of these 12 spiral galaxies to be foreground galaxies with a mean distance of 28 ± 7 Mpc (see §4.3.3 on page 128). If I assume that the mean velocity of the early-type galaxy population gives a better estimate of the Norma cluster's mean radial velocity therefore increases $cz_{\rm CMB}$ by ~ 108 km s^{-1}. This results in Norma cluster's measured peculiar velocity of $v_{\rm pec} = -2 \pm 160$ km s^{-1}.

CHAPTER 4

THE NORMA CLUSTER TULLY-FISHER ANALYSIS AND RESULTS

The Tully–Fisher relation (Tully & Fisher, 1977) relates the maximum observed rotational velocity and total luminosity (or absolute magnitude) for spiral galaxies. The relation can be written in the form:

$$M = b - a\,(\log W - 2.5), \tag{4.1}$$

where M is the absolute magnitude, W is the measured line width corrected for instrumental broadening, turbulent motions, inclination and cosmological effects (see §4.2.4 on page 119) while a and b are fit parameters (a is the slope while b is the zero point of the Tully-Fisher relation). The Tully-Fisher sample selection is described in §2.2.1. Unlike the Fundamental Plane sample which was restricted to within the Norma cluster's Abell radius ($R_{\rm A}$), the Tully-Fisher sample was extended to $1.5R_{\rm A}$ (see §2.2.1). The 1.4 m IRSF telescope was used for high resolution near-infrared imaging. The geometric parameters (the semi-minor and semi-major axes and hence the inclination angles) were measured using the J-band images (see §4.2.1). There were a total of 26 spiral galaxies with quality HI profiles, and hence well and reliably measured line widths. These include WKK 7149 which was later excluded from the final Tully-Fisher sample since it is a very large luminous infrared galaxy (LIRG). The final sample of late-type galaxies used in the Tully-Fisher analysis was restricted to the following selection:

- galaxies located within $1.5R_A$, where R_A is the Norma cluster's Abell radius,
- inclination angles greater than, or equal to, 45°,
- corrected line widths greater than, or equal to, 100 km s^{-1}, that is, $\log W \geq 2$.

The above criteria resulted in a final Tully-Fisher sample of 12 spiral galaxies, 11 of which are marked by $*$ in Table 2.5 (column 12) on page 58. While WKK 6570 was detected by Schröder et al. (2009), I did not. The HI profile for this galaxy shows a low signal-to-noise ratio which is surprising given my longer integration time. For this galaxy, I have adopted line width measurements

from Schröder et al. (2009) and this explains why 11 out of 12 spiral galaxies are marked by $*$. The distances and peculiar velocities were measured using the K_s-band isophotal Tully-Fisher template provided by Said (2013). The list of galaxies and their measured parameters is presented in Table 4.3 on page 128.

4.1 Photometric Analysis

In order to determine the distance and peculiar velocity for the Norma cluster, isophotal magnitudes were used. For each galaxy, the isophotal magnitude was measured using a typical isophote whose surface brightness is ~ 20.0 mag arcsec^{-2} in the K_s-band (Jarrett et al., 2003). The derivation of the distance and peculiar velocity for the spiral galaxies in my sample was done using the isophotal Tully-Fisher template of Said (2013). To avoid possible systematic effects, the photometric analysis was performed following the same procedures that were used to derive the global Tully-Fisher relation. The choice of the isophote used to measure the isophotal magnitude was therefore such that it closely matches that used in the isophotal K_s-band Tully-Fisher template of Said (2013). It is important to point out that the galaxy's geometric parameters were derived using the deeper J-band images, while the choice of the isophote was made using the K_s-band images where the effect of Galactic extinction is reduced.

The ELLIPSE task under the STSDAS-ANALYSIS-ISOPHOTE packages was used to derive the galaxy surface brightness profiles, using the same method applied to the photometric analysis for the Fundamental Plane sample of early-type galaxies (see Chapter 3 of this dissertation or Mutabazi et al., 2014). The following steps were used in the photometric analysis after star-subtraction:

- Use GALFIT to estimate the initial galaxy parameters (position, position angle and ellipticity or axial ratio).
- Use the GALFIT-measured galaxy parameters as the initial input to the ELLIPSE task.
- Determine the new geometric/projection parameters from the output of the ELLIPSE task, using the J-band images. A $3\sigma_s$ isophote where σ_s is the J-band sky background noise was used to determine the position angle and the axial ratio.
- Adopt these new parameters (position angle, axial ratio) and run the ELLIPSE task on the K_s-band images. The ELLIPSE task helps derive galaxy surface brightness profiles.
- Fit the galaxy surface brightness profiles to determine the isophotal magnitudes.

4.1.1 Measuring Isophotal Magnitudes

Two Sérsic components were used to fit the surface brightness profiles. Figure 4.1 shows the fitted galaxy surface brightness profiles for all the 12 spiral galaxies used in the Tully-Fisher analysis. The solid line represents the combined best fit to each galaxy's surface brightness profile. The horizontal dashed lines represent the surface brightness of the $1\sigma_s$ isophote while the vertical dashed lines represent the corresponding semi-major axis radius ($1\sigma_s$ isophotal radius). Note that σ_s is the measured standard deviation in the sky background.

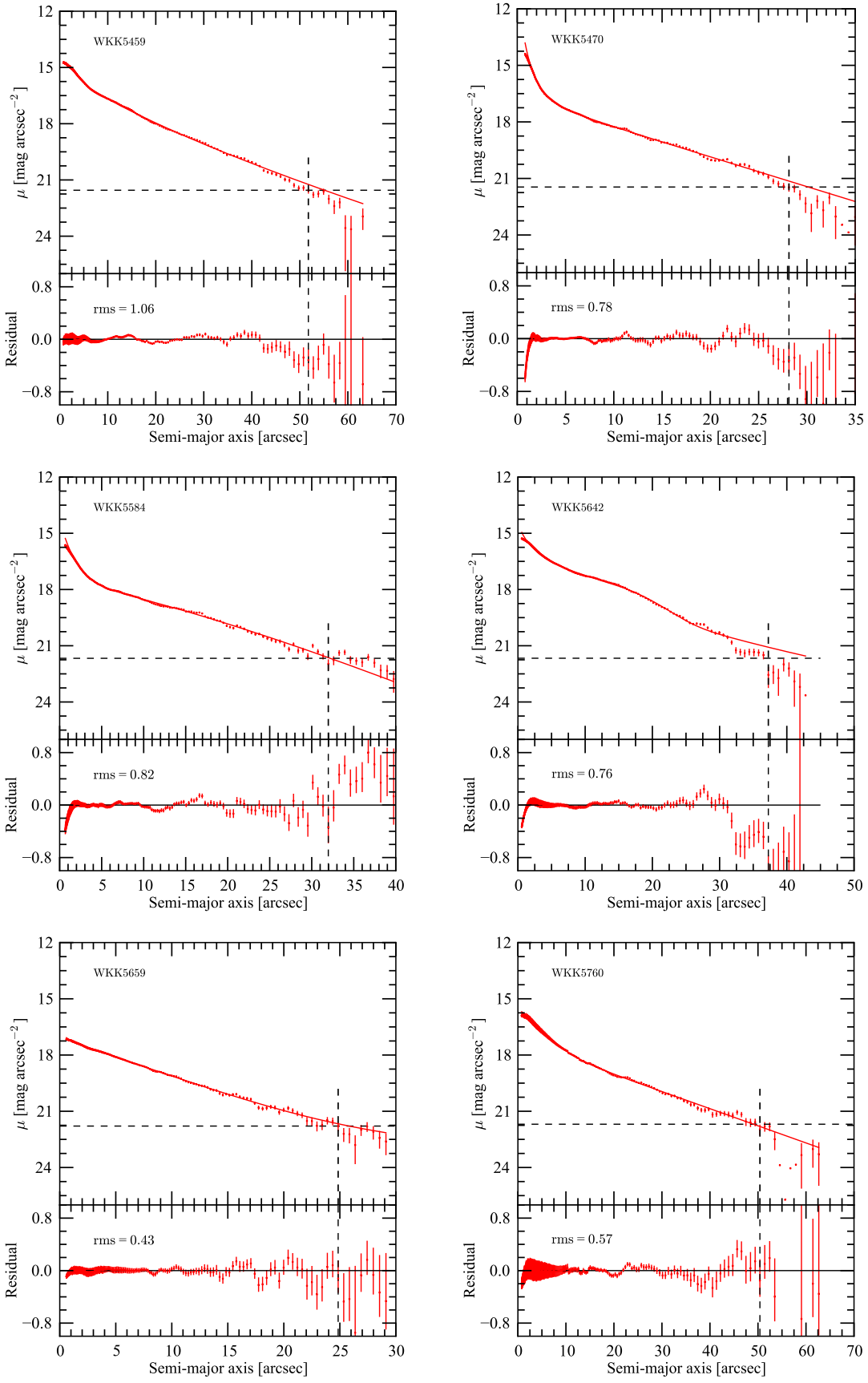

Fig. 4.1: Galaxy surface brightness profiles for all the 12 spiral galaxies in my Tully-Fisher sample. The solid lines represent the best fit to the surface brightness profiles (using two Sérsic components). The vertical dotted lines to the right represent the radius of an isophote whose surface brightness corresponds to 1σ-level in the sky background noise. For the K_s-band images, see Figure 2.13 on page 63.

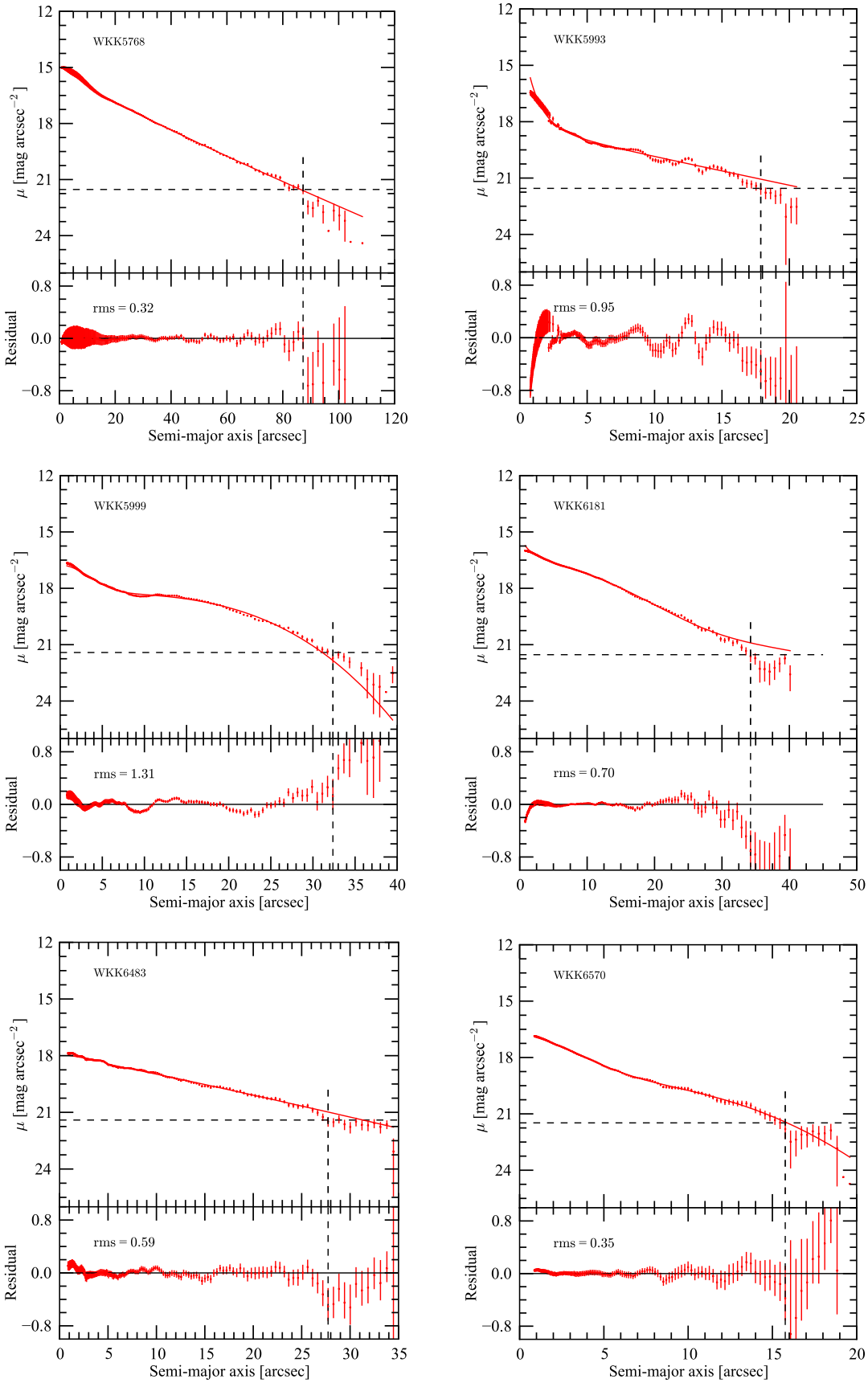

Fig. 4.1: continued ...

4.1.2 *Photometry Comparison with 2MASS XSC*

As an internal check, the measured isophotal magnitudes based on the IRSF images were compared with the values taken from the 2MASS Extended Source Catalogue. Figure 4.2 shows the comparison for 15 late-type galaxies with available 2MASS measurements. Note that not all the galaxies for which I had photometry were used in the final Tully-Fisher analysis. All galaxies with inclination angles $< 45^\circ$ and line widths (rotation velocities) less than 100 km s^{-1} ($\log W < 2$) were excluded. The blue solid circles represent 11 of the 12 galaxies in my final Tully-Fisher analysis with available 2MASS XSC data. The red open circles represent some of the late-type galaxies which were excluded from the final Tully-Fisher analysis. The average difference between the 2MASS and IRSF isophotal magnitudes is 0.09 ± 0.06 mag, with the 2MASS magnitudes being brighter than the IRSF magnitudes. When the four galaxies represented by red open circles are included in the photometry comparison, the average difference reduces to 0.07 ± 0.05 mag. The difference in the isophotal magnitude may be due to the contribution from foreground stars in the 2MASS photometry. Note that the small pixel scale of the SIRIUS imaging camera implies a high resolution for my IRSF images. This in turn makes it possible to effectively subtract stars, which leads to accurate sky background measurements and reliable photometry.

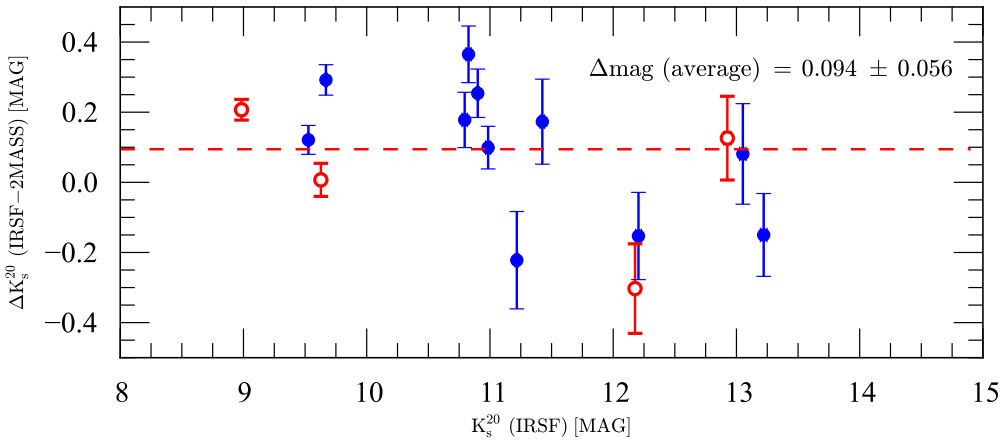

Fig. 4.2: Comparison of the measured isophotal magnitudes for the late-type galaxies in my Tully-Fisher sample. The y-axis shows the difference between the fiducial magnitudes taken from the 2MASS XSC and my IRSF measurements while the x-axis shows the measurements using the IRSF star-subtracted images. The red dashed line represents the average difference. This was computed using the blue filled circles which represent 11 of the 12 spiral galaxies in the final Tully-Fisher analysis.

4.2 Photometric and Spectroscopic Corrections

This section presents the various corrections which were applied to the measured isophotal magnitudes and HI line widths before deriving the distance and peculiar velocity using the calibrated isophotal Tully-Fisher template (Said, 2013). These corrections were applied following very closely the work by Masters et al. (2008) and Said (2013).

4.2.1 *Galaxy Axial Ratio*

The axial ratio is a measure of a galaxy's ellipticity. The accuracy in various parameters, for example, the inclination angle and the internal extinction, depends on the accuracy in measuring the axial ratio. It is therefore crucial that the axial ratio be accurately and reliably measured to

minimise possible systematic effects in both distance and peculiar velocity measurements. The ellipticity, ϵ, is given by

$$\epsilon = 1 - \left(\frac{b}{a}\right)_J,$$

where a and b are the galaxy's semi-major and semi-minor axes, respectively. To better trace the disc and reduce the effect of the bulge (if present), the $3\sigma_s$ isophote in the J-band image was used to determine the values of a and b. However, the measured axial ratio should be corrected for seeing effects. This was done following the prescription by Masters et al. (2003), who provide the correction as

$$\left(\frac{a}{b}\right)_{\rm corr} = \left(\frac{a}{b}\right)_{\rm obs} \left(1 - 0.02x + 0.21x^2 - 0.01x^3\right), \tag{4.2}$$

where $x = \mathrm{FWHM}\left(\frac{a/b}{r_{20}}\right)$, FWHM is the full width at half maximum of the seeing disc. The value of r_{20} corresponds to the radius of a J-band isophote of 20 mag arcsec^{-2}.

In addition, a and b should be corrected for the effect of Galactic extinction. Riad et al. (2010) found through simulations that Galactic extinction affects galaxies' sizes. They modelled this effect following the prescription by Cameron (1990), that is,

$$f(R) = 10^{a'(A_\lambda)^{b'}}; \tag{4.3}$$

$$\Delta m_{\rm iso} = F(A_\lambda)^v; \tag{4.4}$$

where

$$f(R) = \frac{R^o}{R};$$

$$\Delta m_{\rm iso} = m_{\rm iso} - m^o_{\rm iso}. \tag{4.5}$$

$m_{\rm iso}$, $m^o_{\rm iso}$ are, respectively, the intrinsic and absorbed isophotal magnitudes, R and R^o are the intrinsic and absorbed radii while A_λ is the Galactic extinction (see Equation 4.7 for the K_s-band). The corrections applied to my isophotal magnitudes were computed following Riad et al. (2010) by applying Equations 4.3 and 4.4. The fit parameters (a', b', F, and v) presented in Table 4.1 were adopted from Riad et al. (2010). The Galactic extinction in the J and K_s passbands, assuming

Tab. 4.1: Average fit parameters a', b', F, and v for spiral galaxies. These were taken from Riad et al. (2010).

Parameter	K_s-band
a'	0.1453 ± 0.0005
b'	1.4778 ± 0.0032
F	0.1982 ± 0.0009
v	1.7093 ± 0.0049

the Fitzpatrick (1999) reddening law, with $R_{\rm v} = 3.1$ are given as:

$$A_J = 0.937E(B-V); \tag{4.6}$$

$$A_{K_s} = 0.382E(B-V); \tag{4.7}$$

where the colour excess $E(B-V)$ which depends on a galaxy's position, was measured using the near-infrared reddening maps of Schlegel et al. (1998). While applying Equations 4.6 and 4.7, an extinction correction factor, $f = 0.81$, was applied, that is:

$$A_J = 0.937 f E(B-V); \tag{4.8}$$

$$A_{K_s} = 0.382 f E(B-V); \tag{4.9}$$

For details regarding the derivation of the extinction correction factor, f, using the J and K_s bands, refer to §3.2.5 on page 81. The average axial ratio correction for the Norma cluster sample is ~ 1.4%. After correcting a and b for both the Galactic extinction and seeing effects, the ellipticity of the galaxy, ϵ, is given by:

$$\epsilon = 1 - \left(\frac{b}{a}\right)_{\rm corr}. \tag{4.10}$$

4.2.2 Internal Extinction

An internal extinction correction was applied to the measured magnitudes to correct for the dimming effect arising from the gas and dust within the galaxy itself. The applied correction was adopted from Masters et al. (2003). They provide models for the internal extinction as a function of axial ratio, that is,

$$A^i_\lambda = \gamma \log\left(\frac{a}{b}\right)_{\rm corr}. \tag{4.11}$$

The values of A^i_λ were computed using the values of γ taken from Masters et al. (2003). For the K_s-band, I adopted (for all galaxies in my sample), a value of

$$\gamma_{K_s} = 0.26 \pm 0.15. \tag{4.12}$$

4.2.3 Redshift Effect — k-correction

The correction for redshift effects was applied by using the same k-corrections that were used in deriving the isophotal Tully-Fisher template. These, as given by Masters et al. (2003), are:

$$\begin{aligned} k_{_J} &= -0.68z; \\ k_{_{K_s}} &= -1.52z; \end{aligned} \tag{4.13}$$

where z is the galaxy redshift. The redshift for each galaxy was measured from its HI profile (see §2.2.3 under Chapter 2).

4.2.4 Corrections to the Measured Line Width

A number of corrections were applied to the measured HI line widths ($w_{_{50}}$) to take into account:

- the instrumental broadening, $\Delta_{\rm s}$;
- the inclination of the disc;
- the turbulent motion of the HI gas, $\Delta_{\rm t}$ and
- the cosmological redshift.

The instrumental broadening, $\Delta_{\rm s}$, depends on the quality of the spectrum, that is, the signal-to-noise ratio (SNR), the type of smoothing applied, and the channel separation. The applied correction, which was also used in deriving the Tully-Fisher template (Said, 2013), was adopted from Springob et al. (2005). This correction is given by:

$$\Delta_{\rm s} = 2\Delta v\, \lambda, \tag{4.14}$$

where λ is defined as:

$$\begin{aligned} \log({\rm SNR}) < 0.6: &\quad \lambda = \lambda_1(\Delta v); \\ 0.6 \le \log({\rm SNR}) \le 1.1: &\quad \lambda = \lambda_2(\Delta v) + \lambda_2'(\Delta v)\log({\rm SNR}); \\ \log({\rm SNR}) > 1.1: &\quad \lambda = \lambda_3(\Delta v). \end{aligned} \tag{4.15}$$

For Hanning smoothing and channel separation smaller than 5 km s^{-1}, the values of λ_i (adopted from Springob et al., 2005) are

$$\begin{aligned} \lambda_1(\Delta v) &= 0.005 \\ \lambda_2(\Delta v) &= -0.4685 \\ \lambda_2'(\Delta v) &= 0.785 \\ \lambda_3(\Delta v) &= 0.395 \end{aligned} \tag{4.16}$$

The correction for turbulent motion, Δ_t, accounts for, e.g., the non-linear motion of the HI gas. I have adopted the value of $\Delta_t = 6.5$ km s^{-1} given by Springob et al. (2005), which was also used in deriving the isophotal Tully-Fisher template. The fully corrected line width is

$$W = \left[\frac{w_{50} - \Delta_s}{1+z} - \Delta_t \right] \frac{1}{\sin i}. \tag{4.17}$$

The factor $(1+z)$ is due to the cosmological redshift effect (expansion) which leads to the broadening of the HI profile. As noted earlier, the redshift, $z = v/c$, was measured from the HI profile. The factor $\sin i$ is an inclination correction due to projection effects, i being the inclination angle of the disc. The inclination angle, i, was computed using:

$$\cos^2 i = \frac{(1-\epsilon)^2 - q_o^2}{1 - q_o^2}, \tag{4.18}$$

where the galaxy ellipticity is given by Equation 4.10 on page 119. The intrinsic axial ratio q_o is 0.13 for Sc (and later types) and $q_o = 0.2$ for other morphological types.

4.2.4.1 Comparison of Line Width Measurements with Literature

Of the 12 galaxies in my Tully-Fisher sample, one has line width measured by Doyle et al. (2005) and ten by Schröder et al. (2009). I have compared my line width measurements (w_{50}) with their measurements as shown in Figure 4.3. Before comparing the different data sets, a correction for the instrumental broadening was applied. It is important to first apply this correction since the line width measurements are slightly affected by the instrumental set up as well as the data reduction procedure. That is, the instrumental broadening depends on the velocity resolution and the signal-to-noise ratio. Note also that the velocity resolution and the signal-to-noise ratio change with the applied smoothing.

In Figure 4.3, the black stars represent the comparison of the w_{50} measurements in this work with those of Doyle et al. (2005) while the red open and blue filled circles represent the comparison with Schröder et al. (2009). The blue solid circles are 10 of the 12 galaxies used in the final Tully-Fisher analysis. Galaxies represented by the red open circles were excluded from the final Tully-Fisher analysis due to either, small rotation velocities (corrected line width less than 100 km s^{-1}) or inclination angles less than 45°.

There is a significant difference between these and Schröder et al.'s measurements for WKK 5993 and WKK 5796. The galaxy WKK 5796 had a very low-signal-to-noise spectrum for my observations which made it difficult to reliably determine the width of the HI profile. This galaxy is, however, not part of the Tully-Fisher sample since it was identified by Woudt et al. (2008) as belonging to Norma B, one of the Norma cluster's rich infalling sub-groups. The reason for the discrepancy in the line width measurements for WKK 5993 is mainly due to confusion of its HI profile by WKK 5999 (see Figure 2.11).

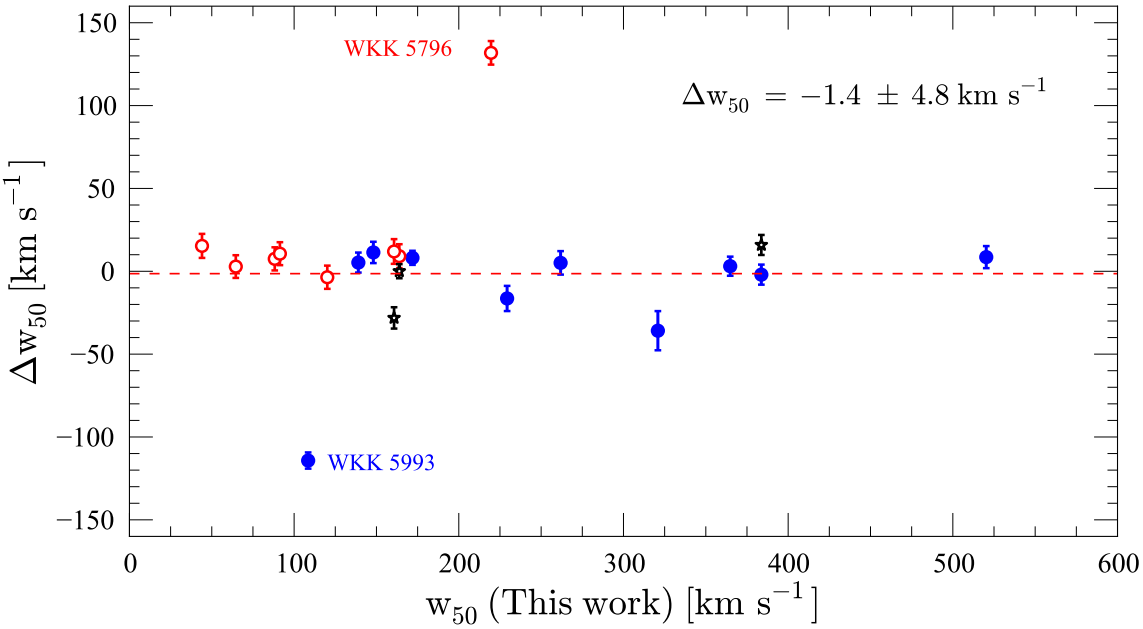

Fig. 4.3: Comparison of the measured line widths (w_{50}) for some of the Norma cluster late-type galaxies in the Tully-Fisher sample. The y-axis shows the difference (this work - other) while the x-axis represents the w_{50} measurements in this work. The black stars represent comparison with Doyle et al. (2005) while the red open and blue filled circles represent the comparison with Schröder et al. (2009). The red dashed line represents the average difference: -1.4 ± 4.8 km s^{-1}, for the galaxies indicated by the blue filled circles but excluding WKK 5993. The rms for the galaxies represented by the blue filled circles is 36.50 km s^{-1} but this reduces to 14.24 km s^{-1} when WKK 5993 is excluded. The red open circles represent some of the galaxies that were excluded from the final Tully-Fisher analysis while the blue filled circles represent some of the galaxies used in the final Tully-Fisher analysis.

However, I trust my HI measurements over Schröder et al.'s for WKK 5993 due to superior velocity resolution compared to the Schröder et al. measurements (my velocity resolution is 1.7 km s^{-1} while that of Schröder et al. is 27 km s^{-1}). WKK 5999 has a very high quality spectrum with high signal-to-noise ratio and well defined line width (see the top panel of Figure 2.9). The profile for WKK 5999 was therefore carefully masked out before determining the HI parameters for WKK 5993.

The average difference between the measurements in this work and Schröder et al. (2009), that is, (this work - Schröder) is -1.4 ± 4.8 km s^{-1}. This is indicated by the red dashed line in Figure 4.3. I should point out that the galaxy WKK 5993 was excluded when computing the average difference of the line width measurements for only the galaxies in the final Tully-Fisher analysis (these are represented by the blue filled circles in Figure 4.3). The difference between my measurements and those taken from literature (Schröder et al., 2009) is consistent with zero, that is, -1.4 ± 4.8 km s^{-1}. My measurements have a higher precision due to the improved velocity resolution.

4.2.5 Line Width Measurements

Table 4.3 on page 128 shows the near-infrared K_s-band Tully-Fisher data and results for the 12 individual galaxies in the final Tully-Fisher sample. In column 12 of the Table, I presented the source of HI line width measurements which are: TM11 if the line width measurements were taken from my HI observations, AS09 if line width was taken from Schröder et al. (2009). In the

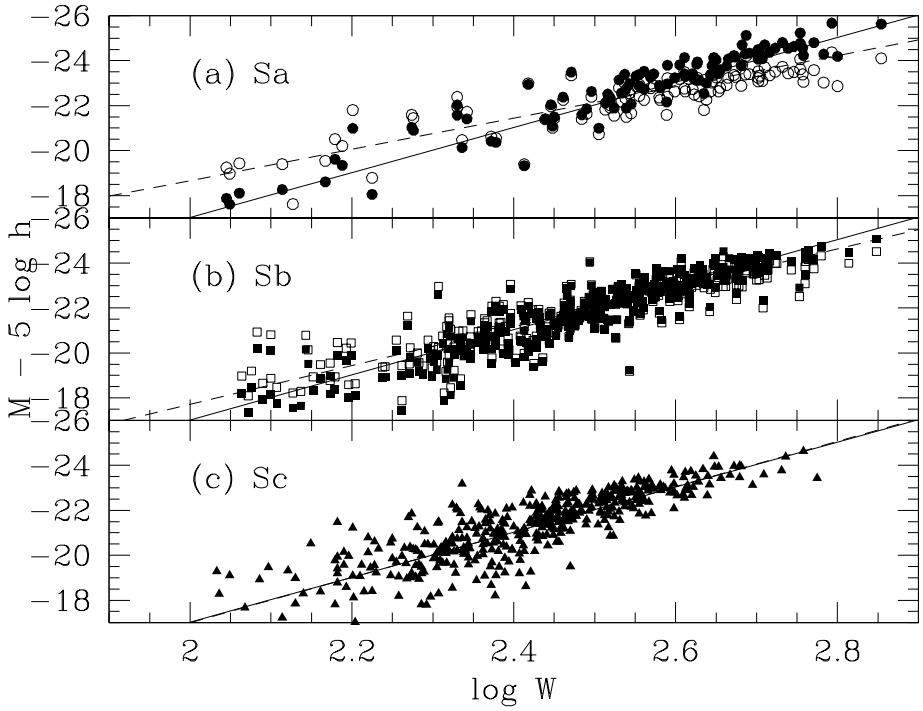

Fig. 4.4: The K_s-band Tully-Fisher relation separated by the morphological type: Sa and earlier (top panel), Sb (middle panel), Sc and later (bottom panel). The open symbols represent the magnitudes corrected for all biases except morphological type. The dashed lines are the best fits to these points. The filled symbols represent the magnitudes after all bias corrections including the morphological type correction have been applied. The solid line represents the best final fit to the full sample. Figure taken from Masters et al. (2008), their Figure 4.

Tully-Fisher analysis, I used w_{50} which is the line width measured at 50% of the peak flux.

4.2.6 Morphological and Wavelength Dependence

The Tully-Fisher relation has been found to depend slightly on the galaxy morphology (Masters et al., 2008), hence the need for a morphological type correction. Figure 4.4 (taken from Masters et al. 2008) shows the variation of the K_s-band Tully-Fisher relation with morphology. The top, middle, and bottom panels show the Tully-Fisher relation for Sa (and earlier), Sb, Sc (and later) types, respectively. The open symbols represent the magnitudes after applying all bias corrections except the morphological type, while the dashed lines are the best fits to these points. The filled circles represent the magnitudes after all bias corrections including the morphological type correction have been applied. The triangles (see bottom panel) represent the full sample after all bias corrections have been applied; the solid line is the best fit to this fully corrected sample. It is clear from Figure 4.4 that the slope and zero point of the Tully-Fisher relation are, respectively, shallower and brighter for the Sa and Sb types than for the Sc-type galaxies.

The Tully-Fisher relation has also been found to vary with wavelength, steepening as the wavelength increases (Pierce & Tully, 1992; Karachentsev et al., 2002; Pizagno et al., 2007; Masters et al., 2008). Figure 4.5 taken from Masters et al. (2008) shows the changes in the Tully-Fisher slope and zero point with wavelength. The Tully-Fisher relation in the I-band is from Masters et al. (2006) while the Tully-Fisher relations in the J, H and K_s-bands are from

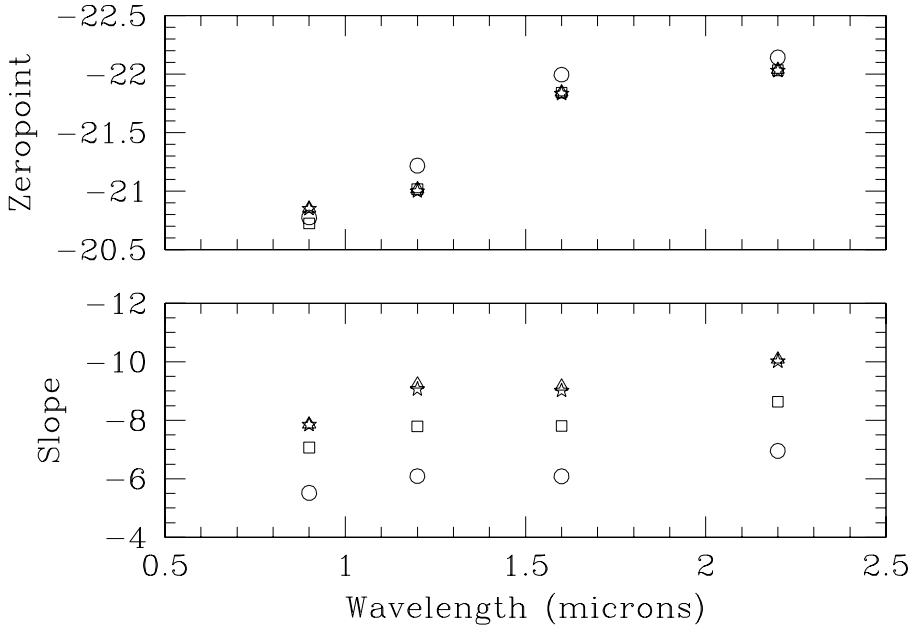

Fig. 4.5: Changes in the zero point and slope of the Tully-Fisher relation with wavelength. The symbols represent the different galaxy morphologies, that is, circles for Sa galaxies, squares for Sbs, and triangles for Scs. The stars represent the combined sample after a morphological type correction has been applied to the Sa and Sb galaxies to match the Scs. Figure taken from Masters et al. (2008), their Figure 3.

Masters et al. (2008). The circles, squares, and triangles represent the Tully-Fisher results for Sa, Sb, and Sc type galaxies, respectively. The stars represent the combined sample after the magnitudes of the Sa and Sb type galaxies have been corrected to the Sc Tully-Fisher relation, i.e., after applying a morphological type correction.

From Figures 4.4 and 4.5, the Tully-Fisher relation steepens as the sample changes from earlier type to later type spirals. The solid line in Figure 4.4 is the Tully-Fisher relation for Sc-type galaxies. Therefore, the galaxies need to be classified according to morphological type and should be corrected or matched to the standard Tully-Fisher relation for the Sc (and later) type galaxies — see Table 4.2 on galaxy classification. In the global 2MASS J, H and K_s-band Tully-Fisher template, Masters et al. (2008) measured a morphological type correction in the K_s-band given as

$$K_s\text{-band:} \qquad T_M = \begin{cases} 0.27 - 3.73(\log W - 2.5) & \text{if } T \le 2 \\ 0.02 - 1.74(\log W - 2.5) & \text{if } 2 < T \le 4; \end{cases}$$

where, in the galaxy classification, $T = 5$ for Sc (and later) type galaxies. The morphological type correction based on the isophotal Tully-Fisher relation calibrated by Said (2013) is

$$K_s\text{-band:} \qquad T_M = \begin{cases} 0.11 - 3.51(\log W - 2.5) & \text{if Sa} \\ 0.13 - 1.44(\log W - 2.5) & \text{if Sb} \end{cases}$$

The final fully corrected isophotal magnitude for the spiral galaxies in my sample is

$$m_{\rm corr} = m_{\rm iso} - A_\lambda - A_\lambda^i + k(z) - T_{\rm M}(W), \tag{4.19}$$

where $m_{\rm iso}$ is the observed (measured) isophotal magnitude, A_λ is the Galactic extinction correction, A_λ^i is the internal extinction, $k(z)$ is the k-correction, $T_{\rm M}(W)$ is the morphological type

Tab. 4.2: Morphological classification for spiral galaxies according to the third reference catalogue of bright galaxies (de Vaucouleurs et al., 1991, 1992). The morphological types for the Norma cluster spiral galaxies were determined by manual inspection, following the classification schemes by Kormendy & Bender (1996); Jarrett (2000) which are revised versions of Hubble (1936). I adopted the morphological type given via NED queries when available.

T	1	2	3	4	5	6	7
Type	Sa	Sab	Sb	Sbc	Sc	Scd	Sd

correction. Note that, the morphological type correction depends on the measured, corrected line width, W. An additional correction to the isophotal magnitudes due to extinction was also applied. Following the prescription of Riad et al. (2010), this correction was found to be very small, that is, an average correction of 0.0054 ± 0.0009 mag (see §4.2.1 for details).

4.2.7 Malmquist Bias Correction

To measure the peculiar velocity and distance to the Norma cluster, I used the global Tully-Fisher template of Said (2013) who used isophotal magnitudes from the 2MASS Extended Source Catalogue. Their calibration used ~888 well inclined spiral galaxies taken from more than 30 galaxy clusters. Such a "basket of clusters" template (Giovanelli et al., 1997b) is more accurate and more reliable than a template relation calibrated using a few clusters. While applying the template, I assumed that the spiral galaxies in the Norma cluster lie at the same distance. The inhomogeneous Malmquist bias was thus assumed to be negligible for the Norma cluster (see for example, Aaronson et al. 1980; Tully 1988; Teerikorpi 1987, 1990; Masters et al. 2006). Note also that no correction for the Malmquist bias was applied when calibrating the template relation, as it was assumed to be neglible for galaxy clusters (Masters et al., 2008; Said, 2013). However, a correction for the bias arising from cluster population incompleteness is necessary.

4.3 Distance and Peculiar Velocity using the Tully-Fisher Template

4.3.1 Deriving the Distance and Peculiar Velocity

The K_s-band isophotal Tully-Fisher template relation from Said (2013), is given by

$$M_{K_s} - 5\log h = -21.959 \pm 0.018 - (10.523 \pm 0.120)(\log W - 2.5). \tag{4.20}$$

The corresponding observed intrinsic scatter which decreases with increasing line widths, is given by

$$\epsilon_{\mathrm{int},K_s} = 0.46 - 0.83(\log W - 2.5). \tag{4.21}$$

There are a total of 12 spiral galaxies in the final Tully-Fisher relation analysis. Figure 4.6 shows the sky positions of these galaxies. The four concentric circles represent $\frac{1}{3}R_{\mathrm{A}}$, $\frac{2}{3}R_{\mathrm{A}}$, R_{A} and $\frac{3}{2}R_{\mathrm{A}}$ while the triangles represent the two rich infalling subgroups of galaxies (Woudt et al., 2008). For each galaxy in my sample, the measured isophotal magnitude was fully corrected as discussed in §4.2.6 (see Equation 4.19). All the necessary corrections were applied to the line width measurements (see §4.2.4). For each galaxy in the sample, the redshift was measured from the HI profile and the measured velocities were transformed into the CMB frame. This was done using the model of Fixsen et al. (1996) – recall Equation 3.45, that is,

$$v_{\mathrm{CMB}} = v_{\mathrm{hel}} + v_{\mathrm{apex}}\left[\sin b \sin b_{\mathrm{apex}} + \cos b \cos b_{\mathrm{apex}} \cos\left(l - l_{\mathrm{apex}}\right)\right], \tag{4.22}$$

where $v_{\mathrm{apex}} = 371$ km s^{-1}, $l_{\mathrm{apex}} = 264.^{\circ}14$, $b_{\mathrm{apex}} = 48.^{\circ}26$.

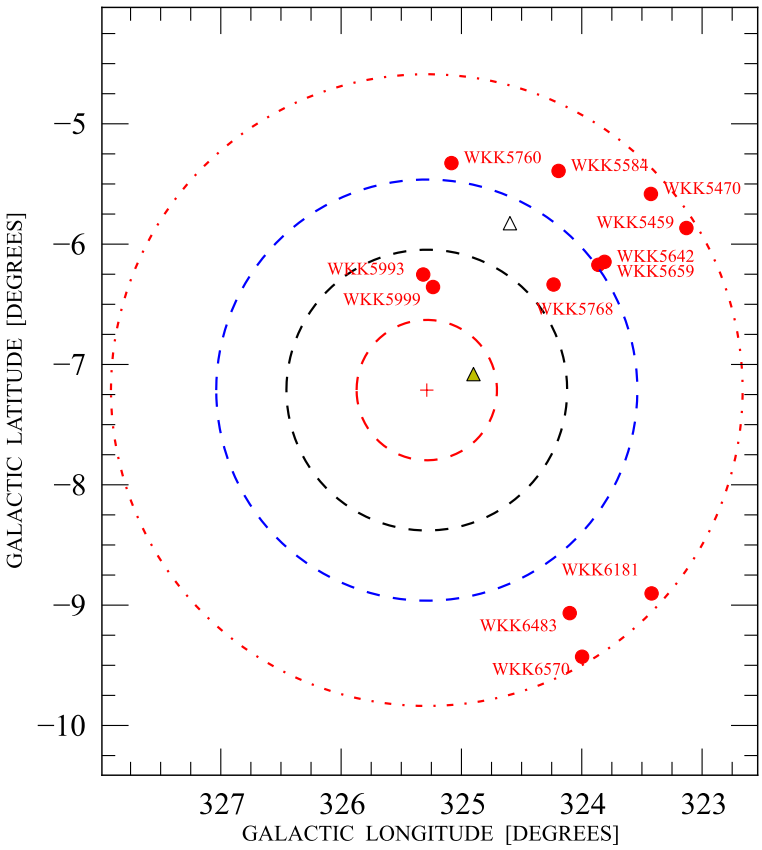

Fig. 4.6: Sky positions of the late-type galaxies used in the final Tully-Fisher analysis. The four concentric circles represent $\frac{1}{3}R_{\rm A}$, $\frac{2}{3}R_{\rm A}$, $R_{\rm A}$ and $\frac{3}{2}R_{\rm A}$, where $R_{\rm A}$ is the Norma cluster's Abell radius. The filled and open rectangles represent Norma A and Norma B, respectively.

From the corrected isophotal magnitude, the corrected absolute magnitude, M, was calculated given the observed HI recession velocity in the CMB frame ($v_{\rm CMB}$ given by Equation 4.22). To position the galaxies in my sample on to the Tully-Fisher template relation, the absolute magnitude for each galaxy was computed using

$$M - 5\log h = m_{\rm corr} - 5\log v_{\rm CMB} - 15. \tag{4.23}$$

The right hand side of Equation 4.23 (see also Giovanelli et al. 1997a), when combined with the measured, corrected line width, gives the location of each individual galaxy on the universal Tully-Fisher relation. The offset of each galaxy from the Tully-Fisher relation is a measure of the galaxy's distance and peculiar velocity. Figure 4.7 shows the location of the galaxies in my sample compared to the template relation. The isophotal Tully-Fisher template of Said (2013) is shown by the black solid line. The dotted lines represent 3σ where σ is the intrinsic scatter measured from the template relation. The offset from the Tully-Fisher template relation is given by

$$\Delta M = M - M_i(W), \tag{4.24}$$

where $M_i(W)$ is the absolute magnitude computed using the Tully-Fisher relation for a galaxy whose measured, corrected line width is W. The peculiar velocity in the CMB frame is then given by (see also Masters et al. 2006):

$$v_{\rm pec} = v_{\rm CMB}\left(1 - 10^{\frac{\Delta M}{5}}\right). \tag{4.25}$$

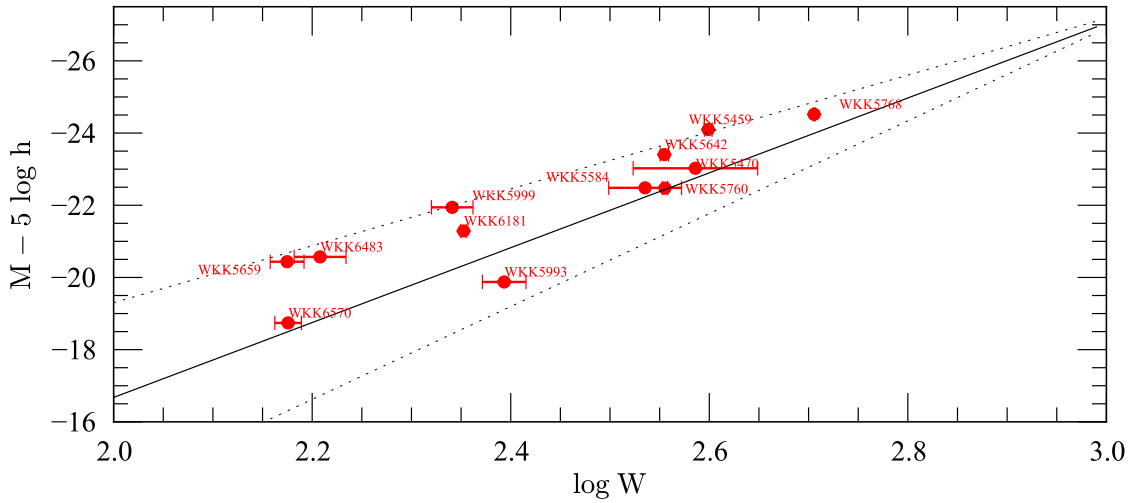

Fig. 4.7: Location of the sample galaxies (red filled circles) on the template Tully-Fisher relation. The solid line represents the template relation. The dashed lines indicate 3σ, where σ is the intrinsic scatter on the template relation given by Equation 4.21.

From $v_{\rm pec} = v_{\rm CMB} - H_0\, d$, the distance, d, in Mpc becomes

$$d = \frac{v_{\rm CMB}}{H_0}\left(10^{\frac{\Delta M}{5}}\right). \tag{4.26}$$

Equation 4.23 is an approximation since its derivation assumes the Hubble law: $v = cz = H_0 d$ which is itself an approximation. It therefore follows automatically that Equations 4.25 and 4.26 are also approximations. Note that at the redshift of Norma, these approximations do not have significant effect on my final results – at the redshift of Norma, the effect is ~ 10 km s^{-1} (Davis & Scrimgeour, 2014).

4.3.2 Uncertainties

Using 1000 Brightest HIPASS galaxies, Koribalski et al. (2004) show the uncertainty in the peak flux density, $\sigma(S_{\rm peak})$, is mainly dominated by the rms noise in the corresponding HI spectrum. The uncertainty, $\sigma(S_{\rm peak})$ also increases slightly with rising peak flux density (Barnes et al., 2001). This was estimated to be $\sim 5\%$ of $S_{\rm peak}$ (Barnes et al., 2001; Koribalski et al., 2004). From simple propagation of errors, the uncertainty in the peak flux density is

$$\sigma(S_{\rm peak}) = \left[{\rm rms}^2 + \left(0.05 S_{\rm peak}\right)\right]^{\frac{1}{2}}. \tag{4.27}$$

Schneider et al. (1986, 1990) give the uncertainty in the systemic velocity, $\sigma\left(v_{\rm sys}\right)$, as:

$$\sigma\left(v_{\rm sys}\right) = 3(SN)^{-1}(P\delta v)^{\frac{1}{2}}, \tag{4.28}$$

where, SN is the ratio of the peak signal to rms noise. Koribalski et al. (2004) slightly modified the estimate by Fouque et al. (1990) and Schneider et al. (1986, 1990), giving the uncertainty in the systemic velocity, $\sigma\left(v_{\rm sys}\right)$, as approximately:

$$\sigma\left(v_{\rm sys}\right) = 3\left(\frac{S_{\rm peak}}{\sigma\left(S_{\rm peak}\right)}\right)^{-1}(P\Delta v)^{\frac{1}{2}}; \tag{4.29}$$

where $P = 0.5\left(w_{20} - w_{50}\right)$ is a measure of the slope or steepness of the HI profile.

From Schneider et al. (1986), the errors on the line widths are simply computed from $\sigma(v_{\rm sys})$ by multiplying it by appropriate coefficients, depending on the level of measurement of the line width:

$$\sigma\left(w_{50}\right) = 2\sigma\left(v_{\rm sys}\right) \tag{4.30}$$

$$\sigma(w_{\rm i}) = \sigma\left(w_{50}\right)\frac{0.25}{\left(f - f^2\right)}, \tag{4.31}$$

where f is the fractional level; $f = 0.20$ at 20% and $f = 0.50$ at 50% levels. Equation 4.31 implies that:

$$\sigma\left(w_{20}\right) = 1.56\,\sigma\left(w_{50}\right) = 3\sigma\left(v_{\rm sys}\right) \tag{4.32}$$

The uncertainties in the w_{20} and w_{50} measured at 20% and 50% velocity line widths are therefore given by (Schneider et al., 1986):

$$\sigma\left(w_{50}\right) = 2\sigma\left(v_{\rm sys}\right) \tag{4.33}$$

$$\sigma\left(w_{20}\right) = 3\sigma\left(v_{\rm sys}\right). \tag{4.34}$$

Standard propagation of errors was used for the measurement errors in the absolute magnitude (σ_M), line width (σ_W), inclination angle (σ_i), offset from the Tully-Fisher relation ($\sigma_{\Delta M}$) and the absolute magnitude measured using the template relation ($\sigma_{M(W)}$). These are given by

$$\begin{aligned}
\sigma_M &= \left[\sigma^2_{m_{\rm iso}} + \sigma^2_{\rm gc} + \sigma^2_{\rm ic} + \left(\frac{5}{v_{\rm cmb}\ln 10}\right)^2 \sigma^2_{v_{\rm cmb}}\right]^{\frac{1}{2}}, \\
\sigma_W &= \left[\left(\frac{1}{1+z}\right)^2 \sigma^2_{w_{50}} \left(W\frac{\cos i}{\sin i}\right)^2 \sigma^2_i\right]^{\frac{1}{2}}, \\
\sigma_i &= \left[\left(\frac{1-\epsilon}{1-q_o^2}\frac{1}{\cos i \sin i}\right)^2 \sigma^2_\epsilon\right]^{\frac{1}{2}}, \\
\sigma_{\Delta M} &= \left[\sigma^2_M + \sigma^2_{M(W)}\right]^{\frac{1}{2}}, \\
\sigma_{M(W)} &= \left[\left(\frac{b}{W\ln 10}\right)^2 \sigma^2_W + \epsilon^2_{\rm int}\right]^{\frac{1}{2}}.
\end{aligned} \tag{4.35}$$

In this case, $\sigma_{\rm gc}$ and $\sigma_{\rm ic}$ which were assumed to be insignificant, are the errors from Galactic and internal extinction corrections, respectively. The uncertainties in Δ_s, Δ_t and z have been assumed to be small compared to the observational error in the line width (σ_W) and inclination (σ_i). Note that the observational error on the inclination angle also depends on the observational error on the measured ellipticity (σ_ϵ).

Through simple propagation of errors, the measurement errors in the measured peculiar velocity and distance are given by

$$\sigma_{v_{\rm pec}} = \left[\left(1 - 10^{0.2\Delta M}\right)^2 \sigma^2_{v_{\rm cmb}} + \left(0.2 v_{\rm cmb} 10^{0.2\Delta M}\ln 10\right)^2 \sigma^2_{\Delta M}\right]^{\frac{1}{2}}, \tag{4.36}$$

$$\sigma_d = \left[\left(\frac{1}{H_0}10^{0.2\Delta M}\right)^2 \sigma^2_{v_{\rm cmb}} + \left(0.2\frac{v_{\rm cmb}}{H_0}10^{0.2\Delta M}\ln 10\right)^2 \sigma^2_{\Delta M}\right]^{\frac{1}{2}}. \tag{4.37}$$

4.3.3 Identifying Foreground Galaxies

Although the final sample of 12 spiral galaxies are all within the projected $1.5R_{\rm A}$ for the Norma cluster and all have systemic velocities consistent with redshifts in the Norma cluster, there is a possibility that not all these galaxies actually belong to the cluster but could be foreground or background galaxies with a range of peculiar velocities. Therefore, before assuming all 12 galaxies were Norma cluster members, I used the Tully-Fisher template relation to compute their individual distances. These are presented in Table 4.3.

Tab. 4.3: Near-infrared K_s-band Tully-Fisher data and results. Presented in the table are: the galaxy name, the measured raw isophotal magnitude, the isophotal magnitude with all corrections applied, the line width, the measured offset of each galaxy from the Tully-Fisher template, the galaxy velocity in the CMB frame, the derived distance in Mpc, the measured peculiar velocity, the inclination angle, the axial ratio (b/a), $\log(a/b)$, and finally, the source of HI line width measurements: TM11 for my September 2011 observations, AS09 for Schröder et al. (2009).

Name	$m_{\rm iso}$	$m_{\rm iso,corr}$	$\log W$	dM	$v_{\rm CMB}$	D (Mpc)	$v_{\rm pec}$	i	b/a	$\log(a/b)$	
WKK5459	9.669	9.177±0.011	2.599±0.004	-0.219 ± 0.378	4517	36±9	1791 ± 710	68	0.41	0.39	TM11
WKK5470	10.795	10.576±0.021	2.586±0.063	-0.032 ± 0.255	5249	65±8	373 ± 607	47	0.70	0.16	TM11
WKK5584	11.218	11.036±0.015	2.535±0.037	-0.030 ± 0.395	5053	62±12	341 ± 907	46	0.69	0.16	TM11
WKK5642	10.901	10.510±0.012	2.555±0.004	-0.174 ± 0.414	6063	54±14	1999 ± 1067	79	0.27	0.58	TM11
WKK5659	12.461	12.841±0.016	2.175±0.017	-0.380 ± 0.726	4522	25±16	2636 ± 1268	60	0.52	0.28	TM11
WKK5760	11.425	11.131±0.017	2.555±0.003	0.014 ± 0.414	5259	72±13	-167 ± 1009	77	0.25	0.60	TM11
WKK5768	9.527	9.206±0.010	2.706±0.001	-0.079 ± 0.289	5558	61±9	927 ± 714	82	0.18	0.73	TM11
WKK5993	13.052	12.906±0.026	2.393±0.022	0.192 ± 0.539	3598	74±13	-2006 ± 976	49	0.65	0.18	TM11
WKK5999	10.826	10.686±0.021	2.341±0.021	-0.331 ± 0.584	3354	20±10	1789 ± 774	47	0.68	0.17	TM11
WKK6181	10.985	11.412±0.021	2.353±0.003	-0.176 ± 0.583	3467	30±11	1155 ± 857	77	0.29	0.54	TM11
WKK6483	12.205	12.070±0.024	2.208±0.026	-0.337 ± 0.692	3371	20±12	1818 ± 920	59	0.52	0.28	TM11
WKK6570	13.221	13.656±0.027	2.176±0.013	-0.039 ± 0.727	3015	36±13	256 ± 991	68	0.41	0.39	AS09

The distribution of sample galaxy distances is presented in Figure 4.8. From the measured distances for the 12 individual spiral galaxies, there seems to be a bimodal distribution (see Figure 4.8) although small number statistics applies. It is unlikely that all these galaxies are in the Norma cluster since the range in distance is very large. The distance of the Norma cluster measured using the combined K_s-band Fundamental Plane is $\sim 68\pm2$ Mpc (assuming $H_0 = 75$ km s^{-1} Mpc^{-1}). It is therefore likely that the most distant galaxies are actually in the Norma cluster while the others are foreground galaxies (mean distance of 28 ± 7 Mpc). This implies a total of 6 spiral galaxies remaining in the sample which belong to the Norma cluster. The mean measured distance for these 6 galaxies is 65 ± 4 Mpc.

4.3.3.1 Relative Distances using the Coma cluster

An additional check for the foreground galaxies was performed by measuring distances of the galaxies in my sample relative to the Coma cluster as opposed to using the template relation. A total sample of 36 spiral galaxies within the Coma cluster was used (Masters et al., 2008). The spectroscopic data ($\log W$) were taken from Masters et al. (2008) while the isophotal magnitudes were taken from the 2MASS Extended Source Catalogue. The isophotal magnitudes were corrected for the Galactic and internal extinction effects, k-correction (or redshift effect) and morphological type dependence. The applied morphological correction is that which was derived by Said (2013) while calibrating the global/universal isophotal Tully-Fisher template.

For this analysis using the Coma cluster sample, I write the Tully-Fisher relation as:

$$m = b + a\,(\log W - 2.5)\,, \tag{4.38}$$

where m is the fully corrected isophotal magnitude. A weighted linear least squares fit was used to determine the slope and intercept by minimising the squares of the residuals. The fit was

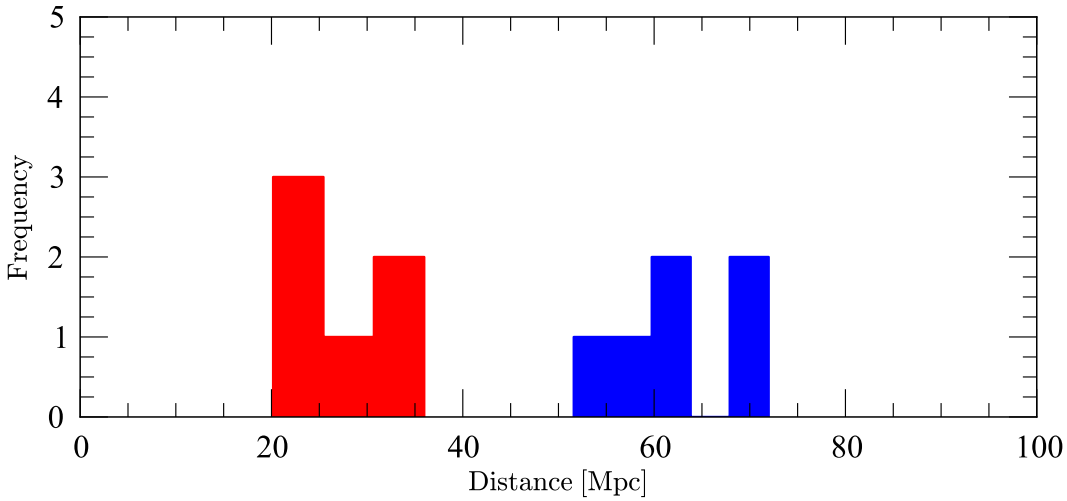

Fig. 4.8: Distribution of distances measured using the template Tully-Fisher relation. Individual galaxy distances were measured using the Tully-Fisher template to help identify foreground galaxies. The blue and red regions show the galaxies considered as cluster member and foreground galaxies, respectively.

performed using the Coma cluster galaxies. For a galaxy with measured and corrected isophotal magnitude m_n in my sample, the distance, d_n, was computed using

$$\Delta m = 5 \log\left(\frac{d_c}{d_n}\right), \tag{4.39}$$

where Δm is the offset of the galaxy from the Coma cluster Tully-Fisher relation, d_c is the distance to the Coma cluster. The Coma cluster was assumed to be at a distance of 96 Mpc, that is, $z_{\rm hel} = z_{\rm CMB} = 0.0240$ (Smith, 1999; Bernardi et al., 2002) and $H_0 = 75$ km s^{-1} Mpc^{-1}.

The black dashed line in Figure 4.9 shows the best fit to the Coma cluster sample represented by the 36 black star symbols. The blue filled circles represent the galaxies whose distance measurements using the global Tully-Fisher template, show they belong to the Norma cluster. The galaxies represented by the red filled circles were identified as foreground galaxies based on their distances measured using the global Tully-Fisher template.

From the bivariate fit to the Coma cluster, used to determine the Tully-Fisher slope and intercept, individual distances were measured for the spiral galaxies in my sample. Figure 4.10 shows the histogram distribution of the measured distances. This further confirms the presence of spiral galaxies in my sample that are not members of the Norma cluster. The distribution of the distances measured using the global Tully-Fisher template and fitting the Coma cluster sample are represented by the blue solid and red dashed lines, respectively. While there are significant differences between these and the distances measured using the global isophotal Tully-Fisher template, the distribution of distances measured relative to the Coma cluster Tully-Fisher relation further confirms the presence of possible foreground galaxies in my Tully-Fisher sample.

4.3.4 Incompleteness Bias Correction

Any sample under study, no matter the selection criteria, can never be expected to be complete. The sample will either be volume-limited, magnitude-limited or both. In either case, the brighter cluster galaxies will most likely make it into the sample. There is also incompleteness in HI line

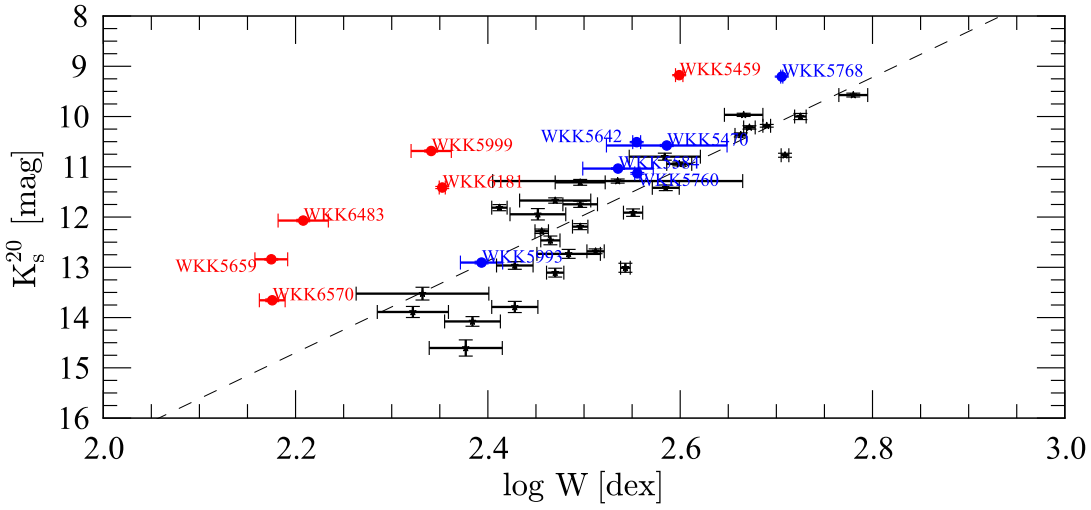

Fig. 4.9: The Coma cluster Tully-Fisher relation based on isophotal magnitudes. The black stars represent galaxies in the Coma cluster sample while the black dashed line shows the best fit to these Coma galaxies. The red and blue filled circles represent the spiral galaxies in my sample. The galaxies represented by the blue filled circles have been identified as belonging to the Norma cluster based on individual distance measurements using the Tully-Fisher template. The red filled circles represent foreground galaxies (see §4.3.3).

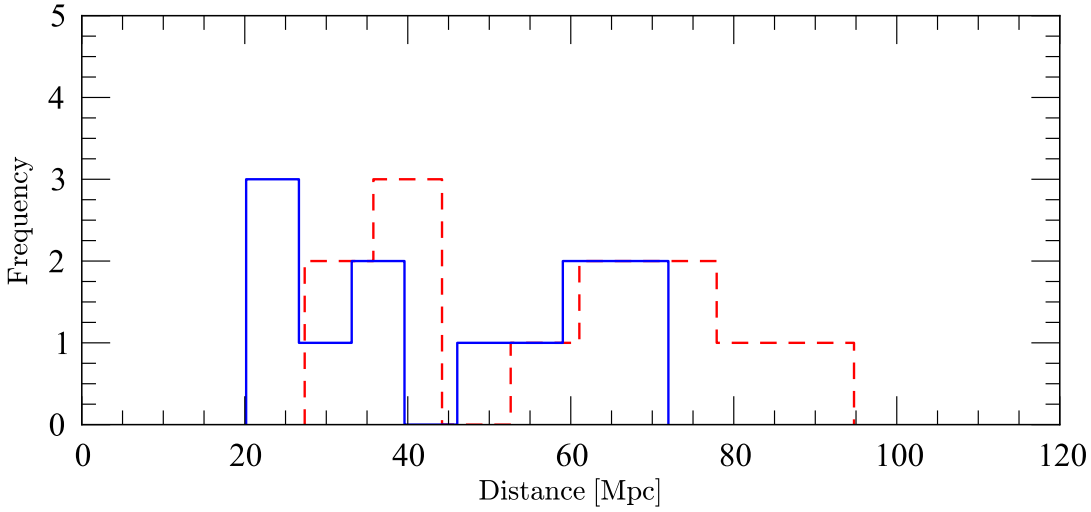

Fig. 4.10: The distribution of distances measured using the Coma cluster Tully-Fisher relation (red dashed line). The distribution of the individual galaxy distances measured using the Tully-Fisher template are overplotted (blue solid line).

widths from blind surveys, where galaxies with very narrow line width tend to not be classified as galaxies. Similarly, late-type galaxies with very broad profiles may be difficult to detect in HI if the signal-to-noise ratio is very low. For a magnitude-limited sample, the mean value of the observed magnitudes close to the limit will always be brighter than the actual average value. This is due to the fact that galaxies brighter than the magnitude limit can be observed while those fainter than the magnitude limit will never make it into the sample even though they are members of the cluster. This can result in under-estimating the distance, and hence incorrect positive peculiar velocities.

The brighter galaxies essentially lie on the upper part of the Tully-Fisher relation. Therefore, the incompleteness bias resulting from a magnitude-limited sample implies a shallower slope and brighter zero point of the Tully-Fisher relation. In addition, the brighter galaxies exhibit a smaller scatter than the fainter galaxies (Federspiel et al., 1994; Freudling et al., 1995; Masters et al., 2006, 2008). The absence of the galaxies fainter than the magnitude limit, which would essentially lie on the lower part of the relation, implies that the scatter in the relation would be under-estimated (see, for example, Strauss & Willick 1995). Although all these bias corrections were applied while deriving the Tully-Fisher template relations (see Said 2013), a proper incompleteness bias correction should also be applied to galaxies whose distances are measured using a calibrated Tully-Fisher template.

However, a proper correction for the incompleteness bias requires a clear understanding of the selection function. While selecting the sample for this study (see §2.2.1 for the selection criteria), a total of 99 late-type galaxies were identified. Only 66.7% of these were observed with priority targets based on the previous HI observations in this region (see Schröder et al. 2009). Previously, Schröder et al. (2009) reported a detection rate for Norma of 43% and 53% out to R_A and 1–2R_A, respectively. The HI observations presented in this dissertation were taken within 1.5R_A. From the previously reported detection rate, this implies a total number of detections $\sim 28 - 35$ galaxies. Note however, even with such numbers, not all these will have HI profiles with reliable measurements for use in the Tully-Fisher relation (due to, e.g, poor baselines and low signal-to-noise ratio).

Figure 4.11 presents Norma and Coma cluster late-type galaxies. The red filled circles represent the Coma cluster spiral galaxies (N = 36) taken from Masters et al. (2008). All corrections including the incompleteness bias correction (taken from Masters et al., 2008) have been applied to the Coma sample (see §4.3.3.1 for more details). The red dashed line is a bivariate fit to the Coma cluster sample. Galaxies identified as Norma cluster members are shown by the blue filled circles while foreground galaxies are represented by the blue open circles. The identification of Norma cluster galaxies is presented in §4.3.3. The effect of cluster incompleteness bias was assumed to be negligible, that is, no incompleteness bias correction was applied to the Norma cluster sample.

4.3.5 Peculiar Velocity for Groups / Clusters of Galaxies

For clusters or galaxies identified as belonging to the same group, the peculiar velocity is measured slightly differently (see Springob et al., 2007). Equation 4.25 on page 125 is modified to

$$v_{\rm pec,i} = v_{\rm CMB,\ cluster}\left(1 - 10^{\frac{\Delta M}{5}}\right), \tag{4.40}$$

where $v_{\rm CMB,\ cluster}$ is the CMB velocity of the cluster or group of galaxies while $v_{\rm pec,i}$ is the peculiar velocity for each individual galaxy that is a member of the group/cluster. For the Norma cluster, $v_{\rm CMB,\ cluster} = 4954$ km s^{-1}. I have identified six galaxies as belonging to the Norma cluster. The peculiar velocity of the Norma cluster based on these 6 galaxies is given by

$$v_{\rm pec,\,Norma} = \frac{\sum_{i=1}^{N} v_{\rm pec,i}/\epsilon_i}{\sum_{i=1}^{N} 1/\epsilon_i}, \tag{4.41}$$

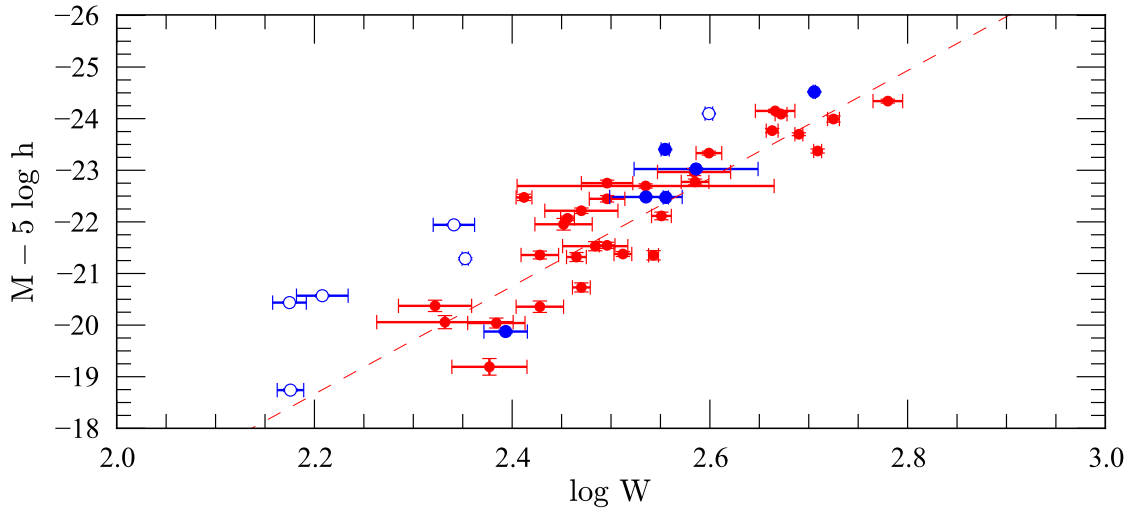

Fig. 4.11: Comparing the Coma and Norma cluster Tully-Fisher relations. The red filled circles represent Coma cluster spiral galaxies while the blue filled circles represent galaxies identified as Norma cluster members (see §4.3.3). The blue open circles represent galaxies identified as foreground members. The solid line represents the Tully-Fisher relation for the Coma cluster which was obtained using a bivariate fit.

where the summation is carried over the total number of galaxies in the cluster. For N galaxies in a group/cluster, the error on the group/cluster peculiar velocity, $\epsilon_{\rm cluster}$ is given by

$$\epsilon_{\rm cluster} = \frac{\sqrt{N}}{\sum_{i=1}^{N} 1/\epsilon_i}, \tag{4.42}$$

where ϵ_i is the error on the individual galaxy peculiar velocities (Springob et al., 2007).

Figure 4.12 shows the 12 galaxies used in the Tully-Fisher analysis. Galaxies belonging to the Norma cluster are represented by the blue filled circles while foreground galaxies are represented by the red filled circles. The peculiar velocity of the Norma cluster measured from the six galaxies using Equations 4.40, 4.41 and 4.42 is 74 ± 332 km s^{-1}. This further indicates that the Norma cluster has a small peculiar velocity which within the errors, is consistent with zero and in good agreement with the peculiar velocity measured using the Fundamental Plane. A summary and comparison of results obtained using the Fundamental Plane and Tully-Fisher relations is presented in Table 5.1 (§5.1 of Chapter 5).

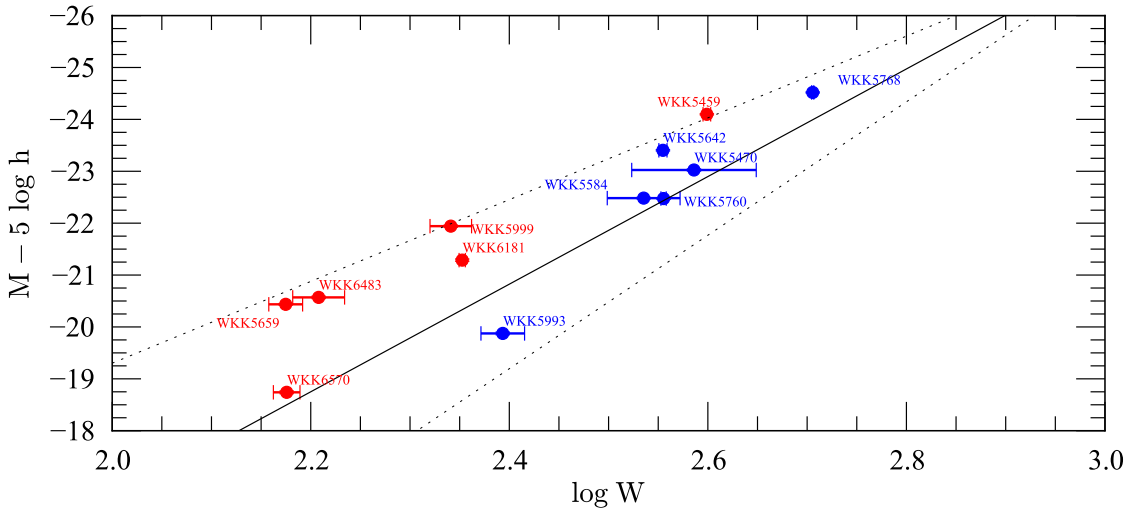

Fig. 4.12: Location of the sample galaxies on the template Tully-Fisher relation. The blue filled circles represent Norma cluster member galaxies while the red filled circles represent foreground galaxies. The solid line represents the template relation. The dashed lines indicate 3σ, where σ is the intrinsic scatter on the template relation given by Equation 4.21 on page 124.

CHAPTER 5

DISCUSSION AND CONCLUSIONS

Our knowledge of the local cosmography in the Great Attractor region has considerably improved due to galaxy redshift surveys that probe close to the Galactic plane (Radburn-Smith et al., 2006; Jones et al., 2009; Riad, 2010; Huchra et al., 2012). These have revealed the complex interconnections of structures in the Great Attractor region (Radburn-Smith et al., 2006; Riad, 2010). However, there are still aspects that are incomplete and some important groups/clusters belonging to the Great Attractor may still remain hidden (Riad, 2010). The application of the mid-infrared Tully-Fisher relation is now being considered as a distance indicator to measure and study the peculiar motions of gas-rich galaxies in the Zone of Avoidance. These include Tully-Fisher relations using *Spitzer* (Sorce et al., 2012), WISE (Lagattuta et al., 2013) and the near-infrared J, H, and K_s passbands (Williams, 2011; Said, 2013; Williams et al., 2014). The application of the two distance indicators (Fundamental Plane and Tully-Fisher relations) for early and late-type galaxies in the Zone of Avoidance will advance our understanding of the velocity flows in the Great Attractor region. The peculiar velocity studies may also help unveil other large scale structures that remain hidden due to obscuration by our Galaxy.

The analysis and results presented in this dissertation have demonstrated, that, despite the challenges of the large Galactic extinction and severe stellar contamination, distances using the Fundamental Plane and Tully-Fisher relations can be derived reliably for galaxies that lie relatively close to the Galactic plane. In Table 3.5 (see also Table 3.6), I have given a summary of possible sources of measurement and systematic errors and the applied corrections for the Fundamental Plane results. Results from simulations showed that the effect of star-subtraction is very small, ranging from $-0^{\rm m}.011$ (NTT K_s-band data) to $-0^{\rm m}.014$ (IRSF K_s-band data), which offsets the measured peculiar velocity by ~ 41 km s^{-1} to ~ 50 km s^{-1}, respectively. The systematic effect arising from possible gradients in the sky background is very small, i.e., $\sim -0^{\rm m}.008$, which corresponds to a change in Norma's measured peculiar velocity of ~ 29 km s^{-1}. For extinction corrections, Bonifacio et al. (2000); Schröder et al. (2007); Schlafly & Finkbeiner (2011) have re-calibrated the Schlegel et al. (1998) extinction values. The correction factor is in the range 70% – 90% (~ -26 km s^{-1} to -41 km s^{-1}). Schlafly & Finkbeiner (2011) estimated that the Schlegel et al. values are over-estimated by 14% (a correction factor of 0.86) with preference

to the Fitzpatrick (1999) reddening law. The worst effect of Galactic extinction corrections for the Norma sample, varies from ~ -33 km s^{-1} to ~ -51 km s^{-1}, based on the minimum and maximum values of the difference between Schlegel et al. (1998) and Schlafly & Finkbeiner (2011), i.e., 0.009 mag to 0.014 mag. Using the near-infrared J and K_s-band images obtained using the IRSF telescope has also helped re-calibrate the Schlegel et al. (1998) extinction values as described in §3.2.5. For the Norma cluster sample, the measured extinction correction factor is 0.81 for the Schlegel et al. maps, which is in good agreement with the Schlafly & Finkbeiner (2011) extinction values.

The combined K_s-band Fundamental Plane sample resulted in the largest cluster sample ($N = 41$) used in the peculiar velocity studies at relatively low Galactic latitudes to date. This has resulted in the most accurate distance and peculiar velocity of the Norma cluster measured to date (see Table 5.2).

5.1 Comparison of the Fundamental Plane and Tully-Fisher Results

The distance and peculiar velocity of the Norma cluster measured using the Fundamental Plane and Tully-Fisher relations are in good agreement (see Table 5.1 below).

Tab. 5.1: Comparison of the distance and peculiar velocity of the Norma cluster measured using the Fundamental Plane and Tully-Fisher relations. The peculiar velocity was calculated using $v_{\rm pec} \equiv cz_{\rm pec}$ where $z_{\rm pec}$ was measured from the Fundamental Plane zero point offset. For the Tully-Fisher relation, $v_{\rm pec}$ was calculated using the offset of each individual galaxy from the Tully-Fisher template. To measure $H_0 d$ for the Norma cluster, the approximation: $v_{\rm pec} \approx cz_{\rm CMB} - H_0\, d$, was used.

Method	N	$H_0\, d$ km s^{-1}	$v_{\rm pec} \equiv cz_{\rm pec}$ km s^{-1}
Fundamental Plane	31	5026 ± 160	−72 ± 170
Fundamental Plane	41	5063 ± 147	−109 ± 157
Tully-Fisher	6	4880 ± 331	74 ± 332

The peculiar velocity for the Norma cluster measured using both the Fundamental Plane and Tully-Fisher relations is small and is within errors, consistent with zero. The peculiar velocity measured using the Tully-Fisher analysis is subject to large statistical errors due to the small sample size. The galaxies in the final Tully-Fisher sample used to determine the distance and peculiar velocity of the Norma cluster presupposes the Fundamental Plane distance of the cluster. While this may be the case given the Fundamental Plane sample of 41 Norma cluster early-type galaxies, the use of the Fundamental Plane measured distance of Norma to determine which galaxies are cluster members and which are foreground, renders the Tully-Fisher result to some extent dependent on the Fundamental Plane results. I have, however, demonstrated that reliable distance measurements using both the Fundamental Plane and Tully-Fisher relations can be achieved for galaxies and galaxy clusters at relatively low Galactic latitudes.

Figure 5.1 shows the location of the galaxies used in the Tully-Fisher and Fundamental Plane analyses. The early-type galaxies used in the Fundamental Plane analysis are represented by the red filled circles (near-infrared imaging from the NTT) and the blue open circles (near-infrared imaging from the IRSF telescope). The spiral galaxies used in the Tully-Fisher analysis are represented by the blue and red open stars. The red stars represent the galaxies taken to be foreground galaxies (see §4.3.3) while the blue stars represent the galaxies that were used in computing the distance and peculiar velocity of the Norma cluster

using the global Tully-Fisher template. The three concentric circles represent $\frac{1}{3}R_{\rm A}$, $\frac{2}{3}R_{\rm A}$ and $R_{\rm A}$, where $R_{\rm A}$ is the Norma cluster's Abell radius. The spiral galaxies shown are all within $1.5R_{\rm A}$.

For the Fundamental Plane analysis, the dominant source of measurement errors is the central velocity dispersion. The combination of the photometric parameters which form the X-component of the Fundamental Plane ($X_{\rm FP} \sim \log r_e - 0.32\langle\mu_e\rangle$) results in a reduced scatter which is smaller than the individual scatter on $\log r_e$ and $\langle\mu_e\rangle$. For the Tully-Fisher relation, the dominant source of error originates from the measurement errors on the line widths. Note that the total observed scatter in the Tully-Fisher relation is a function of W (corrected line width); the scatter is larger for relatively low line widths (mostly faint galaxies) than for the brighter galaxies (with larger line widths). Future improved line widths and central velocity dispersion measurements (and complete samples) will therefore reduce the errors on the Norma cluster's measured peculiar velocity down to ~ 100 km s^{-1}. For example, TAIPAN (Transforming Astronomical Imaging surveys through Polychromatic Analysis of Nebulae) survey will supersede the 6dF Galaxy Survey by using upgraded fibres on the UK Schmidt Telescope. The 6dF Galaxy Survey subsample used for peculiar velocity measurements (6dFGSv; Springob et al., 2014), is limited to heliocentric redshift $z = 0.055$ because the velocity dispersion measurements with the 6dF spectrograph are dominated by systematics beyond $z = 0.055$ (Koda et al., 2014). The new spectrograph for TAIPAN will improve the velocity dispersion measurements from $z = 0.055$ for 6dFGSv to $z = 0.1$, and also decrease the lower limit of the velocity dispersion from 116 km s^{-1} for 6dFGSv to 70 km s^{-1} (Koda et al., 2014). While the current Norma cluster sample ($N = 41$) is the largest sample used for peculiar velocity studies of clusters in the Great Attractor region to date, Woudt et al. (2008) identified a total of 107 early-type galaxies belonging to the Norma cluster. Using reliable central velocity dispersion measurements for such a complete sample would reduce the error on the measured peculiar velocity by $\sim 25\%$.

5.2 Comparison of Results with Literature

The Great Attractor is now widely identified as the Hydra-Cen-Norma supercluster (Courtois et al., 2012; Shaya & Tully, 2013; Tully et al., 2013, 2014). Since the original discovery of the large positive peculiar velocities in the Hydra-Centaurus region (Lynden-Bell et al., 1988), new peculiar velocity measurements in the general Great Attractor region have been obtained by using either the Tully-Fisher, $D_n - \sigma$, or the Fundamental Plane relations as distance indicators. These measurements are from galaxy surveys which include

- Streaming Motions of Abell Clusters (SMAC) survey for which distances were derived using the Fundamental Plane (Hudson et al., 2004),
- ENEARc survey for Early-type NEARby galaxies in clusters (da Costa et al., 2000a,b). Like the SMAC survey, the peculiar velocities were derived from distances measured using the Fundamental Plane and $D_n - \sigma$ relations (Bernardi et al., 2002),
- SFI++ survey for spiral galaxies in the field (Giovanelli et al., 1994; da Costa et al., 1996). The distances were measured using the Tully-Fisher relation (Springob et al., 2007).

A summary of results from the SFI++, SMAC and ENEARc surveys is presented in Table 5.2. For comparison, the peculiar velocity of the Norma cluster measured using both the Fundamental Plane and Tully-Fisher relations is included. Figure 5.2 shows the projections of the peculiar velocity measurements presented in Table 5.2. Shown are the comparisons for the measurements

Tab. 5.2: Peculiar velocities of clusters/groups in the Great Attractor region, sorted by Galactic longitude. N_ϕ is the angle on the sky between the cluster and Norma. SMAC measurements are from Hudson et al. (2004), the SFI++ measurements are from Springob et al. (2007) while ENEARc measurements are from Bernardi et al. (2002). Note that CIZA J1324.7−5736 with $N_\phi = 21$ and is the second richest cluster in the Great Attractor region, has no measured peculiar velocity.

Cluster	ℓ °	b °	N_ϕ °	cz_{CMB} km s^{-1}	N	v_{PEC} km s^{-1}	Source
A1060 (Hydra)	270	26	62	4055	26	+254 ± 223	SMAC
					39	–47 ± 168	ENEARc
					21	–422 ± 169	SFI++
AS636 (Antlia)	272	19	58	3129	17	+292 ± 102	SFI++
AS639	281	11	47	6526	6	+1615 ± 453	ENEARc
N3557 group	282	21	50	3318	7	+281 ± 160	SFI++
A3526A (Cen30)	302	22	37	3300	27	+351 ± 136	SMAC
					21	+500 ± 153	ENEARc
					23	+260 ± 124	SFI++
AS714	303	36	47	3576	7	+559 ± 245	ENEARc
A3537	305	31	43	5370	4	+482 ± 560	SMAC
E508 group	309	39	48	3310	9	+382 ± 122	SFI++
A3574 (K27)	317	31	39	4881	8	+487 ± 351	SMAC
					10	+479 ± 310	ENEARc
					13	–199 ± 210	SFI++
AS753	319	26	34	4431	14	+376 ± 282	SMAC
					18	+812 ± 204	ENEARc
A3581	323	33	40	6714	8	+131 ± 533	SMAC
A3627 (Norma)	**325**	**–7**	**0**	**4954**	**31**	**–72 ± 170**	**This work** †
					41	**–109 ± 157**	**This work** ††
					6	**+74 ± 332**	**This work** †††
AS761	326	32	39	7076	11	+332 ± 483	SMAC
AS805 (Pavo-II)	332	–23	17	4266	9	+293 ± 326	SMAC
					12	–18 ± 268	ENEARc
					8	+304 ± 147	SFI++
Pavo I group	334	–36	30	4055	16	+473 ± 191	SFI++

† Norma cluster early-type galaxies with K_s-band images obtained with the 3.6 m New Technology telescope (NTT). The distance and peculiar velocity were measured using the K_s-band Fundamental Plane analysis. †† Norma cluster early-type galaxies with K_s-band images obtained with the NTT and the 1.4 m Infrared Survey Facility (IRSF). The distance and peculiar velocity were measured using the combined K_s-band Fundamental Plane analysis. ††† Norma cluster late-type galaxies with K_s-band images obtained with the IRSF. The distance and peculiar velocity were measured using the K_s-band isophotal Tully-Fisher template of Said et al. (2015).

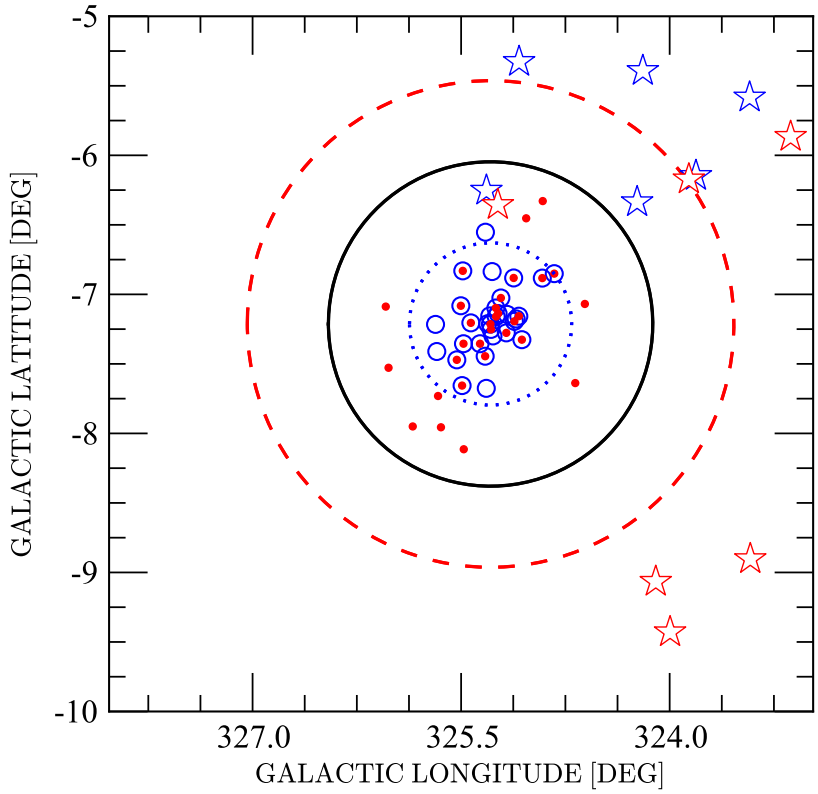

Fig. 5.1: Location of the galaxies used in the Tully-Fisher and Fundamental Plane analyses. The NTT data for early-type galaxies are represented by the red filled circles. The blue open circles represent the early-type galaxies with near-infrared imaging from the IRSF. The spiral galaxies used in the Tully-Fisher analysis are represented by the blue and red open stars. The red stars represent the galaxies taken to be foreground galaxies while the blue stars are the Norma cluster member galaxies. The blue dotted, black solid and red dashed circles represent $\frac{1}{3}R_{\rm A}$, $\frac{2}{3}R_{\rm A}$ and $R_{\rm A}$, respectively ($R_{\rm A}$ is the Norma cluster's Abell radius).

from ENEARc (black diamonds), SMAC (magenta), SFI++ (blue) and this work. The Norma cluster is represented by the black star. The shaded region represents 3σ where $\sigma = 157$ km s^{-1} is the error on the Norma cluster's peculiar velocity derived using the combined K_s-band Fundamental Plane analysis. I should point out that, this is not a complete sample but only for the clusters in the Great Attractor region whose peculiar velocities have been measured (see Table 5.2). Note that although these peculiar velocity measurements have typical measurement errors in the range 150—400 km s^{-1}, most clusters in the Great Attractor region have positive peculiar velocities as can clearly be seen in Figure 5.2.

5.2.1 Great Attractor Versus Shapley Supercluster

Despite more than two decades of study, the fractional contribution of the Great Attractor and Shapley concentration on the Local Group's peculiar velocity remains a topic of debate. Smith et al. (2000) found an equal contribution of $50 \pm 10\%$ from the Great Attractor and Shapley Supercluster to the Local Group's motion. Lucey, Radburn-Smith & Hudson (2005) measured peculiar motions for 98 Type Ia supernovae to $cz = 14000$ km s^{-1} and found a sizable flow towards the Shapley Supercluster (no evidence for backside infall into the Great Attractor). In their analysis, all 9 supernovae in their sample that lie closer than the Shapley Concentration

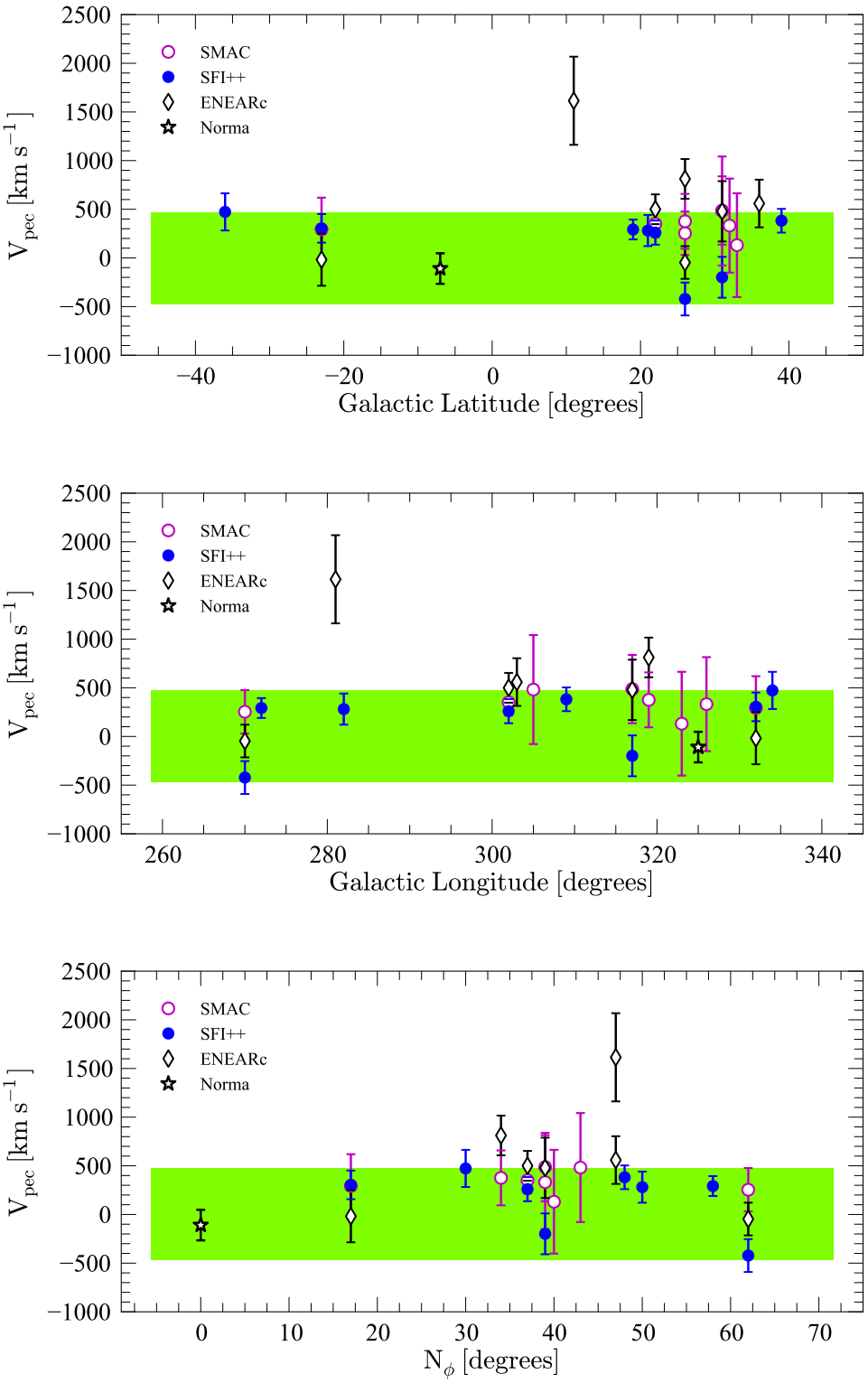

Fig. 5.2: Peculiar velocities of galaxy clusters in the Great Attractor region. Note the poor coverage in the southern Zone of Avoidance and deep in the Zone of Avoidance at low Galactic latitudes close to the Galactic plane. The x-axis indicates the Galactic latitude (top panel), Galactic longitude (middle panel) and the angular separation, N_ϕ (bottom panel). The shaded region shows $\pm 3\sigma$ where σ is the error on the Norma cluster's peculiar velocity measured using the combined K_s-band Fundamental Plane analysis ($v_{\mathrm{pec,\ Norma}} = -109 \pm 157$ km s^{-1}), that is, $\sigma = 157$ km s^{-1}.

and in the direction of the Great Attractor, showed positive peculiar velocities. While this implies a sizable flow towards the Shapley Concentration, their results have significant large random errors making it difficult to disentangle between the Great Attractor and Shapley contributions.

Using an X-ray selected sample, Kocevski & Ebeling (2006) found the Great Attractor to generate $\sim 44\%$ of the observed Local Group's peculiar velocity while the remaining 56% is due to infall into more distant over-densities of which the Shapley Supercluster is the major contributor. In addition, Lavaux et al. (2010) and Bilicki et al. (2011) found no convergence of the Local Group's motion within $120h^{-1}$ Mpc. While Erdoğdu et al. (2006b) detected backside infall into the Great Attractor using the Two-Micron All-Sky Redshift Survey catalogue, Lavaux et al. (2010) did not detect any backside infall. In the analysis by Lavaux et al. (2010), they recovered the majority of the amplitude of the Local Group's peculiar velocity within $120h^{-1}$ Mpc but the direction of motion did not agree with the expected direction of the CMB dipole – they suggested convergence may lie as far as $200h^{-1}$ Mpc which is supported by recent measurements using 2M++ sample (Carrick, 2014; Carrick et al., 2015).

Bardelli et al. (2000) estimated that the Shapley Supercluster was responsible for only 26 km s^{-1} of the Local Group's motion with respect to the cosmic microwave background. Bolejko & Hellaby (2008) estimate that the Shapley Concentration has a net peculiar velocity on the Great Attractor of $\sim +80$ km s^{-1}. Both their results differ significantly from Kocevski & Ebeling (2006) who found a large contribution from the Shapley Supercluster (approximately 70% of the dipole signal coming from distant mass concentrations greater than $60h^{-1}$Mpc^{-1}). Recent results from the 6dF Galaxy Redshift and Peculiar Velocity Survey show positive peculiar velocities in the direction of Shapley and Vela (Springob et al., 2014). On the other hand, Tully et al. (2014) have recently proposed that we live in a Supercluster (the "Laniakea" supercluster) extending up to a diameter of 12 000 km s^{-1}. Their measured local flows within this Supercluster converge towards Centaurus and Norma clusters.

5.2.2 Is the Norma Cluster the Core of the Great Attractor ?

If Norma is the dynamical core of the Great Attractor, its negligibly small peculiar velocity implies that, the Great Attractor and not Shapley, is responsible for all of the observed Local Group motion. If this is not the case, that is, if the Great Attractor is partly responsible for the Local Group motion, then the Norma cluster (and so the Great Attractor), would have a positive peculiar velocity towards Shapley. Using the best measurements from the combined K_s-band Fundamental Plane analysis, the measured line-of-sight component of the peculiar velocity for the Norma cluster is very small, that is, -109 ± 157 km s^{-1}. This is, within the measurement errors consistent with zero. This implies that the Norma cluster, which is by far the major component (in terms of richness and mass) in the Great Attractor region does not significantly share the observed Local Group's motion, at least along the line-of-sight. In addition, the small peculiar velocity for the Norma cluster of -109 ± 157 km s^{-1} is lower than most values found for other Great Attractor clusters (see Table 5.2 and Figure 5.2) – most of the other clusters in the Great Attractor region have positive peculiar velocities yet we would expect to see both positive and negative velocities for clusters in the Great Attractor region, if indeed, the Great Attractor is fully responsible for the observed Local Group motion.

If the Great Attractor contributes only part of the Local Group motion, which implies that, the Great Attractor centre of mass frame is itself moving towards Shapley, the puzzle is why the Norma cluster, the biggest single mass concentration in the Great Attractor region, is at rest in the cosmic microwave background frame. More over, the other observed clusters in the Great

Attractor region generally show positive peculiar velocities. In other words, the main puzzle is the discrepancy between Norma's peculiar velocity and the mean peculiar velocity of all the other observed clusters in the Great Attractor region, as seen in Figure 5.2. There is therefore a need to extend farther and observe clusters in the far side of the Great Attractor. From Table 5.2 (see column 5), the majority of the clusters with measured peculiar velocities are from the near side of the Great Attractor hence the mean Great Attractor velocity may be biased positive.

The uncertainties on the cluster peculiar velocities listed in Table 5.2 are sufficiently large that we can not currently determine whether or not Norma partakes in the general Great Attractor outflow. However, there is strong independent support for the Great Attractor outflow from the Type Ia supernovae data (Lucey et al., 2005) and many studies (e.g., Hudson et al. 1999; Kocevski & Ebeling 2006; Magoulas 2012; Springob et al. 2014) have attributed a major part of this large scale outflow to the Shapley Supercluster that lies ~10 000 km s^{-1} more distant in this general direction.

The idea of determining the mass concentration responsible for the Local Group's peculiar motion is to find a volume within which there is convergence in both the amplitude and direction of the apex of the CMB dipole. In the case of the Great Attractor being the sole cause of the observed motion, then there would be a backside infall into the Great Attractor. While Erdoğdu et al. (2006b) claim to have predicted this, Lavaux et al. (2010) disagree. Although recent studies suggest convergence beyond $200h^{-1}$ Mpc, it remains unclear whether there are structures large and massive enough to influence the Local Group's motion at such large distances. In many of these studies of bulk flows, whose main aim is to determine at what distance the CMB dipole converges, the analyses exclude the Zone of Avoidance. Yet the direction of motion points into or close to the Zone of Avoidance (Ma & Pan, 2014). The reason for excluding the Zone of Avoidance is because of the difficulty in observing galaxies in this region, due to the effects of star-crowding and Galactic extinction.

In this dissertation, I have demonstrated that the effect of star-subtraction is not very significant although a lot of work and effort are needed in subtracting the foreground stars before reliably extracting any photometric parameters. Through simulations, I found the effect of star-subtraction to be less than 0.02 mag. Note that I have used high resolution images from both the NTT and IRSF whose pixel scales are 0.29 arcsec per pixel and 0.45 arcsec per pixel, respectively. The high resolution images minimise the effects of blending (challenges in star-galaxy separation). Thus, including the Zone of Avoidance in future galaxy surveys will be crucial to finally obtain a complete sky sample and a homogeneous data set over the entire sky. There are efforts in place to shed more light on the velocity flows in the Zone of Avoidance using distances measured using an isophotal Tully-Fisher template (Said, 2013). This will supplement the previous findings of the peculiar velocities for groups/clusters in the Great Attractor region. While one has to keep in mind the possible errors that may arise from extinction corrections for late-type galaxies, this study has demonstrated that both the Tully-Fisher and Fundamental Plane relations can reliably be used for distance measurements to structures in the Zone of Avoidance.

5.3 Conclusion

The measurements in this work show that the Norma cluster has a small peculiar velocity, that is consistent with zero. This is smaller than the measured peculiar velocities for groups/clusters in the Great Attractor region (see Table 5.2). However, the errors associated with these measure-

ments are still large. To better constrain the Norma cluster's distance and peculiar velocity, a more complete galaxy sample of the Norma cluster (both spectroscopic and photometric) will be required. By extending the analysis to the larger Great Attractor region, a more comprehensive analysis of the Great Attractor's contribution towards the Local Group's peculiar motion may be determined. In future, new and improved central velocity dispersion measurements suitable for Fundamental Plane studies down to ~ 50 km s^{-1}, will reduce the error on the measured peculiar velocity. For example, if the current Norma cluster sample of early-type galaxies can be doubled, the error on the measured peculiar velocity reduces by $\sim 22\%$. By extending the analysis to other low-latitude clusters in the Great Attractor region, one can better constrain the lower and upper limits of cluster peculiar velocities in the Great Attractor region.

5.4 Future Work

The clusters in the Great Attractor region, especially those lying at low Galactic latitudes, remain not well studied (see the top panel of Figure 5.2). A dynamical analysis and understanding of these clusters and peculiar velocity measurements will lead to a better understanding of the velocity flows within the Great Attractor region. Such measurements could include, for example, CIZA J1324.7-5736, the second richest cluster in the Great Attractor region (Nagayama et al., 2006). Although the size of the Zone of Avoidance has significantly reduced over the years, galaxy detections remain incomplete close to the Galactic Plane, due to severe extinction.

Reliable peculiar velocity measurements for the second richest cluster in the Great Attractor region may give clues to the velocity flows, when such measurements are combined with the existing results presented in Table 5.2. Also, future galaxy surveys covering the Zone of Avoidance will help uncover possible large scale structures still under the veil of the Milky Way, for example, the Vela region (Kraan-Korteweg et al., in preparation). Recently, Hong et al. (2014) used 2,018 bright inclined spiral galaxies to estimate the amplitude and direction of the bulk flow based on the 2MASS Redshift Survey (Huchra et al., 2012). To measure the redshift independent distances using the Tully-Fisher relation calibrated by Masters et al. (2008), Hong et al. (2014) have used the 2MASS near-infrared photometry and high signal-to-noise HI 21-cm data (Hong et al., 2013; Masters et al., 2014). The measured bulk flow within $40h^{-1}$ Mpc using the K_s-band is of amplitude 292 ± 28 km s^{-1} in the direction $\ell = 296.^{\circ}5 \pm 9.^{\circ}8$, $b = 6.^{\circ}5 \pm 9.^{\circ}2$ (Hong et al., 2014) which, like other previous studies of bulk flows, has direction pointing to the Zone of Avoidance. There is therefore a need to probe deeper into the Zone of Avoidance to Galactic latitudes $|b| \lesssim 5^{\circ}$ to include structures that remain hidden so as to obtain galaxy surveys that are truly full-sky. This will advance our understanding of peculiar velocity flows and the large scale distribution of matter.

I have measured a small negative peculiar peculiar velocity for the Norma cluster although most of the other clusters in the Great Attractor region have positive peculiar velocities. Norma is the richest cluster in the Great Attractor region and lies at or close to the centre of the Great Attractor. Based on the measurements of the Norma cluster's peculiar velocity presented in this thesis, there is a clear discrepancy in the measured peculiar velocities for clusters in the Great Attractor region. To resolve this issue (discrepancy), a large Fundamental Plane sample in the Norma cluster is required to tie down its peculiar velocity even better. To better understand the motion of the Great Attractor as a whole, Fundamental Plane observations of a more complete sample of clusters in the Great Attractor region are required.

Since the Norma cluster has been found to be HI-deficient, a more complete sample may be obtained by considering line widths measured using optical observations (e.g., from H_α; Courteau 1997; Dale et al. 1997; Catinella et al. 2005; Pizagno et al. 2007). This would improve the sample by complementing the 21 cm observations. A future consideration using optical observations for example, at the Southern African Large Telescope (SALT), will help improve the sample given the low detection rate ($\sim 48.5\%$ within $1.5\,R_{\rm A}$) recorded through 21 cm observations (see §2.2.2 and also Schröder et al. 2009). Future HI surveys using radio telescopes such as MeerKAT in South Africa, APERTIF in the Netherlands and the Australian SKA Pathfinder (ASKAP) will also improve our understanding of the large scale distribution of matter by detecting many more galaxies hence improving galaxy completeness.

Future galaxy surveys e.g, the Widefield ASKAP *L*-Band Legacy All-sky Blind SurveY (WALLABY[1]; Beutler et al., 2012; Duffy et al., 2012), and TAIPAN (Transforming Astronomical Imaging surveys through Polychromatic Analysis of Nebulae; Beutler et al., 2011, 2012) will detect many more galaxies with their spectroscopic parameters. These will be explored for use in the study of velocity flows with distances measured via the Tully-Fisher (for late-type galaxies) and the Fundamental Plane (for early-type galaxies) methods. Current and upcoming multi-band photometric data from e.g., *Spitzer*, Wide-field Infrared Survey Explorer (WISE), and SkyMapper will improve our current coverage of the Zone of Avoidance and also probe beyond the Shapley Supercluster. This will greatly improve our current understanding of peculiar velocity flows and the large scale distribution of matter.

[1] http://www.atnf.csiro.au/research/WALLABY

References

Aaronson M., Bothun G., Mould J., Huchra J., Schommer R. A., Cornell M. E., 1986, ApJ, 302, 536

Aaronson M., Bothun G. D., Cornell M. E., et al., 1989, ApJ, 338, 654

Aaronson M., Huchra J., Mould J., 1979, ApJ, 229, 1

Aaronson M., Mould J., Huchra J., Sullivan III W. T., Schommer R. A., Bothun G. D., 1980, ApJ, 239, 12

Abazajian K., Adelman-McCarthy J. K., Agüeros M. A., et al., 2003, AJ, 126, 2081

Abazajian K. N., Adelman-McCarthy J. K., Agüeros M. A., et al., 2009, ApJS, 182, 543

Abell G. O., Corwin Jr. H. G., Olowin R. P., 1989, ApJS, 70, 1

Ahn C. P., Alexandroff R., Allende Prieto C., et al., 2014, ApJS, 211, 17

Aihara H., Allende Prieto C., An D., et al., 2011, ApJS, 193, 29

Allen D. A., Staveley-Smith L., Meadows V. S., Roche P. F., Norris R. P., 1990, Nature, 343, 45

Amanullah R., Lidman C., Rubin D., et al., 2010, ApJ, 716, 712

Anderson L., Aubourg É., Bailey S., et al., 2014, MNRAS, 441, 24

Atrio-Barandela F., Kashlinsky A., Ebeling H., Kocevski D., Edge A., 2011, Journal of Physics Conference Series, 314, 1, 012083

Baade W., 1954, Trans. I.A.U., 8, 397

Baade W., 1956, PASP, 68, 5

Baade W., Minkowski R., 1954, ApJ, 119, 206

Balkowski C., Bottinelli L., Chamaraux P., Gouguenheim L., Heidmann J., 1973, A&A, 25, 319

Bardeen J. M., Bond J. R., Kaiser N., Szalay A. S., 1986, ApJ, 304, 15

Bardelli S., Zucca E., Zamorani G., Moscardini L., Scaramella R., 2000, MNRAS, 312, 540

Barnes D. G., Staveley-Smith L., de Blok W. J. G., et al., 2001, MNRAS, 322, 486

Basilakos S., Plionis M., 2006, MNRAS, 373, 1112

Baum W. A., Hammergren M., Thomsen B., et al., 1997, AJ, 113, 1483

Bell E. F., McIntosh D. H., Katz N., Weinberg M. D., 2003, ApJS, 149, 289

Bennett C. L., Banday A. J., Gorski K. M., et al., 1996, ApJ, 464, L1

Bennett C. L., Larson D., Weiland J. L., et al., 2013, ApJS, 208, 20

Bernardi M., Alonso M. V., da Costa L. N., et al., 2002, AJ, 123, 2159

Bernardi M., Sheth R. K., Annis J., et al., 2003, AJ, 125, 1866

Bertin E., Arnouts S., 1996, A&AS, 117, 393

Bertin G., Ciotti L., Del Principe M., 2002, A&A, 386, 149

Bertschinger E., Dekel A., 1989, ApJ, 336, L5

Beutler F., Blake C., Colless M., et al., 2011, MNRAS, 416, 3017

Beutler F., Blake C., Colless M., et al., 2012, MNRAS, 423, 3430

Bilicki M., Chodorowski M., Jarrett T., Mamon G. A., 2011, ApJ, 741, 31

Blakeslee J. P., Cantiello M., Mei S., et al., 2010, ApJ, 724, 657

Blakeslee J. P., Jordán A., Mei S., et al., 2009, ApJ, 694, 556

Blakeslee J. P., Lucey J. R., Barris B. J., Hudson M. J., Tonry J. L., 2001, MNRAS, 327, 1004

Blanton M. R., Roweis S., 2007, AJ, 133, 734

Blumenthal G. R., Faber S. M., Primack J. R., Rees M. J., 1984, Nature, 311, 517

Boehringer H., Neumann D. M., Schindler S., Kraan-Korteweg R. C., 1996, ApJ, 467, 168

Böhringer H., Schuecker P., Guzzo L., et al., 2001, A&A, 369, 826

Böhringer H., Schuecker P., Guzzo L., et al., 2004, A&A, 425, 367

Bolejko K., Hellaby C., 2008, General Relativity and Gravitation, 40, 1771

Bonifacio P., Monai S., Beers T. C., 2000, AJ, 120, 2065

Bottinelli L., Chamaraux P., Gérard E., et al., 1971, A&A, 12, 264

Branchini E., Teodoro L., Frenk C. S., et al., 1999, MNRAS, 308, 1

Bravo-Alfaro H., Cayatte V., van Gorkom J. H., Balkowski C., 2000, AJ, 119, 580

Burstein D., 1990, Reports on Progress in Physics, 53, 421

Burstein D., Faber S. M., Dressler A., 1990, ApJ, 354, 18

Busarello G., Capaccioli M., Capozziello S., Longo G., Puddu E., 1997, A&A, 320, 415

Calabretta M. R., Staveley-Smith L., Barnes D. G., 2014, PASA, 31, 7

Cameron L. M., 1990, A&A, 233, 16

Campbell L. A., Lucey J. R., Colless M., et al., 2014, MNRAS, 443, 1231

Caon N., Capaccioli M., D'Onofrio M., 1993, MNRAS, 265, 1013

Cardelli J. A., Clayton G. C., Mathis J. S., 1989, ApJ, 345, 245

Carpenter J. M., 2001, AJ, 121, 2851

Carrick J., 2014, Virtues of the Visible; Voluminous Vistas & Velocities, Master's thesis, Univ. Waterloo

Carrick J., Turnbull S. J., Lavaux G., Hudson M. J., 2015, MNRAS, 450, 317

Catinella B., Haynes M. P., Giovanelli R., 2005, AJ, 130, 1037

Chilingarian I. V., Melchior A.-L., Zolotukhin I. Y., 2010, MNRAS, 405, 1409

Chincarini G., Rood H. J., 1979, ApJ, 230, 648

Ciotti L., 1991, A&A, 249, 99

Ciotti L., Bertin G., 1999, A&A, 352, 447

Cole S., Percival W. J., Peacock J. A., et al., 2005, MNRAS, 362, 505

Colin J., Mohayaee R., Sarkar S., Shafieloo A., 2011, MNRAS, 414, 264

Colless M., Dalton G., Maddox S., et al., 2001a, MNRAS, 328, 1039

Colless M., Saglia R. P., Burstein D., Davies R. L., McMahan R. K., Wegner G., 2000, in Cosmic Flows Workshop, edited by S. Courteau, J. Willick, vol. 201 of Astronomical Society of the Pacific Conference Series, 54

Colless M., Saglia R. P., Burstein D., Davies R. L., McMahan R. K., Wegner G., 2001b, MNRAS, 321, 277

Courteau S., 1997, AJ, 114, 2402

Courtois H. M., Hoffman Y., Tully R. B., Gottlöber S., 2012, ApJ, 744, 43

Courtois H. M., Pomarède D., Tully R. B., Hoffman Y., Courtois D., 2013, AJ, 146, 69

Cutri R. M., Skrutskie M. F., van Dyk S., et al., 2003, VizieR Online Data Catalog, 2246, 0

da Costa L. N., Bernardi M., Alonso M. V., et al., 2000a, ApJ, 537, L81

da Costa L. N., Bernardi M., Alonso M. V., et al., 2000b, AJ, 120, 95

da Costa L. N., Freudling W., Wegner G., Giovanelli R., Haynes M. P., Salzer J. J., 1996, ApJ, 468, L5

da Costa L. N., Numes M. A., Pellegrini P. S., Willmer C., Chincarini G., Cowan J. J., 1986, AJ, 91, 6

Dai D.-C., Kinney W. H., Stojkovic D., 2011, J. Cosmol. Astropart. Phys., 4, 15

Dale D. A., Giovanelli R., Haynes M. P., Campusano L. E., Hardy E., 1999a, AJ, 118, 1489

Dale D. A., Giovanelli R., Haynes M. P., Campusano L. E., Hardy E., Borgani S., 1999b, ApJ, 510, L11

Dale D. A., Giovanelli R., Haynes M. P., Hardy E., Campusano L. E., 1999c, AJ, 118, 1468

Dale D. A., Giovanelli R., Haynes M. P., Scodeggio M., Hardy E., Campusano L. E., 1997, AJ, 114, 455

Davis M., Huchra J., Latham D. W., Tonry J., 1982, ApJ, 253, 423

Davis T. M., Scrimgeour M. I., 2014, MNRAS, 442, 1117

Dawson K. S., Schlegel D. J., Ahn C. P., et al., 2013, AJ, 145, 10

de la Torre S., Guzzo L., Peacock J. A., et al., 2013, A&A, 557, A54

de Vaucouleurs G., de Vaucouleurs A., Corwin Jr. H. G., et al., 1992, Astronomische Nachrichten, 313, 132

de Vaucouleurs G., de Vaucouleurs A., Corwin Jr. H. G., Buta R. J., Paturel G., Fouqué P., 1991, Third Reference Catalogue of Bright Galaxies. Volume I: Explanations and references. Volume II: Data for galaxies between 0^h and 12^h. Volume III: Data for galaxies between 12^h and 24^h.

Dekel A., 1994, ARA&A, 32, 371

Dekel A., Eldar A., Kolatt T., et al., 1999, ApJ, 522, 1

Djorgovski S., Davis M., 1987, ApJ, 313, 59

Donas J., Deharveng J.-M., Rich R. M., et al., 2007, ApJS, 173, 597

Donley J. L., Koribalski B. S., Staveley-Smith L., Kraan-Korteweg R. C., Schröder A., Henning P. A., 2006, MNRAS, 369, 1741

Donley J. L., Staveley-Smith L., Kraan-Korteweg R. C., et al., 2005, AJ, 129, 220

D'Onofrio M., Fasano G., Varela J., et al., 2008, ApJ, 685, 875

Doyle M. T., Drinkwater M. J., Rohde D. J., et al., 2005, MNRAS, 361, 34

Dressler A., 1980a, ApJS, 42, 565

Dressler A., 1980b, ApJ, 236, 351

Dressler A., 1987, ApJ, 317, 1

Dressler A., 1988, ApJ, 329, 519

Dressler A., Faber S. M., 1990, ApJ, 354, 13

Dressler A., Lynden-Bell D., Burstein D., et al., 1987, ApJ, 313, 42

Duffy A. R., Meyer M. J., Staveley-Smith L., et al., 2012, MNRAS, 426, 3385

Ebeling H., Edge A. C., Allen S. W., Crawford C. S., Fabian A. C., Huchra J. P., 2000, MNRAS, 318, 333

Ebeling H., Kocevski D., Tully R. B., Mullis C. R., 2005, in Nearby Large-Scale Structures and the Zone of Avoidance, edited by A. P. Fairall, P. A. Woudt, vol. 329 of Astronomical Society of the Pacific Conference Series, 83

Ebeling H., Mullis C. R., Tully R. B., 2002, ApJ, 580, 774

Ebeling H., Stephenson L. N., Edge A. C., 2014, ApJ, 781, L40

Ebeling H., Voges W., Bohringer H., Edge A. C., 1993, A&A, 275, 360

Efstathiou G., 2014, MNRAS, 440, 1138

Efstathiou G., Bond J. R., White S. D. M., 1992, MNRAS, 258, 1P

Eisenstein D. J., Weinberg D. H., Agol E., et al., 2011, AJ, 142, 72

Eisenstein D. J., Zehavi I., Hogg D. W., et al., 2005, ApJ, 633, 560

Epchtein N., de Batz B., Capoani L., et al., 1997, The Messenger, 87, 27

Erdoğdu P., Huchra J. P., Lahav O., et al., 2006a, MNRAS, 368, 1515

Erdoğdu P., Lahav O., Huchra J. P., et al., 2006b, MNRAS, 373, 45

Ettori S., Guzzo L., Tarenghi M., 1997, MNRAS, 285, 218

Faber S. M., Jackson R. E., 1976, ApJ, 204, 668

Fairall A. P., Lowe L., Dobbie P. J. K., 1983, Publ. Dep. Astron., Univ. Cape Town, No. 5, 56

Feast M. W., Walker A. R., 1987, ARA&A, 25, 345

Federspiel M., Sandage A., Tammann G. A., 1994, ApJ, 430, 29

Feldman H. A., Watkins R., 2008, MNRAS, 387, 825

Feldman H. A., Watkins R., Hudson M. J., 2010, MNRAS, 407, 2328

Fitzpatrick E. L., 1999, PASP, 111, 63

Fixsen D. J., 2009, ApJ, 707, 916

Fixsen D. J., Cheng E. S., Gales J. M., Mather J. C., Shafer R. A., Wright E. L., 1996, ApJ, 473, 576

Folatelli G., Phillips M. M., Burns C. R., et al., 2010, AJ, 139, 120

Fouque P., Durand N., Bottinelli L., Gouguenheim L., Paturel G., 1990, A&AS, 86, 473

Fraix-Burnet D., Dugué M., Chattopadhyay T., Chattopadhyay A. K., Davoust E., 2010, MNRAS, 407, 2207

Freedman W. L., Burns C. R., Phillips M. M., et al., 2009, ApJ, 704, 1036

Freedman W. L., Madore B. F., 2010, ARA&A, 48, 673

Freedman W. L., Madore B. F., Gibson B. K., et al., 2001, ApJ, 553, 47

Freedman W. L., Madore B. F., Scowcroft V., et al., 2012, ApJ, 758, 24

Freudling W., da Costa L. N., Wegner G., Giovanelli R., Haynes M. P., Salzer J. J., 1995, AJ, 110, 920

Freudling W., Staveley-Smith L., Catinella B., et al., 2011, ApJ, 727, 40

Fumagalli M., Fossati M., Hau G. K. T., et al., 2014, MNRAS, 445, 4335

Gargiulo A., Haines C. P., Merluzzi P., et al., 2009, MNRAS, 397, 75

Garilli B., Guzzo L., Scodeggio M., et al., 2014, A&A, 562, A23

Garmire G. P., Bautz M. W., Ford P. G., Nousek J. A., Ricker Jr. G. R., 2003, in X-Ray and Gamma-Ray Telescopes and Instruments for Astronomy., edited by J. E. Truemper, H. D. Tananbaum, vol. 4851 of Society of Photo-Optical Instrumentation Engineers (SPIE) Conference Series, 28

Geller M. J., Huchra J. P., 1983, ApJS, 52, 61

Geller M. J., Huchra J. P., 1989, Science, 246, 897

Gibbons R. A., Fruchter A. S., Bothun G. D., 2001, AJ, 121, 649

Giovanelli R., Haynes M. P., Freudling W., da Costa L. N., Salzer J. J., Wegner G., 1998a, ApJ, 505, L91

Giovanelli R., Haynes M. P., Herter T., et al., 1997a, AJ, 113, 53

Giovanelli R., Haynes M. P., Herter T., et al., 1997b, AJ, 113, 22

Giovanelli R., Haynes M. P., Salzer J. J., Wegner G., da Costa L. N., Freudling W., 1994, AJ, 107, 2036

Giovanelli R., Haynes M. P., Salzer J. J., Wegner G., da Costa L. N., Freudling W., 1995, AJ, 110, 1059

Giovanelli R., Haynes M. P., Salzer J. J., Wegner G., da Costa L. N., Freudling W., 1998b, AJ, 116, 2632

Giovanelli R., Haynes M. P., Wegner G., da Costa L. N., Freudling W., Salzer J. J., 1996, ApJ, 464, L99

Glass I. S., 1999, Handbook of Infrared Astronomy, Highlights of Astronomy, Cambridge University Press

Gouguenheim L., 1969, A&A, 3, 281

Graham A. W., Driver S. P., 2005, PASA, 22, 118

Guzman R., Lucey J. R., Bower R. G., 1993, MNRAS, 265, 731

Harrison E. R., 1974, ApJ, 191, L51

Haynes M. P., Giovanelli R., Chamaraux P., et al., 1999a, AJ, 117, 2039

Haynes M. P., Giovanelli R., Herter T., et al., 1997, AJ, 113, 1197

Haynes M. P., Giovanelli R., Salzer J. J., et al., 1999b, AJ, 117, 1668

Henning P. A., Springob C. M., Minchin R. F., et al., 2010, AJ, 139, 2130

Hicken M., Wood-Vasey W. M., Blondin S., et al., 2009, ApJ, 700, 1097

Hinshaw G., Larson D., Komatsu E., et al., 2013, ApJS, 208, 19

Hinshaw G., Weiland J. L., Hill R. S., et al., 2009, ApJS, 180, 225

Hoessel J. G., 1980, ApJ, 241, 493

Hong T., Springob C. M., Staveley-Smith L., et al., 2014, MNRAS, 445, 402

Hong T., Staveley-Smith L., Masters K. L., et al., 2013, MNRAS, 432, 1178

Hubble E., 1929a, Contributions from the Mount Wilson Observatory, 3, 23

Hubble E., 1929b, Proceedings of the National Academy of Science, 15, 168

Hubble E. P., 1926, ApJ, 64, 321

Hubble E. P., 1929c, Leaflet of the Astronomical Society of the Pacific, 1, 93

Hubble E. P., 1936, Realm of the Nebulae, New Haven: Yale University Press

Huchra J., Davis M., Latham D., Tonry J., 1983, ApJS, 52, 89

Huchra J., Jarrett T., Skrutskie M., et al., 2005a, in Nearby Large-Scale Structures and the Zone of Avoidance, edited by A. P. Fairall & P. A. Woudt, vol. 329 of Astronomical Society of the Pacific Conference Series, 135

Huchra J., Martimbeau N., Jarrett T., et al., 2005b, in Maps of the Cosmos, edited by M. Colless, L. Staveley-Smith, R. A. Stathakis, vol. 216 of IAU Symposium, 170

Huchra J. P., Macri L. M., Masters K. L., et al., 2012, ApJS, 199, 26

Huchra J. P., Mader J., Schneider S. E., et al., 2000, in Mapping the Hidden Universe: The Universe behind the Mily Way - The Universe in HI, edited by R. C. Kraan-Korteweg, P. A. Henning, H. Andernach, vol. 218 of Astronomical Society of the Pacific Conference Series, 101

Hudson M. J., 1994a, MNRAS, 266, 475

Hudson M. J., 1994b, MNRAS, 266, 468

Hudson M. J., Ebeling H., 1997, ApJ, 479, 621

Hudson M. J., Lucey J. R., Smith R. J., Schlegel D. J., Davies R. L., 2001, MNRAS, 327, 265

Hudson M. J., Lucey J. R., Smith R. J., Steel J., 1997, MNRAS, 291, 488

Hudson M. J., Smith R. J., Lucey J. R., Branchini E., 2004, MNRAS, 352, 61

Hudson M. J., Smith R. J., Lucey J. R., Schlegel D. J., Davies R. L., 1999, ApJ, 512, L79

Humason M. L., Mayall N. U., Sandage A. R., 1956, AJ, 61, 97

Hyde J. B., Bernardi M., 2009, MNRAS, 396, 1171

Jarosik N., Bennett C. L., Dunkley J., et al., 2011, ApJS, 192, 14

Jarrett T., 2004, PASA, 21, 396

Jarrett T. H., 2000, PASP, 112, 1008

Jarrett T. H., Chester T., Cutri R., Schneider S., Skrutskie M., Huchra J. P., 2000, AJ, 119, 2498

Jarrett T. H., Chester T., Cutri R., Schneider S. E., Huchra J. P., 2003, AJ, 125, 525

Jarrett T. H., Koribalski B. S., Kraan-Korteweg R. C., et al., 2007, AJ, 133, 979

Jha S., Riess A. G., Kirshner R. P., 2007, ApJ, 659, 122

Jones D. H., Read M. A., Saunders W., et al., 2009, MNRAS, 399, 683

Jones D. H., Saunders W., Colless M., et al., 2004, MNRAS, 355, 747

Jones D. H., Saunders W., Read M., Colless M., 2005, PASA, 22, 277

Jorgensen I., Franx M., Kjaergaard P., 1993, ApJ, 411, 34

Jorgensen I., Franx M., Kjaergaard P., 1995, MNRAS, 276, 1341

Jorgensen I., Franx M., Kjaergaard P., 1996, MNRAS, 280, 167

Kaiser N., 1984, ApJ, 284, L9

Kaiser N., 1987, MNRAS, 227, 1

Karachentsev I. D., Karachentseva V. E., Kudrya Y. N., Makarov D. I., Parnovsky S. L., 2000, Bulletin of the Special Astrophysics Observatory, 50, 5

Karachentsev I. D., Mitronova S. N., Karachentseva V. E., Kudrya Y. N., Jarrett T. H., 2002, A&A, 396, 431

Kashlinsky A., Atrio-Barandela F., Ebeling H., 2012, arXiv:1202.0717

Kashlinsky A., Atrio-Barandela F., Ebeling H., Edge A., Kocevski D., 2010, ApJ, 712, L81

Kashlinsky A., Atrio-Barandela F., Kocevski D., Ebeling H., 2008, ApJ, 686, L49

Kato D., Nagashima C., Nagayama T., et al., 2007, PASJ, 59, 615

Kelson D. D., Illingworth G. D., van Dokkum P. G., Franx M., 2000, ApJ, 531, 184

Klein C. R., Richards J. W., Butler N. R., Bloom J. S., 2014, MNRAS, 440, L96

Kocevski D. D., Ebeling H., 2006, ApJ, 645, 1043

Kocevski D. D., Ebeling H., Mullis C. R., Tully R. B., 2007, ApJ, 662, 224

Koda J., Blake C., Davis T., et al., 2014, MNRAS, 445, 4267

Kogut A., Lineweaver C., Smoot G. F., et al., 1993, ApJ, 419, 1

Kolatt T., Dekel A., Lahav O., 1995, MNRAS, 275, 797

Koribalski B. S., Staveley-Smith L., Kilborn V. A., et al., 2004, AJ, 128, 16

Kormendy J., 1977, ApJ, 218, 333

Kormendy J., Bender R., 1996, ApJ, 464, L119

Kormendy J., Fisher D. B., Cornell M. E., Bender R., 2009, ApJS, 182, 216

Kraan-Korteweg R. C., Juraszek S., 2000, Publications of the Astronomical Society of Australia, 17, 6

Kraan-Korteweg R. C., Lahav O., 2000, A&A Rev., 10, 211

Kraan-Korteweg R. C., Riad I. F., Woudt P. A., Nagayama T., Wakamatsu K., 2010, in 10 years of IRSF and the Future, edited by T. Nagayama, S. Sato, K. Wakamatsu, Proceedings of International Workshop held as the 10^{th} Anniversary Celebration, p. 89–97

Kraan-Korteweg R. C., Woudt P. A., Cayatte V., Fairall A. P., Balkowski C., Henning P. A., 1996, Nature, 379, 519

La Barbera F., Busarello G., Capaccioli M., 2000, A&A, 362, 851

La Barbera F., Busarello G., Merluzzi P., de la Rosa I. G., Coppola G., Haines C. P., 2008, ApJ, 689, 913

La Barbera F., de Carvalho R. R., de La Rosa I. G., Lopes P. A. A., 2010, MNRAS, 408, 1335

Lagattuta D. J., Mould J. R., Staveley-Smith L., et al., 2013, ApJ, 771, 88

Lauer T. R., Postman M., 1992, ApJ, 400, L47

Lauer T. R., Postman M., 1994, ApJ, 425, 418

Lavaux G., Hudson M. J., 2011, MNRAS, 416, 2840

Lavaux G., Tully R. B., Mohayaee R., Colombi S., 2010, ApJ, 709, 483

Lawrence A., Warren S. J., Almaini O., et al., 2007, MNRAS, 379, 1599

Lewis I. J., Cannon R. D., Taylor K., et al., 2002, MNRAS, 333, 279

Lilje P. B., Yahil A., Jones B. J. T., 1986, ApJ, 307, 91

Linder E. V., 2005, Phys. Rev. D, 72, 4, 043529

Loeb A., Narayan R., 2008, MNRAS, 386, 2221

Longhetti M., Saracco P., Severgnini P., et al., 2007, MNRAS, 374, 614

Lucey J., Radburn-Smith D., Hudson M., 2005, in Nearby Large-Scale Structures and the Zone of Avoidance, edited by A. P. Fairall & P. A. Woudt, vol. 329 of Astronomical Society of the Pacific Conference Series, 21

Lucey J. R., 1986, MNRAS, 222, 417

Lucey J. R., Bower R. G., Ellis R. S., 1991a, MNRAS, 249, 755

Lucey J. R., Carter D., 1988, MNRAS, 235, 1177

Lucey J. R., Guzman R., Carter D., Terlevich R. J., 1991b, MNRAS, 253, 584

Lynden-Bell D., Faber S. M., Burstein D., et al., 1988, ApJ, 326, 19

Lynden-Bell D., Lahav O., Burstein D., 1989, MNRAS, 241, 325

Ma Y.-Z., Gordon C., Feldman H. A., 2011, Phys. Rev. D, 83, 10, 103002

Ma Y.-Z., Pan J., 2014, MNRAS, 437, 1996

Ma Y.-Z., Scott D., 2013, MNRAS, 428, 2017

MacArthur L. A., Courteau S., Holtzman J. A., 2003, ApJ, 582, 689

Macri L. M., Stanek K. Z., Bersier D., Greenhill L. J., Reid M. J., 2006, ApJ, 652, 1133

Magoulas C., 2012, Ph.D. thesis, Univ. Melbourne

Magoulas C., Springob C. M., Colless M., et al., 2012, MNRAS, 427, 245

Malmquist K. G., 1920, Medd. Lund. Astron Obs. Ser. II, 22, 1

Malmquist K. G., 1922, Medd. Lund. Astron Obs. Ser. I, 100, 1

Malmquist K. G., 1924, Medd. Lund. Astron Obs. Ser. II, 32, 64

Marinoni C., Monaco P., Giuricin G., Costantini B., 1998, ApJ, 505, 484

Marleau F. R., Noriega-Crespo A., Paladini R., et al., 2008, AJ, 136, 662

Martini P., Dicken D., Storchi-Bergmann T., 2013, ApJ, 766, 121

Masters K. L., Crook A., Hong T., et al., 2014, MNRAS, 443, 1044

Masters K. L., Giovanelli R., Haynes M. P., 2003, AJ, 126, 158

Masters K. L., Springob C. M., Haynes M. P., Giovanelli R., 2006, ApJ, 653, 861

Masters K. L., Springob C. M., Huchra J. P., 2008, AJ, 135, 1738

Mather J. C., Cheng E. S., Cottingham D. A., et al., 1994, ApJ, 420, 439

Mather J. C., Fixsen D. J., Shafer R. A., Mosier C., Wilkinson D. T., 1999, ApJ, 512, 511

Mathewson D. S., Ford V. L., Buchhorn M., 1992, ApJS, 81, 413

McClure-Griffiths N. M., Pisano D. J., Calabretta M. R., et al., 2009, ApJS, 181, 398

McIntyre T. P., Minchin R. F., Momjian E., Henning P. A., Kaur A., Parton B., 2011, ApJ, 739, L26

Mobasher B., Guzman R., Aragon-Salamanca A., Zepf S., 1999, MNRAS, 304, 225

Monson A. J., Freedman W. L., Madore B. F., et al., 2012, ApJ, 759, 146

Moorwood A., Cuby J.-G., Lidman C., 1998, The Messenger, 91, 9

Mould J. R., Huchra J. P., Freedman W. L., et al., 2000, ApJ, 529, 786

Müller K. R., Freudling W., Watkins R., Wegner G., 1998, ApJ, 507, L105

Mutabazi T., Blyth S. L., Woudt P. A., et al., 2014, MNRAS, 439, 3666

Nagashima C., Nagayama T., Nakajima Y., et al., 1999, in Star Formation 1999, edited by T. Nakamoto, 397–398

Nagayama T., 2012, African Skies, 16, 98

Nagayama T., Nagashima C., Nakajima Y., et al., 2003, in Society of Photo-Optical Instrumentation Engineers (SPIE) Conference Series, edited by M. Iye & A. F. M. Moorwood, vol. 4841 of Presented at the Society of Photo-Optical Instrumentation Engineers (SPIE) Conference, 459–464

Nagayama T., Woudt P. A., Nagashima C., et al., 2004, MNRAS, 354, 980

Nagayama T., Woudt P. A., Wakamatsu K., et al., 2006, MNRAS, 368, 534

Nigoche-Netro A., Ruelas-Mayorga A., Franco-Balderas A., 2008, A&A, 491, 731

Nusser A., Davis M., 2011, ApJ, 736, 93

Nusser A., Davis M., Branchini E., 2014, ApJ, 788, 157

Oemler Jr. A., 1974, ApJ, 194, 1

Oke J. B., Sandage A., 1968, ApJ, 154, 21

Oort J. H., 1983, ARA&A, 21, 373

Opik E., 1922, ApJ, 55, 406

Pahre M. A., 1999, ApJS, 124, 127

Pahre M. A., de Carvalho R. R., Djorgovski S. G., 1998a, AJ, 116, 1606

Pahre M. A., Djorgovski S. G., de Carvalho R. R., 1995, ApJ, 453, L17

Pahre M. A., Djorgovski S. G., de Carvalho R. R., 1998b, AJ, 116, 1591

Peacock J. A., Heavens A. F., 1985, MNRAS, 217, 805

Peebles P. J. E., 1993, Principles of Physical Cosmology

Peng C. Y., Ho L. C., Impey C. D., Rix H., 2002, AJ, 124, 266

Peng C. Y., Ho L. C., Impey C. D., Rix H., 2010, AJ, 139, 2097

Penzias A. A., Wilson R. W., 1965, ApJ, 142, 419

Percival W. J., Reid B. A., Eisenstein D. J., et al., 2010, MNRAS, 401, 2148

Pierce M. J., Tully R. B., 1992, ApJ, 387, 47

Pizagno J., Prada F., Weinberg D. H., et al., 2007, AJ, 134, 945

Planck Collaboration, Ade P. A. R., Aghanim N., et al., 2014a, A&A, 571, A1

Planck Collaboration, Ade P. A. R., Aghanim N., et al., 2014b, A&A, 571, A16

Planck Collaboration, Ade P. A. R., Aghanim N., et al., 2014c, A&A, 571, A23

Planck Collaboration, Aghanim N., Armitage-Caplan C., et al., 2014d, A&A, 571, A27

Plionis M., Basilakos S., Rowan-Robinson M., et al., 2000, MNRAS, 313, 8

Poggianti B. M., 1997, A&AS, 122, 399

Postman M., Lauer T. R., 1995, ApJ, 440, 28

Proust D., Quintana H., Carrasco E. R., et al., 2006, A&A, 447, 133

Radburn-Smith D. J., Lucey J. R., Woudt P. A., Kraan-Korteweg R. C., Watson F. G., 2006, MNRAS, 369, 1131

Raychaudhury S., 1989, Nature, 342, 251

Recillas-Cruz E., Serrano P. G. A., Cruz-Gonzalez I., Carrasco L., 1990, A&A, 229, 64

Riad I. F., 2010, Ph.D. thesis, Univ. Cape Town

Riad I. F., Kraan-Korteweg R. C., Woudt P. A., 2010, MNRAS, 401, 924

Riess A. G., Macri L., Casertano S., et al., 2011, ApJ, 730, 119

Riess A. G., Press W. H., Kirshner R. P., 1995, ApJ, 445, L91

Riess A. G., Press W. H., Kirshner R. P., 1996, ApJ, 473, 88

Roberts M. S., 1969, AJ, 74, 859

Rowan-Robinson M., 1985, The cosmological distance ladder: Distance and time in the universe

Rowan-Robinson M., Harrison E., 1985, Nature, 318, 131

Rowan-Robinson M., Lawrence A., Saunders W., et al., 1990, MNRAS, 247, 1

Rowan-Robinson M., Sharpe J., Oliver S. J., et al., 2000, MNRAS, 314, 375

Rubin V. C., Roberts M. S., Graham J. A., Ford Jr. W. K., Thonnard N., 1976, AJ, 81, 687

Sadler E. M., Ricci R., Ekers R. D., et al., 2006, MNRAS, 371, 898

Said K., 2013, Tully-Fisher Relation in the Zone of Avoidance, Master's thesis, Univ. Cape Town

Said K., Kraan-Korteweg R. C., Jarrett T. H., 2015, MNRAS, 447, 1618

Sandage A., 1975, ApJ, 202, 563

Sandage A., Tammann G. A., 1976, ApJ, 210, 7

Sandage A. R., 1954, AJ, 59, 180

Sargent W. L. W., Schechter P. L., Boksenberg A., Shortridge K., 1977, ApJ, 212, 326

Sarkar D., Feldman H. A., Watkins R., 2007, MNRAS, 375, 691

Saulder C., Mieske S., Zeilinger W. W., Chilingarian I., 2013, A&A, 557, A21

Sault R. J., Teuben P. J., Wright M. C. H., 1995, in Astronomical Data Analysis Software and Systems IV, edited by R. A. Shaw, H. E. Payne, J. J. E. Hayes, vol. 77 of Astronomical Society of the Pacific Conference Series, 433

Saunders W., Sutherland W. J., Maddox S. J., et al., 2000, MNRAS, 317, 55

Scaramella R., Baiesi-Pillastrini G., Chincarini G., Vettolani G., Zamorani G., 1989, Nature, 338, 562

Schlafly E. F., Finkbeiner D. P., 2011, ApJ, 737, 103

Schlegel D. J., Finkbeiner D. P., Davis M., 1998, ApJ, 500, 525

Schneider S. E., Helou G., Salpeter E. E., Terzian Y., 1986, AJ, 92, 742

Schneider S. E., Thuan T. X., Magri C., Wadiak J. E., 1990, ApJS, 72, 245

Schröder A. C., Kraan-Korteweg R. C., Henning P. A., 2009, A&A, 505, 1049

Schröder A. C., Kraan-Korteweg R. C., Mamon G. A., Woudt P. A., 2005, in Nearby Large-Scale Structures and the Zone of Avoidance, edited by A. P. Fairall, P. A. Woudt, vol. 329 of Astronomical Society of the Pacific Conference Series, 167

Schröder A. C., Mamon G. A., Kraan-Korteweg R. C., Woudt P. A., 2007, A&A, 466, 481

Scodeggio M., Giovanelli R., Haynes M. P., 1997, AJ, 113, 101

Scowcroft V., Freedman W. L., Madore B. F., et al., 2013, ApJ, 773, 106

Shapley H., 1930, Harvard College Observatory Bulletin, 874, 9

Shapley H., Curtis H. D., 1921, Bulletin of the National Research Council, Vol. 2, Part 3, No. 11, p. 171-217

Shaya E. J., 1984, ApJ, 280, 470

Shaya E. J., Tully R. B., 2013, MNRAS, 436, 2096

Skelton R. E., Woudt P. A., Kraan-Korteweg R. C., 2009, MNRAS, 396, 2367

Skibba R. A., Engelbracht C. W., Dale D., et al., 2011, ApJ, 738, 89

Skrutskie M. F., Cutri R. M., Stiening R., et al., 2006, AJ, 131, 1163

Smith R. J., 1999, Streaming Motions of Abell Clusters: New Evidence for a High-amplitude Bulk Flow on Very Large Scales, Ph.D. thesis, University of Durham

Smith R. J., Hudson M. J., Lucey J. R., Schlegel D. J., Davies R. L., 2000, in Cosmic Flows Workshop, edited by S. Courteau, J. Willick, vol. 201 of Astronomical Society of the Pacific Conference Series, 39

Smith R. J., Hudson M. J., Nelan J. E., et al., 2004, AJ, 128, 1558

Smoot G. F., Bennett C. L., Kogut A., et al., 1992, ApJ, 396, L1

Sorce J. G., Courtois H. M., Tully R. B., 2012, AJ, 144, 133

Sorce J. G., Courtois H. M., Tully R. B., et al., 2013, ApJ, 765, 94

Sorce J. G., Tully R. B., Courtois H. M., Jarrett T. H., Neill J. D., Shaya E. J., 2014, MNRAS, 444, 527

Spergel D. N., Bean R., Doré O., et al., 2007, ApJS, 170, 377

Springel V., Hernquist L., 2003, MNRAS, 339, 312

Springel V., White S. D. M., Jenkins A., et al., 2005, Nature, 435, 629

Springob C. M., Haynes M. P., Giovanelli R., Kent B. R., 2005, ApJS, 160, 149

Springob C. M., Magoulas C., Colless M., et al., 2014, MNRAS, 445, 2677

Springob C. M., Magoulas C., Proctor R., et al., 2012, MNRAS, 420, 2773

Springob C. M., Masters K. L., Haynes M. P., Giovanelli R., Marinoni C., 2007, ApJS, 172, 599

Springob C. M., Masters K. L., Haynes M. P., Giovanelli R., Marinoni C., 2009, VizieR Online Data Catalog, 217, 20599

Staveley-Smith L., Wilson W. E., Bird T. S., et al., 1996, PASA, 13, 243

Stetson P. B., 1987, PASP, 99, 191

Strauss M. A., Davis M., 1988, in Large Scale Structures of the Universe, edited by J. Audouze, M.-C. Pelletan, A. Szalay, Y. B. Zel'dovich, P. J. E. Peebles, vol. 130 of IAU Symposium, 191

Strauss M. A., Willick J. A., 1995, Phys. Rep., 261, 271

Sun M., Donahue M., Voit G. M., 2007, ApJ, 671, 190

Sun M., Jones C., Forman W., Nulsen P. E. J., Donahue M., Voit G. M., 2006, ApJ, 637, L81

Sunyaev R. A., Zeldovich I. B., 1980, MNRAS, 190, 413

Tabur V., 2007, PASA, 24, 189

Tammann G. A., Sandage A., 1985, ApJ, 294, 81

Tamura T., Fukazawa Y., Kaneda H., et al., 1998, PASJ, 50, 195

Teerikorpi P., 1987, A&A, 173, 39

Teerikorpi P., 1990, A&A, 234, 1

Tonry J. L., Blakeslee J. P., Ajhar E. A., Dressler A., 2000, ApJ, 530, 625

Tonry J. L., Dressler A., Blakeslee J. P., et al., 2001, ApJ, 546, 681

Tonry J. L., Schmidt B. P., Barris B., et al., 2003, ApJ, 594, 1

Trujillo I., Burkert A., Bell E. F., 2004, ApJ, 600, L39

Tully R. B., 1988, Nature, 334, 209

Tully R. B., Courtois H., Hoffman Y., Pomarède D., 2014, Nature, 513, 71

Tully R. B., Courtois H. M., Dolphin A. E., et al., 2013, AJ, 146, 86

Tully R. B., Fisher J. R., 1977, A&A, 54, 661

Tully R. B., Fouque P., 1985, ApJS, 58, 67

Tully R. B., Rizzi L., Shaya E. J., Courtois H. M., Makarov D. I., Jacobs B. A., 2009, AJ, 138, 323

Turnbull S. J., Hudson M. J., Feldman H. A., Hicken M., Kirshner R. P., Watkins R., 2012, MNRAS, 420, 447

van der Bliek N. S., Manfroid J., Bouchet P., 1996, A&AS, 119, 547

Voges W., Aschenbach B., Boller T., et al., 1999, A&A, 349, 389

Vollmer B., Cayatte V., van Driel W., et al., 2001, A&A, 369, 432

Wang L., Steinhardt P. J., 1998, ApJ, 508, 483

Watkins R., Feldman H. A., 2015, MNRAS, 447, 132

Watkins R., Feldman H. A., Hudson M. J., 2009, MNRAS, 392, 743

Whitmore B. C., Gilmore D. M., Jones C., 1993, ApJ, 407, 489

Williams W. L., 2011, Tully-Fisher Relation in the Zone of Avoidance, Master's thesis, Univ. Cape Town

Williams W. L., Kraan-Korteweg R. C., Woudt P. A., 2014, MNRAS, 443, 41

Willick J. A., 1999, ApJ, 522, 647

Willick J. A., Courteau S., Faber S. M., Burstein D., Dekel A., 1995, ApJ, 446, 12

Willick J. A., Courteau S., Faber S. M., Burstein D., Dekel A., Kolatt T., 1996, ApJ, 457, 460

Willick J. A., Courteau S., Faber S. M., Burstein D., Dekel A., Strauss M. A., 1997, ApJS, 109, 333

Woudt P. A., 1998, Ph.D. thesis, Univ. Cape Town

Woudt P. A., Kraan-Korteweg R. C., 2001, A&A, 380, 441

Woudt P. A., Kraan-Korteweg R. C., Cayatte V., Balkowski C., Felenbok P., 2004, A&A, 415, 9

Woudt P. A., Kraan-Korteweg R. C., Fairall A. P., 1999, A&A, 352, 39

Woudt P. A., Kraan-Korteweg R. C., Fairall A. P., Boehringer H., Cayatte V., Glass I. S., 1998, A&A, 338, 8

Woudt P. A., Kraan-Korteweg R. C., Lucey J., Fairall A. P., Moore S. A. W., 2008, MNRAS, 383, 445

Wright E. L., 2006, PASP, 118, 1711

Wright E. L., Meyer S. S., Bennett C. L., et al., 1992, ApJ, 396, L13

Yahil A., Tammann G. A., Sandage A., 1977, ApJ, 217, 903

Yasuda N., Fukugita M., Schneider D. P., 2007, AJ, 134, 698

York D. G., Adelman J., Anderson Jr. J. E., et al., 2000, AJ, 120, 1579

APPENDIX A

STAR-SUBTRACTION: NTT SAMPLE

Presented in Figure A.1 are the star-subtracted images for the NTT K_s-band images used in the Fundamental Plane analysis. The original galaxy image is shown on the left-hand side of the corresponding image after star-subtraction. Each image is $68'' \times 68''$.

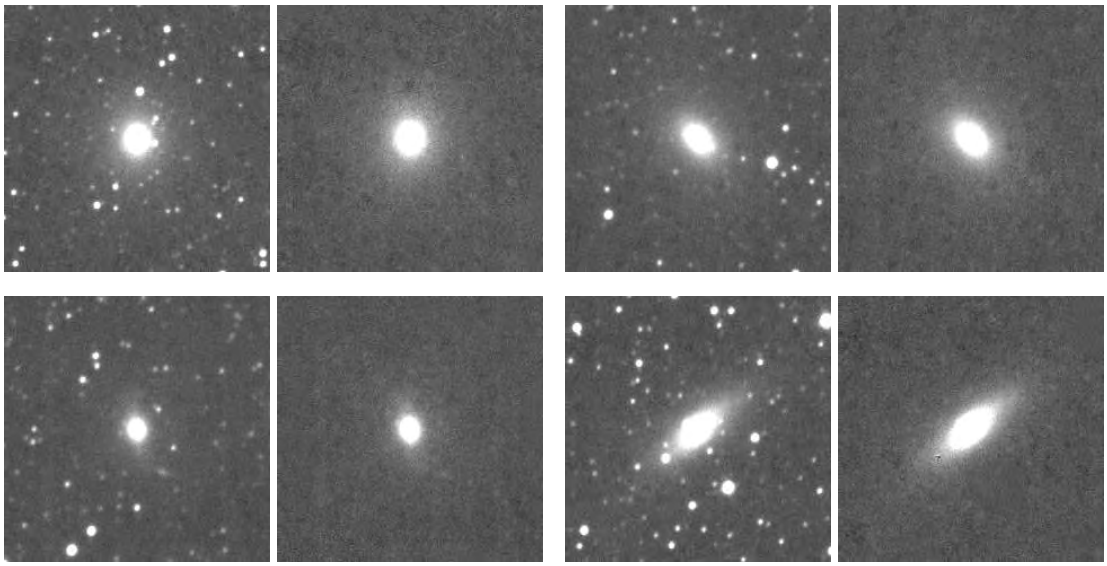

Fig. A.1: Foreground star subtraction for the Norma cluster early-type galaxies used in the Fundamental Plane analysis of the NTT sample. The images presented here are: WKK 5920 (two images on the top left-hand side), WKK 5972 (two images on the top right-hand side), WKK 6012 (two images on the bottom left-hand side), and WKK 6019 (two images on the bottom right-hand side). The original images are shown on the left side of the corresponding star-subtracted images. The size of each image is $68'' \times 68''$.

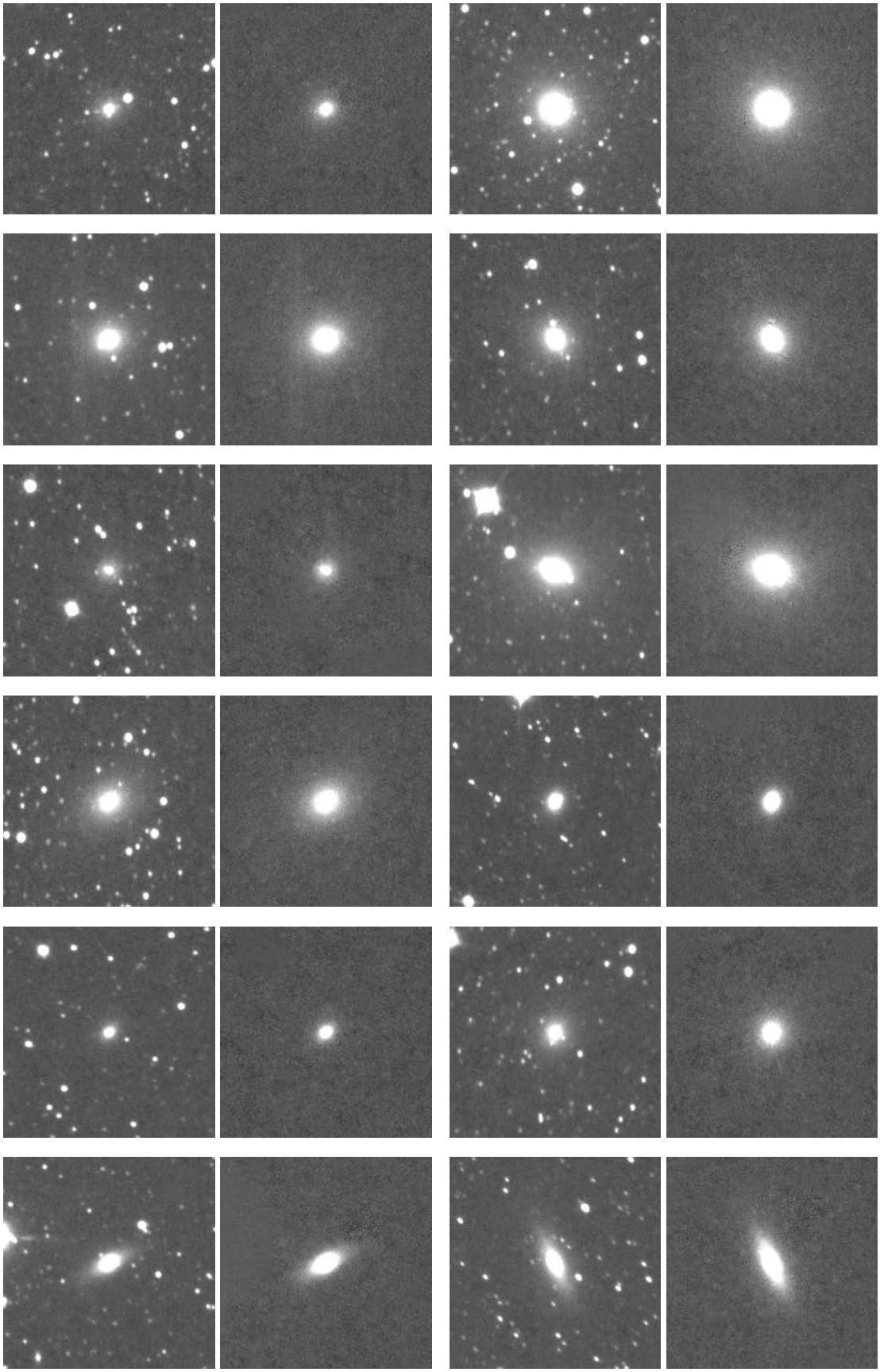

Fig. A.1: Continued for WKK 6047, WKK 6116, WKK 6180, WKK 6183, WKK 6198, WKK 6204, WKK 6221, WKK 6229, WKK 6233, WKK 6235, WKK 6242, WKK 6250.

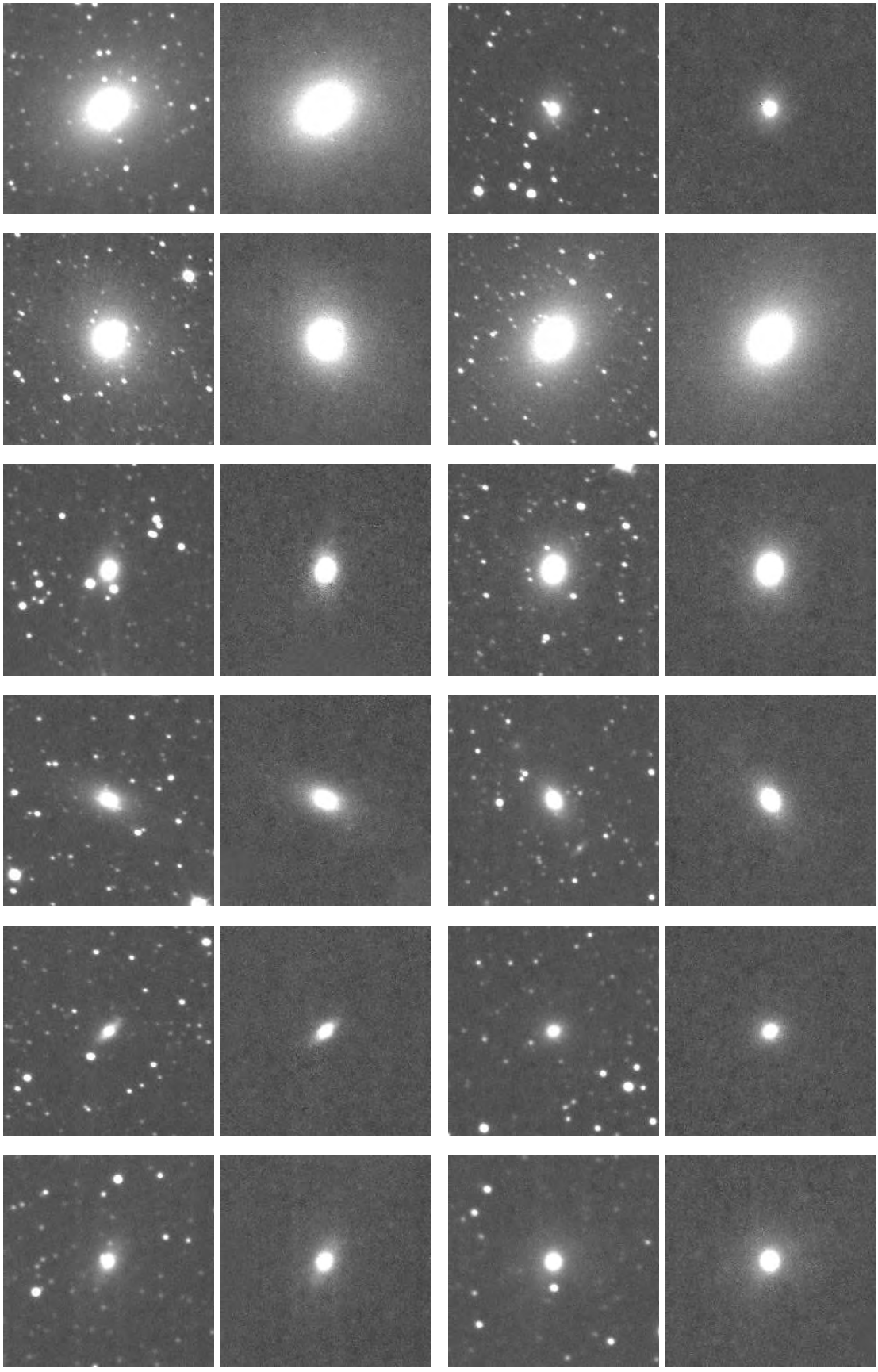

Fig. A.1: Continued for WKK 6269, WKK 6282, WKK 6305, WKK 6318, WKK 6342, WKK 6360, WKK 6383, WKK 6431, WKK 6473, WKK 6477, WKK 6555, WKK 6600.

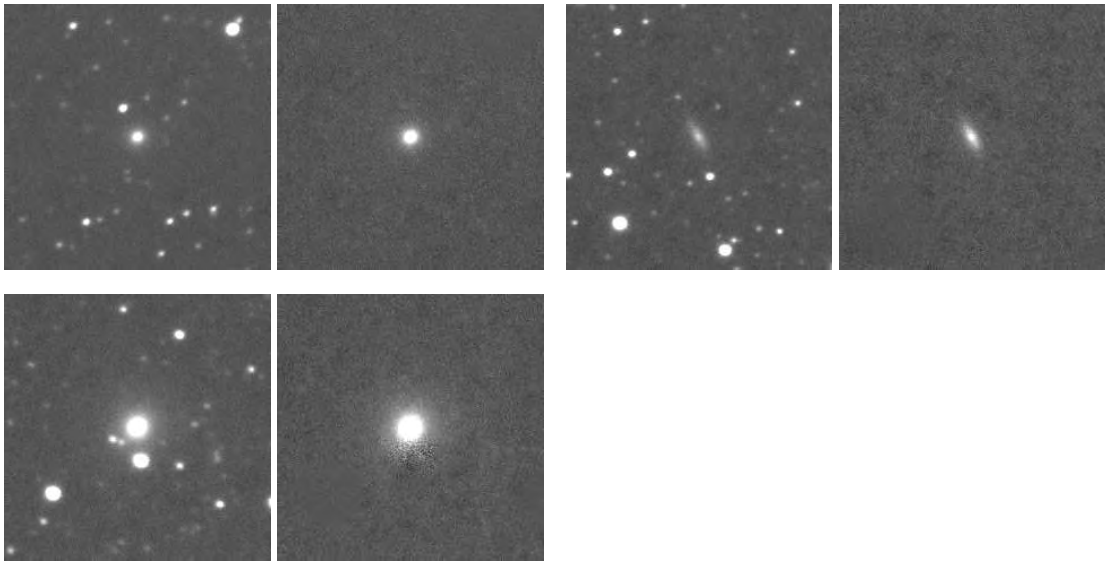

Fig. A.1: Continued for WKK 6615, WKK 6620, WKK 6679.

APPENDIX B

SKY BACKGROUND ESTIMATION: NTT AND IRSF SAMPLES

The sky background was measured as the median value of the sky measured within an annulus. An iterative procedure was used through σ-clipping. Figure B.1 shows the image and the size of the annulus used (see the left-hand panel). The right-hand panel shows the histogram distribution of the pixel values. The distribution is Gaussian in nature, with the mean value approximately equal to the median sky value. The blue dashed and black dotted lines represent the median and mean sky values, respectively. The vertical red solid lines represent $\pm 2\sigma_s$, where σ_s is the standard deviation in the sky background. Only the pixels within the used annulus and sky values lying within the area defined by the two red solid (vertical) lines were used in determining the sky background. That is, an iterative procedure was applied in the measurements of the sky background through σ-clipping.

Figure B.2 shows the sky distribution within an annulus for some of the IRSF J and K_s-band images used in the J and K_s-band Fundamental Plane analysis. The left and right-hand panels represent the J and K_s-band images, respectively. As expected, the sky is brighter in the K_s-band than the J-band images.

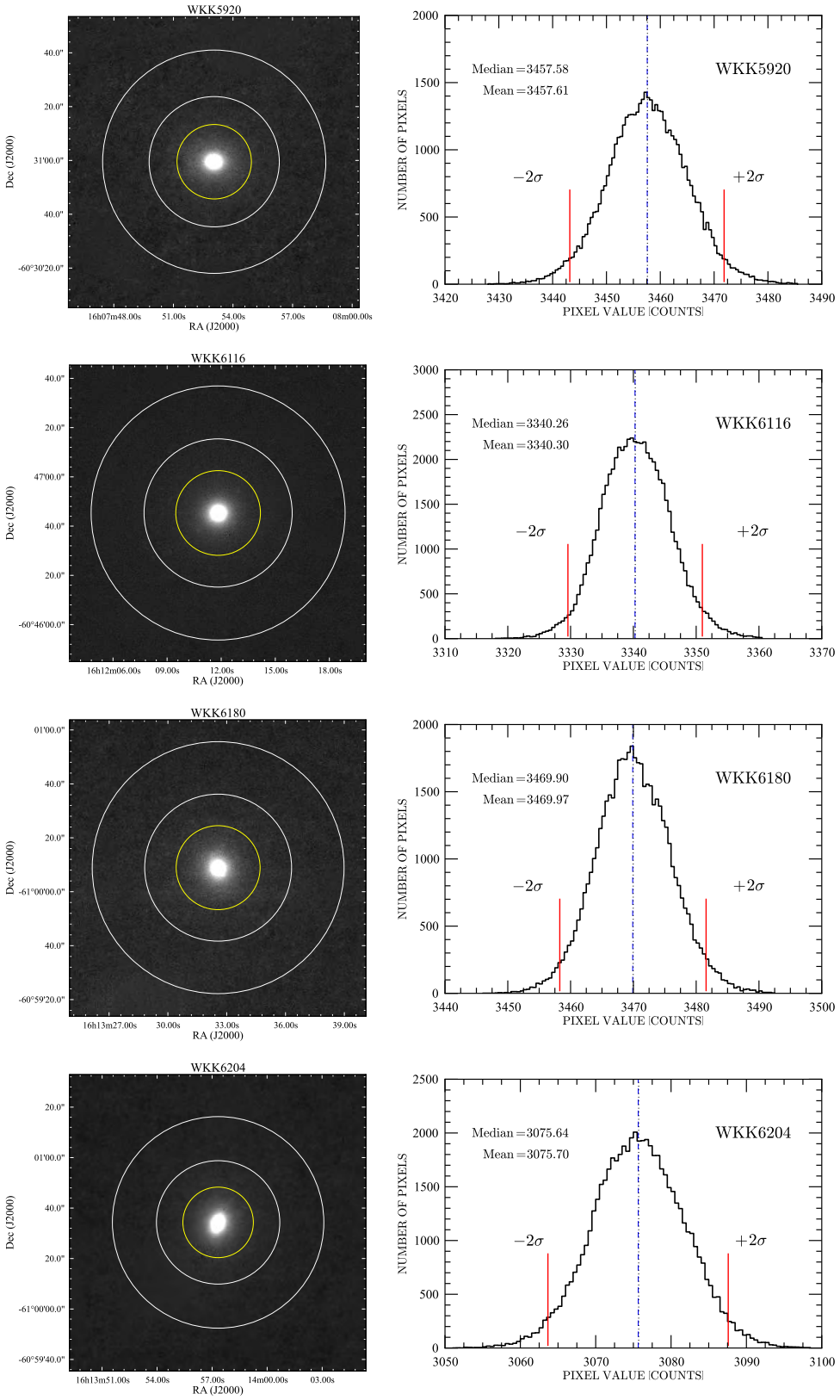

Fig. B.1: Norma sample sky level determination using an annulus. The annulus is represented by the white circles (see the left-hand panels). The right-hand panels show the distribution of the pixel values within the annulus used. The red solid (vertical) lines represent $\pm 2\sigma_s$ clipping where σ_s is the deviation in the sky background.

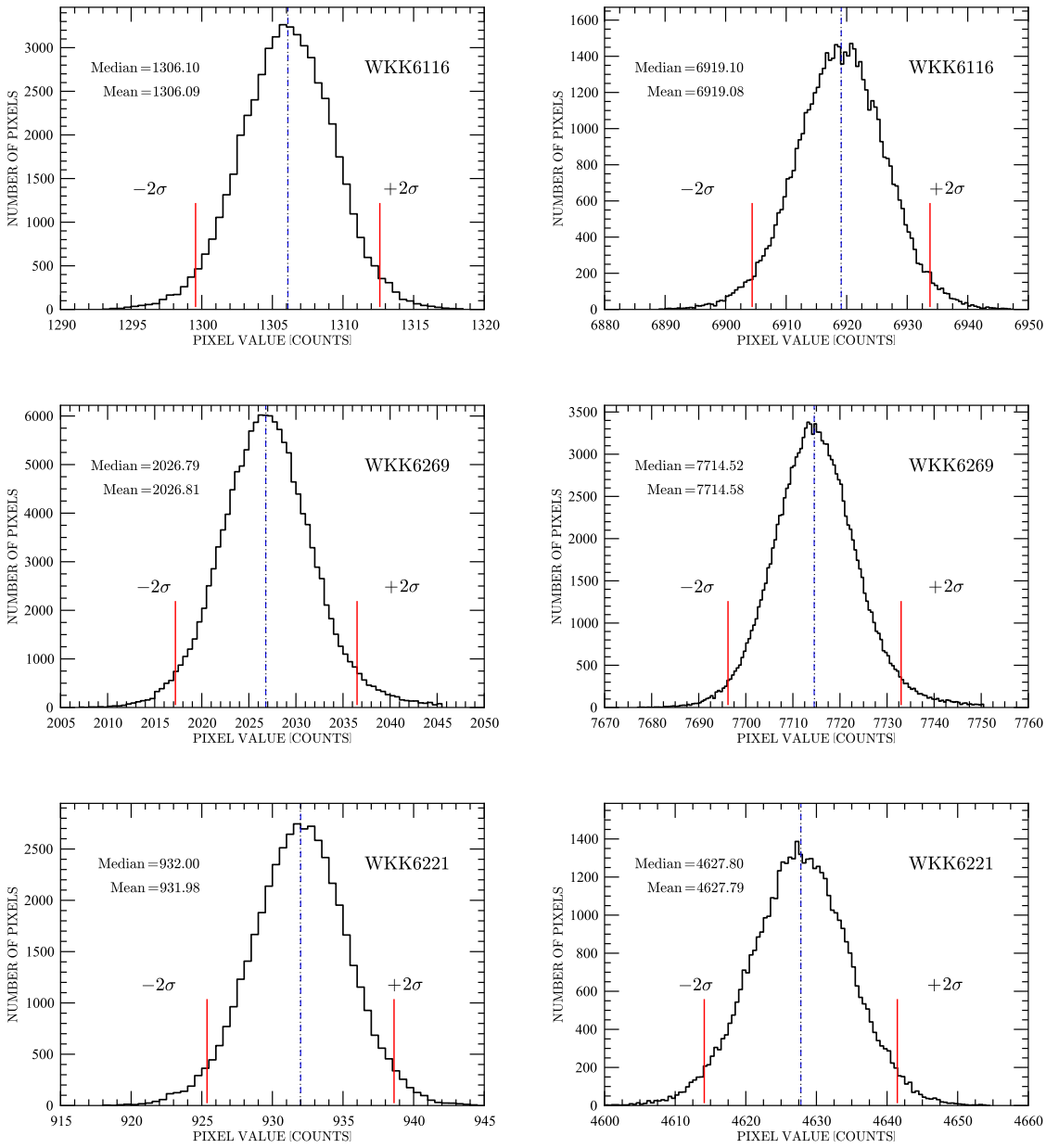

Fig. B.2: Distribution of pixel values within a given annulus for the J-band (left-hand panels) and the K_s-band (right-hand panels). The blue dashed and black dotted lines represent the median and mean sky values, respectively (same as described for the right-hand panels of Figure B.1).

APPENDIX C

GALAXY SURFACE BRIGHTNESS PROFILES: NTT/SOFI SAMPLE

The galaxy surface brightness profiles for a representative sample of the NTT K_s-band images are shown in Figure C.1. A double Sérsic function was used in fitting the galaxy surface brightness profiles by applying a simple least-squares fit. The left-hand panel shows the galaxy surface brightness profile. The best fit is represented by the red solid line which is a combination of the two Sérsic components. The double (best) fit was extrapolated to determine the total extrapolated magnitude. From the measured total extrapolated magnitude, the radius of the circle containing half the total flux was measured by interpolation. The right-hand panel shows the curve of growth, the effective radius is shown by the vertical blue dashed lines.

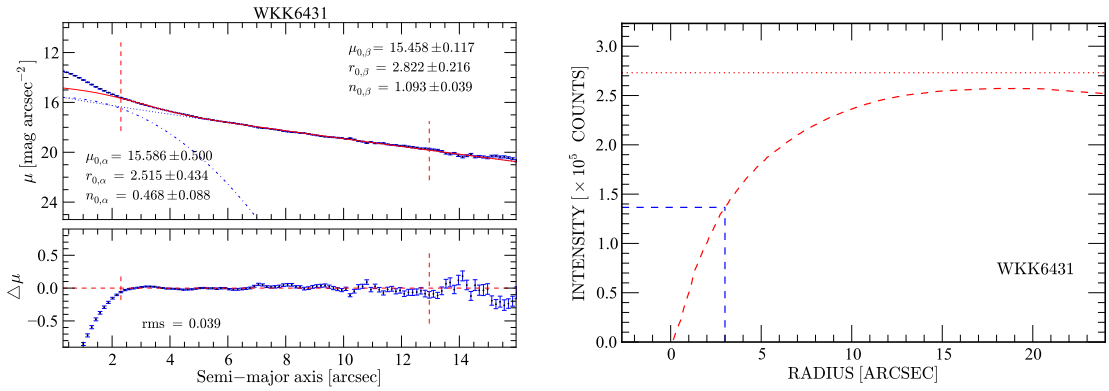

Fig. C.1: Left-hand panel: Surface brightness profile fits to the NTT K_s-band images used in the Norma cluster Fundamental Plane sample. Two Sérsic components were used and are indicated by the dotted and dot-dashed lines. The best fit which is a combination of the two Sérsic components is represented by the red solid line. The small vertical red dashed lines represent twice the seeing and the radius (semi-major axis) at which the galaxy surface brightness is equivalent to the standard deviation in the sky background. Only the data points lying within these two vertical lines were used to fit the galaxy surface brightness profile. The right-hand panel is the curve of growth, the effective radius (obtained through interpolation) is represented by the vertical blue dashed line.

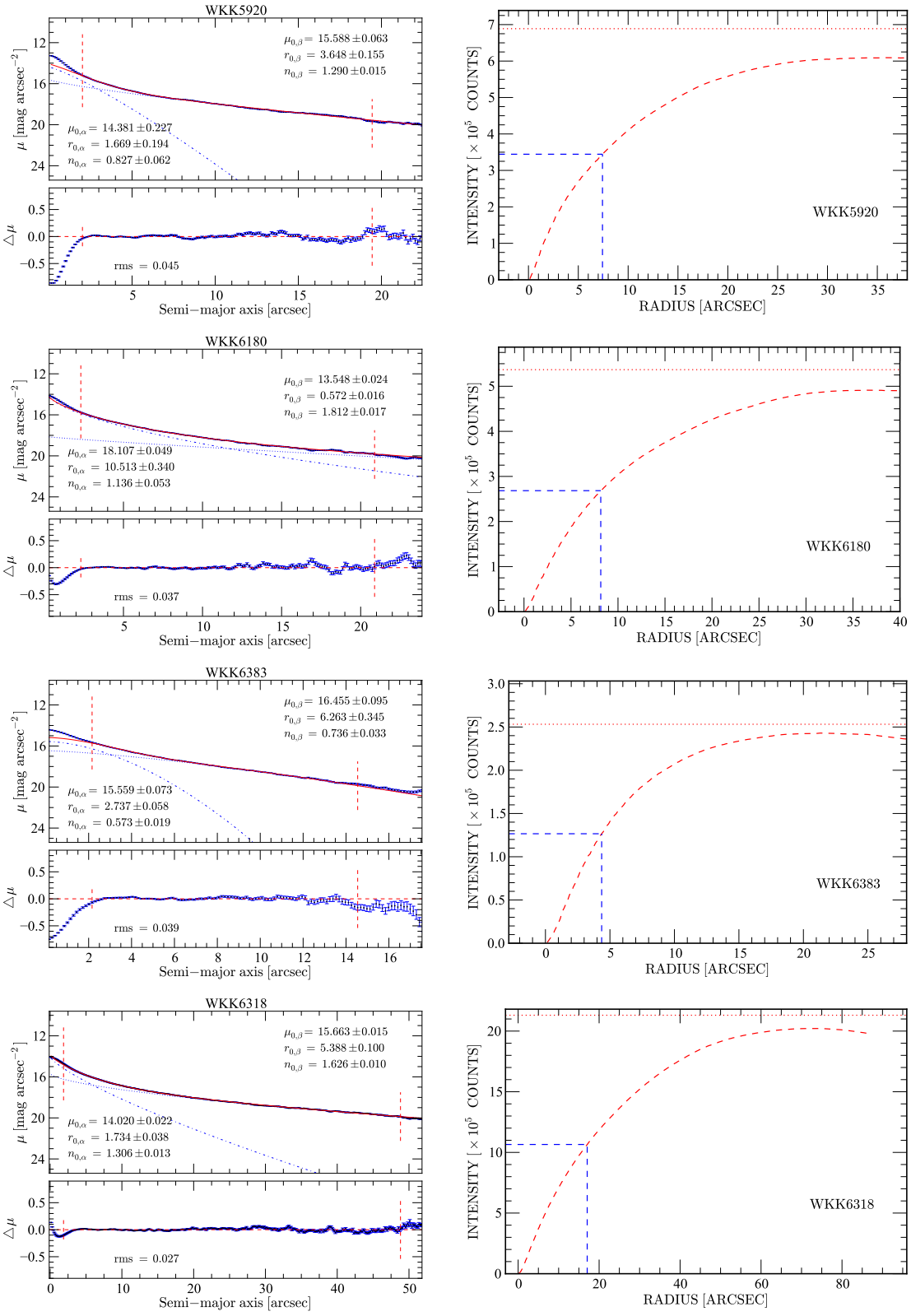

Fig. C.1: Continued . . .

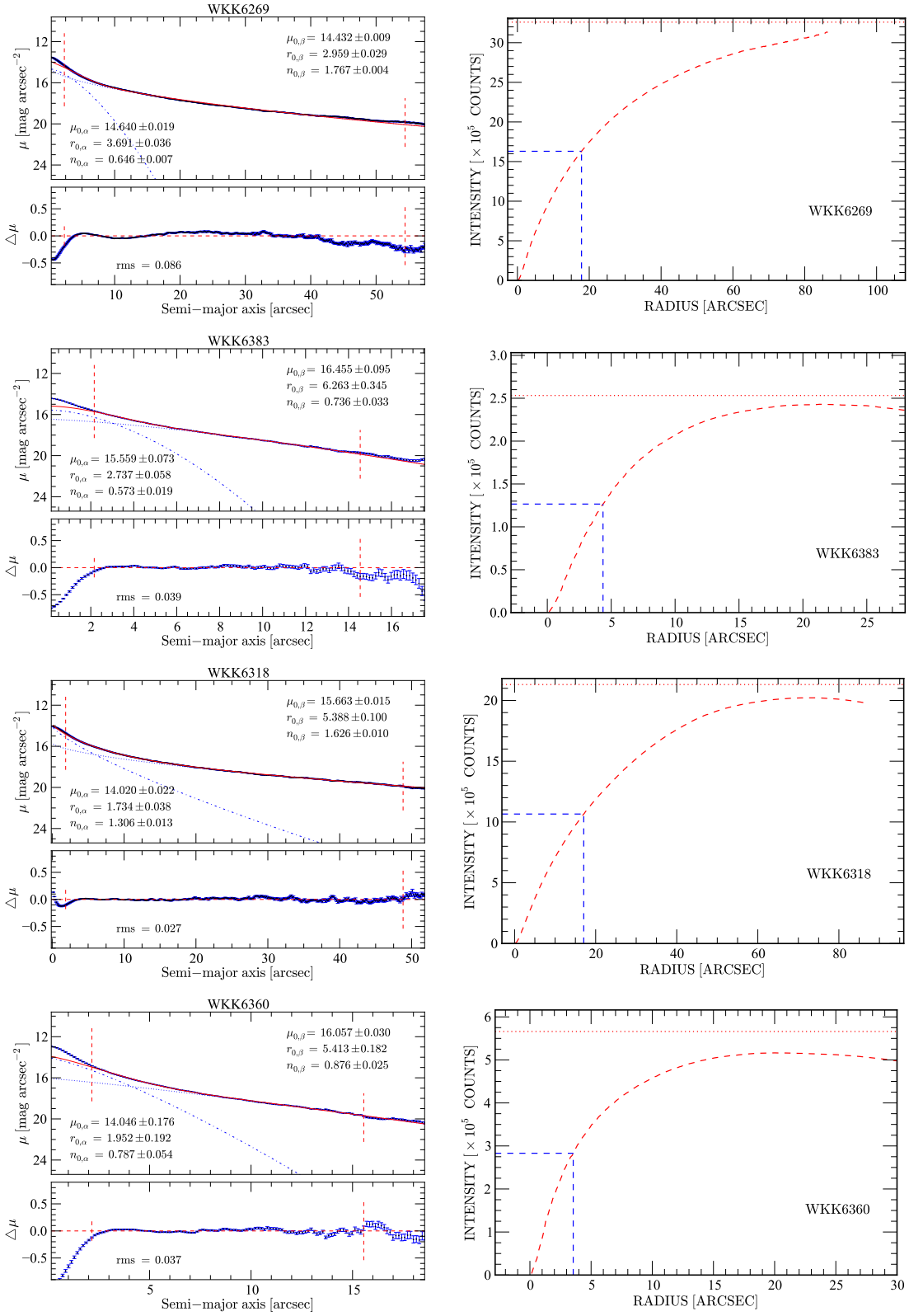

Fig. C.1: Continued ...

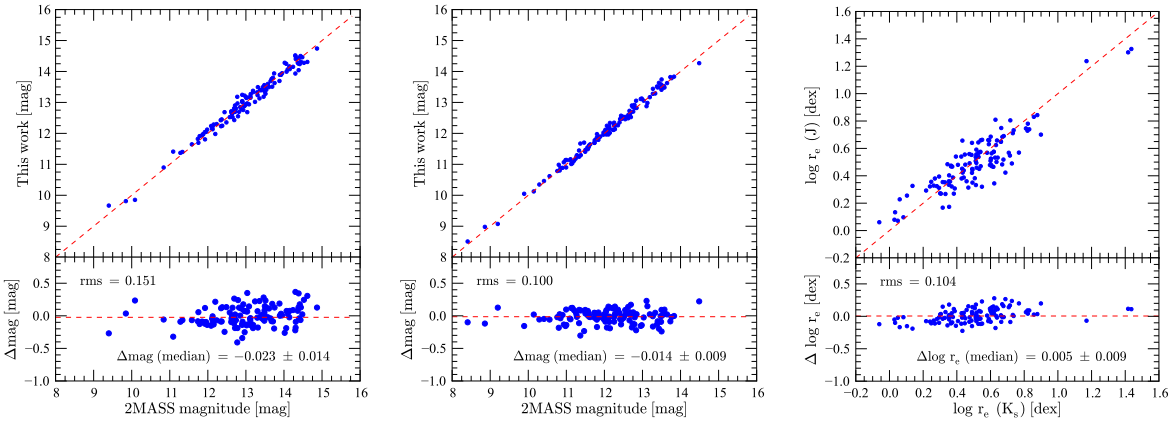

Fig. C.2: Comparison of the total extrapolated magnitudes in this work with the total extrapolated magnitudes taken from the 2MASS XSC. The comparison for the 121 early-type galaxies which were used as the reference sample in the Fundamental Plane analysis. The left-hand and middle panels show my total extrapolated magnitudes compared to 2MASS XSC in the J and K_s-band, respectively. The right-hand panel shows a comparison of my PSF-corrected effective radii for the J and K_s-band images. The red dashed lines in the lower sub-panels represent the median difference while those in the upper sub-panels represent a one-to-one relation.

C.1 Photometric quality Check – Coma cluster Calibration Sample

As a photometric quality check, I have compared my total extrapolated magnitudes measured using the 2MASS J and K_s-band Atlas images with values taken from the 2MASS XSC for 121 early-type galaxies within the Coma cluster. This sample was used as a reference in the J and K_s-band Fundamental Plane analysis. Figure C.2 shows the results of the comparison. The left and right-hand panels show the comparison of the total extrapolated magnitudes in the J and K_s-band, respectively. The right-hand panel shows a comparison of the measured effective radii in the J and K_s-band after applying PSF (seeing) corrections. Note that, the right-hand panel compares the J and K_s-band effective radii (this work) measured using the 2MASS Atlas images and not those taken from the 2MASS XSC. Table C.1 presents the identification (2MASS ID) and the magnitude difference for the 9 Coma cluster galaxies that were excluded from the Fundamental Plane analysis after their photometry measurements were deemed unreliable (see §3.3).

Tab. C.1: Summary for the 9 galaxies excluded from the Coma cluster reference sample. These are represented by the blue stars in the top left-hand panel of Figure 3.18 (see §3.3). Δmag is the difference between the measurements in this work and those from the 2MASS XSC, that is, (Δmag = 2MASS – this work).

2MASS Id.	Δmag
2MASXJ12593064+2747288	−0.590
2MASXJ13015023+2753367	−0.303
2MASXJ12592265+2753488	−0.508
2MASXJ12592529+2758048	−0.270
2MASXJ12590006+2758029	−0.289
2MASXJ13004277+2758166	−0.389
2MASXJ12564283+2801138	−0.457
2MASXJ12582169+2808557	−0.599
2MASXJ12594129+2830257	−0.400

APPENDIX D

TULLY-FISHER ANALYSIS: PARKES HI DATA

The HI profiles and parameters were measured using the MIRIAD task MBSPECT on the spectra generated from the observed raw data using LIVEDATA and GRIDZILLA. The HI parameters were measured by first fitting and subtracting the baseline fit. Some of the measured HI parameters are indicated on the HI profiles shown in Figure D.1. The filled circle shows the galaxy total intensity. The width-maximised and width-minimised values (w_{20} and w_{50}) are indicated by the open circles and crosses, respectively. The dash-dotted lines represent the HI emission spectrum whose size was measured and set manually to correspond to the galaxy under inspection. The baseline fit was performed on the parts of the HI profile outside the HI emission spectrum. The red solid lines shown in Figure D.1 represent the baseline fit.

D.1 HI-detected galaxies used in the Tully-Fisher analysis

In Figure D.1, I present HI detected galaxies which were used in the Tully-Fisher analysis. The HI detected galaxies which were excluded from my Tully-Fisher analysis are given in §D.2 (see Figure D.2).

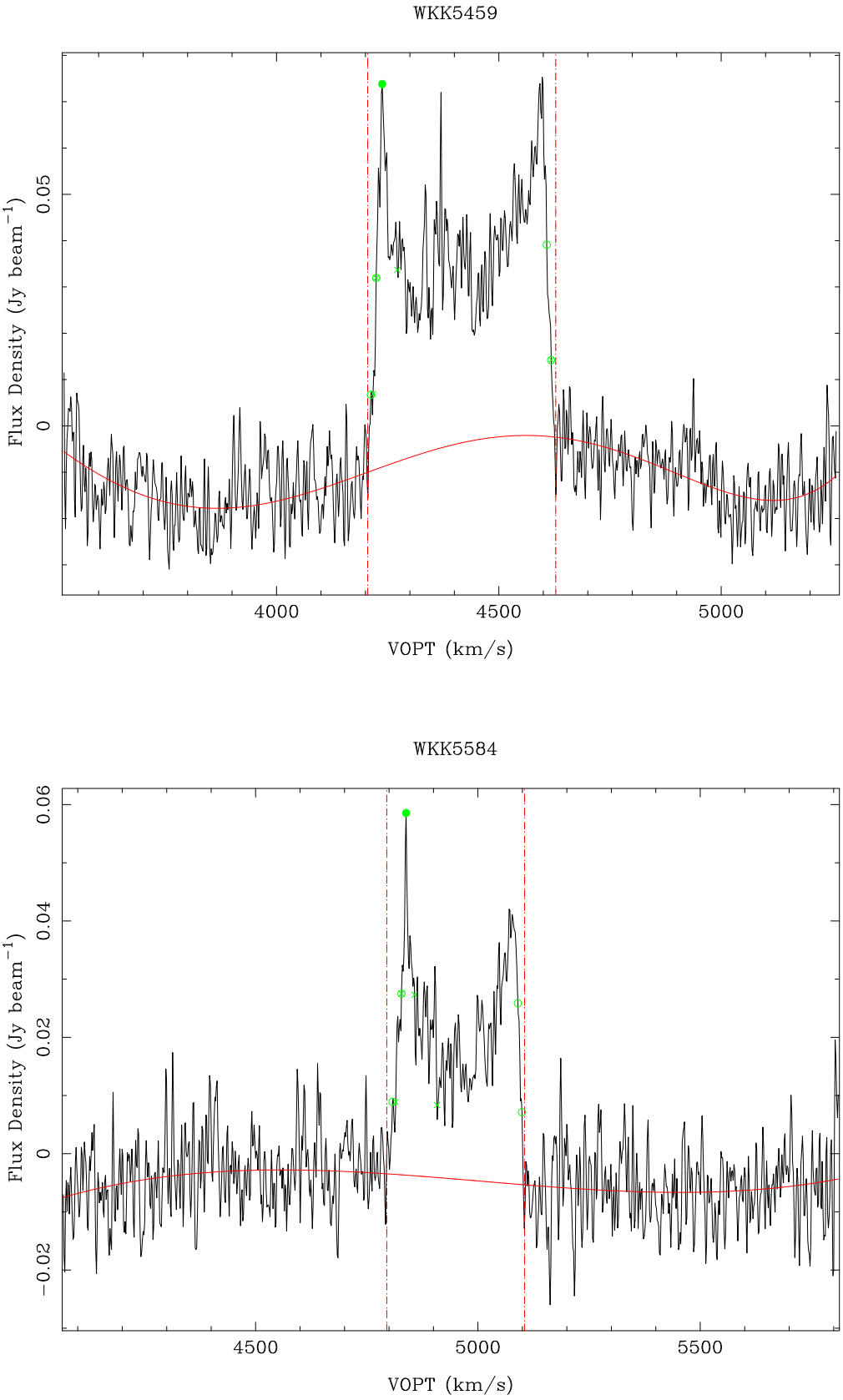

Fig. D.1: HI profiles for the late-type galaxies in the K_s-band Tully-Fisher sample. The red dashed lines indicate masked regions while the red dotted lines represent the region of the HI profile used to measured the galaxy parameters after fitting and subtracting the baseline. The baseline fit is shown by the red solid lines.

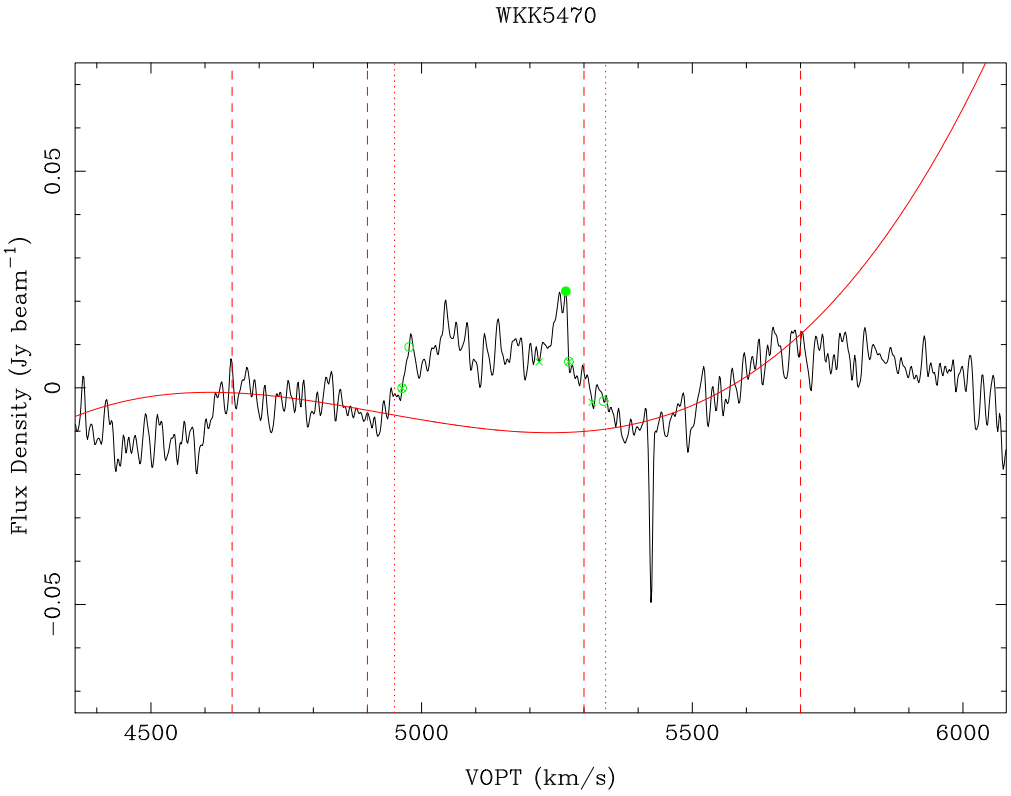

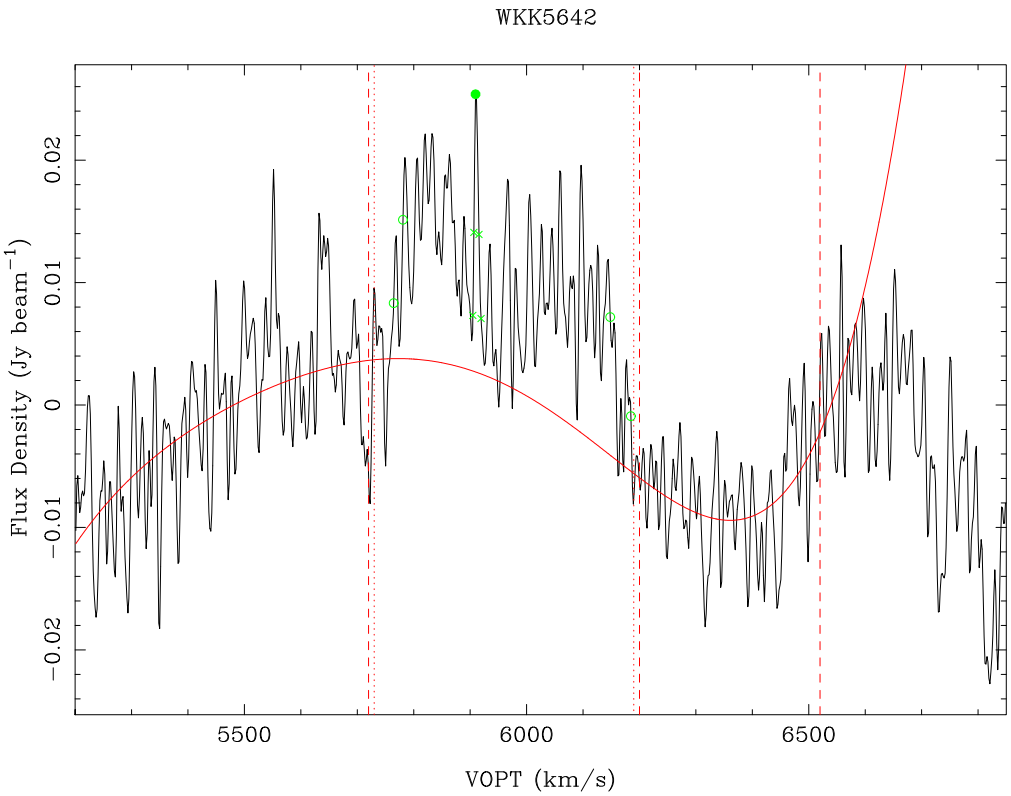

Fig. D.1: Continued ...

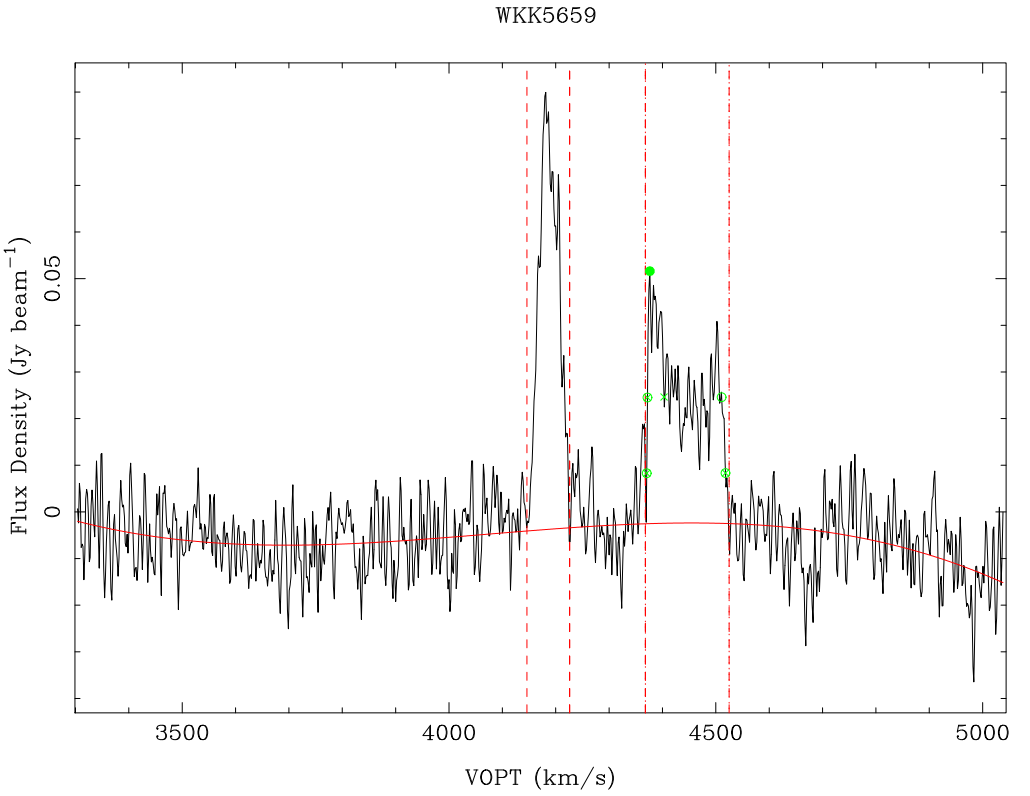

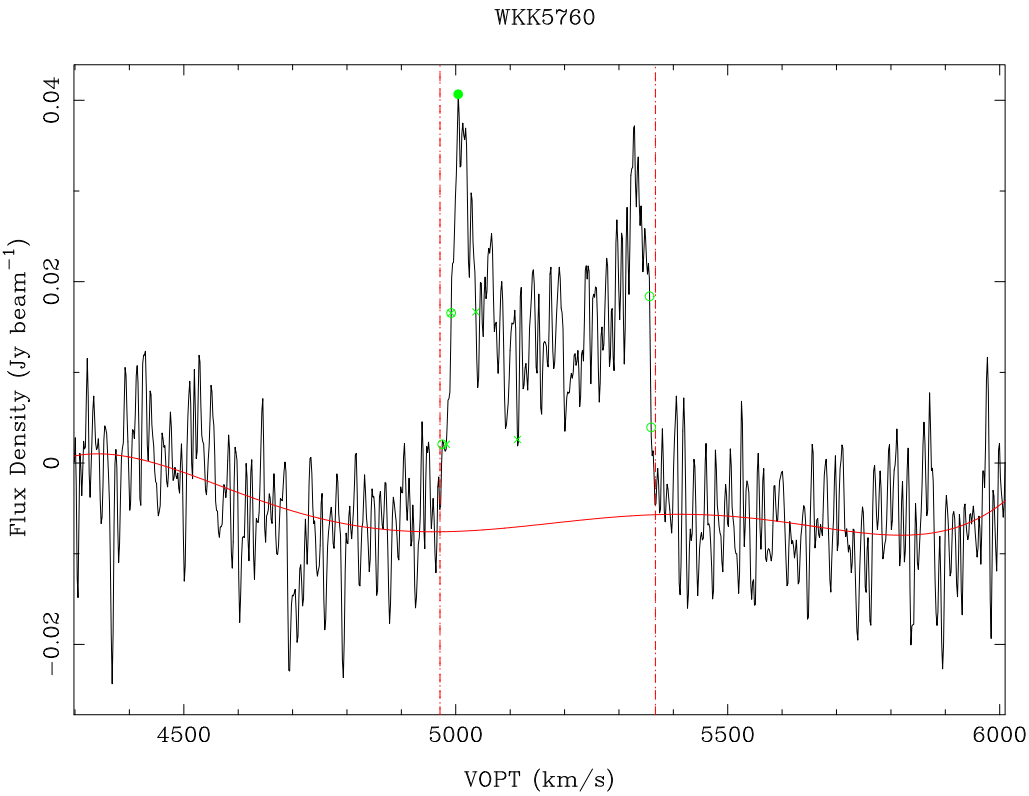

Fig. D.1: Continued . . .

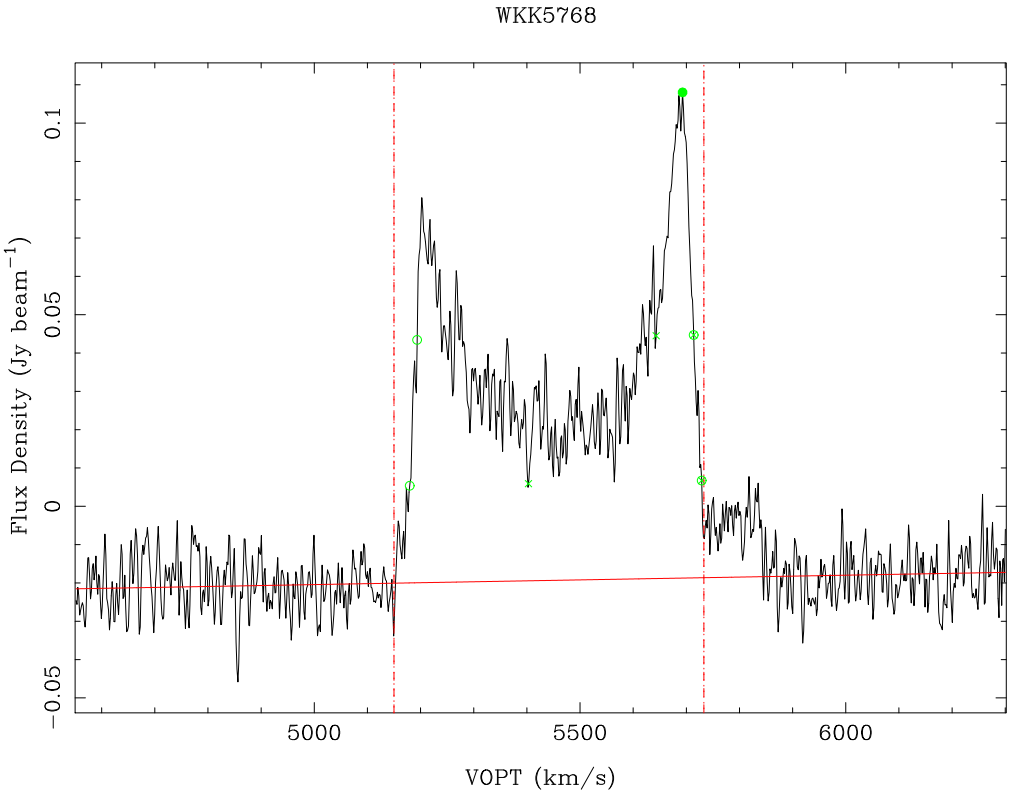

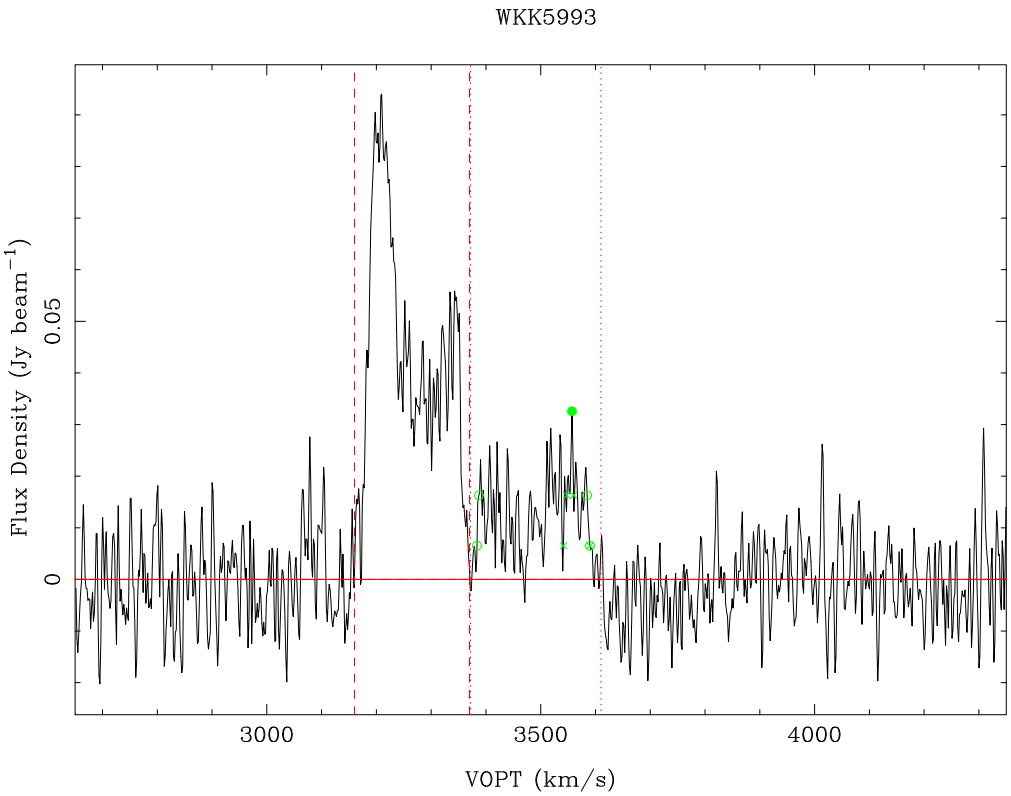

Fig. D.1: Continued . . .

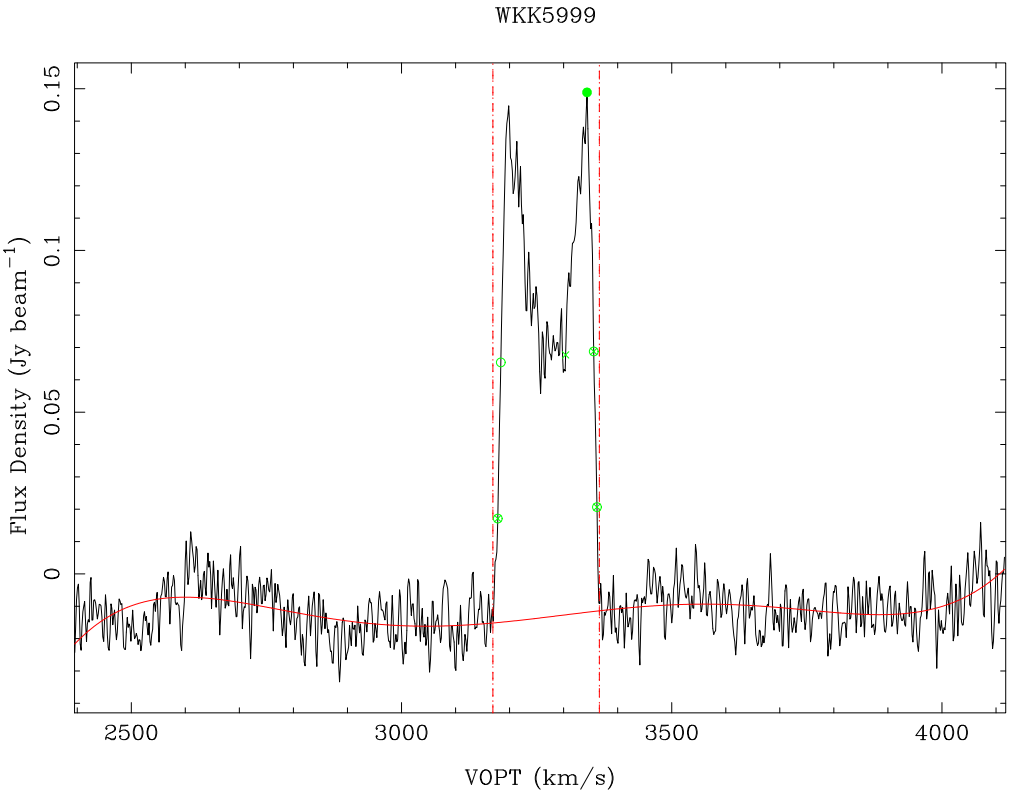

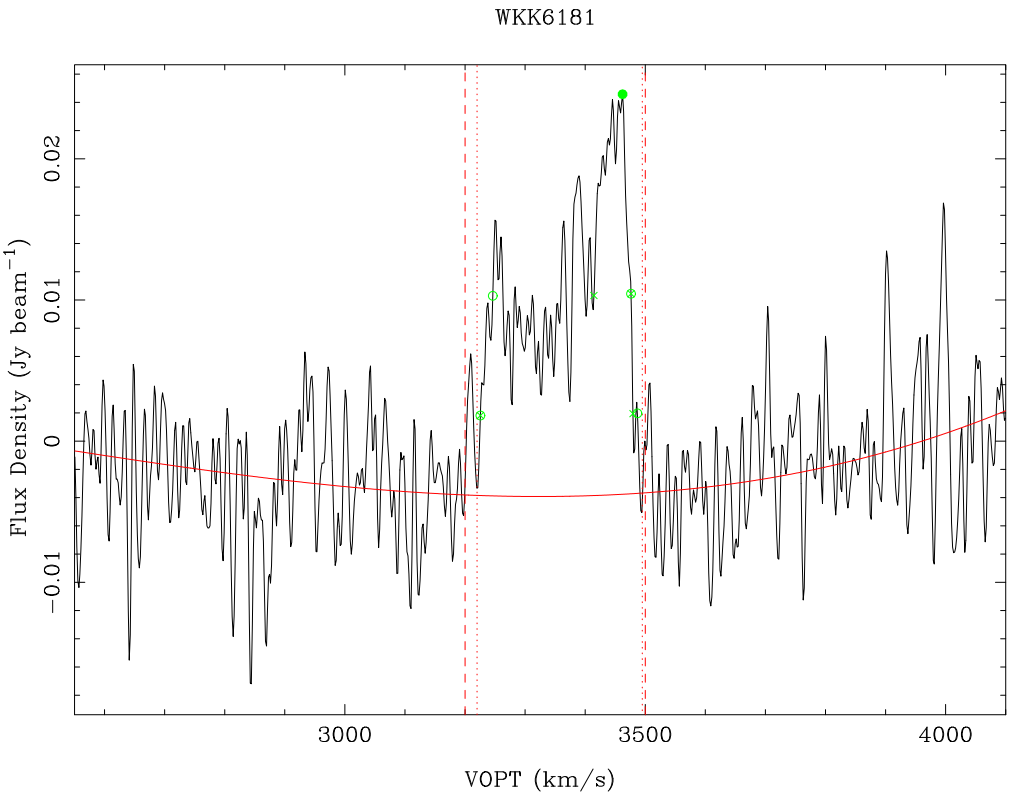

Fig. D.1: Continued ...

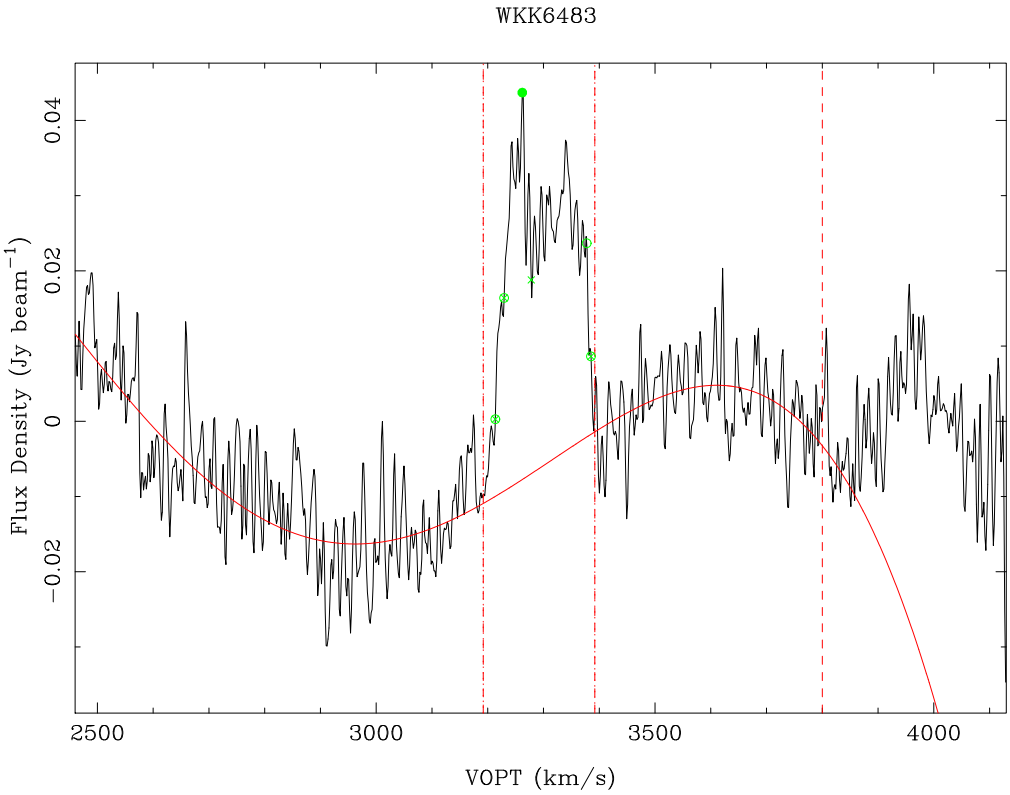

Fig. D.1: Continued ...

D.2 HI-detected galaxies not used in the Tully-Fisher analysis

In Figure D.2, I present HI detected galaxies which were not used in the Tully-Fisher analysis. These galaxies were excluded from the final analysis due to, either, signal-to-noise ratio which was too low that it was difficult to reliably measure the HI line width, the inclination angle measured from the near-infrared J-band image is less than 45°, or the fully corrected line width is less than 100 km s^{-1}. In the beam of WKK 5642, there are two prominent detections. The peak located at $v = 4183$ km s^{-1} belongs to WKK 5616. The signal at $v = 4444$ km s^{-1} seems to come from WKK 5659. In the HI profile of WKK 5659, the measured velocity is 4428 ± 41 km s^{-1}. WKK 5659 lies 8.′6 away from WKK 5616.

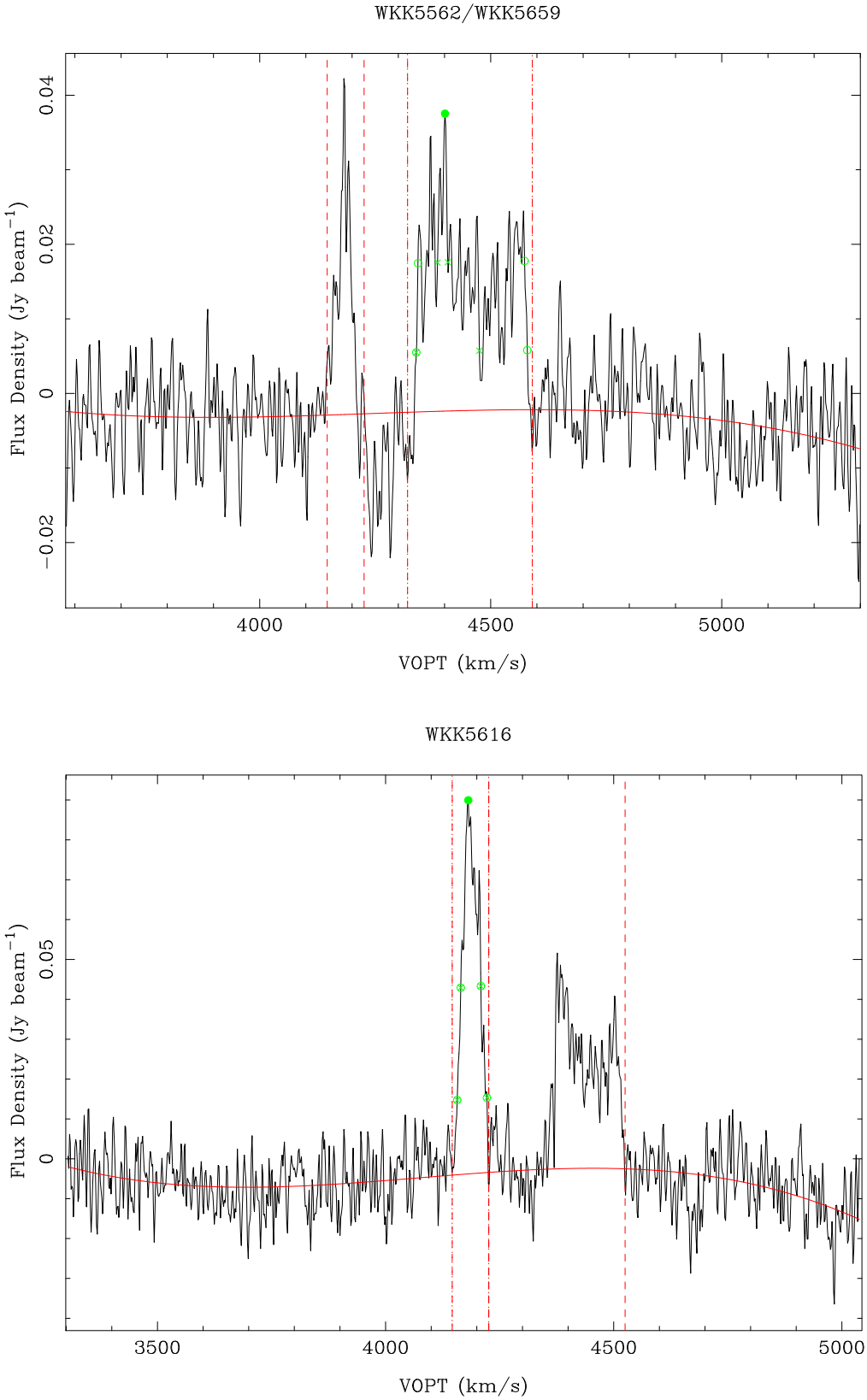

Fig. D.2: Other HI detected galaxies but not used in the Tully-Fisher analysis. Either the signal-to-noise is too low that it was difficult to reliably measure the HI width or the inclination angle measured from the near-infrared J-band image is less than 45°, or the fully corrected line width is less than 100 km s^{-1}. The target galaxies in the top and bottom panels are WKK 5562 and WKK 5616, respectively. Note the high signal-to-noise ratio of the spectrum in the bottom panel as compared to the top panel.

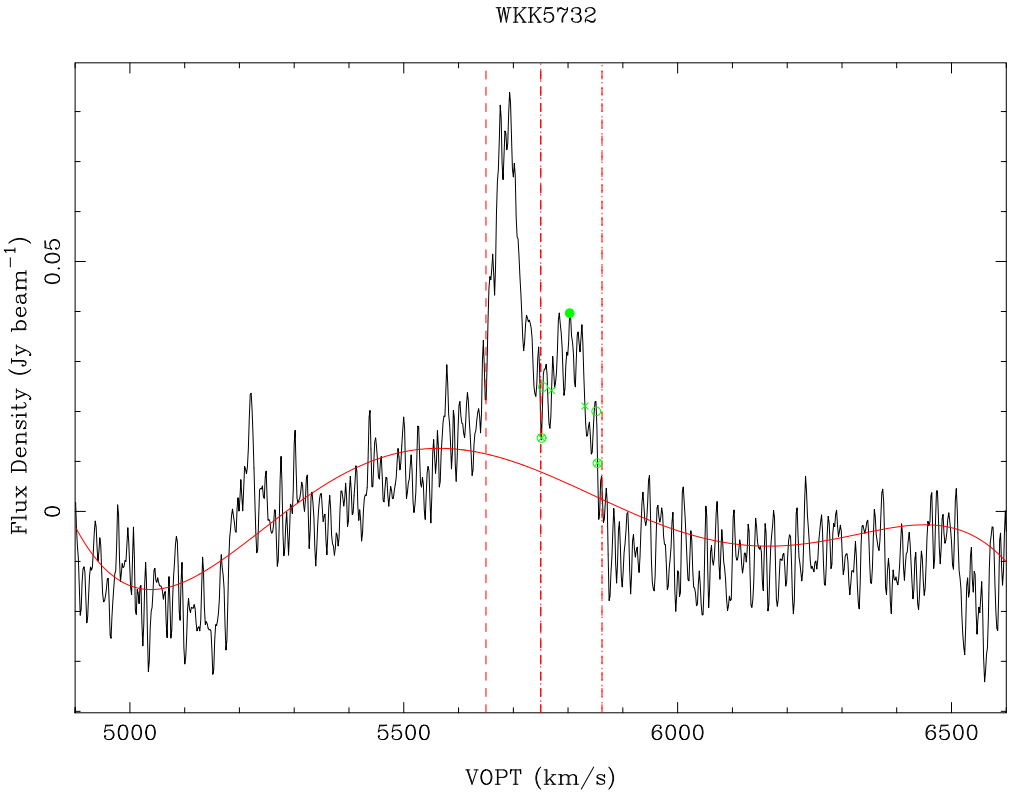

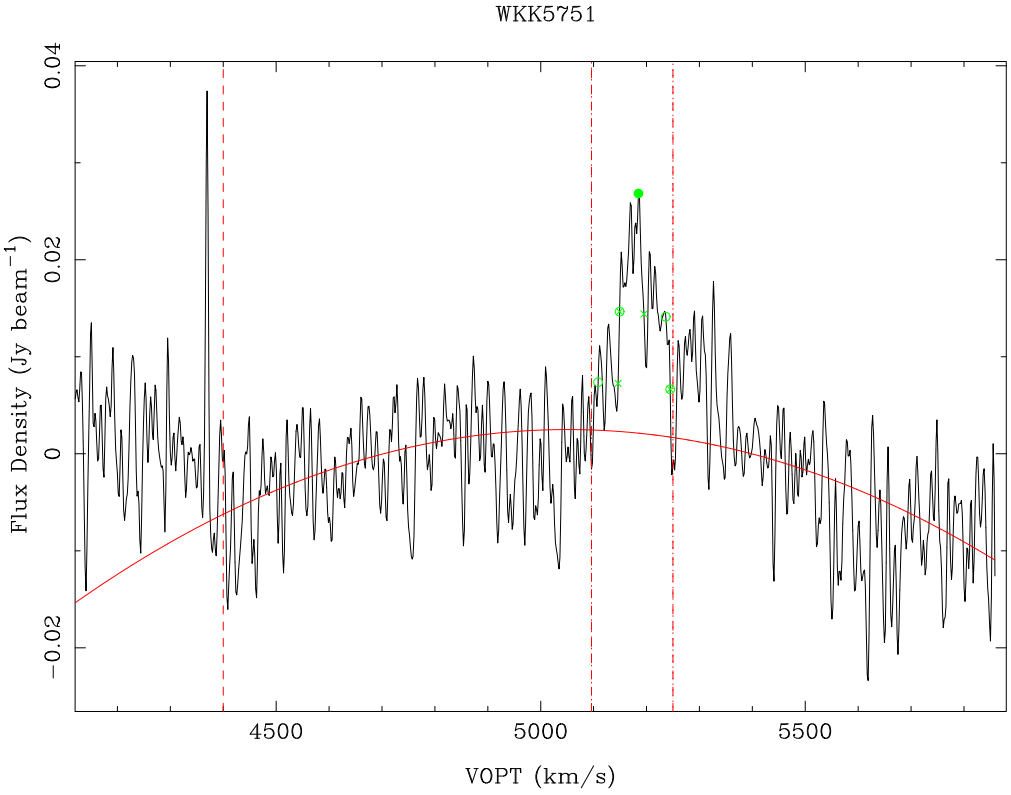

Fig. D.2: Continued ...

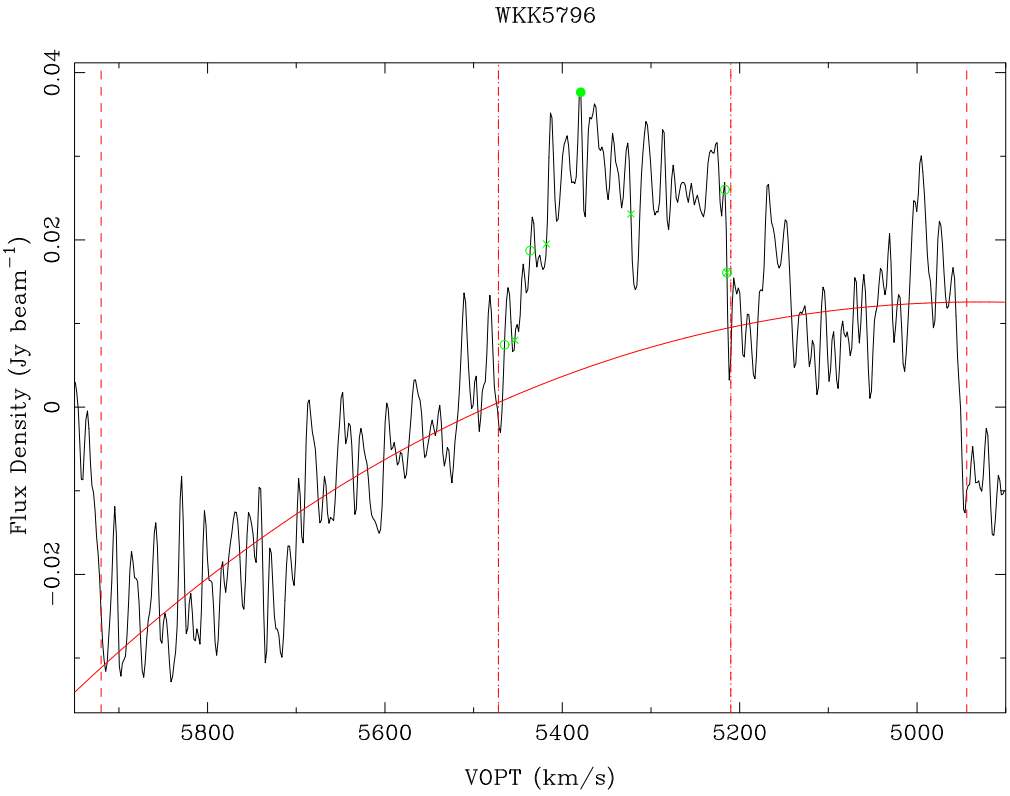

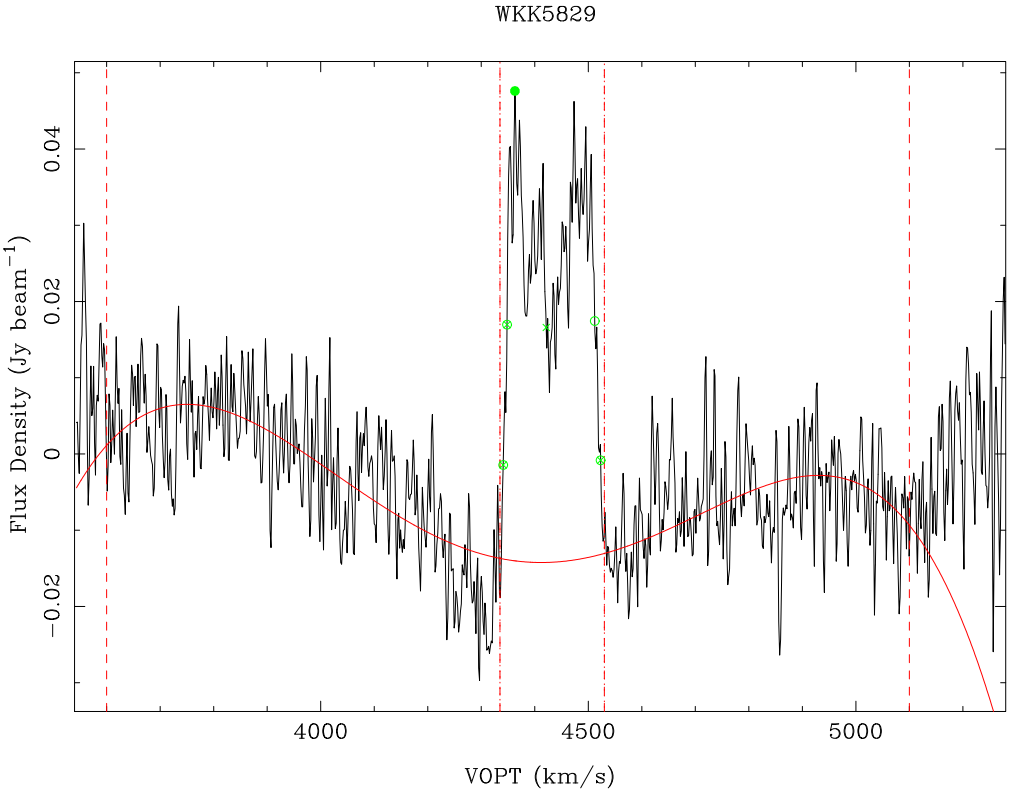

Fig. D.2: Continued ...

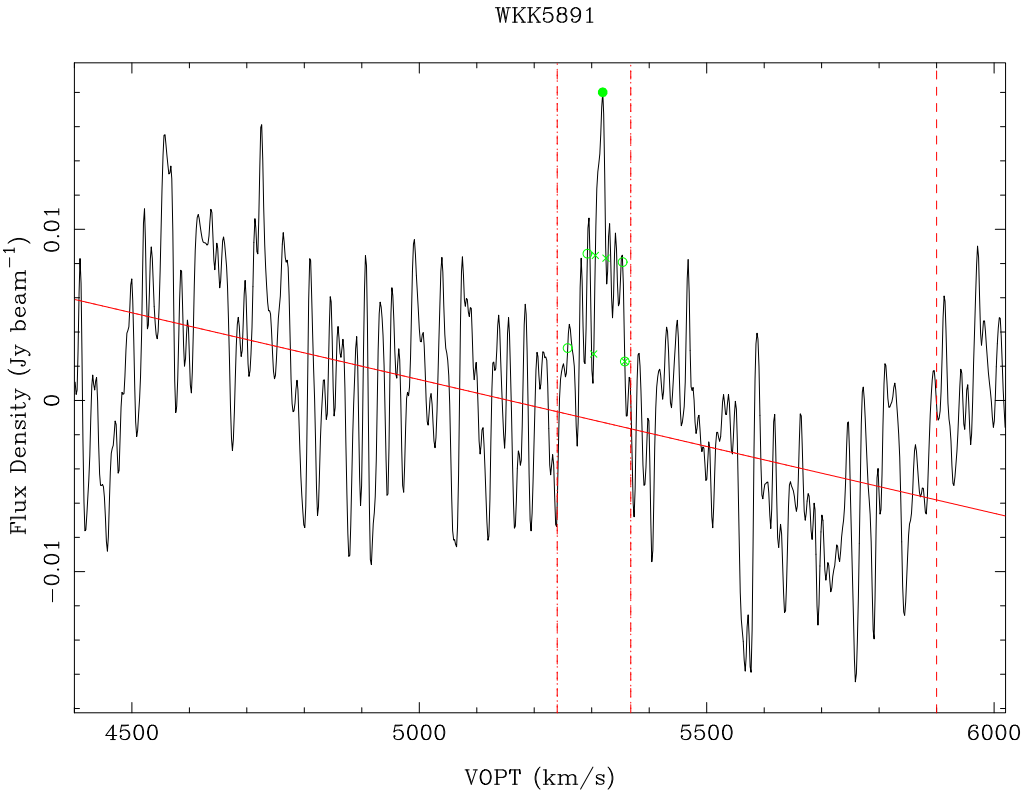

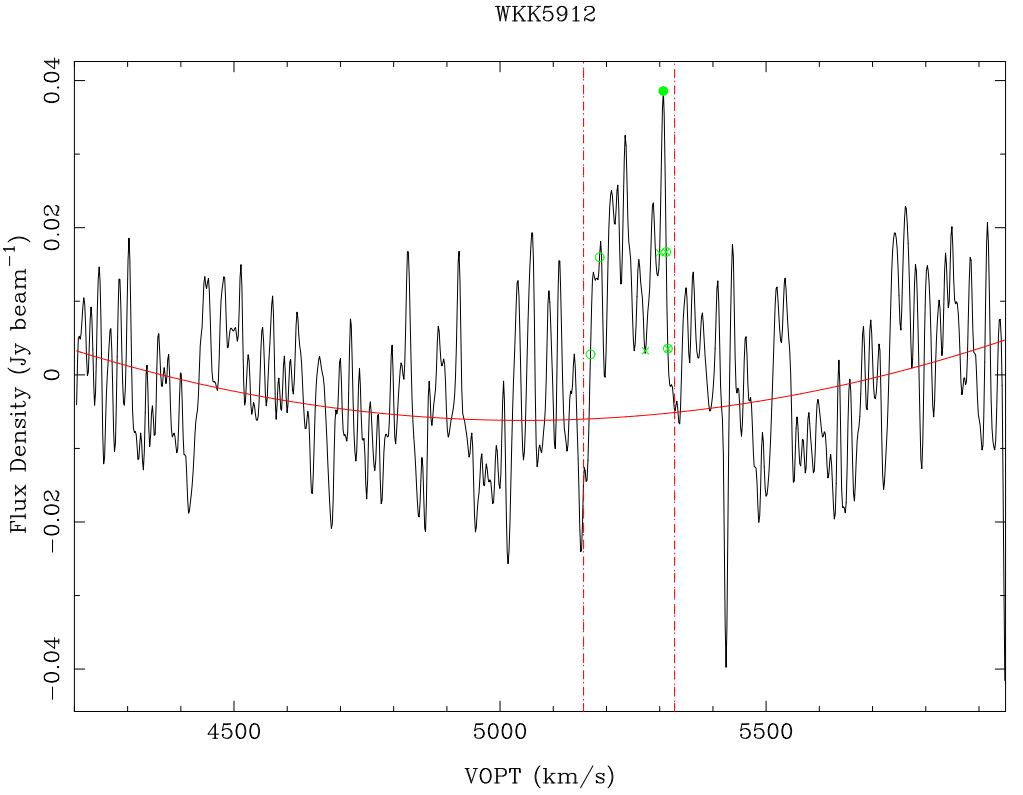

Fig. D.2: Continued ...

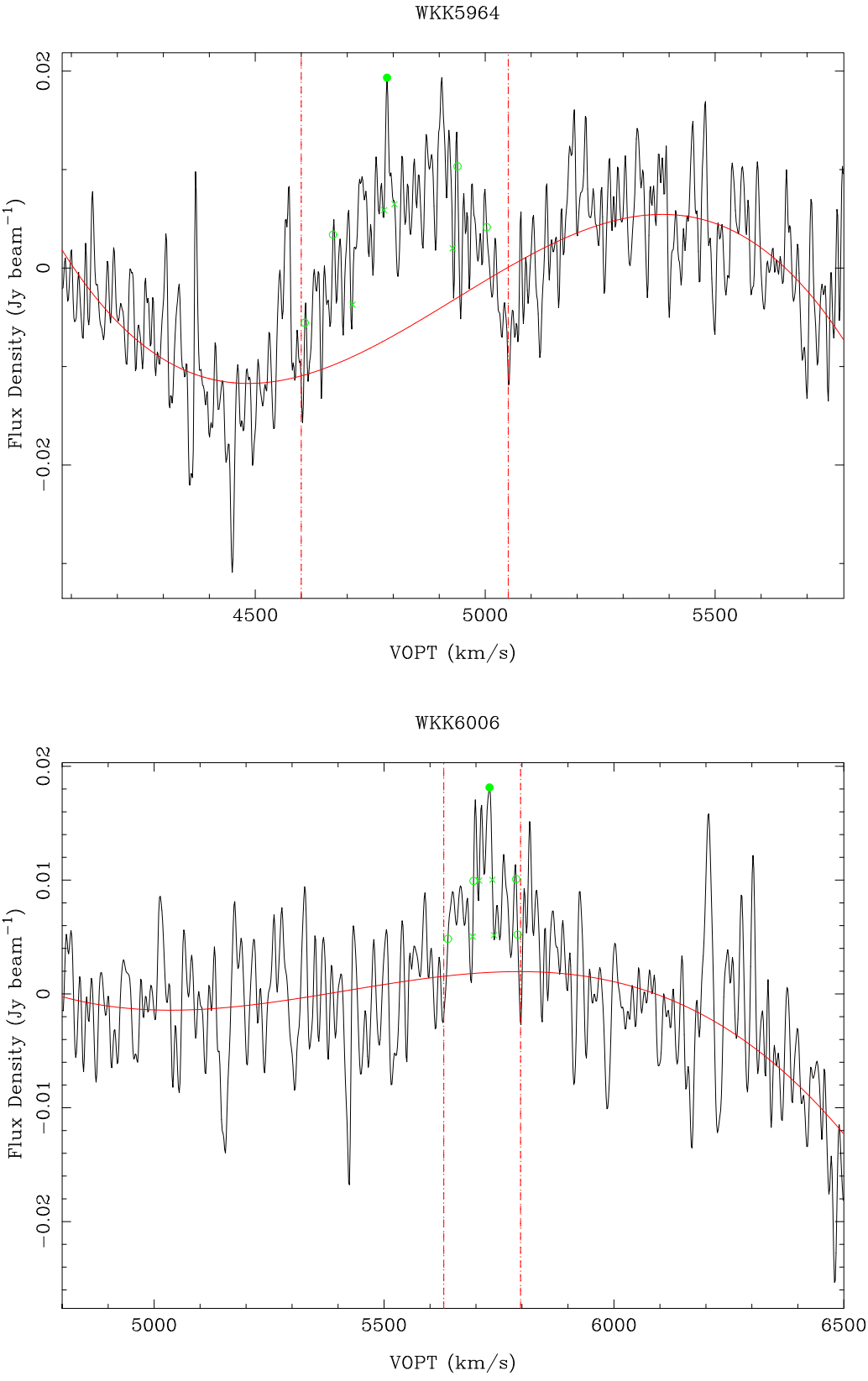

Fig. D.2: Continued . . .

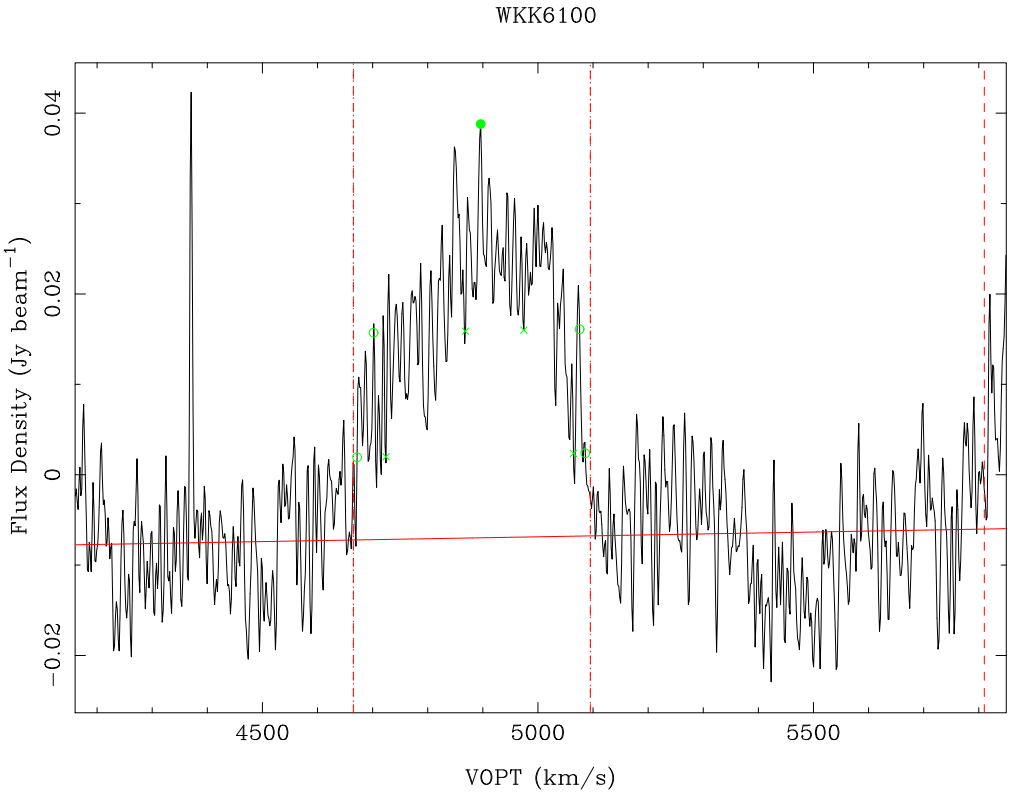

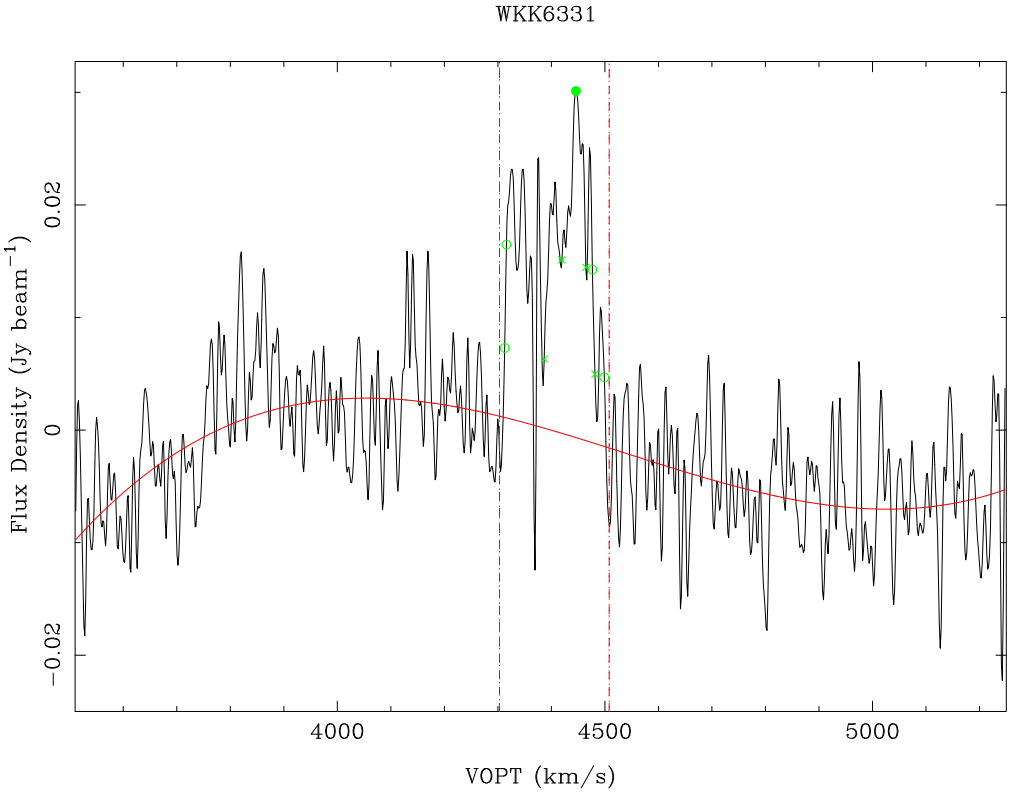

Fig. D.2: Continued . . .

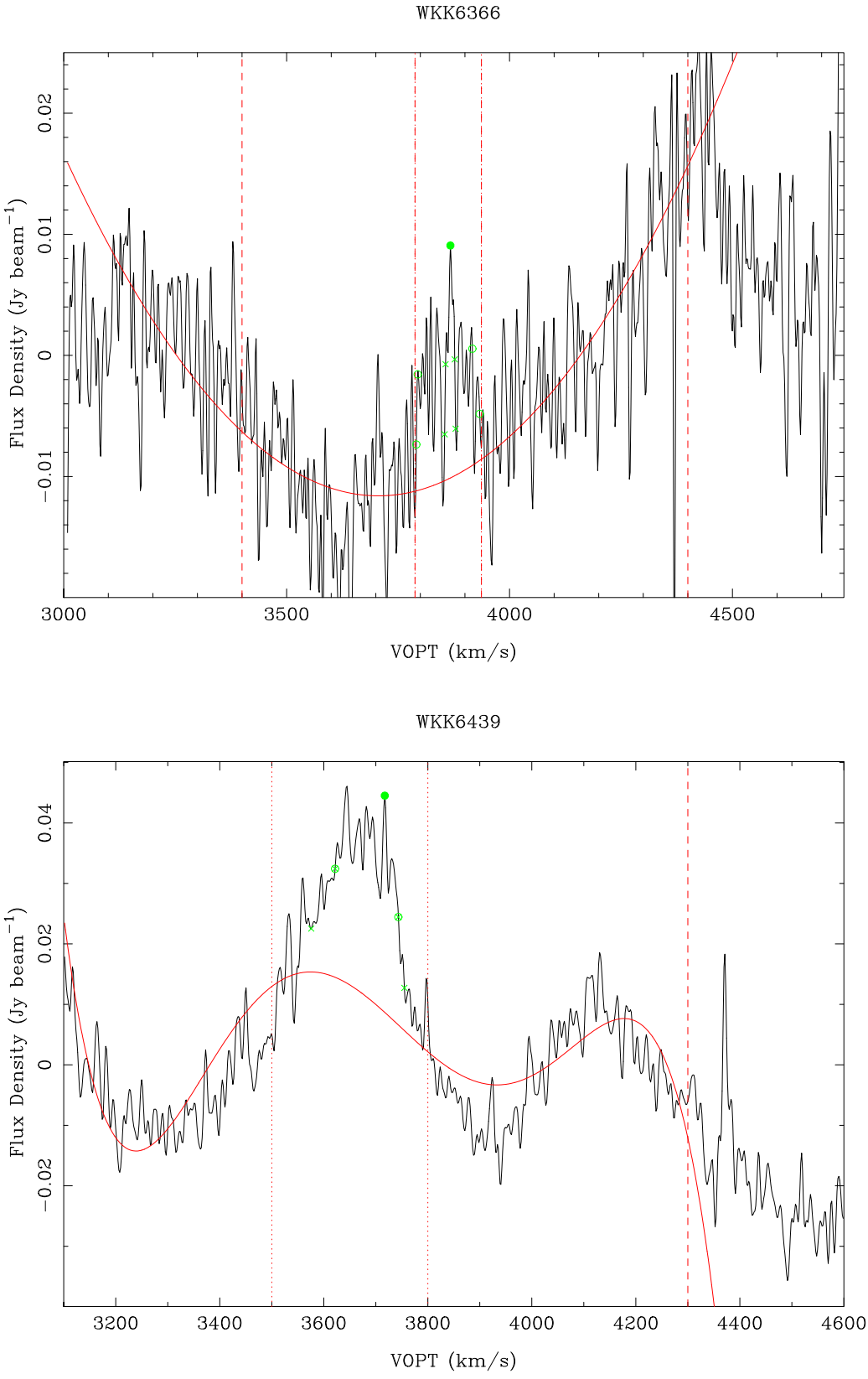

Fig. D.2: Continued . . .

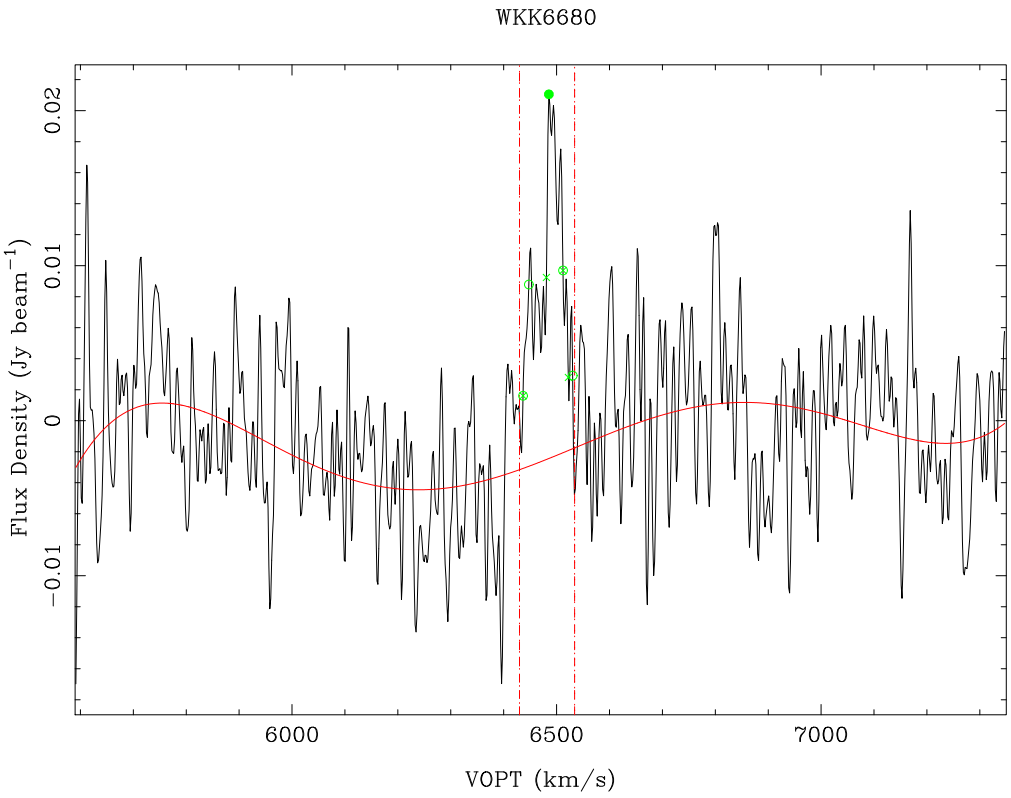

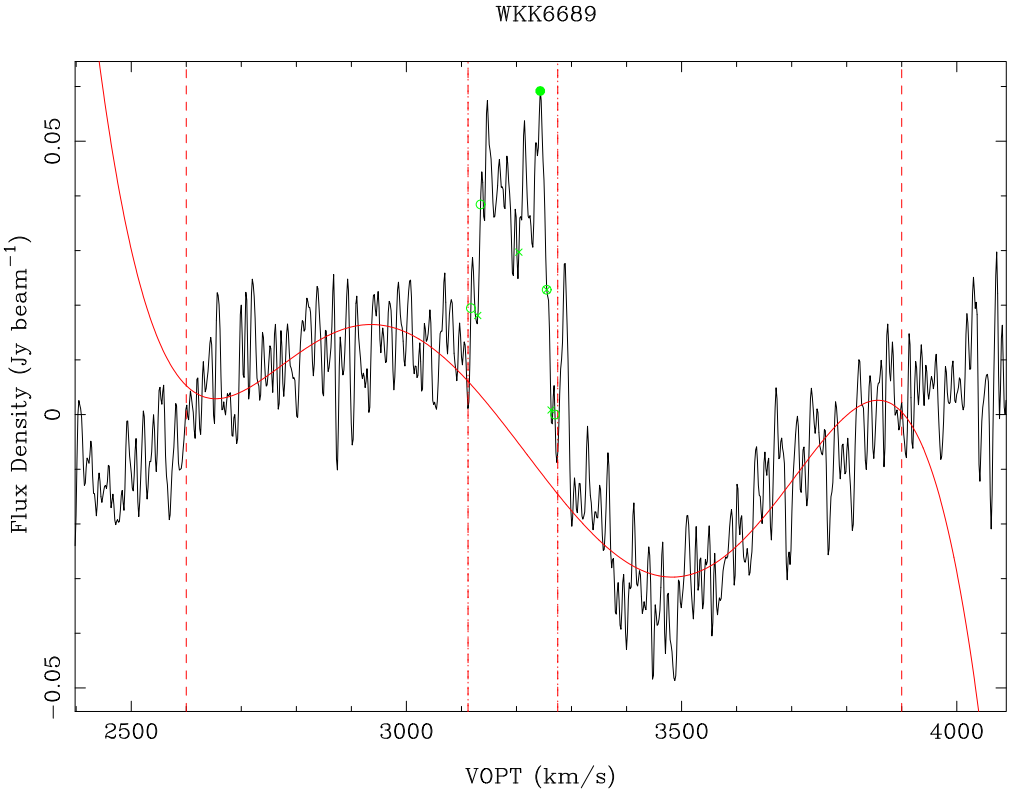

Fig. D.2: Continued ...

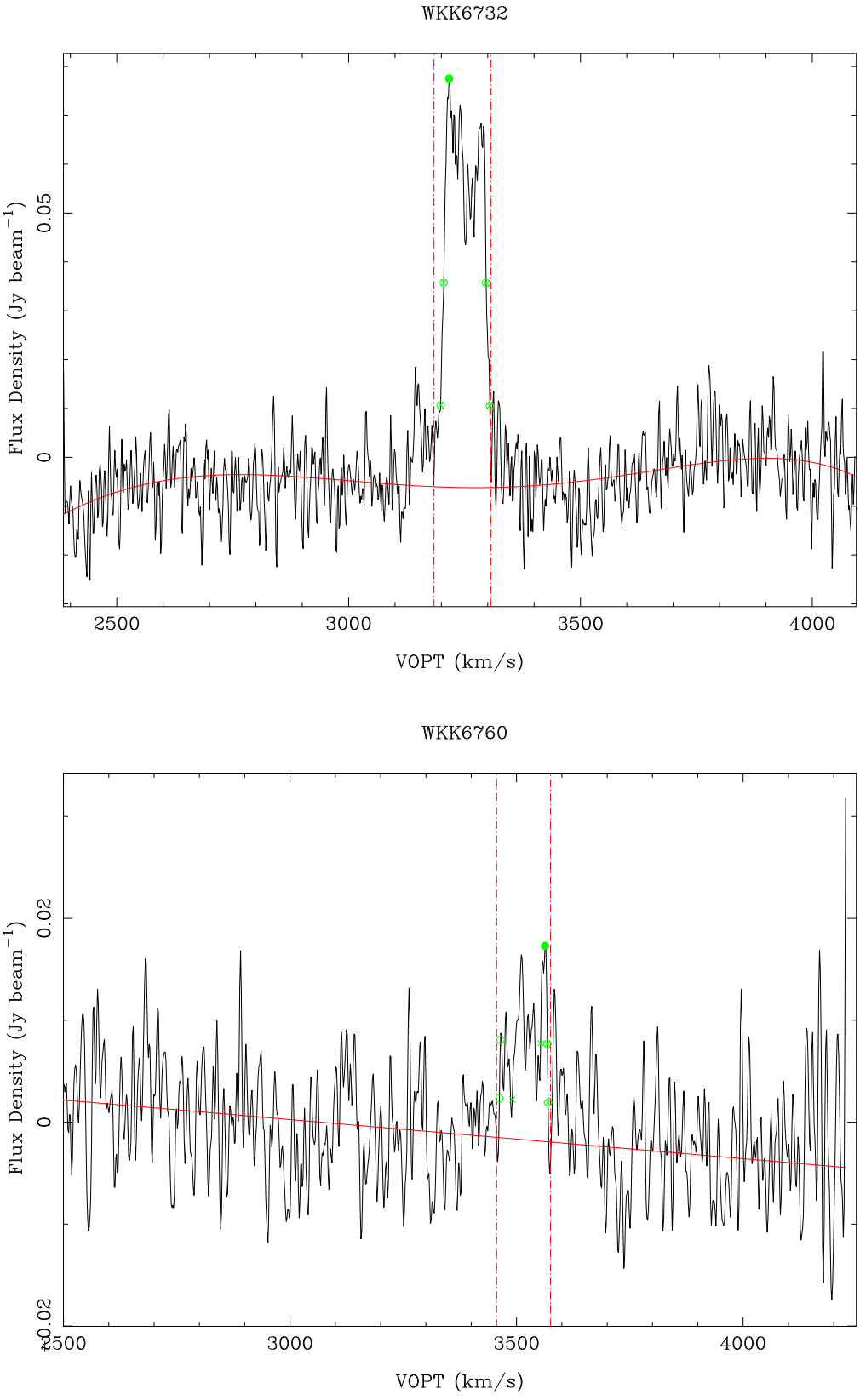

Fig. D.2: Continued ...

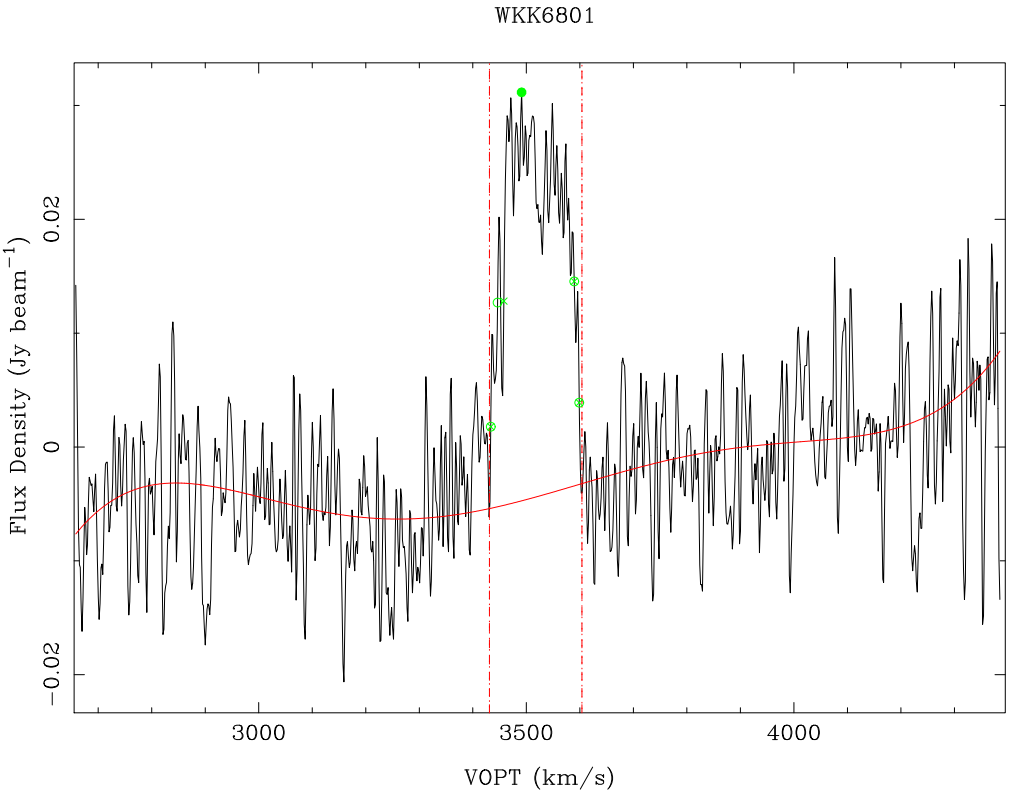

Fig. D.2: Continued ...

D.3 HI Non-detections

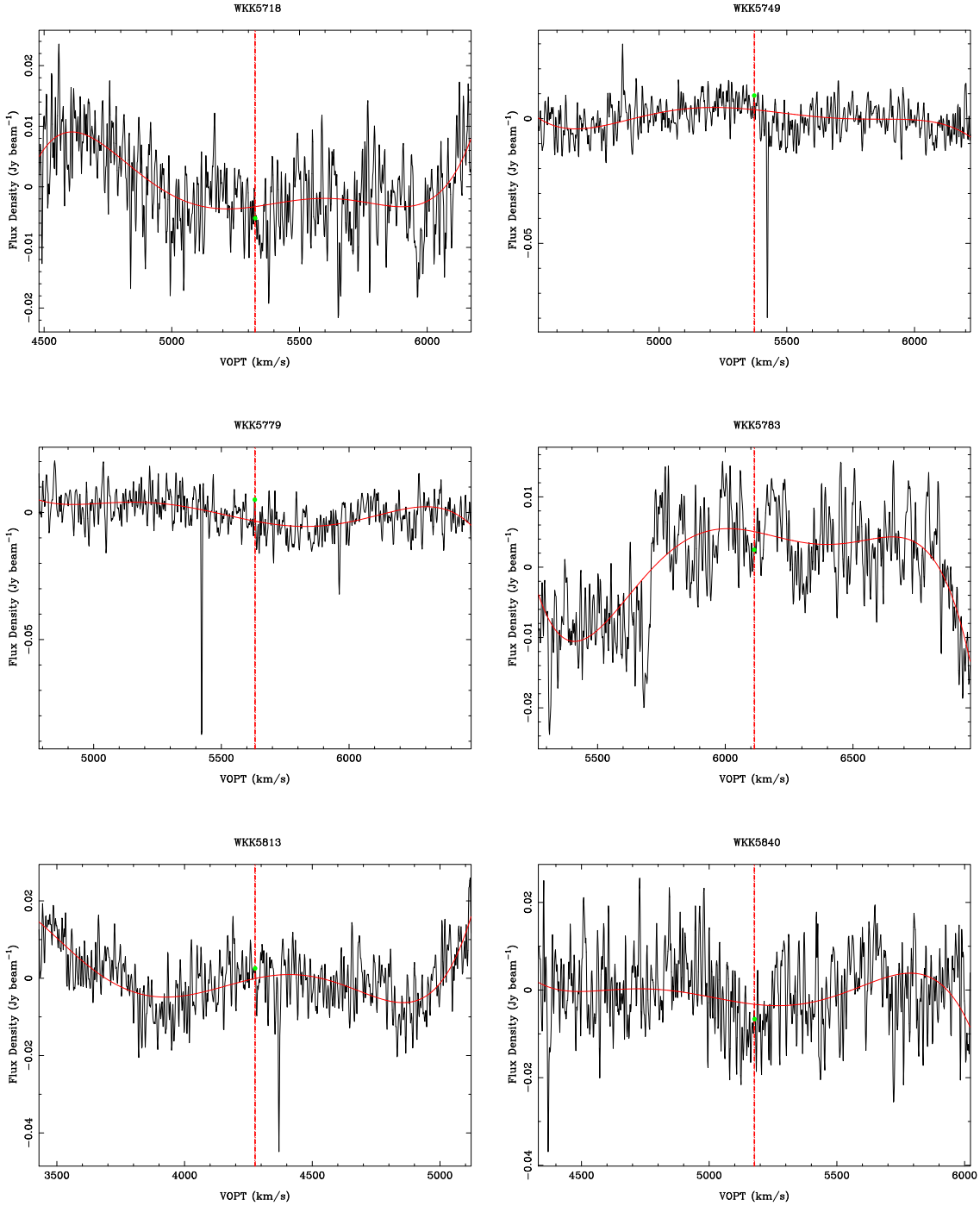

Fig. D.3: HI non-detections. In most cases, there is very poor baseline. The expected central position of the galaxy is shown by the vertical red dashed line at the centre of each spectrum.

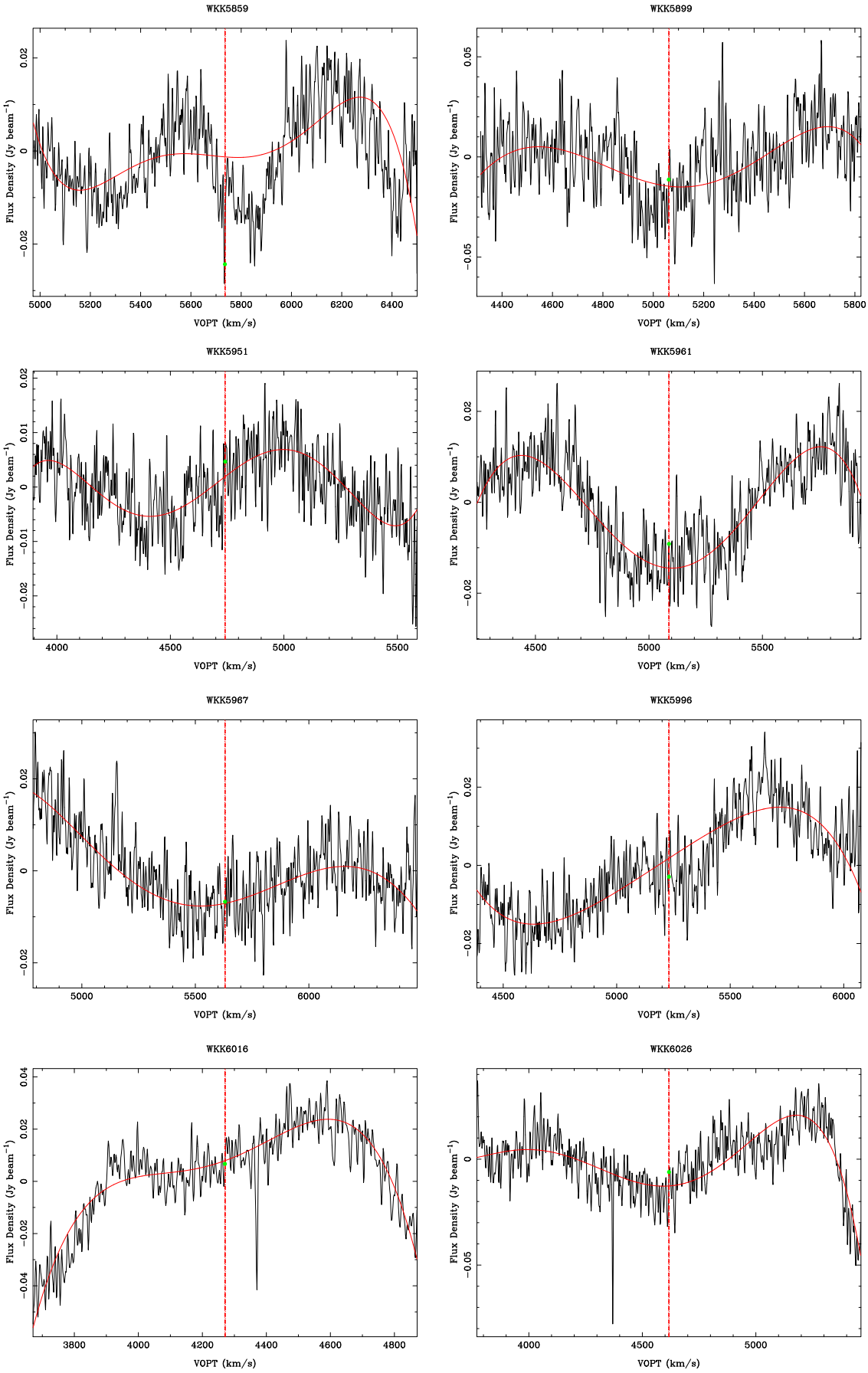

Fig. D.3: Continued ...

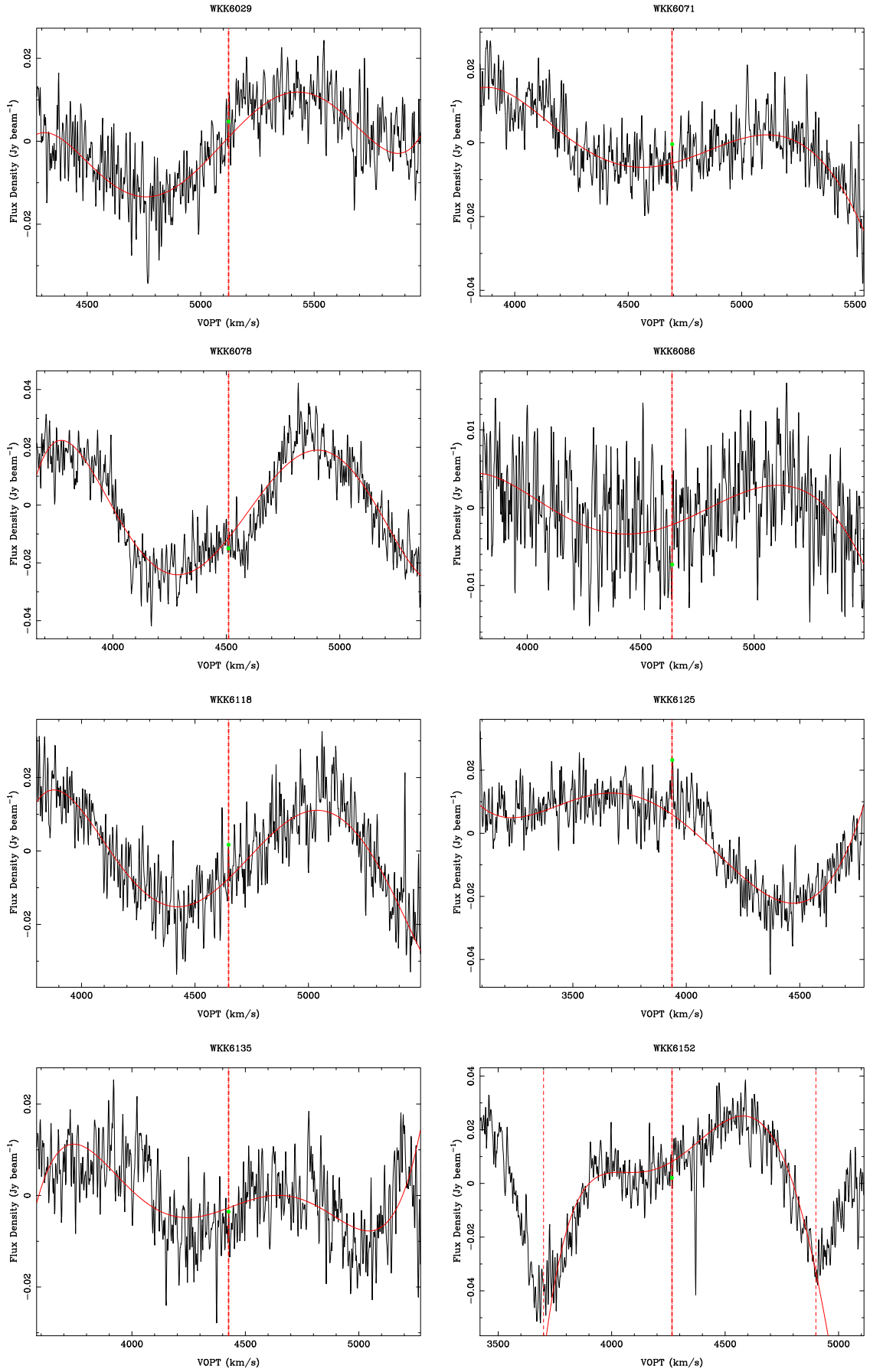

Fig. D.3: Continued ...

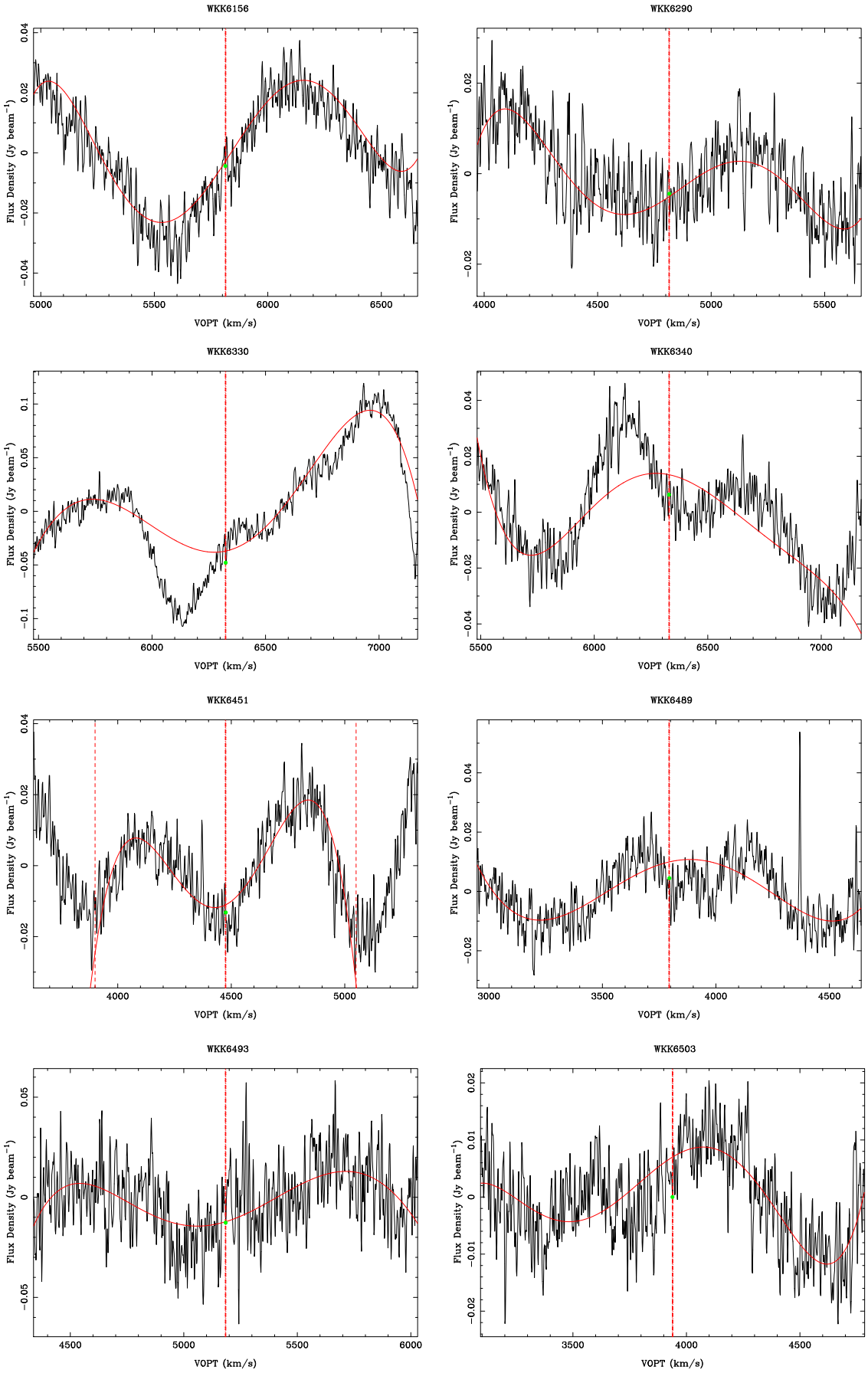

Fig. D.3: Continued ...

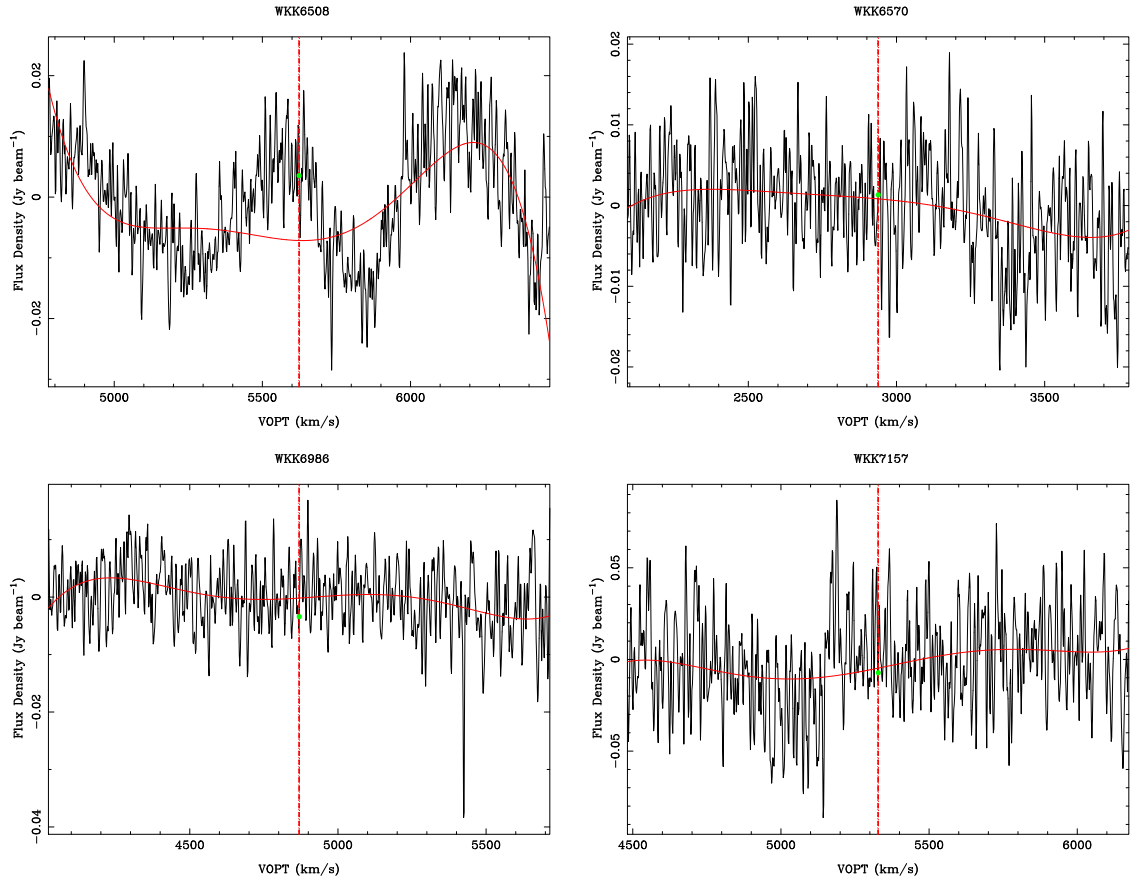

Fig. D.3: Continued .... Note that WKK 6570 was detected by Schröder et al. (2009).